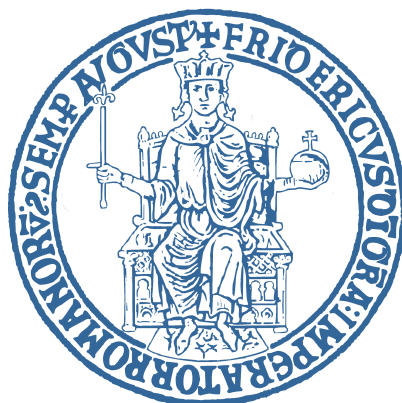


UNIVERSITÀ DEGLI STUDI DI
NAPOLI
FEDERICO II



SCUOLA POLITECNICA E DELLE SCIENZE DI BASE

Department of Industrial Engineering

Doctoral Dissertation in

INDUSTRIAL ENGINEERING

Conceptual Design of Hybrid-Electric Aircraft

Candidate:

Eng. Orefice Francesco

Tutor:

Prof. Nicolosi Fabrizio

Contents

List of Figures	iv
List of Tables	x
1 Introduction	1
1.1 Motivations and Objectives	1
1.2 Airworthiness of Hybrid-Electric Aircraft	6
1.3 State of The Art	9
1.3.1 Enabling Technologies	10
1.3.2 Design Methods	20
1.4 Research Proposal	25
2 Aircraft Model	28
2.1 Powertrain Architectures	29
2.1.1 Powertrain Equations	33
2.1.2 Engine and E-Motor Drive Decks	39
2.1.3 Fuel Cell Modelling	46
2.1.4 Battery Modelling	57
2.1.5 Cabling Sizing	64
2.1.6 Fuel Storage	71
2.2 Aero-propulsive Interactions	76
2.2.1 Distributed Electric Propulsion (DEP)	76
2.2.2 Tip-Mounted Propeller	83
2.2.3 Validation of the Methods	86
2.3 Airworthiness	100
2.3.1 One Engine Inoperative Condition (OEI)	101
2.3.2 Trim and Stability	107
2.3.3 Stall Speed and Minimum Control Speed	115
2.3.4 Flight Load Envelope	123
2.4 Weight estimation	129
2.4.1 I Class Weight Estimation	130
2.4.2 II Class Weight Estimation	132
2.4.3 III Class Weight Estimation	135

3	Point Performance of the Aircraft	148
3.1	Introduction	148
3.2	Performance and Regulation Constraints	153
3.2.1	Take-Off Constraints (FAR-23 or CS-23)	153
3.2.2	Take-Off Constraints (FAR-25 or CS-25)	154
3.2.3	Take-Off Constraints: alternative method	156
3.2.4	Landing Constraints (FAR-23 or CS-23)	158
3.2.5	Landing Constraints (FAR-25 or CS-25)	159
3.2.6	Landing Constraints: alternative method	161
3.2.7	Climb Constraints (FAR-23 or CS-23)	164
3.2.8	Climb Constraints (FAR-25 or CS-25)	167
3.2.9	Cruise Constraints	173
3.3	Preliminary Weight Assessment	174
3.4	Validation and Sensitivity Analysis	178
3.4.1	FAR-23 or CS-23	181
3.4.2	FAR-25 or CS-25	191
4	Flight Performance Analysis	199
4.1	Dynamic Model of the Propulsive System	204
4.1.1	Engine Deck Querying	205
4.1.2	Battery Discharging Cycle	210
4.2	The Flight Mission	211
4.2.1	Take-Off and Balanced Field Length	212
4.2.2	Climb and Ceiling	217
4.2.3	Cruise	222
4.2.4	Descent	224
4.2.5	Alternative Cruise	225
4.2.6	Loiter	226
4.2.7	Approach	227
4.2.8	Landing	227
4.3	Validation of the Algorithm	232
5	Application of the design process	245
5.1	PROSIB	246
5.1.1	Regional Turboprop Aircraft	247
5.1.2	Commuter Aircraft	260
5.2	ELICA	269
5.2.1	Hybrid-Electric Commuter Aircraft	273
5.2.2	Hydrogen Commuter Aircraft	281

6	Conclusions and perspectives	293
6.1	Added value and State of the Art	293
6.2	Achievements and Considerations	306
6.3	Roadmap to Clean Aviation	308
	Bibliography	313

List of Figures

1.1	Objectives of the EU research framework Clean Sky 2.	4
1.2	History of commercial aircraft fuel burn per seat-mile [32].	12
2.1	Example of hybrid-electric powertrain with AC distribution and DC e-motor drives.	30
2.2	Different propulsive systems which can be described by coupling the two hybridization factors.	32
2.3	The most general propulsive system considered in the present work. For each element, the entering and exiting powers are reported. . .	33
2.4	E-Motor drives powers calculated solving Eq. (2.5) for different operating modes and shaft power ratio at constant efficiencies and supplied power ratio ($\Phi = 0.1$, $\eta_{GT} = 0.30$, $\eta_{EM1} = \eta_{EM2} = 0.95$, $\eta_{GB} = 0.99$, $\eta_{P1} = \eta_{P2} = 0.70$, $\eta_{PM} = 1.00$).	40
2.5	Gasturbine power and fuel flow for Take-off setting (maximum throttle setting).	42
2.6	Powertrain system including fuel cells and e-storage as power sources.	46
2.7	Characteristic curve of a SINAVY FCM120 PEM fuel cell stack. . .	52
2.8	Example of compressor map.	56
2.9	Example of cells discharging curves in terms of battery capacity and state of charge for three different C-rates.	59
2.10	Chopper functional scheme.	61
2.11	Example of battery discharging curves in terms of battery capacity and state of charge for three different C-rates.	64
2.12	Derating factor related to the number of conductors in each bundle and the current load of the bundle.	68
2.13	Derating factor related to the operating altitude.	69
2.14	Ampacity in free air with respect to wire diameter at different rated and operating temperatures.	70
2.15	Ampacity of a cable considering different combinations of size and number of conductors. The minimum required current is 555 A (150 kW and 250 V DC).	71
2.16	Conventional fuel system map.	72

2.17	Geometric parameters of the distributed electric propulsive system.	77
2.18	Induced speeds and angles.	83
2.19	Induced speeds and angles.	84
2.20	Wing geometry (semi-span) considered for the first study case. . . .	87
2.21	Comparison of the results for lift and drag coefficients for different flap configurations in case of 8 distributed propellers (test case 1-1).	90
2.22	Comparison of the results for lift and drag coefficients for different flap configurations in case of 12 distributed propellers (test case 1-2).	90
2.23	Comparison of the results for lift and drag coefficients for different flap configurations in case of 16 distributed propellers (test case 1-3).	91
2.24	Particular of the wing section in take-off configuration at an angle of attack equal at 14 <i>deg</i>	92
2.25	Lift and drag coefficients in clean and take-off configurations with 8 distributed propellers.	93
2.26	Effect of the forward offset of the propeller with respect to the leading edge.	93
2.27	Drag polar variations associated to different characteristics of the tip-mounted propeller.	94
2.28	Comparison of the aerodynamic coefficients before and after the scaling at constant wingspan. The coefficients account for the aero-propulsive interaction with 16 distributed propellers. The values circled are calculated considering a linear regression.	95
2.29	Wing geometry considered for the second case study.	96
2.30	Lift curve and drag polar of the model in Fig. 2.29.	98
2.31	Lift curve and drag polar of the model in Fig. 2.29 with and without the effect of the tip-propellers.	98
2.32	Lift curve and drag polar of the model in Fig. 2.29 with and without the effect of distributed propellers.	99
2.33	Lift curve and drag polar of the model in Fig. 2.29 with and without aero-propulsive effects.	99
2.34	Propulsive subsystems for an hybrid-electric aircraft with distributed electric propulsion.	105
2.35	Body reference frame, position of the aerodynamic centers of the two lifting surfaces, and the center of gravity.	110
2.36	Characteristic angles.	110
2.37	Body reference frame and bank angle (ϕ).	113
2.38	Body reference frame and sideslip angle (β).	113
2.39	Hybrid-electric commuter aircraft.	119
2.40	Minimum control speed calculated with and without power re-distribution.	122

2.41	Doghouse plot of a commuter aircraft.	124
2.42	Manoeuvre diagram of a regional turboprop.	125
2.43	Geometry of the regional turboprop similar to ATR-42.	126
2.44	Geometry of the regional turboprop similar to ATR-42.	126
2.45	Manoeuvre diagrams of a regional turboprop similar to ATR-42 (left) and its hybrid-electric version (right) having the same maximum take-off weight (18500 kg).	128
2.46	Manoeuvre diagrams of a hybrid-electric regional turboprop with a maximum take-off weight of 22455 kg.	128
2.47	Tail load comparison a regional turboprop similar to ATR-42 (left) and its hybrid-electric version (right) (Table 2.24).	129
2.48	Turbofan engine dry mass vs thrust.	133
2.49	Turboprop engine dry mass vs shaft horse power.	133
2.50	The curves of power density (W/kg) with respect to energy density (Wh/kg) are reported for three different technological levels associated with as many years of entrance in service.	139
2.51	Flutter speed variation with respect to the dimensionless location of the engine along the wingspan (η) for the case of an engine mass concentrated on the elastic axis or forward from it up to the order of a mean aerodynamic chord.	146
2.52	Variation of the flutter speed calculated through finite element method and semi-empirical approach.	147
3.1	Conceptual Design process as proposed by the author and integrated in the design tool HEAD.	151
3.2	Take-off distance breakdown, Ref. [138].	157
3.3	x-axis and z-axis in different reference frames.	159
3.4	Landing distance breakdown, Ref. [138].	162
3.5	Sizing Plot of each component of the propulsive system.	176
3.6	Comparison of the results in terms of PREE associated to different values of the supplied power ratio and design range.	180
3.7	Comparison of the results in terms of PREE associated to different values of the supplied power ratio for a design range of 396 km and a maximum payload mass of about 1960 kg.	181
3.8	Boxplot of design range against number of passengers for FAR-23 certified aircraft. The central mark indicates the median, the bottom and top edges of the box indicate the 25th and 75th percentiles, respectively and the whiskers extend to the most extreme data points not considered outliers. The median for a 19 passenger is about 800 nmi.	184

3.9	Sizing plot.	185
3.10	Sizing plots of turbo-electric and conventional concepts. The sizing points are both referred to the same turbo-electric aircraft.	185
3.11	Comparison of three different commuter aircraft designed on a range of 400 <i>nmi</i> ($\phi = 0.90$ and 16 distributed propellers).	186
3.12	Fuel saving against shaft power ratio for three different values of battery specific energy, at constant design range (200 <i>nmi</i>) with 10% of power supplied by the e-storage in all phases and 20 distributed electric propellers enabled at take-off, landing and climb.	187
3.13	Comparison of MTOW increments with respect to CS-23 regulation constraint against range and shaft power ratio for three different values of battery specific energy. The white area refers to diverged mass estimations.	189
3.14	Comparison of fuel saving percentage against range and shaft power ratio for two different numbers of distributed propellers (8 and 12) and supplied power ratios (0 and 0.5).	190
3.15	Fuel saving percentage against range and shaft power ratio referred to two different enabling strategies of 12 distributed electric propellers mounted on a turbo-electric regional turboprop.	192
3.16	Fuel saving percentage against range and shaft power ratio for two different values of battery specific energy.	193
3.17	Sizing plot.	194
3.18	Comparison of two different regional-turboprop aircraft designed on a range of 600 <i>nmi</i> ($\phi = 0.90$ and 16 distributed propellers).	195
3.19	Sizing plots of turbo-electric and conventional concepts. The sizing points are both referred to the same turbo-electric aircraft.	195
3.20	Sizing plot curves related to take-off and landing constraints.	196
3.21	Fuel saving percentage against range and shaft power ratio for two different sizing points.	197
4.1	Analysis workflow.	203
4.2	Procedure for the interpolation of an engine deck including efficiency data.	209
4.3	Battery characteristic curves and associated power supplied.	211
4.4	Take-Off phase characteristics speeds.	212
4.5	Take-Off phase main segments.	213
4.6	Take-off ground run equilibrium of forces.	214
4.7	Regional turboprop considered.	215
4.8	Balanced field length.	217
4.9	Illustration of a general ICAO procedure to climb up to 10000 ft.	218

4.10	Different climb strategies adopted.	218
4.11	Altitude sensitivity of a fuel cell composed by 6 parallel stacks, with a resulting total design power of about 1167 kW.	221
4.12	Altitude sensitivity of a turboshaft climb power rating with a rated power of about 1167 kW.	222
4.13	Illustration of the standard procedure for descent up to 1500 ft. . .	225
4.14	Landing phase.	227
4.15	Hybrid-electric regional turboprop.	230
4.16	Particular of air brakes mounted on the tail cone the regional turboprop.	231
4.17	Comparison of different landing procedures for different values of the shaft power ratio and the throttle. The nominal thrust of the thermal engine at take-off is 1888 kW (the supplied power ratio is equal to zero).	232
4.18	Simulation for the validation of the powertrain model used in the framework of the European project ELICA (ELectric Innovative Commuter Aircraft) [183].	234
4.19	Serial/parallel partial hybrid-electric powertrain.	235
4.20	Comparison of the inputs used to describe the power supplied by the turboshaft to the propulsive system.	236
4.21	Comparison of the inputs used to describe the fuel flow associated with the thermal power supplied.	236
4.22	Comparison of the inputs used to describe the dynamics of the battery discharge cycle.	237
4.23	Comparison of the efficiency maps provided as input for the simulation of the e-motor drives.	237
4.24	Comparison of the power distribution calculated through low and high fidelity methods during the take-off phase. The take-off run covers a distance of about 730 m in about 25 seconds.	239
4.25	Geometry of ATR-42 (Source: cabin crew operating manual).	240
4.26	Cruise normalized thrust.	240
4.27	Cruise fuel flow.	241
4.28	Geometry of the Piaggio reference aircraft [184].	243
5.1	Conventional regional turboprop designed for the PROSIB project.	250
5.2	Hybrid-electric regional turboprop designed for the PROSIB project.	252
5.3	Shear forces acting on the wing at dive speed and unitary load factor.	256
5.4	Total shear force on the wing at dive speed and unitary load factor.	257
5.5	Turboprop engine at take-off.	257
5.6	Hybrid-electric powertrain at take-off.	258
5.7	Hybrid-electric commuter aircraft designed for the PROSIB project.	263

5.8	The hybrid-electric powertrain considered for the commuter aircraft of the PROSIB project.	264
5.9	Hybrid-electric commuter aircraft with a scheme of the cabling required to power the propulsive system.	266
5.10	Available power and energy with respect to the battery mass for three e-storage units with different values of specific power and specific energy.	272
5.11	DEP concept of the ELICA project.	274
5.12	Cabin section.	274
5.13	Sizing of the horizontal tailplane.	275
5.14	TIP concept of the ELICA project.	280
5.15	Propulsive architectures considered in this section.	283
5.16	Hydrogen tank.	283
5.17	House of quality comparing the four concepts designed to enter in service in 2025.	286
5.18	House of quality comparing the four concepts designed to enter in service in 2035.	287
5.19	Roadmap toward a green aviation by 2035.	288
5.20	Propulsive system of the H2-TIP concept.	289
5.21	Loading diagram of the H2-TIP concept.	290
5.22	Sizing of the horizontal tailplane for the H2-TIP concept.	290

List of Tables

1.1	Projects on Hybrid-electric or Full-electric Concepts.	7
1.2	Sustainable aviation fuels certified for blending with conventional fuel.	15
1.3	Different battery pack technologies and associated characteristics.	17
2.1	The nine operating modes.	31
2.2	Solution scenarios for Eq. (2.5) (operating mode 1)	37
2.3	Solution scenarios for Eq. (2.5) (operating mode 6)	38
2.4	Typical Engine-Deck table reporting for a set of input parameters the associated power and fuel flow.	43
2.5	Efficiency of a gearbox as a function of the rotational speed and the mechanical power.	44
2.6	The six operating modes of the system in Fig. 2.6.	47
2.7	American Wire Gauge standard and related resistivity for two differ- ent wire materials.	65
2.8	Ampacity of aluminium and copper wires at different rated tempera- tures ($60^{\circ}C$, $75^{\circ}C$ and $90^{\circ}C$) referred to an ambient temperature of $30^{\circ}C$	66
2.9	Geometric characteristics of the wing in Fig. 2.20.	88
2.10	Geometric characteristics of the wing sections.	88
2.11	Flaps geometric characteristics.	88
2.12	Design variables of interest associated with the study of the depen- dency of the aero-propulsive effects from the wing geometry.	89
2.13	Operative conditions studied.	89
2.14	Test cases considered to study the effect of different numbers of distributed propellers.	91
2.15	Geometric characteristics of the second model.	96
2.16	Geometric characteristics of the propellers.	97
2.17	Test conditions.	97
2.18	Geometric parameters of a 19-passenger hybrid-electric concept.	120
2.19	Reference power of single powerplant components.	120
2.20	Aerodynamic derivatives for the calculation of the minimum control speed.	121

2.21	Residual yawing moment and propulsive power loss at the occurrence of the failure of each possible scenario. Propulsive power before failure occurrence is 1255.5 kW.	121
2.22	Power distribution after the failure of gasturbine no. 1 (left half-wing).	123
2.23	Results for the case of one inoperative gasturbine no. 1, with and without power redistribution.	123
2.24	Characteristics of the two concepts of interest.	127
3.1	Constraints about climb phase - <i>FAR-23</i> (or <i>CS-23</i>)	165
3.2	Constraints about climb phase - <i>FAR-25</i> or <i>CS-25</i>	169
3.3	Comparison of the sizing activity of the three methods with respect to the same reference aircraft (DO-228NG).	179
3.4	Comparison of the sizing activity of the three methods varying both the supplied power ratio and the range at constant payload mass (1960 kg).	182
3.5	Comparison of the sizing activity of the three methods varying the supplied power ratio at constant range (396 km) and payload mass (1960 kg).	182
3.6	Top Level Aircraft Requirements - <i>FAR-23</i> (or <i>CS-23</i>)	183
3.7	Lift coefficient increment associated to distributed electric propulsion ($T_0 = 23130$ N, $\phi = 1$ and 62% of the wing covered by DEP).	184
3.8	Technological level	187
3.9	Top Level Aircraft Requirements - <i>FAR-25</i> or <i>CS-25</i>	191
3.10	Lift Coefficient increment associated to distributed electric propulsion ($T_0 = 60000$ N, $\phi = 1$ and 62% of the wing covered by DEP).	193
4.1	Definition of characteristics airspeeds for take-off phase.	212
4.2	Take-off stall speed and lift coefficient associated to different shaft power ratios.	216
4.3	Take-off stall speed and run associated to different shaft power ratios.	216
4.4	Balanced field length and decision speed associated to different shaft power ratios.	217
4.5	Definition of characteristic velocities of the landing phase.	228
4.6	Stall speed and maximum lift coefficient at landing for two different power ratings of a turboshaft powering eight distributed electric propellers.	230
4.7	Results of the landing simulation performed considering the first procedure described.	231
4.8	Geometric characteristics of the lifting surfaces.	238
4.9	Geometric characteristics of the fuselage.	238

4.10	Flight mission (200 <i>Nmi</i>).	241
4.11	Comparison of the results (200 <i>Nmi</i>).	242
4.12	Flight missions for the commuter reference aircraft.	243
4.13	Comparison of the results concerning the two flight simulations for the commuter reference aircraft. For the two mission profiles, the time required to complete each flight segment, the fuel consumed, and the range flown are reported.	244
5.1	Top-Level Aircraft Requirements (TLAR) for the regional turboprop configuration of the PROSIB project.	247
5.2	Main characteristics of the enabling technologies.	248
5.3	Main geometric characteristics of the conventional baseline.	250
5.4	Weight breakdown of the conventional baseline.	251
5.5	Main geometric characteristics of the hybrid-electric concept.	252
5.6	Comparison of installed power for the two regional turboprop of interest.	253
5.7	Battery model considered for the regional turboprop of the PROSIB project.	253
5.8	Aerodynamics coefficients of the hybrid-electric concept.	254
5.9	Comparison of the weight estimated for the two 40-pax concepts of the PROSIB project.	255
5.10	Comparison of performance estimated for the two 40-pax concepts of the PROSIB project.	258
5.11	Hybridization factors considered for the two mission profiles.	259
5.12	Energy consumption provided by fuel and battery for the two mission profiles.	259
5.13	Emission indexes of the turboprop engine PW150A [188].	260
5.14	Top-Level Aircraft Requirements (TLAR) for the commuter configuration of the PROSIB project.	261
5.15	Aerodynamics coefficients of the hybrid-electric commuter aircraft.	262
5.16	Main geometric characteristics of the hybrid-electric commuter aircraft.	263
5.17	Sizing power of each element of the propulsive system.	264
5.18	Battery model considered for the commuter aircraft of the PROSIB project.	265
5.19	Thrust loss and yaw moment associated with the failure of each element of the propulsive system.	266
5.20	Mass breakdown of the hybrid-electric commuter aircraft.	268
5.21	Energy consumption provided by fuel and battery for the two mission profiles flown by the commuter aircraft of the PROSIB project.	269
5.22	Top-level aircraft requirements of the ELICA project.	270

5.23	Weight breakdown of the reference aircraft.	273
5.24	Main geometric characteristics of DEP configuration.	276
5.25	Aerodynamics coefficients of the DEP concept.	277
5.26	Comparison of DEP concepts with respect to the reference aircraft.	278
5.27	Results of the design mission analysis of the DEP concepts compared the reference aircraft.	278
5.28	Results of the typical mission analysis of the DEP concepts compared the reference aircraft.	279
5.29	Comparison of DEP concepts with respect to the reference aircraft in terms of fuel consumed to accomplish design and typical missions.	279
5.30	Emissions of DEP concepts in kg of equivalent carbon dioxide for the two mission profiles considered.	280
5.31	Aerodynamics coefficients of the TIP concept.	281
5.32	Comparison of TIP concepts with respect to the reference aircraft in terms of fuel consumed to accomplish design and typical missions. .	282
5.33	Ground performance of the hybrid-electric concepts designed for the ELICA project.	282
5.34	Characteristics of the hydrogen tank.	284
5.35	Comparison of the four commuter aircraft concepts powered by fuel cells considering two different years of entrance in service (2025 and 2035).	285
5.36	Main geometric characteristics of H2-TIP configuration.	289
5.37	Weight breakdown of the H2-TIP concept.	291
6.1	Aircraft fleets and the associated battery mass required to hybridize each aircraft.	310
6.2	Production absorbed by aviation each year for battery substitution on the 10 major mainline fleets and the 10 major regional fleets. . .	311

List of Symbols

Symbol	Description
(t)	Time dependence
$A.o.A.$	Angle of attack
AC	Alternate current
$a_{c/4}$	Axial induction at 1/4 of the chord
A_{\bullet}	Area of a generic structural element
AEO	All engine operative
$AEPP$	Aircraft Electric Propulsion and Power
$AIAA$	American Institute of Aeronautics and Astronautics
a_p	Axial induction
APU	Auxiliary power unit
AR	Aspect ratio
AWG	American Wire Gauge
BAT	Battery
BFL	Balanced field length
b_w	Wingspan length
\bar{c}	Mean aerodynamic chord
C	Surface concentration of reacting species
C	Compressor torque
c	Chord length
CAS	Calibrated airspeed
C_D	Drag coefficient
C_d	2D drag coefficient
C_{D_0}	Minimum drag coefficient
C_{d_0}	2D minimum drag coefficient
C_{D_i}	Induced drag coefficient
C_{d_i}	2D induced drag coefficient
C_f	Skin friction coefficient
CFD	Computational fluid dynamics
CGR	Climb gradient rate
C_L	Lift coefficient
C_l	2D lift coefficient

Symbol	Description
$C_{L_{max}}$	Maximum lift coefficient
$C_{L_{maxL}}$	Maximum lift coefficient at landing
$C_{L_{maxTO}}$	Maximum lift coefficient at take-off
$C_{L_{\alpha}}$	Lift slope coefficient
$C_{l_{\alpha}}$	2D lift slope coefficient
$C_{L_{\alpha t}}$	Lift slope coefficient of the tail
$C_{L_{\alpha w}}$	Lift slope coefficient of the wing
$C_{M_{ac}}$	Pitching moment coefficient w.r.t. the aerodynamic center
$C_{m_{ac}}$	2D pitching moment coefficient w.r.t. the aerodynamic center
$C_{M_{acw}}$	Pitching moment coefficient w.r.t. the aerodynamic center of the wing
C_{ξ}	Roll moment coefficient
$C_{\xi \bullet}$	Roll moment control derivative coefficient
$C_{\xi \beta}$	Roll moment stability derivative coefficient
$C_{M_{c.g.}}$	Pitching moment coefficient with respect to the center of gravity
$C_{M_{f_0}}$	Pitching moment coefficient of the fuselage at null α_{wb}
$C_{M_{f\alpha}}$	Pitching moment slope coefficient of the fuselage
$C_{M_{wbacw}}$	Pitching moment coefficient w.r.t. the aerodynamic center of the wing-body
C_N	Yaw moment coefficient
$C_{N_{\beta}}$	Yaw moment stability derivative coefficient
$C_{N_{\delta \bullet}}$	Yaw moment control derivative coefficient
CO	Carbon monoxide
CO_2	Carbon dioxide
CS	Certification Specification
C_Y	Lateral force coefficient
$C_{Y_{\beta}}$	Side force coefficient slope
$C_{Y_{\delta \bullet}}$	Side force coefficient derivative
DC	Direct current
DEP	Distributed electric propulsion
DOD	Depth of discharge
D_p	Propeller diameter
e	Oswald factor

Symbol	Description
$E.I.$	Emission index
$EASA$	European Aviation Safety Agency
E_{\bullet}	Energy of a generic element
$EM1$	Primary e-motor drive/generator
$EM2$	E-motor drive powering the secondary propulsive line
EU	European Union
$EUETS$	EU emissions trading system
F	Faraday constant
f_*	Fraction of power delivered to a certain element
FAR	Federal Aviation Regulation
FC	Fuel cell
FF	Fuel flow
g	Gravity acceleration
GB	Gearbox
GDP	Gross domestic product
GT	Gasturbine
h	Planck's constant
HC	Unburned hydrocarbons
h_{H_2}	Latent heat of vaporization of liquid hydrogen
i_0	Open circuit current of a generic element
I_0	Open circuit current of a generic system
$ICAO$	International Civil Aviation Organization
$ICAO$	International Civil Aviation Organization
i_{\bullet}	Current of a generic element
i_{\bullet}	Circuit current of a generic system
I_{\bullet}	Moment of inertia (if \bullet is x, y, or z)
i_p	Propeller incidence
I_p	Power index
ISA	International Standard Atmosphere
i_w	Wing incidence
j	Current density

Symbol	Description
\dot{j}_0	Open circuit current density
k	Constant rate of reaction
L_\bullet	Length of a generic element
Li	Lithium
$Li - ion$	Lithium ions
$Li - O_2$	Lithium-oxygen
$Li - S$	Lithium-sulfur
LNG	Liquid natural gas
\dot{m}	Mass flow rate
M	Mach number
M	Boil-off mass rate
M_{bend}	Bending moment
$MTOW$	Maximum take-off weight
$MZFW$	Maximum zero-fuel weight
n	Load factor
$NASA$	National Aeronautics and Space Administration
N_{cells}	Number of fuel cells
NO_x	Nitrogen oxides
N_p	Number of battery cells in parallel
N_s	Number of battery cells in series
N_{stacks}	Number of stacks
N_{wire}	Number of wires per bundle
OEI	One engine inoperative
OEW	Operative empty weight
P	Pressure
$P1$	Primary propulsive line
$P2$	Secondary propulsive line
PAV	Personal air vehicles
P_\bullet	Power entering in a certain element
PEM	Proton exchange membrane fuel cells
PM	Particulate matter
$PMAD$	Power management and distribution unit

Symbol	Description
$PREE$	Payload-range energy efficiency
Q_{\bullet}	Capacity of a generic element
q_{∞}	Dynamic pressure infinitely upstream
q_t	Dynamic pressure at tail location
R	Universal gas constant
RC	Rate of climb
$R_{c/4}$	Radius of the slipstream at 1/4 of the wing chord
R_{\bullet}	Resistance of a generic element
RCP	Rate of climb parameter
RD	Rate of descent
Re	Reynolds number
R_p	Propeller radius
S	Shear force
$S.M.$	Safety margin
$S1$	Shaft primary propulsive line
$S2$	Shaft of the secondary propulsive line
S_a	Airborne distance
SAF	Sustainable aviation fuel
SAT	Small air transports
S_{\bullet}	Surface of the generic element
SE	Specific energy
SFC	Specific fuel consumption
S_{ground}	Ground run
S_{ground}	Ground run
S_L	Landing run
S_{LANDFL}	Landing field length
$S_{LAND_{ground}}$	Ground run of the landing phase
SOC	State of charge
$SOFCs$	Solid oxide fuel cells
SO_x	Sulphur oxides
SP	Specific power

Symbol	Description
S_{TO}	Take-off run
S_{TOFL}	Take-off field length
$S_{TO_{ground}}$	Ground run of the take-off phase
T	Temperature
T	Thrust
T	Torsion
T/W	Thrust to weight ratio
TAS	True airspeed
t_{\bullet}	Thickness of a generic element
TIP	Tip-mounted propeller
$TLAR$	Top-level aircraft requirements
TOP	Take-off parameter
TRL	Technological readiness level
$TSFC$	Thrust specific fuel consumption
u	Axially induced airspeed
US	United States of America
USD	US dollars
V_0	Open circuit voltage
V_A	Approach speed
V_{\bullet}	Voltage of a generic element
V_{\bullet}	Volume of a generic element
V_{FL}	Flare speed
V_{Fl}	Flutter airspeed
$V_{green\ dot}$	Airspeed at maximum efficiency attitude
V_{∞}	Airspeed
VLM	Vortex lattice method
V_{LO}	Lift-off speed
V_{MC}	Minimum control speed
V_p	Inlet airspeed
V_r	Rotation speed
V_S	Stall speed

Symbol	Description
V_{SL}	Stall speed in landing configuration
V_{STO}	Stall speed in take-off configuration
V_{stall}	Stall speed
V_{stall_L}	Stall speed in landing configuration
$V_{stall_{TO}}$	Stall speed in take-off configuration
\bar{V}_t	Tail volume ratio
V_{TD}	Touch-down speed
$VTOL$	Vertical take-off and landing
w	Tangentially induced airspeed
W/P	Power load
W/S	Wing load
W_{\bullet}	Weight of a generic element
w_i	Downwash speed
x_{ac}	Position of the aerodynamic center
x_{cg}	Position of the center of gravity
x_{\bullet}	Longitudinal position of a generic element
x_{O_2}	Ratio of oxygen in the air
x_p	Propeller position
y_{\bullet}	Spanwise position of a generic element
z_{\bullet}	Vertical position of a generic element
α	Transfer coefficient of the electrons
α	Angle of attack
α_{eff}	Effective angle of attack
α_i	Induced angle of attack
α_p	Angle of attack of the propulsive system
α_{wb}	Angle of attack of the wing-body
β	Compressor pressure ratio
β	Sidewash angle
δ_a	Aileron deflection angle
Δ_{\bullet}	Variation of the generic element
δ_e	Elevator deflection angle

Symbol	Description
δ_f	Flap deflection angle
ΔG	Gibbs free energy
δ_r	Rudder deflection angle
Δy_b	Fraction of the wing covered by DEP
ϵ	Downwash
η_{\bullet}	Efficiency of a generic element
η_t	Pressure ratio
θ_a	Flight path approach angle
γ	Ratio of air specific heat
Γ	Vortex intensity
$\Lambda_{c/2}$	Sweep angle at 1/2 of the chord
$\Lambda_{c/4}$	Sweep angle at 1/4 of the chord
$\Lambda_{L.E.}$	Sweep angle at leading edge
Λ_{O_2}	Ratio of oxygen supplied/required
μ_g	Brake friction
μ_{roll}	Rolling friction coefficient
ν	Number of electrons
ρ	Air density
ρ_{\bullet}	Density of a generic material
ρ_{Ω}	Resistivity
σ	Compressive and tensile stress
σ	Air density ratio w.r.t. sea level
σ_{\bullet}	Longitudinal stress along the generic axis
τ	Efficiency of the control surface
τ_{\bullet}	Shear stress along the generic axis
ϕ	Shaft power ratio
Φ	Supplied power ratio
ϕ	Bank angle
χ	Thrust ratio
ω	Induced angular speed
Ω	Angular speed

*This monument is to acknowledge that we know what
is happening and what needs to be done.
Only you know if we did it.*

— Memorial on the first Iceland glacier melted

1

Introduction

Contents

1.1	Motivations and Objectives	1
1.2	Airworthiness of Hybrid-Electric Aircraft	6
1.3	State of The Art	9
1.3.1	Enabling Technologies	10
1.3.2	Design Methods	20
1.4	Research Proposal	25

1.1 Motivations and Objectives

Nowadays, society is facing important efforts to manage modern technologies sustainably. The increasing perception of the environmental impact of technological progress drives new demands that the scientific community should face. In particular, two main objectives are mandatory: the efficient use and management of existing technologies and the introduction of new technologies specifically aimed at sustainability. Direct emissions from aviation account for about 3% of the European Union’s (EU) total greenhouse gas emissions and more than 2% of global emissions [1]. The main pollutants emitted by aircraft engines, as for the majority of technologies involving combustion, are carbon dioxide (CO_2), nitrogen oxides (NO_X), sulphur oxides (SO_X), unburned hydrocarbons (HC), carbon monoxide

(CO), particulate matter (PM), and soot. The contribution of aircraft emissions to climate change has been established in literature by different studies [2,3]. Moreover, noise emissions are part of the pollutant aircraft are responsible for and, when looking at the environmental cost of the emissions, noise turns out to be a dominant part of the total (almost 75% of the total cost [4]).

Despite aviation's contribution to global emissions is only about 2%, the aircraft is the most unsustainable means of transport currently available [5]. If nothing changes, the situation will get worse due to the rapid expansion of the sector caused by globalisation, liberalisation, combined with current matured technology, and the appearance of the low fares business models. Integrating aviation into discouraging policies will have negligible impacts both on future market growth and emissions, as stated in Ref. [6–8], where aviation activity growth rate has been fixed at 2.5% and the fuel efficiency improvements per year has been fixed at 1%. The growth rate proposed is conservative if compared with other studies, but it is in line with the recovery rate expected after the crisis due to the Covid-19 pandemic [9,10]. The most recent evaluations suggest an increment of the air transport demand by an average of 4.3% per annum over the next 20 years [11].

In 2017, air traffic carried around 4.1 billion passengers and transported 56 million tonnes of freight. In other words, every day of 2017, more than 11 million passengers and around 18 billion USD of goods were moved by air transports [11]. These figures are symptomatic of the significant impact of aviation on the global economy, which is also demonstrated by the fact that aviation represents 3.5% of the gross domestic product (GDP) worldwide. However, if the market growth estimated will be realised, countermeasures to aviation environmental impact will be mandatory to avoid suffering irreparable consequences.

When, in 2016, in order to make operative the commitments accepted by signing the Paris Agreement in 2015, the European Commission held public consultations¹ on market-based measures to reduce the environmental impact of international aviation, some cornerstones emerged. The organizations consulted stated that a

¹European Commission webpage: https://ec.europa.eu/clima/consultations/articles/0029_en

real change would be introduced starting from a different attitude towards emitters and, thus, changing the principles on which the **EU emissions trading system (EU ETS)** is based. In particular, since emissions per capita from small emitters far exceed those of commercial fare-paying passengers who are often charged an EU ETS levy, it was established the firsts should not continue to be exempted from EU ETS beyond 2020. An additional objective highlighted, which is also one of the most promising solutions, is to improve any technology, even those considered virtuous in terms of environmental impact or globally less significant. The other cornerstone considered of great importance by the most of the stakeholders is the necessity to preserve fair market competitiveness preventing competitive distortions; promoting equal treatment on same routes for operators; considering global principles on international routes and being founded on a robust Monitoring, Reporting, and Verification system.

The pillars proposed at the end of these consultations materialized in a renewed EU ETS system² and, at the same time, in a different market evolution toward new ambitions. However, as demonstrated in studies that took place before the consultations and aforementioned, the foretasted benefits of these actions will be negligible. The only possible way to reduce global emissions is through disruptive technologies and concepts integrated by innovative design methods.

When looking at the expected outcomes of research activities, moving from long-range aircraft to rotorcraft, the percentage of emission reductions change depending on the technologies and the expected improvement margins left for the employed technologies, as exemplified by Fig. 1.1 for the European research framework **Clean Sky**. The highest margins of CO_2 and NO_x reduction are related to rotorcraft and short-medium range aircraft. In these two cases, the emissions per capita are higher than those calculated in the case of regional turboprop or large transport jets which are already a matter of taxation for airlines. However, these commitments could not be sufficient. In fact, in 2018, the US-based International Council for Clean Transport warned about the fact that the actual annual growth rate of emissions,

²European Commission webpage: https://ec.europa.eu/clima/consultations_en

5.7%, is 70% higher than those used to develop ICAO's projections [12].

Large Air Transports are the main responsible for aviation emissions due

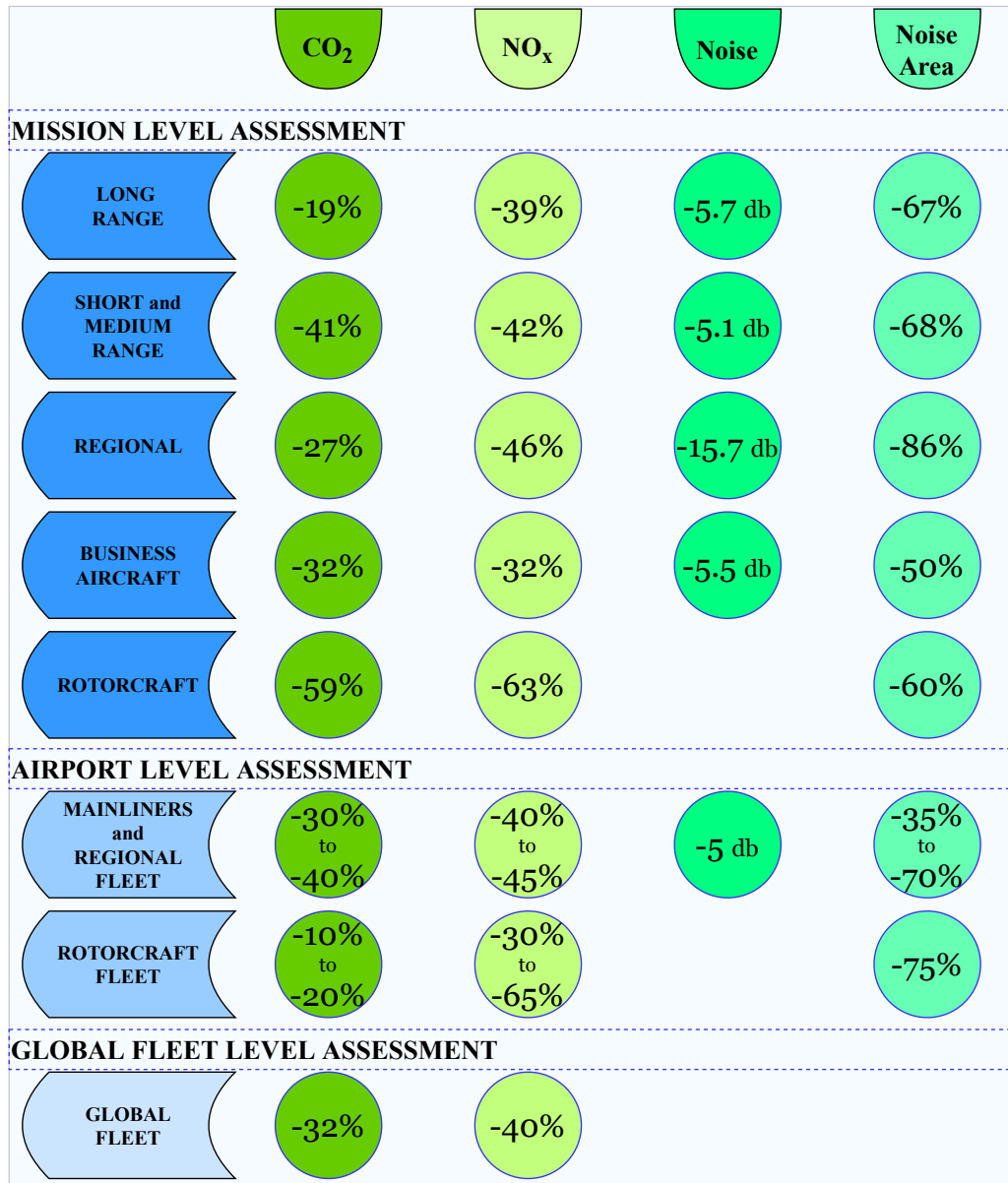


Figure 1.1: Objectives of the EU research framework Clean Sky 2.

to airlines activity, except for noise emissions [13], and even if the new Airbus A380, Boeing 787, ATR-600, Embraer E2, and Bombardier CSeries aircraft use less than 3 litres of fuel per 100 passenger kilometres³, it is also true that the most of the fleets is composed by older aircraft, most of them designed on lower

³ATAG webpage: www.atag.org/facts-figures.html

numbers of passengers. For this reason and anticipating the renewing of the fleets, some industrial projects are pushing on the reduction of emission introducing new enabling technologies: ultra-high-bypass ratio, electric propulsive systems, etc.. On the other hand, the interest in the general aviation market is growing pushed by the increment of domestic flight and, at the same time, by the possibility to rapidly apply the new hybrid technologies [14]. Furthermore, new market opportunities have been opened by the introduction of hybrid-electric propulsive systems. In particular, reduced noise and pollutants are the key factors for the introduction of these new air transports in urban contexts. This is the market segment filled by **Personal Air Vehicles** and **Small Air Transports**.

The case of small air transport (SAT) introduces different green goals with respect to the case of large air-transports [15]. Nowadays one of the major challenges of commuter transports is to make possible door-to-door travels compatibly with sustainability and environmental constraints while remaining competitive. As a matter of fact, more than 90% of global emissions is produced by large commercial aircraft that carry more than 100 passengers [16]. Thus, reduction of carbon emissions from general aviation and commuter airline operations will not impact the total carbon emission from global commercial aviation but could slowly reduce emissions of urban transports by partially sustaining the public transport in areas densely populated.

Passenger air vehicles (PAV) is an emergent aviation market that would provide on-demand aviation services. In 2003, NASA introduced this new market segment as part of its development research program. Since then, many other research projects have been developed in this direction introducing different subsections of the same market segment (e.g.: air taxis). These vehicles aim to integrate different new technologies such as vertical take-off and landing, autonomous systems, and electric propulsion.

In the end, what emerges is a list of objectives shared by research projects worldwide.

- 1 Lower emissions in terms of CO_2 , NO_x and *Noise* through new technologies or concepts. From this perspective, the introduction of boundary layer ingestion concepts, ultra-high-bypass ratio turbofan, and distributed propulsion increases the efficiency of the propulsive systems requiring a lower nominal power and/or a lower fuel consumption consequently affecting the pollutant emitted. On the other hand, new technologies (e.g.: electric motors, piezoelectric actuators, etc.) are aimed to reduce noise emissions.
- 2 Lower fuel consumption and costs. This is a crucial step for the future economy which will deal with reduced natural and financial resources. The introduction of e-storage modules, batteries, fuel-cells, and electric motors, which have high efficiency, can be considered the first important step in this direction, even if the enabling technologies for an electric powertrain still need improvements.
- 3 New routes are considered of great importance to expand the aviation market and, at the same time, to solve some problems connected to other means of transport. In fact, by reducing noise and pollutants, aircraft can be a valid candidate to substitute trains by opening new national short-range routes and cars by the introduction of urban services of air-taxi.

The efforts to achieve the aforementioned objectives have led to projects aimed to develop the enabling technologies for the future aviation. The major part of this projects fall in the hybrid-electric or full-electric field⁴ (Table 1.1).

1.2 Airworthiness of Hybrid-Electric Aircraft

The design of flying machines is strictly dependent on the regulations on which they must be certified to be operative. Airworthiness codes are constantly updated, and they must be able to merge technological improvements with an increasing level of safety. Researchers push towards disruptive concepts in aircraft design, which must be compliant with current regulations. On the other hand, aviation safety agencies draw ideas from such unconventional configurations, amending and making modifications to existing codes, as exemplified by Ref. [17, 18].

⁴ICAO webpage: www.icao.int/environmental-protection/Pages/electric-aircraft.aspx

Project	Type	Category	Entry in Service
aEro	Electric	General Aviation	2017
aEro 2	Electric	VTOL	N.A.
Airbus (A ³) Vahana	Electric	VTOL	2020
Alice	Electric	Business Aircraft	2021
Ampaire TailWind	Electric	Business Aircraft	N.A.
Aurora eVTOL	Electric	VTOL	2020
Bell Nexus	Electric	VTOL	N.A.
Boeing Sugar VOLT	Hybrid-electric	Large Commercial Aircraft	2030-2050
Bye Aerospace Sun Flyer 2	Electric	General Aviation	N.A.
City Airbus	Electric	VTOL	2023
Dreammaker	Electric	VTOL	2024
E-Fan X	Hybrid-electric	Large Commercial Aircraft	2030
eFusion	Hybrid-electric	General Aviation	N.A.
Ehang 184	Electric	VTOL	N.A.
Eviation ALICE	Electric	General Aviation	2022
Extra 330LE	Electric	General Aviation	2016
H3PS	Electric	General Aviation	N.A.
Kitty Hawk Cora	Electric	VTOL	2022
Kitty Hawk Flyer	Electric	VTOL	N.A.
Lilium	Electric	VTOL	2025
NASA X-57 Maxwell	Electric	General Aviation	2020-2021
One Solar	Electric	General Aviation	N.A.
Pipistrel Alpha Electro	Electric	General Aviation	2018
Pop up	Electric	VTOL	N.A.
SkySpark	Electric	General Aviation	N.A.
Solar Impulse 2	Electric	General Aviation	N.A.
Solar Trainer	Electric	General Aviation	N.A.
Two Solar	Electric	General Aviation	N.A.
Uber Elevate	Electric	VTOL	2023
Volocopter 2X	Electric	VTOL	2018
Volta Volare DaVinci	Hybrid-electric	General Aviation	2017
Wright Electric	Electric	Large Commercial Aircraft	2027
Yuneec International E430	Electric	General Aviation	N.A.
Zunum Aero ZA10	Hybrid-electric	Business Aircraft	2020

Table 1.1: Projects on Hybrid-electric or Full-electric Concepts.

Transport airplanes are mainly regulated by part 23 [19], *Certification Specifications for Normal, Utility, Aerobatic, and Commuter Category Aeroplanes*, and part 25 [20], *Certification Specifications for Large Aeroplanes*, of the **Certification Specification (CS)** or **Federal Aviation Regulation (FAR)**. According to subpart A of CS-23 §23.1, *Applicability*, CS-23 airworthiness code applies to *Aeroplanes in the normal, utility and aerobatic categories that have a seating configuration, excluding the pilot seat(s), of nine or fewer and a maximum certificated take-off weight of 5670 kg (12500 lb) or less; and Propeller-driven twin-engined aeroplanes in*

the commuter category that have a seating configuration, excluding the pilot seat(s), of nineteen or fewer and a maximum certificated take-off weight of 8618 kg (19000 lb). On the other hand, CS-25 §25.1 states *this Airworthiness Code is applicable to turbine powered Large Aeroplanes*, and it is applicable for a generic weight and aircraft size.

Regarding unconventional aircraft, it is not possible to estimate a priori how regulation will affect the design process. Of course, the designer can orient sizing in a simplified, cheaper direction (it means under part 23) or must consider also the possibility to certify aircraft under part 25, depending on aircraft maximum take-off weight (MTOW), for example. Nevertheless, the increment in terms of the power required and weight can greatly vary depending on the fault tolerance analysis outcomes and the safety limits imposed on the use of innovative technologies.

The regulations in force do not account for the future electric aircraft and, in most cases, the innovative configurations proposed are introducing new risks that are not explored in the current certification process. In Europe, the absence of a specific certification code for hybrid-electric and full-electric aircraft made necessary the introduction of *Special Conditions* by the **European Aviation Safety Agency (EASA)**. These give designers a framework in which aircraft can be certified in the future. In the specifications, EASA also defines the *Small Category* class, including vertical take-off and landing (VTOL) air-taxis. The category accounts for air transports up to nine passengers and a maximum take-off weight of 3175 kg. A subdivision into the certification categories *Basic* and *Enhanced* is also planned. Air-taxis fall under the latter category and will be allowed to fly over urban areas.

In many cases related to hybrid-electric technologies, regulations are still in development. For example, in case of distributed electric propulsion (DEP), the use of the aero-propulsive interactions to increase the maximum lift coefficient during take-off and landing phases is still something that should be explicitly regulated, since the reliability of high-lift devices is still considered unsatisfactory by current regulation. However, a modification to small aircraft certification regulation about the stall margin has been recently introduced making high-lift propellers a possible application [21, 22].

In the same way, the One Engine Inoperative (OEI) condition can be highly difficult to determine when distributed electric propellers and conventional propellers are applied on the same architectures. In this case, a driving factor could be the thrust provided by each propeller, or the power management architecture making some propellers more reliable than others, or the position of the propellers by virtue of the yawing moment provided with respect to the center of gravity, which is crucial when dimensioning the vertical tailplane. In literature, different solutions have been suggested [23–25], even if they cannot be considered always suitable for any type of electric configuration.

Another issue dealing with differential thrust, which is a minor but not negligible advantage of electric propulsion, is related to the possibility of reducing the vertical tail area with respect to conventional aircraft [26,27]. Since OEI condition is questionable in case of distributed electric propulsion, the critical condition considered to size the vertical tail cannot be preliminary determined. Moreover, in case of distributed propulsion, the yawing moment provided by each propeller is different, so that the OEI condition considered for to size the vertical tail could be different from the one considered to calculate the maximum thrust loss.

For these cases where regulation does not provide specific guidelines, peer-to-peer solutions will be proposed.

1.3 State of The Art

When the designer approach a new unprecedented challenge, creativity cannot be his only means. Design methodologies and enabling technologies are the cornerstones of innovation, regardless of the industrial field considered, and the designer can provide new solutions by innovating one of the two aspects or both of them. Nevertheless, the complexity of the aircraft discourages the radical innovation of the whole product, preferring to devote the efforts to the single system. The engineering challenges to make possible the design of hybrid-electric concepts are on both sides of this coin. On the one hand, the enabling technologies necessary are far from the perming solutions required to power future aircraft. On the other hand, conceptual

design methods still lack the generality necessary to investigate a wide range of possible concepts. In the present section, the state of the art is discussed.

1.3.1 Enabling Technologies

To achieve the near-zero emission target, several technologies and approaches are reviewed in this work. These enabling technologies include advanced propulsion and energy systems such as all-electric and hybrid-electric propulsion systems, high-power batteries and fuel cells for propulsion, electric motors and generators, hybrid compound engines (which combine a gasturbine and another internal combustion engine such as diesel one), thermodynamic alternatives to the simple Brayton cycle, and alternative fuels such as sustainable jet fuels, hydrogen and liquefied natural gas (LNG).

Electrical propulsion can reduce carbon and nitrogen oxide emissions if technological progress enables higher specific powers and reliability. Batteries and fuel cells provide electrical power with no emissions, but only if the electrical energy sources are sustainable. Fuel cells convert the chemical energy of fuel into electrical power without any combustion and, when hydrogen is used, the exhaust is totally carbon-free. If a hydrocarbon fuel is used, the fuel cell exhaust still contains CO_2 in direct proportion to the amount of fuel consumed, but there are no NO_X or particulate emissions. However, safety in storage and utilization is of paramount concern if hydrogen is used as fuel. Cryogenic systems and superconducting materials (operating at temperatures from 20 to 77 K) seem not feasible for commuter aircraft because of their size, weight, and safety constraints (due to the required robustness and redundancy). The same goes for LNG stored at 112 K. On the other hand, preliminary sizing of regional aircraft from literature [28, 29] highlighted advantages on the global power requirements deriving from the introduction of superconducting materials. Sustainable aviation fuels (SAF) should produce approximately the same amount of CO_2 as conventional jet fuel, but recycling the carbon already present in the biosphere and with reduced NO_X emissions. They may be an option in the near future since they do not require radical changes in the engine architecture.

Apart from the energy sources, airframe-propulsion integration shall increase the impact of advanced propulsion systems, as in case of distributed propulsion, which use multiple propulsors to achieve beneficial aero-propulsive interaction [30, 31]. Furthermore, boundary layer ingestion and laminar flow technology may contribute improving the aerodynamic efficiency by reducing the aircraft parasite drag.

All these technologies are briefly discussed in the present section, highlighting benefits and drawbacks, mainly related to the technological trends.

Conventional Propulsive System

The power needed to propel an aircraft increases at more than the airspeed squared. Thus, high powers and large energies are needed to fly at high speeds over long distances. Requirements that determine the power levels include considerations on runway length, airport elevation and ambient temperatures, climb rate, and cruise efficiency. Fuel efficiency has always been a primary design criterion for commercial aircraft since it is an important determinant of aircraft range, size, and economics. Overall, the fuel burn per seat mile of gasturbine-powered commercial aircraft has been reduced by 70% since service started in the '50s, at an average rate of about 2% per year since 1970, as shown in Fig. 1.2. About half the gain has been the result of technological improvements to the airplane, the rest to the engine. From this perspective, the evolution of current technologies plays a major role in future fuel burn reduction. In the present paragraph, the evolution of the gasturbine is discussed.

Gasturbines convert the fuel's chemical energy into rotating shaft mechanical energy. Then, the shaft power is converted into propulsive power by a propeller or by a propulsive system made of a ducted fan and a nozzle. Alternatively, in case of a prop-fan, the propulsor can consist of two large contra-rotating propellers. The mechanical complexity, weight, and maintenance cost of such a feature often shadow the aerodynamic advantages of the swirl recovery, so that the solution with a single propeller per engine is preferred.

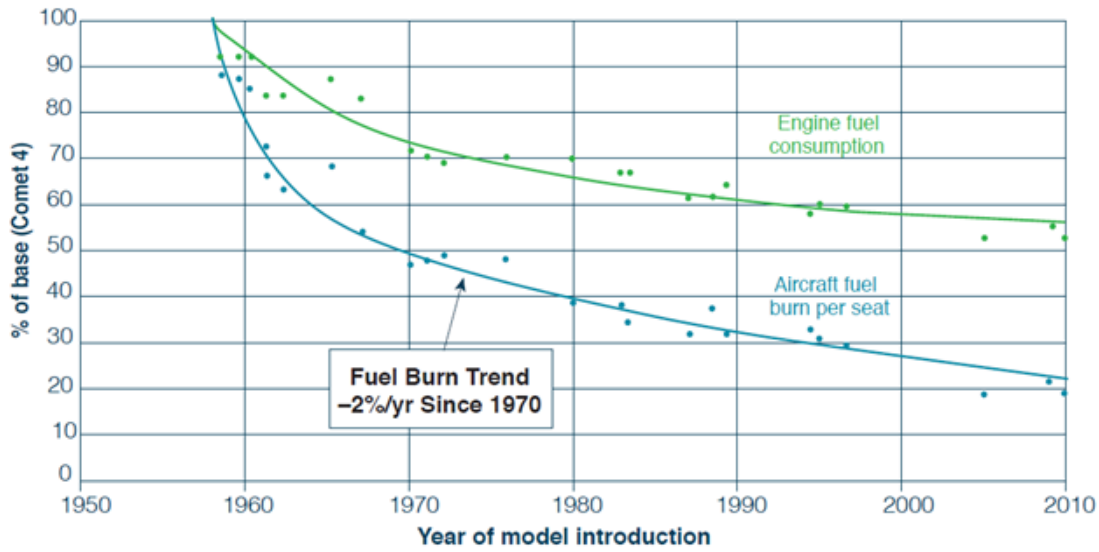


Figure 1.2: History of commercial aircraft fuel burn per seat-mile [32].

Recent studies have investigated the practical limits for simple cycle gas turbines given the potential of new materials, engine architectures, and component technologies [29, 33]. A possible improvement of 30 – 35% is estimated in overall efficiency with respect to nowadays engines in service. It may be possible to achieve thermodynamic efficiencies of 65 – 70% and propulsive efficiencies of 90 – 95%. Improvements in turbomachinery performance and reduction in cooling losses could improve thermodynamic efficiency by 19% and 6%, respectively. This gain will not be achieved only by adopting new technologies in existing engines, but it will require the optimization of the thermodynamic cycle from specific levels of component performance characteristics, temperature capability, and cooling. The practical limits of propulsive efficiency cannot be addressed at the engine level alone, but require integration within the airframe and aircraft configuration.

Concerning propulsive efficiency, it is a matter of aerodynamics studies and optimizations. The adoption of high-fidelity numerical simulations into design and a swirl recovery system should provide the achievement of the aforementioned increase in propulsive efficiency. Also, it is known that the flow accelerated through a propulsor contains energy that is pushed away from the aircraft. Thus, for a given thrust, a large propeller accelerating a large air mass is more efficient than a turbofan engine providing a significant acceleration to a small air mass. For

the same reason, several distributed small propellers instead of two big propellers may further increase the overall efficiency, provided that the weight and system complexity does not offset this advantage.

Improvement of thermodynamic efficiency requires larger pressure at compressor exit and higher turbine inlet temperatures while reducing structural weight and aerodynamic losses. Improvements in materials and manufacturing should continue the trend of the last 40 years, which provided forged titanium alloys, several nickel superalloys, single-crystal turbine airfoils, forged high-temperature powder metal alloys, coatings for environmental protection and thermal barriers, and, most recently, titanium aluminides. Advanced materials can reduce fuel burn by decreasing the engine structural weight and by further improving the heat resistance of turbine blades up to 1700°C . This includes ceramic matrix composites (CMCs) and other monolithic ceramics, which should enter into service within few years. Advances in high-temperature metallic alloys, such as nickel-based alloys as well as new materials classes such as niobium and molybdenum, have temperature capability comparable to that of CMCs and much higher fracture toughness and thermal conductivity, but a higher density. They seem suitable for static cooled parts such as combustors or turbine vanes. Additionally, coatings can increase the performance of engine parts. For cooled parts, the thermal barrier coating can significantly increase the temperature capability and reduce cooling requirements. Erosion coating can extend the operative life of the part and retain performance.

Manufacturing techniques, such as additive manufacturing, play a crucial role in innovation, offering the possibility to produce structures or properties that would otherwise be unrealisable or prohibitively expensive.

At the time of writing, it is difficult to further quantify the impact of the evolution of the gasturbine. If the overall increment (about 30%) of engine efficiency is directly linked to fuel burn, then it may be argued that carbon and presumably also NO_x emissions will reduce by the same amount in the 2035-2050 time frame. This improvement is consistent with the 2% fuel burn reduction achieved from the '70s shown in Fig. 1.2. Over 40 years, the specific fuel consumption of jet engines

has been reduced by about 25% for cruise power rating, and turboprop gained from 10% to 30% more efficiency over regional jets and large turbofans. However, fuel consumption and emissions related to cruise power rating are not sufficient to describe the impact of the advancing technology. As concerns turbofan engines, it has been shown [29,34] that during the last 40 years, thrust specific emissions during a landing-take-off cycle have been almost constant. Also, despite significant investments in aero engine technology, emissions savings are decreasing over time. This is due to several factors: emissions of carbon monoxide and hydro-carbons significantly increase at low thrust settings (landing), while NO_x high emissions at high thrust settings (take-off) and high thermal efficiency are counterbalanced by high bypass ratios engines. The emissions of CO_2 follow the same trend of thrust specific fuel consumption with engine ratings. Similar conclusions may be drawn for turboprop engines. Also, the impact of emissions at low altitudes, especially during take-off and landing phases, may be critical because of the highly urbanized areas nearby the airports and photochemical reactions in the low troposphere [35].

Sustainable Aviation Fuel

Sustainable aviation fuels (SAF) are alternative to petroleum-based jet fuels, fully compatible with the existing aircraft and fuel infrastructure, miscible with conventional jet fuels, and sustainable from environmental and socio-economic points of view. While burning SAF produces nearly the same amount of CO_2 per unit of fuel as conventional jet fuel, the net life-cycle carbon footprint is near-zero because SAF production subtracts carbon from the biosphere. If their commercialization takes place on a large scale, aviation can significantly lower its net carbon emissions more quickly and effectively than improving operations, infrastructure, and aircraft. This reduction can also be achieved without impacting the time frame or suitability of other potential carbon-lowering approaches.

Jet fuel is a generic term that encompasses many specific variants, such as Jet A, Jet A-1, JP-5, and JP-8. Jet A is the most common form of jet fuel used by commercial aviation in the United States, while Jet A-1 predominates in the rest of

the world [28]. To be fully compatible with conventional jet fuels, SAF must have high energy per unit mass, high energy per unit volume, low freezing point, low vapor pressure, materials compatibility, low toxicity, must be stable and non-volatile. These properties ensure safety and meet the required performance. Any synthetic fuel that has such characteristics is also called a drop-in fuel, in the sense that it can substitute conventional jet fuel without changing the existing aircraft fuel system or airport infrastructure. SAF production exploits woody biomass, hydrogenated fats and oils, recycled waste, and other renewable sources. The American Society for Testing and Materials (ASTM) International has developed standards ASTM D4054 and D5766 to approve new bio-based aviation fuels, and currently six production pathways have been certified for blending with conventional aviation fuel, reported in Table 1.2⁵⁶⁷. Additional pathways are currently in the ASTM certification process.

Name	Abbreviation	Feedstock	FRL	Max Blend
Fischer-Tropsch Synthetic Paraffinic Kerosene	FT-SPK	Wastes, coal, gas, sawdust	7	50%
Fischer-Tropsch Synthetic Paraffinic Kerosene and Aromatics	FT-SPK/A	Wastes, coal, gas, sawdust	7	50%
Hydroprocessed Fatty Acid Esters and Free Fatty Acid	HEFA	Vegetable oils	9	50%
Hydroprocessing of Fermented Sugars Iso-Paraffinic Kerosene	HFS-SIP	Sugarcane, sugar beet	5-7	10%
Alcohol-to-Jet Synthetic Paraffinic Kerosene	ATJ-SPK	Sugarcane, lignocellulosic, sawdust	7	50%
Co-processing		Lipidic Feedstocks	6-7	5%

Table 1.2: Sustainable aviation fuels certified for blending with conventional fuel.

Power Electronics, Distribution and Thermal Management

Power electronics already plays a key role for aircraft electrical power systems and that role becomes more critical with turbo-electric propulsive systems. Power electronics units are used for power conversion and power distribution.

Silicon carbide (SiC) power electronics enable MW-class aircraft power due to their improved efficiency and high voltage performance characteristics compared to

⁵IATA webpage: <https://www.iata.org/contentassets/d13875e9ed784f75bac90f000760e998/saf-technical-certifications.pdf>

⁶Fuel Readiness Level: http://caafi.org/information/pdf/FRL_CAAFI_Jan_2010_V16.pdf

⁷EASA webpage dedicated to SAF: <https://www.easa.europa.eu/eaer/climate-change/sustainable-aviation-fuels>

today's silicon-based power electronics. SiC is also a more reliable technology than silicon in commercial aircraft environments. Specific power for silicon-based power electronics systems today is approximately 2.2 kW/kg for aircraft applications, and their use for circuit protection is limited to 25 A at 270 VDC (7 kW). Higher powered circuit protection is provided by mechanical breakers and relays up to 500 A at 270 VDC (135 kW) using state-of-the-art equipment. It is envisioned that in 20 years SiC-based power electronics systems for aircraft applications will have a specific power of 30 kW/kg for power conversion and circuit protection using electronic components up to 200 A at $\pm 270 \text{ V}$ (essentially 540 V , for a power capacity of 108 kW) or using mechanical breakers up to 1000 A at $\pm 270 \text{ V}$ (540 kW). High specific powers will be facilitated by advances in components that make power electronics heavy: switching components, materials, switching topologies, passive filter components such as transformers, packaging, and thermal management components. The power density of power electronic devices can be increased significantly by increasing the switching frequency and by integrating the inverter into the electric machine. SiC technology can promote the increment of the frequency, due to the low switching losses. High switching frequencies reduce the amount of energy for which the passive filters and capacitors are sized.

Concerning power distribution, standard systems work at 115 VAC 400 Hz . Smaller and older aircraft systems use 28 VDC . A third option is the 270 VDC standard [36]. As matter of fact, a higher DC voltage has several advantages, such as the lower weight of cabling and inverters. Thus, $\pm 270 \text{ V}$ (or 540 V) standard seems to be the limit for the foreseeable future due to physics-based limits referred to as Paschen curve limits [37].

The ability of aircraft to manage heat is a limiting factor for the high-power electrical power systems needed for turbo-electric propulsion. The thermal management system itself requires electrical power to operate, and that power demand needs to be considered along with the demands of other non-propulsive power systems.

E-storage Unit

Batteries are electrochemical cells that store chemical compounds holding a voltage difference between the electrodes. The battery (which usually is made up of several individual cells in series and parallel) provides electric energy with a chemical reaction when the electric circuit at its poles is closed. Electrochemical cells convert the energy stored in the chemical bonds directly into electricity, without producing heat or thermal energy as an intermediate stage of the energy conversion process. Because of this, electrochemical cells are not subjected to the Carnot limitations, hence their efficiency is very high. The total chemical energy that may be converted to electric energy is equal to the energy of the electrode materials [38].

Batteries are theoretically an alternative to fossil fuels since no emissions are generated during the operative life. However, when compared to jet fuel in terms of energy stored, the current battery technology loses its attraction. The most important parameter is the equivalent specific energy, which determines how much energy can be stored per mass unit. Jet fuel stores about 12000 Wh/kg , while actual batteries are below 250 Wh/kg [39,40]. For regional hybrid-electric turboprop specific energies higher than 500 Wh/kg , ideally, 800 Wh/kg , are needed [41,42]. Current trends in battery technology concern Lithium-Ion, Lithium-Sulphur, and Lithium-Oxygen cells. Expected achievements by the year 2035 at cell level are reported in Table 1.3 [43].

Parameter	Unit	Li-Ion	Li-S	Li-O2
Specific energy	Wh/kg	250-350	600-700	800-1500
Specific power	kW/kg	500-600	350-500	300-400
Energy density	Wh/l	600-800	300-350	1000-1700
Charge/Discharge efficiency	%	90-95	70-90	60-85
Useful charge	%	70-90	90-100	70-90
Number of cycles	—	1000-3000	1000-2500	500-1000
Cost	$\$/kg$	250-350	250-500	400-800

Table 1.3: Different battery pack technologies and associated characteristics.

While theoretical specific energy is much higher than those reported, in practice the attained value will be significantly lower, because of the added weight of current

collectors, electrolytes, separators, battery cases, and terminals. At pack level, the specific energy will further decrease, due to the additional weight of casing and connectors. Packaging of electrochemical cells is necessary to achieve the desired voltage. A single Li-ion cell has a nominal voltage from 3.3 V to 4.0 V, with a typical value of 3.7 V, depending on the component bound to the lithium [38].

Lithium-ion batteries currently dominate the market in both consumer electronics and electric vehicles. Batteries can be scaled to meet power and energy requirements for aviation, as lithium-ion battery systems with power capability greater than 10 MW and energy storage capacity greater than 10 MWh have already been demonstrated in stationary energy storage for electric utility applications [29]. The maximum theoretical specific energy that can be obtained by a chemical reaction is about 550 Wh/kg. In practice, a single cell is around 210 Wh/kg and a cell pack, necessary to achieve the desired voltage, is about 150 Wh/kg [44, 45]. Improvements of Li-ion batteries regard lighter casing and safer electrodes and electrolytes. This should lead to specific energies between 250 and 350 Wh/kg at cell level by the year 2035 [43].

Lithium-sulphur batteries have been studied with the purpose of increasing the specific energy of lithium batteries. The chemical reaction provides a maximum of 2500 Wh/kg, while specific energies of 300-350 Wh/kg at cell level and 200-250 Wh/kg at pack level are available [44]. Lower TRL Li-S batteries with a specific energy of 600 Wh/kg have been tested in a controlled environment, hence it is expected that such a value could be achieved by the year 2035. The practical application of Li-S batteries is limited by a low life cycle and low efficiency that does not permit the full extraction of the chemical energy [43].

Lithium-oxygen batteries (also known as lithium-air) are the most promising concepts. The maximum theoretical specific energy is about 3450 Wh/kg, with actual battery packs for ground vehicles ranging from 300 to 700 Wh/kg and 400 Wh/kg at system level (including the gas delivery system) [46, 47]. Similar to the Li-S battery, Li-air cells have safety-related issues, low charge and discharge rates, poor energy efficiency, and limited life cycles.

The main challenge is the range of acceptable specific energies needed for the commercial introduction of battery-powered electric and hybrid aircraft propulsion systems before these systems can make a significant contribution to reducing carbon emissions in aviation. To address this problem in the short term, ongoing studies on structural batteries are considering multifunctional materials to substitute structural components (generally skin) [48].

Fuel Cell

Fuel cells convert the chemical energy of fuel into electrical power without any combustion. The exhaust from fuel cells is carbon-free if hydrogen is used as fuel. However, if a hydrocarbon fuel is used, the exhaust still contains CO_2 in direct proportion to the amount of fuel consumed, but there are no NO_X or particulate emissions [29]. Fuel cells are similar to batteries but are open thermodynamic systems, which may operate without stopping. They are continuously supplied with fluid fuels and oxidants, their electrodes are not part of the reaction process and, hence, do not need to be regenerated or recharged. In general, the oxidant is taken from air at sea level pressure, when the fuel is hydrogen or a hydrocarbon. Each fuel cell produces a nominal voltage of about 1 V, therefore, higher values of the output voltage require the packaging of several fuel cells in series, called stack. Typically, fuel cells are in stacks of 20-30 units, which provide operational voltages close to 30 V [38].

Fuel cells have been investigated for a variety of applications and, in the end, two types of fuel cells are considered for aviation [49–57]. The **proton exchange membrane (PEM) fuel cells** operate at $80^\circ C$ to $120^\circ C$ and require pure hydrogen as fuel. If a hydrocarbon fuel is used for them, it will have to be first reformed to produce pure hydrogen without any carbon oxide, which causes the catalytic poisoning of PEM fuel cells. An advantageous application of these fuel cells is the APU. However, when sized for primary propulsion, the low efficiency (up to 60%) and the low operating temperature (up to $120^\circ C$) make the cooling particularly

challenging. In contrast, **solid oxide fuel cells (SOFCs)** operate between 750°C and 1000°C and can use a variety of hydrocarbon fuels, including jet fuels.

Hydrogen is an attractive alternative to jet fuel because of its enormous amount of specific energy (about 40000 Wh/kg against the 12000 Wh/kg of kerosene) [51, 52, 58], it is stable, uniformly available on Earth, the outputs of the chemical reaction with oxygen are pure water and heat, and it can be produced by electrolysis of water. As a drawback it is a flammable and explosive gas so that it must be carefully stored and transported in special containers, it has a very low density at ambient conditions, and it must be compressed or liquefied to store a significant mass.

In the context of hydrogen storage or production on aircraft, there are at least four solutions available. Pure hydrogen may be stored as a compressed gas in a pressurized tank or as a liquid in a cryogenic tank [59]. It may be also safely stored as a metal hydride, a heavier compound that is stable at ambient conditions that can be safely heated to separate the hydrogen. Finally, the hydrogen can be extracted from a hydro-carbon like jet fuel, a process known as reformation. It has been shown that the reformation process is the lightest solution to generate hydrogen on-board for long-range applications [56]. However, the pressurized hydrogen seems to be the most efficient solution, followed by the cryogenic tank.

A fuel cell can be represented as a power conversion unit when continuously fuelled to produce electric power, and sized based on power, while at system level the energy is the sizing parameter [53].

1.3.2 Design Methods

The design process always starts from the identification of an unheeded request coming from a group of stakeholders. When the need is not clearly expressed by a project brief or a call for proposals, the design activity is intended to anticipate the market demand that could result from disruptive changes in the socio-economic and political fabrics. This latter case is often pushed by an unfair advantage that the designer has on his competitors, making him aware of something unknown by

the others. When the expectations that the new product should meet are defined, the actual design process can start [60].

Generally, the design process involves several distinct parts, each one associated with a different level of complexity and detail. Following the path of Ref. [61, 62], the design steps identified are the following:

- Conceptual design;
- Preliminary design;
- Detailed design.

In the early stages of the design process, the foresight of the designer is limited by many aspects. Firstly, the objective of meeting new market demands improving an original baseline. Secondly, the necessity of approaching a multidisciplinary design from different perspectives, typically involving informal or semi-formal representations or drawings of the concept. Finally, the inclusion of multiple tools created for the specific type of architecture, which could be a limiting factor in case of wide design spaces.

The **conceptual design** phase is intended to answer the following question: *what is the configuration meeting performance and regulation requirements?* This design phase is a fluid and iterative process equally driven by top-level aircraft requirements generated by different stakeholders and regulatory constraints. The first step is the choice of the available technologies, summarized for the present work in 1.3.1. An optimistic estimation of the availability could result in an increment of time and costs at the following design phases, as well as higher development risks [62]. This design phase is the main focus of the present work and it is divided in two different steps. The first one is the sizing activity properly so-called, defining the boundaries of the design space by estimating the minimum point performance requirements. The results of this activity are proposed in the form of trade-off studies, providing a guideline of the sensitivity of the concept to the different parameters (e.g.: technological levels, high-lift propulsion geometric parameters). The following one is the flight performance analysis, which requires a preliminary yet reliable estimation of aerodynamics, weights, and propulsive characteristics.

The following step, conventionally named **preliminary design**, is intended to design the single systems sizing the components at subsystems level. With the purpose of saving time and reduce costs, this design phase begins when the configuration has been frozen. This could be a limiting factor in case of hybrid, where the propulsive system architecture can have a high impact at configuration level. The objective of this phase is the preparation of the full-scale development.

The last phase, named **detail design**, is associated with high technological readiness levels since the actual parts composing the aircraft are made ready to be produced.

In literature, different methods approaching the conceptual design of conventional aircraft are documented [60–64]. The first step of the design process, the conceptual design activity, is commonly divided into two major parts: the estimation of point performance, which would provide information about the design space in terms of maximum wing loading and power loading, and the mission performance, aimed to verify the compliance of the configuration with expectations. The classical sizing approach is here discussed in order to highlight the inadequacy of classical methods to face future challenges. Point performance of hybrid-electric aircraft is highly penalized by classical methods which do not take into account the propulsive architecture. When approaching the estimation of the constraints curves delimiting the design space in the sizing plot, the presence of tip-mounted propellers, distributed electric propulsion (DEP) or boundary layer ingestion is not considered by classical methods [64]. When approaching concepts including high-lift propulsion or other propulsive architectures specifically designed to take advantage of aero-propulsive interactions, the required power loading, and wing loading can be drastically increased from the early stages of the design process if methods intended to account for these effects are available. When referring to the estimation of the required power loading, conventional design methods measure the constraints in terms of total shaft power. Considering the different efficiencies of the propulsive lines (e.g.: electric propulsive line and thermal propulsive line), as well as the thrust distribution, depending on the architecture, it could be that electrically-powered

propellers have a different efficiency with respect to those directly coupled to a gas-turbine. To avoid the necessity of referring to an equivalent conventional propulsive system, the present work proposes the estimation of point mass performance in terms of total propulsive power loading [41, 65] and wing loading. In order to take into account the aero-propulsive interactions affecting the constraints curves, a similar approach to the one presented in Ref. [41] is adopted. Point performance at aircraft level is, then, considered as starting point to estimate the sizing power of each element of the propulsive system, depending on the chosen architecture depending on the energy path [41, 66].

When analysing mission performance, some characteristics need to be frozen: masses, aerodynamics, and propulsive characteristics. The maximum take-off weight (MTOW) can be estimated through two different approaches: the first one is based on statistical correlations between the operative empty weight and the maximum take-off weight of flying aircraft [64], the second one is based on a first well-educated guess about the maximum take-off weight and the energetic requirements [41]. The statistical approach performs a first order weight estimation based on the intersection of two different equations, as shown in 2.4.1. Since no flying hybrid aircraft or innovative configurations can be considered to define the regression lines, this method cannot be considered to design concepts proposed in the present work. The second approach proposed in literature is limited by the reliability of the initial well-educated guess on the MTOW. This first attempt is, then, corrected by the estimation of the fuel and e-storage masses necessary to accomplish the design mission. In classical methods, when the tank volume has not been fixed yet, the energy required to complete the design mission is estimated in order to calculate the fuel weight [61, 63]. In literature, some improvements to this method have been proposed to make it suitable for hybrid-electric concepts [67]. The energetic requirements can be calculated considering an equivalent conventional propulsive system or the Breguet equations, whose correction in case of two power sources has been discussed in Ref. [68]. In 2.4.2, from the enhancement of the mass estimation method proposed in Ref. [61, 63], an additional method is suggested

that can be applied when the characteristics of each single system are known. The aerodynamic characteristics of the aircraft can be estimated with classical methods. Conversely, the aero-propulsive interactions require a different approach [22, 69, 70]. Differently from drag polars or lift curves, the aero-propulsive interactions cannot be preliminary determined. This would require the simulation of the flight mission and the querying of an appropriate engine deck to calculate the thrust provided. Finally, the propulsive characteristics are the last set of inputs required for estimating mission performance. Conventionally, the engine deck provides information about the thrust or shaft power provided. Associated to each point of the engine deck, the quantity of fuel necessary to power the engine is reported in terms of specific fuel consumption. However, when an electric propulsive line is present, the powertrain model is complicated to the point where a thermal engine deck is not sufficient. A suitable alternative is proposed in 2.1.

The present work introduces the conceptual design process for conventional, hybrid-electric, and full-electric aircraft, developed at the University of Naples Federico II by the author. As already mentioned, this part of the design process is divided in two different steps which will be extensively investigated in the following chapters, namely 3 and 4. However, before proceeding to detail the single procedures, an overview is necessary to provide the reader with all the instruments to link the single parts of this research work. As noted above, everything starts from the top-level aircraft requirements, regardless of the objective. Nevertheless, some reference points are necessary to guide the project and assure its competitiveness in the market. In general, this point is covered by collecting all the information available about similar aircraft. The Pre-Design tool designed at the University of Naples Federico II collects the information regarding a wide range of aircraft and, based on the set of top-level aircraft requirements, provides a baseline for the comparison. Once the conventional aircraft serving the same market segment has been identified, the design process can start. Clearly, the estimation of the point performance is the first step. Since the objective of the sizing activity is to highlight the sensitiveness of the design space to some specific parameters, it can

be assumed that the geometry is similar to the one provided by the Pre-Design tool without loss of generality. In this way, it can be investigated how some design parameters affect the constraints of the design space when the others are frozen. The end of this phase provides the necessary information to create the first concept. For example, the wing load and the maximum lifting capability are the driving factors for the lifting surfaces. In the same way, the sensitivity analysis drives the design of the propulsive system. All these considerations contribute to the design of the aircraft from which the following step of the conceptual design phase starts. The estimation of flight performance is used to refine this concept. This can require some iterations, particularly if design and typical missions are studied with the objective of optimizing the energy sources to reduce emissions while containing the weight increment. The refined concept obtained closes the conceptual design chain.

1.4 Research Proposal

The work titled *Conceptual Design of Hybrid-Electric Aircraft* has the high goal of proposing a unique workflow applicable to hybrid-electric, full-electric, and conventional aircraft. The design process described is composed of a group of activities, conventionally referred to as conceptual design, that aims to choose the most promising configuration of an electric aircraft.

Traditionally, the conceptual design drives the choice of the configuration by trade-off studies among the feasible concepts, then, the preliminary design refines the aircraft sizing at system level. However, this approach has the disadvantage to make the designer blind to the strong connection between the configuration competitiveness and the design of the single systems. For example, when designing an electric propulsive system, the cabling is a critical aspect of the aircraft weight estimation that was once left to the preliminary design due to its lower impact on the total take-off mass. Another example is the efficiencies of the single elements or the fuel tank size in case of hydrogen, aspects that could drastically affect the competitiveness of an aircraft when the main requirement deals with the fuel saving percentage. Finally, another example is the impact of the electric

powertrain architecture when sizing the vertical tailplane, due to the possibility of redistributing power among the subsystems.

The refinement of some major systems during the design activity could increase the required time to choose the configuration, making it costly inefficient. In fact, time-demanding high or medium-fidelity methods are commonly applied to design powertrain systems. Moreover, the inconsistency of the fidelity levels could produce results that cannot be properly interpreted to choose the right design element. Thus, the challenge is the introduction of low and medium-fidelity methods that can provide reliable results in a short time.

Thus, the research problem can be summed up by the following question: *how can the conceptual design process be revised to design electric concepts?*

Classical design procedures are limited when dealing with unconventional configurations [71]. The objective of this work is the enhancement of the conceptual design to account for the effects that the single systems have on flight performance. The structure of the work reflects the design procedure following the progress of the research. The following list introduces each step of the research path indicating the associated chapter of this work where it is treated.

- The first step is the definition of the scientific background necessary to model the different aircraft systems and their effects on flight performance. In this context, the mathematical models created, their applicability, and the limits are discussed in chapter 2.
- The trade-off studies of the possible configurations, designed with a chosen set of technologies and aimed to fulfil specific top-level aircraft requirements, are based on the sizing methods proposed in chapter 3. The estimation of point performance is a quick way to understand the effect of the propulsive architecture on flight performance when the mathematical models are based on the preliminary information available.
- The last step is the mission analysis, discussed in chapter 4, which is based on the simulation of each time step of the mission profile.

The last chapter, chapter 5, deals with the application of the design process for two different research projects.

Let the future tell the truth, and evaluate each one according to his work and accomplishments. The present is theirs; the future, for which I have really worked, is mine.

— Nikola Tesla

2

Aircraft Model

Contents

2.1	Powertrain Architectures	29
2.1.1	Powertrain Equations	33
2.1.2	Engine and E-Motor Drive Decks	39
2.1.3	Fuel Cell Modelling	46
2.1.4	Battery Modelling	57
2.1.5	Cabling Sizing	64
2.1.6	Fuel Storage	71
2.2	Aero-propulsive Interactions	76
2.2.1	Distributed Electric Propulsion (DEP)	76
2.2.2	Tip-Mounted Propeller	83
2.2.3	Validation of the Methods	86
2.3	Airworthiness	100
2.3.1	One Engine Inoperative Condition (OEI)	101
2.3.2	Trim and Stability	107
2.3.3	Stall Speed and Minimum Control Speed	115
2.3.4	Flight Load Envelope	123
2.4	Weight estimation	129
2.4.1	I Class Weight Estimation	130
2.4.2	II Class Weight Estimation	132
2.4.3	III Class Weight Estimation	135

2.1 Powertrain Architectures

When modelling hybrid-electric, full-electric, or conventional aircraft, the first and most important difference from which the design process starts is the propulsive system. Regardless of the configuration, innovative or not, the propulsive system is what characterizes the electrification of the aircraft. In the present work, the systems are described considering, where possible, the figures of merit chosen by the Aircraft Electric Propulsion and Power (AEPP) Working Group. This team formed by the American Institute of Aeronautics and Astronautics (AIAA) with the aim of coordinating the various technical and program committees working on this topic has standardized some common parameters to the various electric aircraft design projects. Nevertheless, many others will be introduced to describe in the most simple way complex and various systems from the early stages of the design process.

When approaching these innovative configurations, the most common idea is the coupling of propellers and/or fans with e-motor drives. This can be the first issue when accounting for the different optimal speeds of a propeller and an electric motor. However, regardless of the details which will be further discussed, the direct coupling of a propulsive unit (propeller or fan) with an e-motor drive is addressed as *secondary propulsive line*. This type of coupling is generally aimed to power high-speed propellers, often characterized by high-solidity and lower dimensions. This is the case of distributed electric propulsion, also called high-lift propellers. On the other hand, the coupling of a large propeller with an e-motor drive requires the presence of a gearbox. This propulsive line is addressed as *primary propulsive line*. An accurate and general model of the propulsive system should include every element contributing to the power management and its distribution (buses, power units, and so on), as shown in Fig. 2.1. However, the main objective of the present paragraph deals with system modelling, thus, some hypotheses can simplify the task without lacking generality. In this perspective, switchers, inverters, and converters can be neglected in the mathematical model considering their efficiency is close to one. Yet, their presence will be accounted for their contribution to the total powertrain system mass. The same goes for cabling.

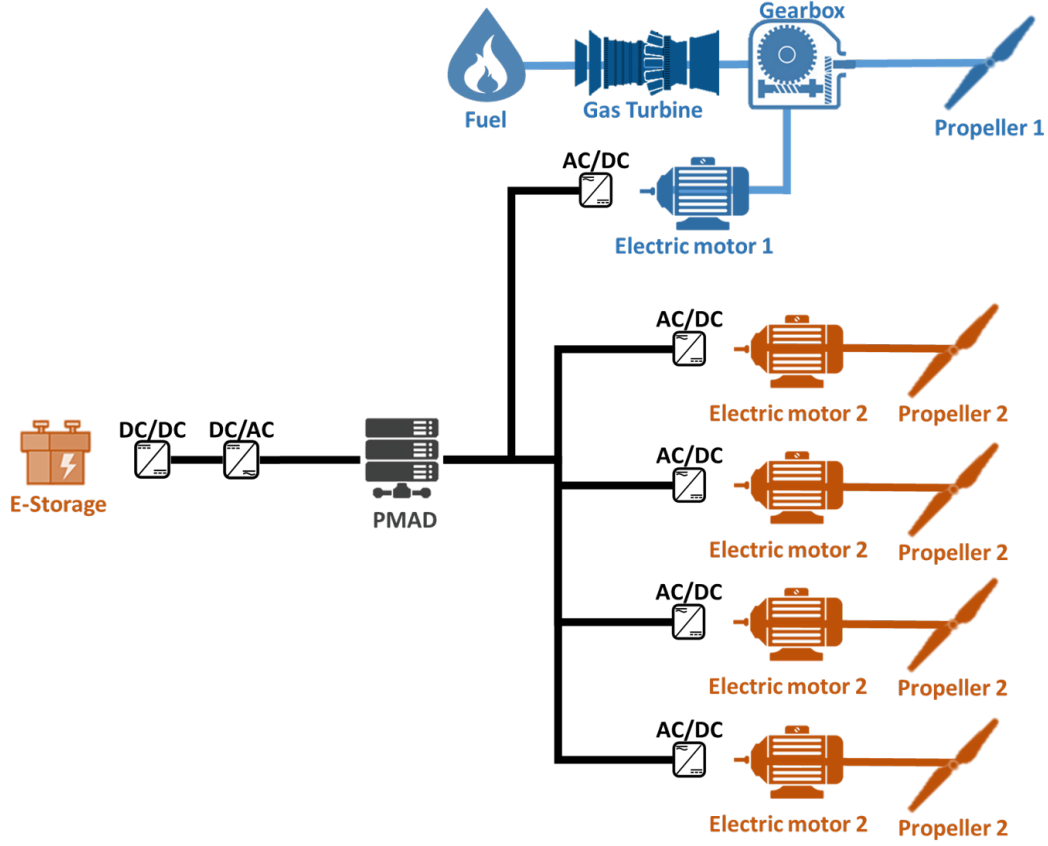


Figure 2.1: Example of hybrid-electric powertrain with AC distribution and DC e-motor drives.

The **shaft power ratio**, ϕ , as called in literature [41, 72], is the ratio of shaft power provided by the secondary propulsive line with respect to the total shaft power of the propulsive system.

$$\phi = \frac{P_{s2}}{P_{s1} + P_{s2}} \quad (2.1)$$

Pushed by the increasing interest in greener aviation, the presence of battery and fuel cells is a major topic in most industrial and research projects. However, the difficult coupling of power sources suggests the presence of no more than two different power sources. In general, the presence of a thermal engine or a fuel cell coupled to an e-storage unit is quite common with respect to the coupling of a thermal engine with a fuel cell. Thus, in the present case, regardless of the unit transforming the chemical power to mechanical, kinetic, or electric power, the e-storage is addressed as *secondary power source* and the *primary power source* is the fuel.

Considering these two power sources, the other hybridization factor considered is the **supplied power ratio**, which is the ratio of power provided by the e-storage with respect to the total power provided to the propulsive power system.

$$\Phi = \frac{P_{e-storage}}{P_{fuel} + P_{e-storage}} \quad (2.2)$$

The combination of different hybridization parameters can be used to describe a wide range of propulsive systems, as shown in Fig. 2.2. Typically, the secondary e-motor drive can be coupled with a high-speed/high-solidity propeller without a gearbox.

The two power ratios are not sufficient to describe the operating conditions of a propulsive architecture. For this purpose, different operating modes are introduced [41]. The **operating modes** can be used to describe the path of the energy along the propulsive system. The operating modes are described by the direction of the entering power in four different elements of the propulsive system, as reported in Table 2.1. The general propulsive architecture to which the following discussion is referred is shown in Fig. 2.3. As stated previously, the mathematical model proposed in the present work does not include the power units (inverters, converters, and choppers) or the cabling. Furthermore, the two different propulsive lines can be recognized by their colors: the first propulsive line powered by the gasturbine is coloured blue in Fig. 2.3, while the second one is powered by the battery through the *e-motor drive 2* and is coloured red in the same figure. Obviously, depending on the hybridization factors, some operating modes can be non-physical depending on the different powertrain architecture considered. For example, the first operating mode is not feasible in case of supplied power ratio equal to one and shaft power ratio equal to zero, since the e-motor drive should work as motor, but the operating mode imposes it as generator.

	Operating modes								
	1	2	3	4	5	6	7	8	9
<i>Propeller 1</i>	Thrust	Thrust	Thrust	Thrust	Thrust	Thrust	Harvest	Harvest	Harvest
<i>Propeller 2</i>	Thrust	Thrust	Harvest	Thrust	Harvest	Harvest	Thrust	Thrust	Harvest
<i>E-storage</i>	Discharge	Charge	Charge	Discharge	Discharge	Charge	Discharge	Charge	Charge
<i>E-motor drive 1</i>	Generator	Generator	Generator	Motor	Motor	Motor	Generator	Generator	Generator

Table 2.1: The nine operating modes.

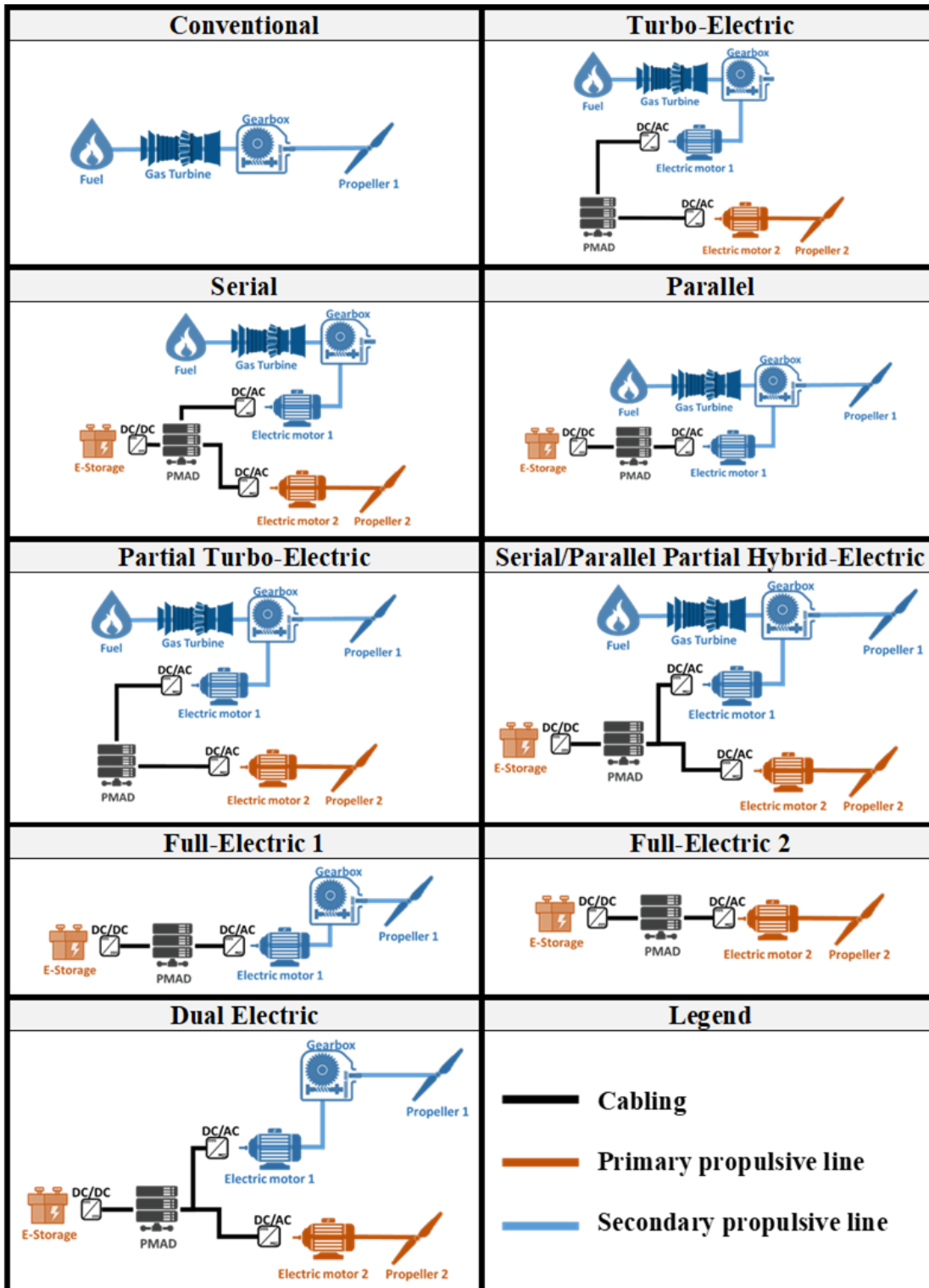


Figure 2.2: Different propulsive systems which can be described by coupling the two hybridization factors.

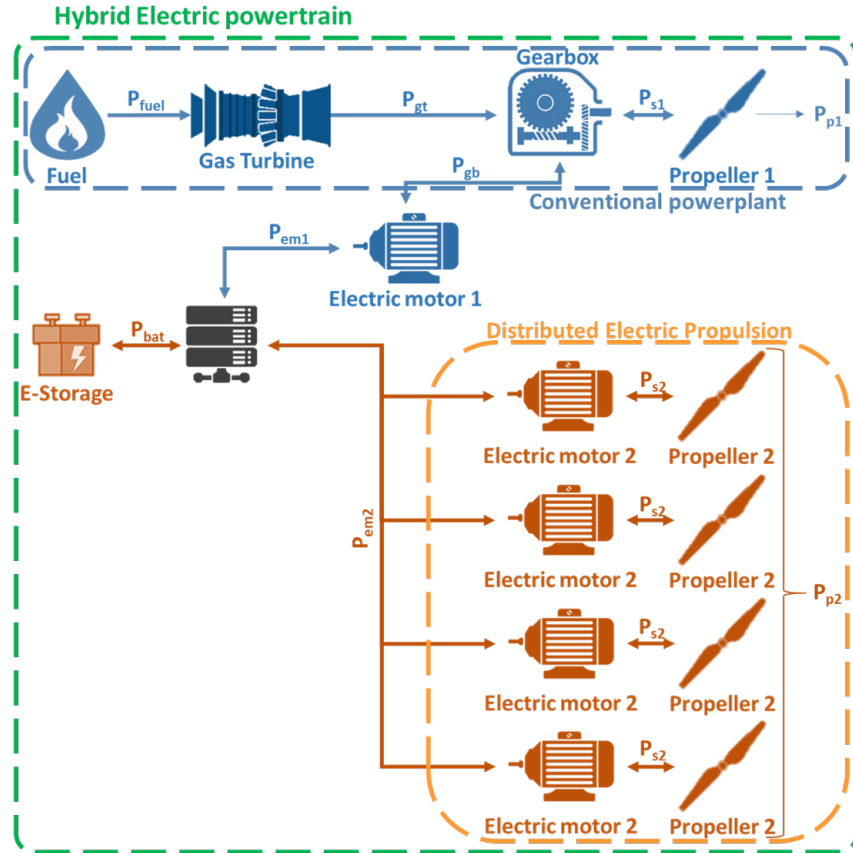


Figure 2.3: The most general propulsive system considered in the present work. For each element, the entering and exiting powers are reported.

2.1.1 Powertrain Equations

The propulsive system has been described up to this point considering the shaft power ratio and the supplied power ratio, regardless of the connection between the propulsive units and power sources. Including both the operating modes and the hybridization factors, the power distribution along the powertrain shown in Fig. 2.3 can be described considering a system of ten equations based on the energy conservation principle. In other words, the sum of the entering power is equal to the sum of the exiting power and the dissipated power. Each operating mode presented requires a different system of equations to be described. Thus, nine different systems of equations should be identified. Each of them is written differently depending on which power value is known. In conclusion, nine different systems of equations are identified for each known power value. In general, this

group of equations is called **Powertrain Equations**. Four different cases are here reported depending on the different steps of the design process. The first system of equations considered deals with the system of equations written when the required propulsive power is estimated at aircraft level, but the dimensioning power of each element should be calculated. Differently from this case, when a flight simulation is performed, an engine deck describes the shaft power or the thrust supplied by a conventional powerplant. However, for hybrid-electric powertrain, the relationship between engine deck and shaft power is complicated by the presence of two different power sources. For this reason, before discussing the type of engine deck necessary to describe this type of propulsive architecture, three more groups of powertrain equations are introduced which depend on assigned values of gasturbine power and e-motor drive power (primary or secondary). The powertrain equations can be written both in terms of power or inverse of the power loading.

The first set of equations is referred to the case of known propulsive power and nine different forms can be proposed depending on the operating mode chosen. Eq. (2.3) describes the power distribution in case of the first operating mode. It is here highlighted both the strong dependence on the efficiency, η , of each element and on the hybridization factors. Equations are proposed considering the direct coupling of secondary e-motor drive and propellers.

$$\begin{bmatrix} -\eta_{GT} & 1 & 0 & 0 & 0 & 0 & 0 & 0 & 0 & 0 \\ 0 & -\eta_{GB} & 1 & 1 & 0 & 0 & 0 & 0 & 0 & 0 \\ 0 & 0 & 0 & -\eta_{P1} & 0 & 0 & 0 & 0 & 1 & 0 \\ 0 & 0 & -\eta_{EM1} & 0 & 1 & 0 & 0 & 0 & 0 & 0 \\ 0 & 0 & 0 & 0 & -\eta_{PM} & -\eta_{PM} & 1 & 0 & 0 & 0 \\ 0 & 0 & 0 & 0 & 0 & 0 & -\eta_{EM2} & 1 & 0 & 0 \\ 0 & 0 & 0 & 0 & 0 & 0 & 0 & -\eta_{P2} & 0 & 1 \\ \Phi & 0 & 0 & 0 & 0 & (\Phi - 1) & 0 & 0 & 0 & 0 \\ 0 & 0 & 0 & \phi & 0 & 0 & 0 & (\phi - 1) & 0 & 0 \\ 0 & 0 & 0 & 0 & 0 & 0 & 0 & 0 & 1 & 1 \end{bmatrix} \begin{bmatrix} P_{Fuel} \\ P_{GT} \\ P_{GB} \\ P_{S1} \\ P_{EM1} \\ P_{BAT} \\ P_{EM2} \\ P_{S2} \\ P_{P1} \\ P_{P2} \end{bmatrix} = \begin{bmatrix} 0 \\ 0 \\ 0 \\ 0 \\ 0 \\ 0 \\ 0 \\ 0 \\ 0 \\ 0 \end{bmatrix} \quad (2.3)$$

The linear system of equations proposed for the first operating mode is characterized by a certain energy flow. In this case, the e-motor drive 1 works as generator, transforming the mechanical power from the thermal engine into electrical power. At the same time, the battery supplies energy to the propulsive system, and the total power supplied arrives at the propellers where thrust is produced. The application

of the energy conservation principle can be applied in other operating conditions to derive the resulting powertrain equations. Eq. 2.4 provides the same linear system for the sixth operating mode.

$$\begin{bmatrix} -\eta_{GT} & 1 & 0 & 0 & 0 & 0 & 0 & 0 & 0 & 0 \\ 0 & -\eta_{GB} & -\eta_{GB} & 1 & 0 & 0 & 0 & 0 & 0 & 0 \\ 0 & 0 & 0 & -\eta_{P1} & 0 & 0 & 0 & 0 & 1 & 0 \\ 0 & 0 & 1 & 0 & -\eta_{EM1} & 0 & 0 & 0 & 0 & 0 \\ 0 & 0 & 0 & 0 & 1 & 1 & -\eta_{PM} & 0 & 0 & 0 \\ 0 & 0 & 0 & 0 & 0 & 0 & 1 & -\eta_{EM2} & 0 & 0 \\ 0 & 0 & 0 & 0 & 0 & 0 & 0 & 1 & 0 & -\eta_{P2} \\ \Phi & 0 & 0 & 0 & 0 & (\Phi - 1) & 0 & 0 & 0 & 0 \\ 0 & 0 & 0 & \phi & 0 & 0 & 0 & (\phi - 1) & 0 & 0 \\ 0 & 0 & 0 & 0 & 0 & 0 & 0 & 0 & 1 & 1 \end{bmatrix} \begin{bmatrix} P_{Fuel} \\ P_{GT} \\ P_{GB} \\ P_{S1} \\ P_{EM1} \\ P_{BAT} \\ P_{EM2} \\ P_{S2} \\ P_{P1} \\ P_{P2} \end{bmatrix} = \begin{bmatrix} 0 \\ 0 \\ 0 \\ 0 \\ 0 \\ 0 \\ 0 \\ 0 \\ 0 \\ P_P \end{bmatrix} \quad (2.4)$$

When the required propulsive power is one of the unknown variables in the system of equations, it is necessary to interrogate an engine deck. The engine deck provides information about the gasturbine power when the supplied power ratio is lower than one, otherwise, the power provided is the primary e-motor drive power, if the shaft power ratio is equal to zero, or, on the contrary, the secondary e-motor drive. Moving from this power and the efficiencies of each element of the propulsive system, a set of equations provides the value of propulsive power. Differently from the powertrain equations presented previously (Eq. 2.3), where the known value is the total propulsive power, three different linear systems are here proposed depending on the supplied or shaft power ratios. In fact, the linear systems have a singularity for certain values of the hybridization factors. Considering the nine operating modes introduced in Tab. 2.1, nine different linear systems for each case should be proposed. Eq. (2.5) shows one of these linear systems of equations in terms of gasturbine power for the first operating mode.

$$\begin{bmatrix} -\eta_{GT} & 0 & 0 & 0 & 0 & 0 & 0 & 0 & 0 & 0 \\ 0 & 1 & 1 & 0 & 0 & 0 & 0 & 0 & 0 & 0 \\ 0 & 0 & -\eta_{P1} & 0 & 0 & 0 & 0 & 1 & 0 & 0 \\ 0 & -\eta_{EM1} & 0 & 1 & 0 & 0 & 0 & 0 & 0 & 0 \\ 0 & 0 & 0 & -\eta_{PM} & -\eta_{PM} & 1 & 0 & 0 & 0 & 0 \\ 0 & 0 & 0 & 0 & 0 & -\eta_{EM2} & 1 & 0 & 0 & 0 \\ 0 & 0 & 0 & 0 & 0 & 0 & -\eta_{P2} & 0 & 1 & 0 \\ \Phi & 0 & 0 & 0 & (\Phi - 1) & 0 & 0 & 0 & 0 & 0 \\ 0 & 0 & \phi & 0 & 0 & 0 & (\phi - 1) & 0 & 0 & 0 \\ 0 & 0 & 0 & 0 & 0 & 0 & 0 & 1 & 1 & -1 \end{bmatrix} \begin{bmatrix} P_{Fuel} \\ P_{GB} \\ P_{S1} \\ P_{EM1} \\ P_{BAT} \\ P_{EM2} \\ P_{S2} \\ P_{P1} \\ P_{P2} \\ P_P \end{bmatrix} = \begin{bmatrix} -P_{GT} \\ \eta_{GB}P_{GT} \\ 0 \\ 0 \\ 0 \\ 0 \\ 0 \\ 0 \\ 0 \\ 0 \end{bmatrix} \quad (2.5)$$

Similar sets of equations can be written for the case of known value of electric motor drives power. Eq. (2.6) and Eq. (2.7) are referred to the case of known values

of primary e-motor drive power and secondary e-motor drive power, respectively.

$$\begin{bmatrix} -\eta_{GT} & 0 & 0 & 1 & 0 & 0 & 0 & 0 & 0 & 0 \\ 0 & 1 & 1 & -\eta_{GB} & 0 & 0 & 0 & 0 & 0 & 0 \\ 0 & 0 & -\eta_{P1} & 0 & 0 & 0 & 0 & 1 & 0 & 0 \\ 0 & \eta_{EM1} & 0 & 0 & 0 & 0 & 0 & 0 & 0 & 0 \\ 0 & 0 & 0 & 0 & -\eta_{PM} & 1 & 0 & 0 & 0 & 0 \\ 0 & 0 & 0 & 0 & 0 & -\eta_{EM2} & 1 & 0 & 0 & 0 \\ 0 & 0 & 0 & 0 & 0 & 0 & -\eta_{P2} & 0 & 1 & 0 \\ \Phi & 0 & 0 & 0 & (\Phi - 1) & 0 & 0 & 0 & 0 & 0 \\ 0 & 0 & \phi & 0 & 0 & 0 & (\phi - 1) & 0 & 0 & 0 \\ 0 & 0 & 0 & 0 & 0 & 0 & 0 & 1 & 1 & -1 \end{bmatrix} \begin{bmatrix} P_{Fuel} \\ P_{GB} \\ P_{S1} \\ P_{GT} \\ P_{BAT} \\ P_{EM2} \\ P_{S2} \\ P_{P1} \\ P_{P2} \\ P_P \end{bmatrix} = \begin{bmatrix} 0 \\ 0 \\ 0 \\ P_{EM1} \\ \eta_{PM} P_{EM1} \\ 0 \\ 0 \\ 0 \\ 0 \\ 0 \end{bmatrix} \quad (2.6)$$

$$\begin{bmatrix} -\eta_{GT} & 0 & 0 & 1 & 0 & 0 & 0 & 0 & 0 & 0 \\ 0 & 1 & 1 & -\eta_{GB} & 0 & 0 & 0 & 0 & 0 & 0 \\ 0 & 0 & -\eta_{P1} & 0 & 0 & 0 & 0 & 1 & 0 & 0 \\ 0 & -\eta_{EM1} & 0 & 0 & 0 & 1 & 0 & 0 & 0 & 0 \\ 0 & 0 & 0 & 0 & \eta_{PM} & \eta_{PM} & 0 & 0 & 0 & 0 \\ 0 & 0 & 0 & 0 & 0 & 0 & 1 & 0 & 0 & 0 \\ 0 & 0 & 0 & 0 & 0 & 0 & -\eta_{P2} & 0 & 1 & 0 \\ \Phi & 0 & 0 & 0 & (\Phi - 1) & 0 & 0 & 0 & 0 & 0 \\ 0 & 0 & \phi & 0 & 0 & 0 & (\phi - 1) & 0 & 0 & 0 \\ 0 & 0 & 0 & 0 & 0 & 0 & 0 & 1 & 1 & -1 \end{bmatrix} \begin{bmatrix} P_{Fuel} \\ P_{GB} \\ P_{S1} \\ P_{GT} \\ P_{BAT} \\ P_{EM1} \\ P_{S2} \\ P_{P1} \\ P_{P2} \\ P_P \end{bmatrix} = \begin{bmatrix} 0 \\ 0 \\ 0 \\ 0 \\ P_{EM2} \\ \eta_{EM2} P_{EM2} \\ 0 \\ 0 \\ 0 \\ 0 \end{bmatrix} \quad (2.7)$$

In addition to non-physical configurations, certain sets of hybridization factors and operating modes could lead to singularity in the solution of the associated powertrain equations. The designer choices leading to these undesired conditions and the fundamental role of the efficiencies are here discussed. When setting the system of equations, the assigned efficiencies are assumed to be positive, as well as the power constituting the quantity known on the right-hand side. The physical results are those composed of all positive powers, with only two exceptions to this rule: the harvest condition of the propellers and the charging battery require a shaft, propulsive and the e-storage powers to be negative. The following study case discussed deals with the powertrain architecture described by Eq. (2.5), but it is here remarked that specific considerations are necessary for each mathematical model chosen and operating mode. The objective of this study is to provide preliminary guidelines for the automatic management of critical operating conditions that could support the design of the power management and distribution unit.

Before focusing the attention on singularities, the corrective procedures to exclude non-physical conditions are here discussed. The imposed positivity of supplied power ratio, gasturbine efficiency, and power imply that the battery power

is always positive by virtue of Eq. (2.2). Also, the secondary electric power is always non-negative. In fact, a scenario with $P_{EM1} < 0$ and $P_{EM1} \leq 0$ is impossible, since this would determine a positive P_{P2} and a negative P_{P1} , inconsistently with the ninth of Eq. (2.5), when $\phi > 0$; at the same time, a scenario with both $P_{EM2} < 0$ and $P_{EM1} > 0$ is also impossible since this would imply negative values of P_{BAT} .

With respect to the first operating mode, as shown in Table 2.2, a solution with $P_{EM1} < 0$ and $P_{EM2} \geq 0$ may occur, violating the positivity constraint on all the resulting powers. As a matter of fact, combinations of low values of shaft power ratio and high values of supplied power ratio determine a negative primary electric motor power. In other words, a non-physical solution is obtained for the first operating mode when the power demand of the secondary propulsive line is lower than the power supplied by the battery. In this case, the switch to the fourth operating mode can be sufficient to satisfy the positivity constraint. Similarly, focusing on the fourth operating mode, which is non-physical for high values of shaft power ratio and low values of supplied power ratio, switching to the first operating mode excludes non-physical solution.

P_{EM1}	P_{EM2}	Interpretation
≥ 0	≥ 0	Acceptable solution.
< 0	≥ 0	More primary propulsive power absorbed than supplied.
< 0	< 0	$P_{S1} > 0, P_{S2} < 0$: impossible since $\phi > 0$
> 0	≤ 0	$P_{BAT} < 0$: impossible since $\Phi \geq 0$.

Table 2.2: Solution scenarios for Eq. (2.5) (operating mode 1)

Differently from the operating conditions discussed previously, the sixth operating mode is characterized by a harvest propulsive unit ($P_{P2} \leq 0$) and the battery recharging ($P_{BAT} \leq 0$). Consistent with these assumptions, positive values of electric power, primary shaft power, and primary propulsive power are expected, as well as negative values of secondary propulsive power, secondary shaft power, and battery power. In this case, the interpretation of the results is less intuitive, but the following non-physical conditions can be identified. For relatively small values of shaft power ratio and large values of supplied power ratio, P_{EM1} and

P_{EM2} can be simultaneously negative, with $|P_{EM1}| > |P_{EM2}|$, meaning that the battery power demand is excessive and not compatible with the assigned shaft power ratio. The same happens in the case of a high shaft power ratio, where the power required from the primary shaft is excessive and reduces the power available for recharging the battery. For values of shaft and supplied power ratios both relatively low, or both relatively high, it happens that only P_{EM1} has a negative value, meaning that more power must be shifted from the primary propulsion system towards the battery and the secondary propulsion system. Some corrective procedures are proposed in Table 2.3.

\mathbf{P}_{EM1}	\mathbf{P}_{EM2}	Interpretation
≥ 0	≥ 0	Acceptable solution.
< 0	≥ 0	More battery power required than supplied. Less primary propulsive power required.
< 0	< 0	More battery power required than supplied. More secondary propulsive power required.
≥ 0	≤ 0	$P_{BAT} < 0$: impossible since $\Phi \leq 0$.

Table 2.3: Solution scenarios for Eq. (2.5) (operating mode 6)

All the corrective procedures for non-physical solutions are managed remaining the operating conditions of the battery unchanged. The other operating modes can be studied as proposed for the previous examples. Regardless of the implementation strategy adopted, the definition of high and low values here reported is strongly dependent from the efficiencies of the powertrain elements and cannot be fixed a priori. Additionally, the matrix of coefficients is characterized by singularity points that depend on the efficiency or the hybridization factors chosen. Considering a generic set of efficiencies, the following equations identify the shaft power ratios for which the matrices of each operating mode are singular. The singularity condition of the third operating mode is presented in Eq. (2.8). For the fifth and sixth operating modes, Eq. (2.9) determines the singularity condition, while the seventh and eighth operating modes matrices are singular for the shaft power ratio presented in Eq. (2.10). It is here highlighted that ϕ_7 is always smaller than ϕ_5 .

$$\phi_3 = \frac{\eta_{EM1}}{\eta_{EM1} + \eta_{EM2}} \quad (2.8)$$

$$\phi_5 = \phi_6 = \frac{1}{1 + \eta_{EM1}\eta_{EM2}\eta_{PM}\eta_{GB}} \quad (2.9)$$

$$\phi_7 = \phi_8 = \frac{\eta_{EM1}\eta_{EM2}\eta_{PM}\eta_{GB}}{1 + \eta_{EM1}\eta_{EM2}\eta_{PM}\eta_{GB}} \quad (2.10)$$

For shaft power ratios close to the singularity, the corresponding system matrix is poorly conditioned. The understanding of the singularity condition is a mandatory step when programming the automatic switch from an operating mode to another when a certain event happens. Switching to a singular destination mode could open infinite loops between non-physical interconnected modes. On the other hand, apparently complementary modes may be both non-physical due to the different efficiencies of the system. For instance, considering the sixth mode (Table 2.1), high values of ϕ and low values of Φ would require switching to the eighth mode, after checking the singularity condition: $\phi > \phi_8$. In this case, the condition $\phi > \phi_6$ is not sufficient, since the interval between ϕ_6 and ϕ_8 may not correspond to physical solutions for either mode 6 or mode 8. Thus, in this condition, it could be advisable to switch from the sixth operating mode to the ninth. The mathematical model cannot neglect the study of the solution space, as shown in Fig. 2.4 before assessing the reliability of the results.

As already pointed out, the present section deals with powertrain equations solved considering an assigned gas turbine power. Since these equations badly conditioned for $\Phi = 1$, the same study on the reliability of the solutions should be performed on Eq. (2.6) and Eq. (2.7).

2.1.2 Engine and E-Motor Drive Decks

When simulating the flight mission, the characteristics influencing the flight dynamics need to be estimated, thus, total thrust, aerodynamics, aero-propulsive interactions, and energy consumption should be estimated step by step during the flight path. In the present section, the thrust estimation is the main purpose. Thus, after discussing engine decks that would be most suited to describe a general hybrid-electric aircraft, the coupling with the powertrain equations is presented.

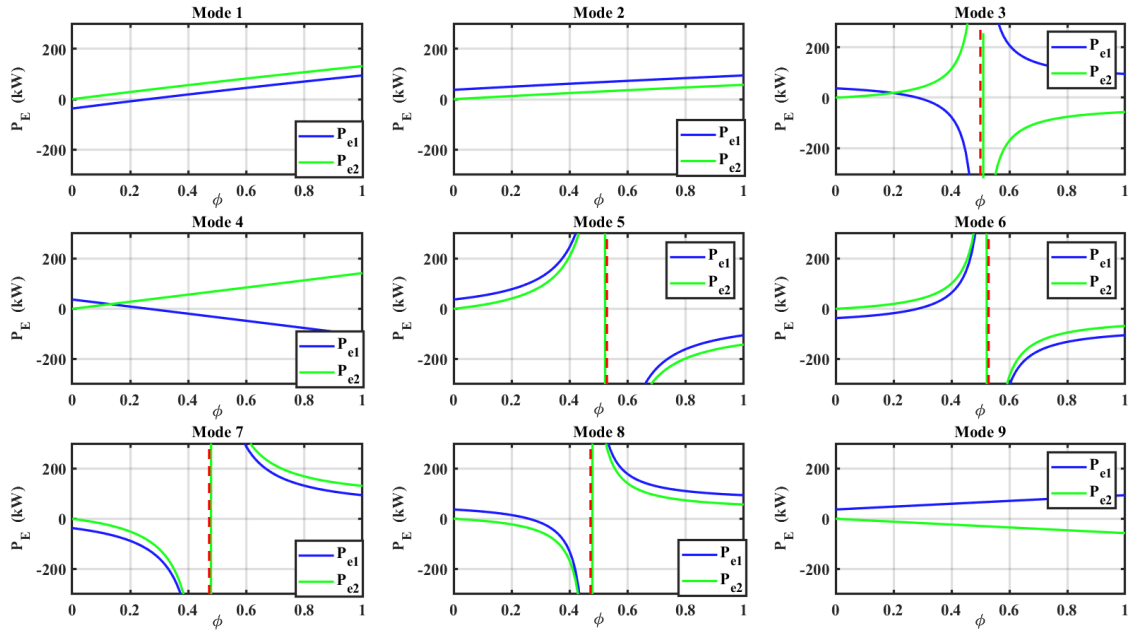


Figure 2.4: E-Motor drives powers calculated solving Eq. (2.5) for different operating modes and shaft power ratio at constant efficiencies and supplied power ratio ($\Phi = 0.1$, $\eta_{GT} = 0.30$, $\eta_{EM1} = \eta_{EM2} = 0.95$, $\eta_{GB} = 0.99$, $\eta_{P1} = \eta_{P2} = 0.70$, $\eta_{PM} = 1.00$).

Considering the most general propulsive system introduced in Fig. 2.3, the importance of defining the fraction of thrust due to thermal power source can be considered a major issue for mission analysis. However, in the present case, differently from other approaches where the propulsive architecture is reported to an equivalent thermal engine, the powertrain system is considered in its original definition. In fact, by approaching the powertrain architecture considering all the nodes of the energy path, architectures, where the same propulsive element is alimeted by both power sources, are easy to manage. The **engine deck** is a data matrix providing information about the propulsive system in terms of shaft power or thrust and the fuel burnt is calculated considering the specific fuel consumption (SFC) or the thrust specific fuel consumption (TSFC) associated [23, 73]. This data matrix is provided by the engine manufacturer divided into different power ratings which refers to different flight segments. In the present work, the engine deck is provided in terms of gastrubine power, when the thermal power source is present, or, if the thermal power source is not present, in terms of e-motor drive power, which can be referred to the motor drive providing power to the secondary

propulsive system or the primary propulsive system depending on the shaft power ratio (Eq. (2.59)) considered. The power considered is thus directly connected to the thermal power source, if present, or to the shaft power ratio, if the thermal power is not present and no fuel is consumed. When the gasturbine is substituted by a fuel cell, the same approach is valid, but the power considered for the engine deck is in terms of fuel cell power, which is the power provided by this element to the propulsive architecture. On the other hand, even if the fuel consumed is generally based on TSFC or SFC, which depends on thrust or power, respectively, in the present case, the fuel flow is more suited to describe the fuel consumed to provide the thermal power. In fact, in case of partial hybrid-electric architecture, it could be difficult to calculate the exact percentage of power provided to the two propulsive lines (Fig. 2.3) related to the thermal power source. Thus, the first step is the definition of the engine deck in terms of power ratings: Take-off, Automatic Power Reserve (APR), Flight Idle, Ground Idle, Max Continuous, Climb, and Cruise. Each power rating should provide a response surface defining for a wide range of Mach number, altitude, throttle and deviation from standard temperature, the values of power, the efficiency of each element of the powertrain, the fuel flow, and the emissions. For hybrid-electric concepts, the engine deck will provide the values of gasturbine power (Fig. 2.5), then, depending on the combination of powertrain elements efficiencies, supplied power ratio and shaft power ratio, the power managed by each power unit is estimated through the powertrain equations (Eq. (2.5)).

To interrogate the engine deck, four different parameters are assigned: altitude, Mach number, throttle, and deviation from ISA temperature¹ [74]. Altitude, Mach number, and temperature depend on mission requirements. The throttle setting, on the other hand, can be assigned, but it should be compliant with mission constraints and sizing powers of the electric components of the powertrain. The throttle is set considering two different constraints. The first one is the optional condition of constant speed, which requires the equilibrium between thrust and drag. This is a typical condition to calculate the required throttle during flight phases like

¹The ICAO Standard Atmospheric Model provides the temperature as a function of the altitude. The deviation from this temperature is reported as a positive or negative value in the engine deck.

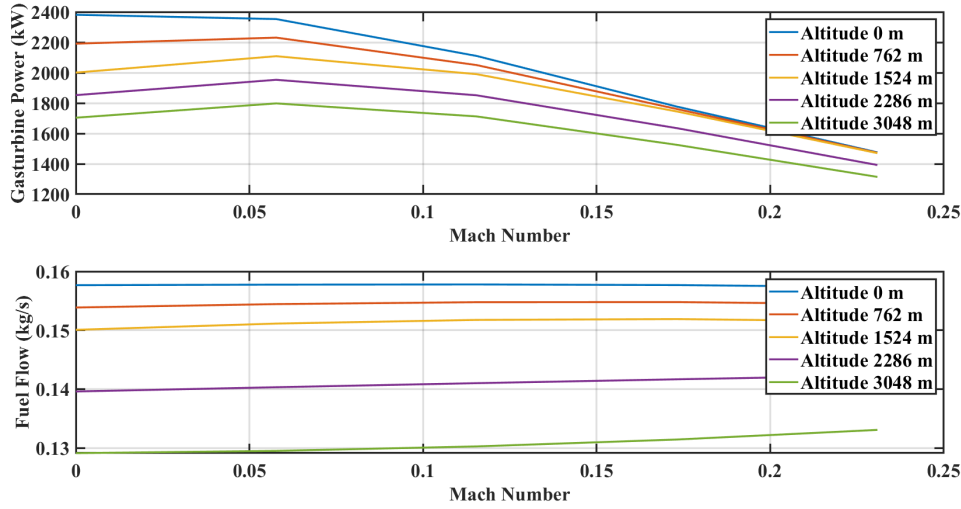


Figure 2.5: Gasturbine power and fuel flow for Take-off setting (maximum throttle setting).

cruise, alternative cruise, and loiter. The second constraint considered is due to the particular architecture of hybrid-electric aircraft and deals with the sizing power of the powertrain elements. The powertrain equations drive the estimation step by step of the propulsive power and allow the estimation of the power entering in each e-motor drive. This is a crucial factor to estimate the maximum throttle permitted during a certain segment of the flight mission for that combination of supplied and shaft power ratios. When the measured power entering the e-motor drives is higher than the sizing power of the element, a new and lower value of throttle is calculated to be compliant with the dimensioning power. It is also possible to maintain the same throttle calculating a different supplied power ratio. 4.1 provides a detailed algorithm for propulsive power estimation.

In general, when the right combination of throttle, ISA temperature deviation, Mach number, and altitude is determined, the gasturbine power is obtained and the value of propulsive power is calculated by Eq. (2.5), as well as the corresponding fuel flow. At that point, aero-propulsive interactions and flight dynamics can be studied. The use of Eq. (2.5), or the corresponding equations in terms of e-motor drives power (Eq. (2.6) and Eq. (2.7)), depending on the shaft and supplied power ratios, drives the estimation of the battery consumption in terms of power required

step by step. However, since the power calculated is the power required by the propulsive system to the electric power source, the battery energy consumption should be estimated considering its dynamic discharging model.

The typical form of an engine deck is reported in Tab. 2.4, where the minimum set of input parameters is associated with the resulting power and fuel flow. However, to estimate the emissions of hybrid-electric and conventional aircraft, the fuel flow is not sufficient. When the aim of a flight simulation is the estimation of the environmental impact of a particular mission profile, other columns complete the engine decks providing information about the emission indices (in grams per fuel kilogram) of NO_x , CO , HC , CO_2 , SO_x , H_2O and soot [23]. The interpolation of the engine deck, in this latter case, provides information about the emissions by multiplying the fuel flow, the time step range, and the emission index. The sum of the emissions of each step is the environmental impact of the mission profile without accounting for the noise emissions. The **propulsive efficiency** is

Altitude (m)	Mach number	ISA ΔT	Throttle	Gasturbine Power (kW)	Fuel flow (kg/s)
0	0	0	1	2600	0.4639
0	0.1	0	1	2500	0.4355

Table 2.4: Typical Engine-Deck table reporting for a set of input parameters the associated power and fuel flow.

the fraction of the net mechanical output of the engine which is converted into propulsive power [23], η_{P1} and η_{P2} . The **mechanical efficiency** is the ratio of net mechanical power at shaft with respect to the one entering the gearbox, η_{GB} . The **thermal efficiency** (η_{GT}) is the ability of an engine to convert the chemical energy inherent in the fuel to a net kinetic energy gain of the working medium [23]. In literature, when approaching simulation based flight performance, the aircraft propulsive characteristics are described by thrust or shaft power, as said. Thrust already accounts for both thermal, mechanical, and propulsive efficiencies of the thermal engine. Shaft power only accounts for the first and second efficiencies. Considering the particular powerplant here discussed and the engine decks proposed in this section, the single efficiency of each power unit should be measured to provide the total propulsive power from the powertrain equations.

In order to associate at each power value of the engine deck the right propulsive power of the powertrain, a few more steps are required. The objective of this procedure is to model the complex system by linking at each point of the engine deck the efficiencies of the different power units. To link power and efficiency, some lookup tables are required. Sometimes, lookup tables provide the efficiency of a certain element as a function of multiple parameters. For example, the gearbox efficiency is often provided as a function of the rotational speed, the reduction ratio, and the entering power, as shown in Tab. 2.5. In the same way, the efficiency

Reduction ratio		Rotational speed (rpm)				
5		4000	8000	16000	32000	45000
Mechanical power (kW)	150	0.99	0.99	0.99	0.99	0.99
	225	0.99	0.99	0.99	0.99	0.98
	300	0.99	0.99	0.99	0.98	0.98
	450	0.99	0.99	0.98	0.98	0.96
	600	0.99	0.98	0.98	0.96	0.96
	900	0.98	0.98	0.98	0.96	0.96

Table 2.5: Efficiency of a gearbox as a function of the rotational speed and the mechanical power.

of some electric components is provided as a function of multiple parameters including voltage, rotational speed, and power. The designer choices can fix some of these parameters, as for example the reduction ratio and the e-motor drive voltage. Some other parameters can be fixed or calculated, as, for example, the rotational speed associated with a certain mechanical torque and power. Moving from these lookup tables, after fixing all the other parameters, the efficiency of each element is a function of the entering power. To preserve the linearity of the powertrain equations, for each point of the engine deck, the efficiency of the powertrain elements is calculated with an iterative process.

Starting from the engine deck power associated to a set of Mach number, altitude, throttle, and temperature, Eq. (2.5), Eq. (2.6) or Eq. (2.7) provide the entering and exiting power of each element of the propulsive system for the efficiencies considered as first attempt. The entering power is used to interpolate the lookup tables and, then, to update the efficiencies element by element. From the same

point of the engine deck, the power distribution along the propulsive system is calculated using the powertrain equations with the new efficiencies. These two steps are repeated iteratively until convergence.

The use of efficiencies data can vary depending on the available information on the propulsive system and designer choices, is here proposed an alternative method that apply information from response surface and lookup tables to extend the engine deck. Even if the main objective is to reduce the degrees of freedom of the design process, four main parameters are required to be fixed before applying this method: the **gear ratio**, the **energy density of the fuel**, the **sizing power of e-motor drives** and the **dimensioning power of the gearboxes**. These characteristics are generally known after a preliminary design activity. Starting from each point of the engine deck, the first efficiency associated at each point is the *gasturbine efficiency*. This thermal efficiency can be calculated by Eq. (2.11), where P_{GT} (kW) is the gasturbine exiting power, FF (kg/s) is the fuel flow and SE_{Fuel} (kWh/kg) is the specific energy of the fuel.

$$\eta_{GT} = \frac{P_{GT}}{FF SE_{Fuel} 3600} \quad (2.11)$$

The propeller efficiency, whose lookup table depends on shaft power, RPM, and speed, is provided in the same form of the engine deck previously discussed. The only difference is that the throttle setting is here referred as the shaft power ratio with respect to the maximum shaft power delivered to that propeller for the same conditions of speed (Mach number), altitude, and temperature. The angular speed is generally fixed for a certain power rating of the engine deck, thus, for each combination of altitude, Mach number, throttle, and temperature, the propeller efficiency can be unequivocally determined. This would permit the organization of the efficiencies as output parameters of the same engine deck used to organize the gasturbine power (or the e-motor drive powers), with the exception of the throttle definition which has a different meaning depending on which is the output desired.

The gearbox efficiency depends on three different parameters: rotational speed, entering power, and gear ratio. Since the gear ratio is fixed by the designer and the

rotational speed of the propeller has been fixed previously at each power rating, the rotational speed of the gearbox can be calculated. Since it is calculated from the propeller rotational speed, this value only depends on the power rating and, thus, dependence from the rotational speed is substituted by the power rating. Defining the throttle setting as the ratio between the entering power and the sizing power of the gearbox, the dependence of the gearbox efficiency from the power can be substituted by the throttle. From these considerations, the gearbox efficiency is modelled similarly to an engine deck. The same approach is valid in case of e-motor drive efficiency considering the e-motor drive rotational speed is equal to the gearbox entering rotational speed.

2.1.3 Fuel Cell Modelling

In the previous sections, the powertrain equations have been introduced considering a general architecture powered by two power sources and solved from the input data provided by an engine deck. However, as discussed, different propulsive systems would require different powertrain equations based on the connection between the elements. The modelling of the system shown in Fig. 2.6 introduces two main issues:

- a different set of powertrain equations taking the power supplied by fuel cells as input;
- the definition of a mathematical model describing the dependence between the power supplied and the operating conditions.

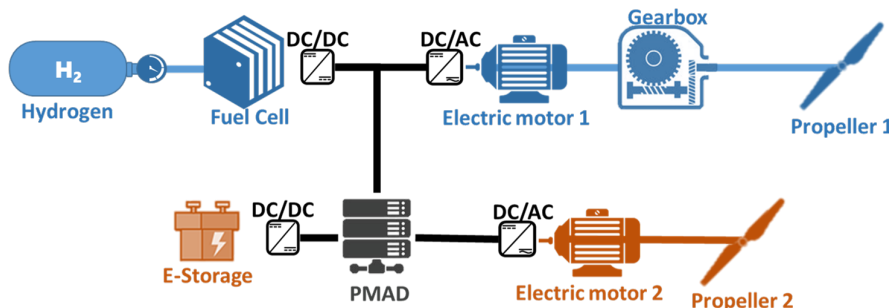


Figure 2.6: Powertrain system including fuel cells and e-storage as power sources.

Differently from the powertrain system discussed previously, the one proposed in Fig. 2.6 has both propulsive lines powered by e-motor drives. The primary propulsive

line is connected to the secondary propulsive line by the power management and distribution unit. This particular configuration increases the efficiency of the system that is capable of withstanding the loss of an e-motor drive or the gearbox without a critical thrust loss. Another difference with the hybrid-electric powertrain modelled in Fig. 2.1 deals with the operating modes. The number of operating modes is reduced to six, as shown in Table 2.6 since the e-motor drives can only operate according to the propellers operating conditions.

	Operating Modes					
	1	2	3	4	5	6
<i>Propeller 1</i>	Thrust	Thrust	Thrust	Thrust	Harvest	Harvest
<i>Propeller 2</i>	Thrust	Thrust	Harvest	Harvest	Thrust	Thrust
<i>E-storage</i>	Discharge	Charge	Discharge	Charge	Discharge	Charge

Table 2.6: The six operating modes of the system in Fig. 2.6.

On the other hand, a fuel system as the one proposed in Fig. 2.6 requires a new system of equations to be described. Eq. (2.12), representing the first operating mode in Table 2.6, introduces two new sizing powers. The first one is the power delivered by the fuel cell, P_{FC} , while the second one is the power going from the fuel cell to the secondary power system or from the battery to the primary propulsive line, depending on the operating mode, P_{PM} .

$$\begin{bmatrix}
 -\eta_{FC} & 0 & 0 & 0 & 0 & 0 & 0 & 0 & 0 & 0 \\
 0 & 1 & 0 & 1 & 0 & 0 & 0 & 0 & 0 & 0 \\
 0 & 0 & -\eta_{P1} & 0 & 0 & 0 & 0 & 0 & 1 & 0 \\
 0 & 0 & 1/\eta_{GB} & -\eta_{EM1} & 0 & 0 & 0 & 0 & 0 & 0 \\
 0 & -\eta_{PM} & 0 & 0 & -\eta_{PM} & 1 & 0 & 0 & 0 & 0 \\
 0 & 0 & 0 & 0 & 0 & -\eta_{EM2} & 1 & 0 & 0 & 0 \\
 0 & 0 & 0 & 0 & 0 & 0 & -\eta_{P2} & 1 & 0 & 0 \\
 \Phi & 0 & 0 & 0 & (\Phi - 1) & 0 & 0 & 0 & 0 & 0 \\
 0 & 0 & \phi & 0 & 0 & 0 & 0 & (\phi - 1) & 0 & 0 \\
 0 & 0 & 1 & 0 & 0 & 0 & 0 & 0 & 0 & -\eta_{GB}
 \end{bmatrix}
 \begin{bmatrix}
 P_{H_2} \\
 P_{PM} \\
 P_{S1} \\
 P_{EM1} \\
 P_{BAT} \\
 P_{EM2} \\
 P_{S2} \\
 P_{P2} \\
 P_{P1} \\
 P_{GB}
 \end{bmatrix}
 =
 \begin{bmatrix}
 P_{FC} \\
 P_{FC} \\
 0 \\
 0 \\
 0 \\
 0 \\
 0 \\
 0 \\
 0 \\
 0
 \end{bmatrix}
 \quad (2.12)$$

As discussed previously, the power units' efficiencies are included in the single efficiencies of each element associated. The modelling of fuel cells as primary power source, similarly to what has been done with the thermal engine, suggests the idea of a parallel type of engine deck, necessary to calculate the starting power to solve Eq. (2.12). In the present context, a simplified but effective model of fuel cells is derived [75]. Due to the high power demand in aviation applications, the cells are

packed in series forming what is called *stack* and the stacks are packed in parallel to provide the necessary power. The following *model assumptions* are considered:

- the gases are ideal;
- the fuel cell stack is fed with hydrogen and air;
- a cooling system controls the temperature;
- a water management system controls the humidity inside the cells;
- the pressure drops across flow channels are negligible;
- the cell voltage drops are due exclusively to reaction kinetics and charge transport;
- the cell resistance is constant regardless of the operating condition.

The *limits of the model* are reported in the following list:

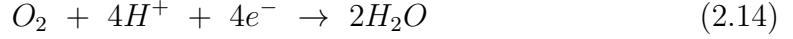
- the mass flow through the membrane is not considered;
- the effect of temperature and humidity on stack's resistance is not considered.

In the present context, PEM fuel cells will be considered as a green alternative for future aviation. These fuel cells are electrochemical cells converting the chemical energy of fuel into electrical power through a pair of redox reactions using an oxidizing agent. Regardless of the type of fuel cell, it consists of three components:

- **anode**, the electrode at which the oxidation reaction occurs;
- **cathode**, the electrode at which the reduction reaction occurs;
- **electrolyte**, a substance that dissolves into ions, allowing the passage of electric current.

At the anode, a catalyst causes the fuel to undergo oxidation reactions that generate ions and electrons [50, 51, 76, 77]. The ions move from the anode to the cathode through the electrolyte. At the same time, electrons flow from the anode to the cathode through an external circuit, producing direct current electricity. At the cathode, another catalyst causes ions, electrons, and oxygen to react forming water. PEM fuel cells are based on the following electrochemical reactions happening on the anode and the cathode, respectively [78, 79].





Faraday's law of electrolysis implies that *current density* (j) is proportional to the charge transferred and the consumption of reactant per unit area [76]:

$$j = \nu F j_{reactants} \quad (2.15)$$

Where j is the current density, ν is the number of electrons involved in the reaction, F is the Faraday constant (96485 C/mol) representing the electrical charge of one mole of electrons, and $j_{reactants}$ is the flux of reactant per unit area. At equilibrium, the net flux of reactants is equal to zero, although the reactions on the cathode and the anode proceed in both directions at a rate that is called *exchange current density*, j_0 . As shown in Eq. (2.16), the flux of reactants can be expressed as a function of the surface concentration of reacting species, C , and the constant rate of reaction, k .

$$j_{reactants} = kC \quad (2.16)$$

The rate of reaction can be calculated according to **transition state theory**, as shown in Eq. (2.17).

$$k = \frac{k_B T}{h} e^{-\frac{\Delta G}{RT}} \quad (2.17)$$

In Eq. (2.17), T is the temperature, R is the universal gas constant ($8.314 \frac{J}{Kmol}$), k_B is the Boltzmann's constant ($1.384e-23 \frac{J}{K}$), h is the Planck's constant ($6.626e-31 Js$), and ΔG is Gibbs free energy. Considering the equilibrium condition, the current density can be derived by combining the previous equations. At equilibrium, the current density is zero since the reactions proceed in both directions at the same rate. However, anode polarization is generally negligible compared to cathode polarization, due to the slower reaction. The exchange current density of the cell is calculated as follows.

$$j_0 = \frac{\nu F k_B T}{h} e^{-\frac{\alpha F E_R}{RT}} \quad (2.18)$$

In Eq. (2.18), C_0 is the oxidant surface concentration, α is the transfer coefficient in moles and E_R is the equilibrium potential associated with the reaction. Multiplying

by the area of the membrane, the exchange current i_0 is obtained, from which the current intensity i_{cell} is calculated as shown in Eq. (2.19) [77, 79], obtained from Butler-Volmer equation, valid under the hypothesis of negligible polarization of the anode with respect to the cathode.

$$i_{cell} = i_0 e^{-\frac{\alpha F (E_{cell} - E_R)}{RT}} \quad (2.19)$$

Inverting Eq. (2.19), Nernst equation (Eq. (2.20)) is used to calculate the cell potential.

$$E_{cell} = E_R - \frac{RT}{\alpha F} \ln\left(\frac{i_{cell}}{i_0}\right) \quad (2.20)$$

Eq. (2.20) introduces polarization losses with respect to the reaction potential. Other losses affecting the fuel cells are due to internal currents generated by the flow of electrons finding a short-circuit across the membrane and modelled as ohmic losses. In general, considering that fuel cell stacks are composed of a certain number of cells (N_{cells}) arranged in series, the overall voltage is given by the following equation [79, 80], where V_0 the open-circuit voltage, i_{cell} is the electric current of the single fuel cell, i_{stack} is the electric current of the whole stack, and R is the internal resistance. Since the cells are packed in series, i_{stack} is equal to i_{cell} .

$$V_{stack} = V_{0_{stack}} - N_{cells} \frac{RT}{\alpha F} \ln\left(\frac{i_{cell}}{i_0}\right) - R i_{stack} \quad (2.21)$$

It is here explicitly remarked that $V_{0_{stack}}$ is not simply the equilibrium potential multiplied by the number of cells since it accounts for the internal losses that are present even in absence of electric current. Thus, for a single cell, the open-circuit voltage operating in standard conditions is generally around 1 V against the expected 1.23 V. Additional potential losses due to fuel crossover, that is due to small amounts of H_2 diffusing from anode and cathode, are not included. Furthermore, the unsteady effects are not considered.

The number of cells packed in series is chosen to fulfil the nominal voltage requirement. The required voltage is often chosen to be equal to the e-motor drive nominal voltage. In the end, assuming a certain required voltage (V_0) and

a nominal voltage of the stack ($V_{0_{stack}}$), the number of cells in series is calculated as shown in Eq. (2.22) [79].

$$N_{cells} = \frac{V_0}{V_{0_{cell}}} \quad (2.22)$$

On the other hand, the choice of the number of stacks in parallel is based on the power required. Indeed, a major problem affecting fuel cells is connected to the strong voltage drop as the current intensity increases and the consequently limited value of the rated power. This problem can be overcome by connecting more stacks in parallel. Assumed a certain required power (P_0) and calculated the nominal power of the single stack ($P_{0_{stack}}$), which is the product of the nominal electric current and nominal voltage, the number of stacks packed in parallel is calculated as shown in Eq. (2.23) [79].

$$N_{stacks} = \frac{P_0}{P_{0_{stack}}} \quad (2.23)$$

The equations presented so far in this paragraph lead to a system describing the operative conditions of a stack starting from a limited number of input data. Conversely, when datasheets describing the stack operating conditions are available, the entire voltage-current curve is assigned point by point and, from that curve, the resulting power is derived. The power of the stack is calculated as the product of voltage and current intensity. In both cases, the power delivered by a single stack is then multiplied by the number of stacks connected in parallel.

As stated previously, the characteristics of the fuel cells are provided as a function of altitude, speed, and throttle ratio, or, in other words, in the form of a fuel cell deck. The first and simplest function deals with the throttle, which is the way by which the pilot regulates the power level by varying the flow of hydrogen towards the membrane or by excluding several parallel stacks from the circuit. In order to assure the commanded power level, parallel stacks are added or excluded to maximize the efficiency of the system. The efficiency is calculated as the ratio between the useful power produced and the power that can be extracted from the redox reaction. The latter can be obtained from the flow of moles of

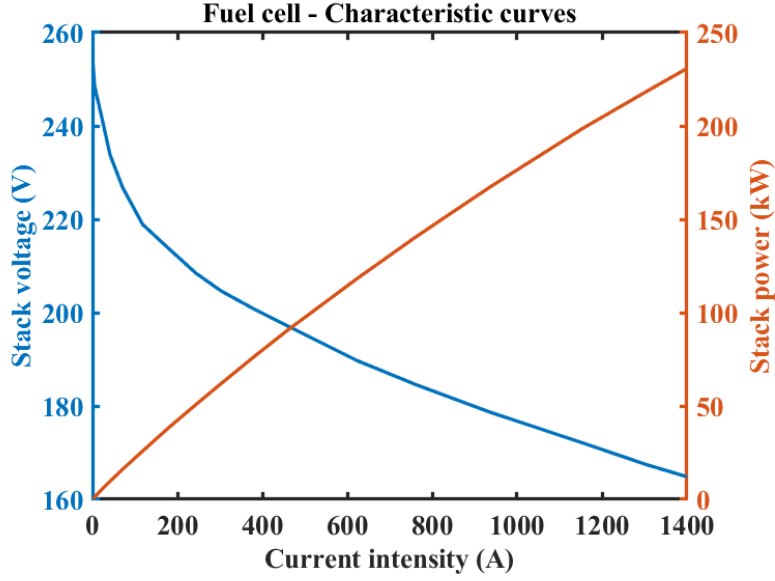


Figure 2.7: Characteristic curve of a SINAVY FCM120 PEM fuel cell stack.

hydrogen in mol/s, N_{H_2} , multiplied by the hydrogen's heating value (ΔH_2), ranging between 286 kJ/mol and 241 kJ/mol , depending on whether the water is leaving the stack as vapour or liquid. The power supplied by a single stack is calculated through Fick's equation (Eq. (2.24)).

$$P_{H_2 \text{ stack}} = \frac{I_{\text{stack}} N_{\text{cells}}}{\nu F} \Delta H_2 \quad (2.24)$$

The resulting efficiency of the fuel cell is calculated as shown in Eq. (2.25) [79], where the percentage of hydrogen utilization (η_{reaction}) in the reaction can be assumed to be equal to one [81], two electrons are involved and a high-temperature fuel cell is considered ($\Delta H_2 = 241 \text{ kJ/mol}$).

$$\eta_{FC} = \frac{P_{\text{stack}}}{P_{H_2 \text{ stack}}} = \frac{V_{\text{stack}}}{1.482 N_{\text{cells}}} \eta_{\text{reaction}} \quad (2.25)$$

As shown in Fig. 2.7, increasing the current intensity, the power supplied increases while the voltage slightly drops. This causes a reduction of the global efficiency when increasing the power supplied, according to Eq. (2.25). This can be avoided using a set of stacks connected in parallel, opportunely excluded or connected depending on the power demand. Starting from a single stack, when the power required increases, an additional fuel stack is added preventing the efficiency drop by

keeping the voltage constantly higher than a convenient value. However, the number of stacks and the throttle can be accurately connected only after determining the dependency of the power supplied on altitude and Mach number.

Associated to the number of stacks connected, the consumption of hydrogen is calculated through Eq. (2.26) [78, 82] in terms of mass flow (in g/s).

$$\dot{m}_{H_2} = \frac{I_{stack} N_{cells} N_{stacks}}{\nu F} \eta_{reaction} M_{H_2} \quad (2.26)$$

M_{H_2} (2.016 g/mol) is the molecular mass of hydrogen. However, the redox reaction requires a certain air mass flow, which depends on the molecular mass of air, M_{air} (28.97 g/mol), on the oxygen fraction in the air, x_{O_2} (0.21), on the ratio of oxygen supplied versus the oxygen necessary for the reaction, λ_{O_2} [83, 84] (2.0 in optimal conditions [79, 85]) and on the number of electrons involved, ν (4). Eq. (2.27) is used in this work to calculate the required air mass flow [78, 82].

$$\dot{m}_{air} = \frac{I_{stack} N_{cells} N_{stacks}}{\nu F} \lambda_{O_2} \frac{M_{air}}{x_{O_2}} \quad (2.27)$$

Finally, the H_2O emission index can be deduced as the ratio between the molar masses of water and consumed hydrogen. The air provided to feed the redox reaction is required to be at a specific temperature and pressure, regardless of flight conditions [86]. Mach number or altitude could be limiting factors when looking at these requirements, motivating the introduction of centrifugal compressors. However, the air compressor does not necessarily work in nominal conditions during the flight mission, and this can affect the pressure at which the fuel cell operates and therefore the power produced. The major difficulty consists in the lack of studies in literature on the impact of altitude and flight speed on the performance of a fuel cell system. Without analytic methods linking the cell voltage and the air pressure, the effect should be evaluated through experimental campaigns, as suggested in Ref. [87]. Without appropriate data supporting the fuel cell model, the theoretical approach can hardly grasp the effects of air mass flow and operating pressure on the performance of a fuel cell.

In this work, results reported in Ref. [87] have been used to obtain a dimensionless law linking the voltage variation of the stack with flow rate and pressure, scaling the experimental data with respect to the size of the stack and the real voltages involved. However, this function should be determined case by case. The indissoluble connection between fuel cell, air intake, and compressor requires an overall design of the propulsive system. The effect of altitude and Mach number can be captured considering the different pressure ratios that the compressor can guarantee as a function of the incoming air flow supplied by the air intake in the subsonic regime.

Under the strong hypothesis of absence of leaks and purely isentropic flow, temperature and pressure at each section of the air intake are given by the following equations, where p is the static pressure, p_0 is the total pressure, M is the Mach number, γ is the ratio of air specific heat (1.4), T is the static temperature, and T_0 is the total temperature.

$$\frac{p}{p_0} = \left(1 + \frac{\gamma - 1}{2} M^2\right)^{-\frac{\gamma}{\gamma - 1}} \quad (2.28)$$

$$\frac{T}{T_0} = \left(1 + \frac{\gamma - 1}{2} M^2\right) \quad (2.29)$$

The air mass flow at each section of the intake with a certain area A (in square meters) is calculated according to the following equation.

$$\dot{m}_{air} = \frac{Ap_0}{\sqrt{T_0}} \sqrt{\frac{\gamma}{R}} M \left(1 + \frac{\gamma - 1}{2} M^2\right)^{-\frac{\gamma + 1}{2(\gamma - 1)}} \quad (2.30)$$

Being in a subsonic regime, the air intake can be imagined as a diverging duct aimed at slowing down the air and recovering its dynamic pressure [88]. The outlet section can be set equal to the compressor inlet section or based on the available space according to designer choice. The inlet section, on the other hand, is designed to guarantee air inlet without external expansion or compression in cruise conditions, corresponding to the minimum aerodynamic drag. In other words, based on the law of mass conservation, the required inlet area is calculated according to Eq. (2.27) and Eq. (2.30). However, while the air mass flow required by the stack is constant, what is provided by the centrifugal compressor depends on Mach number and altitude. This effect is described by the compressor performance map [89–91] or

theoretically reconstructed according to the principle of energy conservation [92]. In this second case, Eq. (2.31) [92] is used to describe the balance between the power supplied to the flow and the total enthalpy variation.

$$C \frac{2\pi RPM}{60} = \dot{m}_{air} \frac{\gamma R}{\gamma - 1} \frac{T_0}{\eta_c} (\beta^{\frac{\gamma-1}{\gamma}} - 1) \quad (2.31)$$

In Eq. (2.31), C is the torque (in Nm), RPM are the revolutions per minute, T_0 is the total temperature at the compressor inlet, η_c is the compressor efficiency and β is the pressure ratio. The isentropic compressor efficiency itself is a function of the rotational speed and the pressure ratio, and it can be assigned according to designer know-how or theoretical laws [93]. Starting from the design air flow rate and pressure ratio, a compressor can be designed. The value of the pressure ratio is generally chosen considering the gap between the operating pressure of the fuel cell stack and the highest altitude flight conditions. For example, in Fig. 2.8, the compressor map is created assuming a design pressure ratio equals 2.6, optimizing the design RPM to avoid a drop in efficiency, limiting the blades to unitary tip Mach number (choking condition), and considering the sea level conditions at inlet. For operational purposes, it is assumed that the electric motor powering the compressor adapts the number of revolutions in order to maximize efficiency while the pressure ratio changes (red curve in Fig. 2.8). The operating map of the fuel cell system is reconstructed by evaluating the operating pressure and air flow at different altitudes, flight Mach numbers, and throttle ratios. For each different altitude and flight speed, stagnation temperature and pressure are evaluated. A first value of the compression ratio is selected to ensure an ideal pressure at stack level. Starting from this, the required air flow rate is determined following the red curve of Fig. 2.8. Finally, the functioning of the air intake is determined. If the Mach number is less than 1 at each section of the inlet or the compressor, the operating conditions are determined, otherwise, the process is repeated considering a lower compression ratio. Thus, the maximum air flow rate and pressure available downstream of the compressor are determined by this procedure and, therefore, also the maximum stack power obtainable under a prescribed set of flight conditions.

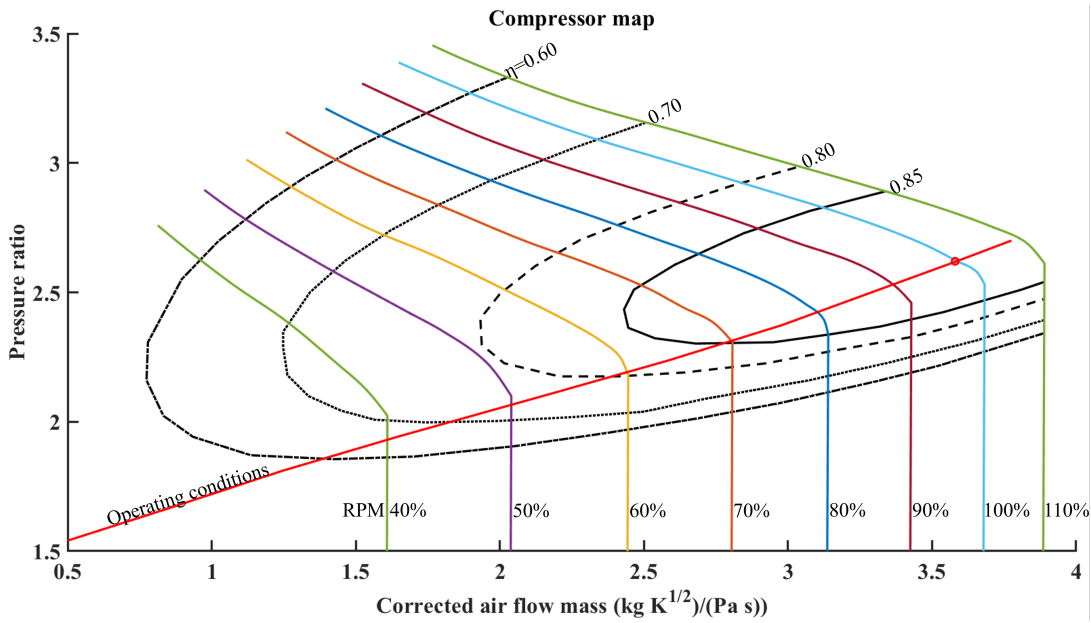


Figure 2.8: Example of compressor map.

However, it is here explicitly remarked that the maximum power could be further limited by reaching the maximum current intensity value at stack level.

As stated previously, the variation of power supplied with the throttle setting is associated with the number of stacks connected. Firstly, the designer defines the range of allowed current intensity and, therefore, the limit values of minimum and maximum voltage. A throttle ratio value equal to 1% is associated with the minimum power obtainable at each altitude and speed with a single stack, or at the minimum established current intensity. On the other hand, the value of 100% is associated with the maximum power obtainable when all stacks are operative. As the throttle increases, one more parallel stack is connected as soon as it becomes possible to respond to the power demand with an additional stack with the maximum voltage allowed. In this way, the condition of maximum efficiency is pursued, as evident from Eq. (2.25). When all the stacks are connected, the power supplied by each one is uniformly increased until the maximum current intensity is reached.

For each condition, the fuel flow is determined based on the current intensity and the number of connected stacks, according to Eq. (2.26). Finally, the contribution necessary to power the compressor (Eq. (2.31)) is subtracted from the generated power. In conclusion, the analogue of an engine deck for fuel cells is obtained.

2.1.4 Battery Modelling

The battery is one of the power sources described in the present work, whose characteristics and dynamic behaviours are modelled as proposed in literature [94–97]. Hybrid and electric aircraft require high voltage battery packs that consist of individual modules and cells organized in series and parallel [98]. A cell is the smallest unit considered for the packaged form of a battery. A module consists of several cells generally connected in either series or parallel. A battery pack is assembled by connecting modules together, again either in series or parallel. Batteries designed for hybrid and electric vehicles are rechargeable. In order to correctly identify the peculiar characteristics defining the performance of a battery, it is appropriate to explicit some definitions. The *discharge current*, I_B , is often expressed in terms of *C-rate* in order to normalize against battery capacity. A C-rate equal to 1 means that the assigned discharge current will discharge the entire battery in 1 hour. At the same time, the total discharge capacity is equal to the C-rate multiplied by the current intensity. The current output from any battery cell is limited by the maximum C-rate of the battery. It is also useful to express the instantaneous battery capacity, Q_B , as a percentage of maximum capacity, named state of charge (*SOC*) of the battery. Similarly, the depth of discharge (*DOD*) represents the percentage of maximum capacity already discharged. Nominal voltage (V_B), discharge current, and capacity of the battery are different with respect to those measured at cell level. In fact, as electric current flows through cells, the battery efficiency decreases, and thermal stability is reduced as part of the energy is converted into heat, implying also that the actual terminal voltage is reduced. When modelled as a linear phenomenon, this reduction is proportional to the current intensity, and the constant of proportionality is called internal resistance, R_C , of the battery cell. To avoid damage connected to excessively low voltages, batteries are equipped with a safety circuit that prevents the passage of current if the battery is below a certain threshold (cut-off voltage). This implies that the maximum useful capacity could be lower than the nominal one if the internal losses cause the voltage to drop below this threshold. Similarly, exceeding a maximum voltage

would produce harmful and dangerous chemical processes. Finally, even in case of an open circuit, the battery voltage is a function of the SOC.

A wide variety of battery models has been developed considering various degrees of complexity, ranging from detailed electrochemical models to mathematical models. In the present work, two different approaches are considered. The first one is based on the concept that the battery is a tank of electric energy, accounting for neither the cells packaging nor the power losses. This is the simplest model and is used for preliminary estimation of the battery mass moving from two main characteristics of the power unit: specific power and specific energy. Measuring the maximum power demand and the total energy required to accomplish the mission profile, the battery is sized in power or energy considering the highest mass value (Eq. 2.32).

$$W_{BAT} = \max\left(\frac{E_{BAT}}{\text{Specific Energy}}, \frac{P_{BAT}}{\text{Specific Power}}\right) \quad (2.32)$$

When current, voltage, and resistance of the battery are not specified, which is a typical condition for the early stages of the design process, this model is the only possible available.

Electrical models [99,100], with an accuracy that lies between electrochemical and mathematical models (error on energy consumption goes from 1% to 5%), are considered for the simulation based mission analysis when the aircraft model has been refined and voltage and current requirements have been frozen based on cabling and electric-motors design. These models use a combination of voltage sources, resistors, and capacitors to design and simulate the battery packs. Some models describe the battery as a network of series and parallel resistors (R_C) predicting its response to transient load at a particular SOC value, but neglecting the dependence of V_B on the state of charge. Other runtime-based models include variations in open-circuit voltage with SOC at fixed current intensity, excluding the prediction of voltage response for varying currents. Lastly, complex impedance-based models use an equivalent network to model the response in the frequency domain, neglecting voltage response due to both SOC and load variations. Combinations of these three models groups are constantly being developed in order to simultaneously

capture the complex set of phenomena that occur during the battery discharge and charge processes.

The simple approach considered in the present work ensures that most phenomena are captured, and the error is minimized. In analogy to the use of an engine deck for the description of thermal engine and e-motor, for the correct battery modelling, the starting point is the description of the discharging characteristics of the individual cell in terms of the voltage values associated with different battery capacity values or states of charge at different C-rates (Fig. 2.9). The voltage response of the cell can be interpolated linearly starting from the assigned curves, given a value of the state of charge and the C-rate. The transient responses are not modelled, but can be reasonably considered negligible. For SOC values between

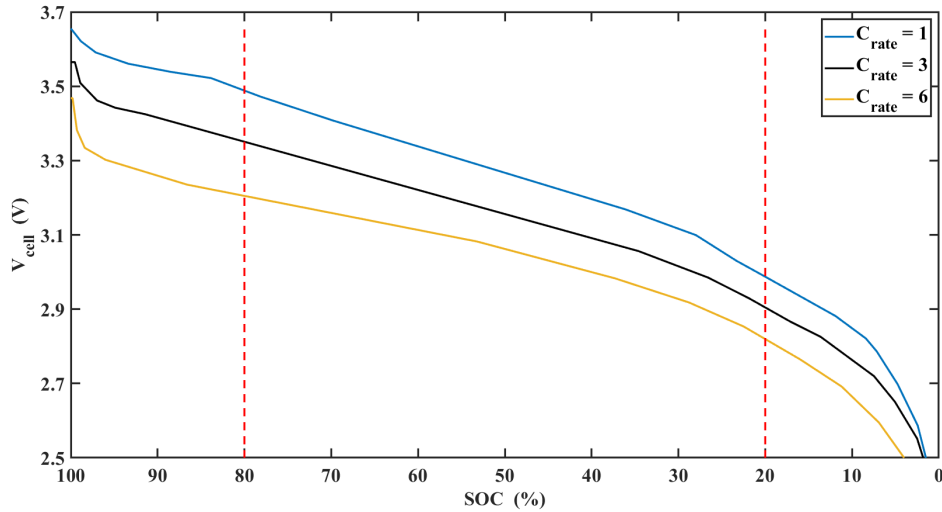


Figure 2.9: Example of cells discharging curves in terms of battery capacity and state of charge for three different C-rates.

typical threshold values (between 20% and 80%), voltage typically behaves linearly. In other words, indicating with V_{C_0} the open circuit voltage at 100% SOC, V_C can be approximated as described in Eq. (2.33) [101].

$$V_C = V_{C_0} - R_C I_C - V_{SOC} SOC \quad (2.33)$$

Where V_{SOC} is the slope of the discharge curve. V_{SOC} and R_C are functions of both C-rate and SOC, as shown in Fig. 2.9. These dependencies can be described for any

operating condition by interpolating available cell information for different C-rates and state of charge between the open-circuit values and the maximum C-rate curve. The usable energy supplied by the cell, E_C , is calculated as in Eq. (2.34).

$$E_C = \int_{Q_{Cmin}}^{Q_{Cmax}} V_C(Q_C) dQ_C \quad (2.34)$$

The power instantaneously supplied by the cell, P_C , can be calculated as the product of the voltage and the current intensity, where the current intensity can be derived from C-rate and capacity by multiplying the two elements ($I_C = CQ_C$).

$$P_C = V_C I_C \quad (2.35)$$

An assigned total voltage of the battery pack, V_B , can be achieved considering an appropriate number of cells packed in series (N_s), constituting a battery module.

$$N_s = \frac{V_B}{V_C} \quad (2.36)$$

V_C is the nominal cell voltage that can be fixed, as a first approximation, at an average voltage between the maximum and minimum values deliverable by a single cell. The minimum voltage value corresponds to the minimum SOC and the maximum permitted current intensity. The maximum voltage is related to the maximum allowed SOC. The other parameter of this equation, V_B , is chosen considering the limits of the motor controller and e-motor drive, such that the inverter can operate properly. Since the choice of the nominal battery voltage is a mandatory step to fix the number of serial cells, some considerations are here introduced to guide the designer. As first attempt, the electric potential difference can be considered a mean value of the operative range in which the e-motor drives operate. However, this preliminary estimation should be refined in the following steps of the design process. In fact, the connection between the e-storage and the e-motor drives is through a power line generally working at 270 V or 540 V in direct current (DC) [36, 102]). That means that, especially in case of high supplied power, a *chopper* is necessary to avoid excessive increments of battery current and, thus, power losses. The chopper is an electronic switch capable of

converting a fixed DC input to a variable DC output voltage. It is commonly used to vary with a specific function the voltage of DC e-motor drives on railway locomotives with the objective of controlling speed or torque. Without further

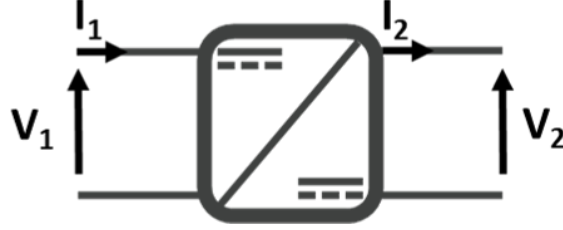


Figure 2.10: Chopper functional scheme.

details and assuming negligible power losses, the entering power is equal to the exiting power, which means that considering the entering voltage and current, V_1 and I_1 , respectively, and the outputs V_2 and I_2 , the key relationship of the functional scheme in Fig. 2.10, is the one reported in Eq. (2.37).

$$V_1 I_1 = I_2 V_2 \quad (2.37)$$

A step-up chopper increases the electric potential difference, which means that V_2 is higher than V_1 , the contrary happens in case of step-down choppers. Step-up/down choppers are not discussed in the present work. In the present introduction, the objective of the chopper is unlinking the battery voltage from the value managed by the power grid, making the choice of V_B independent from this value.

The number of battery modules packed in parallel (N_p) is calculated considering the capacity required to the battery (Q_B) in order to comply with peak power and total energy requirements.

$$N_p = \frac{Q_B}{Q_C} \quad (2.38)$$

From the practical point of view, aircraft designers have greater familiarity with the concepts of peak power and total energy, more than with the battery capacity. For this reason, the present work will translate the battery capacity in terms of power and energy requirements, choosing the most demanding condition to determine the

number of cells in parallel. The number of parallel cells needed to meet the total energy demand, E_B , is calculated by Eq. (2.39), which is derived from Eq. (2.38).

$$N_{\text{energy}} = \frac{E_B}{E_C N_s} \quad (2.39)$$

As first attempt, the useful energy provided by each cell, E_C can be calculated through Eq. (2.40) considering the nominal voltage of the cell at 50% of the state of charge and an intermediate C-rate. Alternatively, cell energy can be calculated as the mean between the discharging curve integral (Fig. 2.9) at maximum C-rate and at C-rate equals to 1.

$$E_C = V_C Q_C \quad (2.40)$$

Considering the peak power (P_B) required during the mission, the minimum number of parallel cells necessary to comply the power required is given by Eq. (2.41).

$$N_{\text{power}} = \frac{P_B}{P_{C_{\max}} N_s} \quad (2.41)$$

The maximum power that can be delivered by each cell, P_C can be calculated as shown in Eq. (2.42).

$$P_{C_{\max}} = V_C Q_C C_{\max} \quad (2.42)$$

In the end, the number of parallel modules is the maximum among the values calculated by Eq. (2.39) and Eq. (2.41). The total number of battery cells is the product between the cell and parallel cells (Eq. (2.43)).

$$N_C = N_p N_s \quad (2.43)$$

In order to simulate the discharge process, the curves reported in Fig. 2.9 are used. At each time step during the mission, once the power required to the battery is known, the useful power delivered by each cell can be calculated. The fundamental hypothesis is that all the cells have the same discharging cycle and operating conditions. In addition to the power required to each cell (P_C), the battery further discharges due to losses associated with Joule's first law (Eq. (2.44)).

$$P_{C_{\text{loss}}}(t) = R_C I_C^2 \quad (2.44)$$

$$P_{C_{used}}(t) = P_{C_{loss}}(t) + P_C(t) \quad (2.45)$$

In order to minimize losses, the battery controller imposes the minimum current load sufficient to deliver the required power (Eq. (2.45)) and, so, the minimum C-rate needed. When only one discharge curve is available to describe cells behaviour, the minimum and maximum operating C-rates will coincide with the one assigned, but the user will still be prompted for information about the equivalent internal resistance for the purposes of calculating losses. The cumulative value of $E_{C_{used}}$, $E_{C_{usedTOT}}$, is calculated at each time step to update the total value of the remaining energy, and finally, update the SOC.

$$SOC(t) = \frac{E_{C_{start}} - E_{C_{usedTOT}}(t)}{E_{C_{start}}} 100 \quad (2.46)$$

Where $E_{C_{start}}$ is the initial energy stored in each cell.

One last parameter of interest is the battery efficiency, which is measured as reported in Eq. (2.47)

$$\eta_B(t) = \frac{P_C(t)}{P_{C_{used}}(t)} \quad (2.47)$$

The discharging cycle of the battery can be considered as the sum of the single cell discharging curves. Starting from the single cell curve characteristics, point by point, the voltage is multiplied by the number of cells packed in series and the capacity is multiplied by the number of cells in parallel. The curves obtained are generally reported in terms of voltage as a function of the state of charge or discharge capacity. In Fig. 2.11, the discharging of the battery is described for the case of a regional turboprop typical mission profile where the e-storage is used at take-off and climb. The battery has been appropriately sized for the mission, imposing a minimum SOC of 20% and a maximum of 80% (red dashed lines in figure). Each red point represents the state of charge and the output voltage at a different time step.

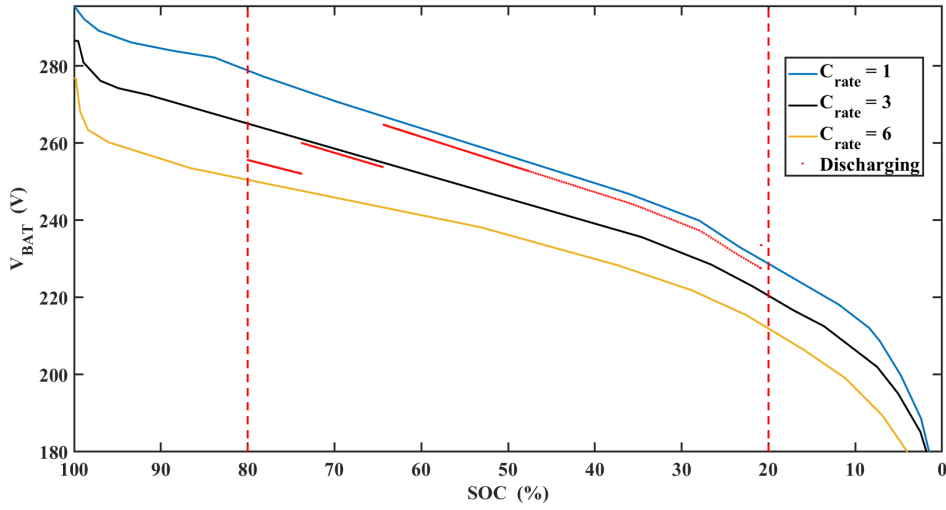


Figure 2.11: Example of battery discharging curves in terms of battery capacity and state of charge for three different C-rates.

2.1.5 Cabling Sizing

Cables are assembly of wires grouped side by side or bundled. Wires are the conductive elements deputed to the transmission and distribution of electric power, or, in other words, electric current, between two elements at different electric potential. The design of wires depends on many factors [102, 103]: the mechanical strength to face the operating conditions, the maximum power losses allowed, and the electric load to manage. The choice of wire material is based on conductivity and density. Therefore, mainly copper and aluminium will be discussed in the present work. These types differ in cable structure, mass, and transmission characteristics. The typical structure of a conventional transmission cable can be divided into three components: conductor, insulation and sheath. The core component of a cable is the conductor, which is responsible for electron transmission. A cable is composed of multiple bundles of conductors, each of them made up of a single or multiple wires. Insulation surrounds the conductors and insulates them from each other. The sheath protects the cable from the environment. The sizing of aircraft wiring system proposed in the present work is a procedure compliant with regulation already in force [36, 104]. Wires are manufactured according to the American wire gauge (AWG) standard (Table 2.7). Typical wire sizes range from

Wire Size			Resistivity (Ω/km)	
AWG	Diameter (mm)	Area (mm ²)	Copper	Alumium
4/0	11.68	107	0.16	0.25
3/0	10.40	85	0.20	0.31
2/0	9.27	67.4	0.26	0.39
1/0	8.25	53.5	0.32	0.50
1	7.35	42.4	0.41	0.63
2	6.54	33.6	0.51	0.79
3	5.83	26.7	0.65	0.99
4	5.19	21.2	0.81	1.25
5	4.62	16.8	1.03	1.58
6	4.11	13.3	1.30	1.99
7	3.67	10.5	1.64	2.52
8	3.26	8.37	2.06	3.17
9	2.91	6.63	2.60	4.00
10	2.59	5.26	3.28	5.04
11	2.30	4.17	4.13	6.35
12	2.05	3.31	5.21	8.01
13	1.83	2.62	6.58	10.11
14	1.63	2.08	8.29	12.74
15	1.45	1.65	10.45	16.06
16	1.29	1.31	13.16	20.23
17	1.15	1.04	16.58	25.48
18	1.02	0.823	20.95	32.20
19	0.91	0.653	26.40	40.58
20	0.81	0.518	33.28	51.16
21	0.72	0.41	42.05	64.63
22	0.65	0.326	52.88	81.29

Table 2.7: American Wire Gauge standard and related resistivity for two different wire materials.

gauge 0000 to 40, corresponding to 11.68 mm to 0.08 mm, respectively, and the associated resistivity can be calculated assuming the resistivity of the material per unit surface. According to aerospace standard *AS 50881* [104], it is permitted the general use of size 22 as the minimum wire size, otherwise, the use of smaller size requires procurement activity approval. This restriction in applications is due to maintenance difficulties. This is the first design constraint that will be considered in the proposed cabling sizing process.

The second constraint deals with the current carrying capacity, or, in other

words, **ampacity**, that is the maximum electric current an insulated conductor can safely carry without exceeding its rated temperature. The ampacity of a cable should equal or exceed the maximum current the cable will be expected to carry during its operative life. Graphics and tabular information about conductor ampacity are provided by aerospace standards as a function of wire size and temperature difference between rated value and free air condition, as reported in Table 2.8. The **rated temperature** depends on the heat resistance of the materials used for the insulation and jacket of the cable. Common rated temperatures range from $60^{\circ}C$ up to $90^{\circ}C$, but higher values could be required for the case of the aircraft propulsive system. The current that causes a temperature steady state condition equal to the rated temperature of the wire should not be exceeded.

Size AWG	Copper			Alumium		
	$60^{\circ}C$	$75^{\circ}C$	$90^{\circ}C$	$60^{\circ}C$	$75^{\circ}C$	$90^{\circ}C$
18			14			
16			18			
14	25	30	35			
12	30	35	40	25	30	35
10	40	50	55	35	40	40
8	60	70	80	45	55	60
6	80	95	105	60	75	80
4	105	125	140	80	100	110
3	120	145	165	95	115	130
2	140	170	190	110	135	150
1	165	195	220	130	155	175
1/0	195	230	260	150	180	205
2/0	225	265	300	175	210	235
3/0	260	310	350	200	240	275
4/0	300	360	405	235	280	315

Table 2.8: Ampacity of aluminium and copper wires at different rated temperatures ($60^{\circ}C$, $75^{\circ}C$ and $90^{\circ}C$) referred to an ambient temperature of $30^{\circ}C$.

The third constraint deals with the voltage drop. The allowable voltage drop is about 2% of the rated voltage and this, in turn, is determined by the characteristics of the electric utilization equipment to which the electric power sources shall supply power. The distribution system is designed according to standards: 115 V (400 Hz) for AC Voltage system and 270 V for DC Voltage system [105]. However,

due to the increase of electrical power required by more electric concepts, some companies proposed the introduction of high voltage systems limited to 540 V in DC and 230/400 V (360-800 Hz) in AC.

The design methods from literature [106–108] have been considered the starting point for the cabling sizing procedure here reported for the case of hybrid-electric propulsive systems. The first step of this design process is the subdivision of the electric network in segments connecting two elements of the power grid. Each segment is dimensioned separately considering two inputs: the maximum electrical power managed (or the apparent power in case of AC segments) and the nominal voltage (or the root mean square voltage). From these two inputs, the required total electrical current is calculated (Eq. (2.48)).

$$I = \frac{P}{V} \quad (2.48)$$

The required electrical current is derated before the comparison with the ampacity of the cable. The derating operation is aimed to prolong the wire operating life making each segment operate at less than its rated maximum capability. In the present case, the operation aims to operate at a required current lower than the rated one, as shown in Eq. (2.49). In the same equations, some parameters are introduced: the ampacity of the conductor I_{wire} , the derating factors related to altitude and loading percentage (K_1 and K_2 , respectively), the loading percentage L_I , and the number of wires N_{wire} . The number of bundle N_{bundle} will be fixed at 1.

$$I < K_1 K_2 I_{wire} L_I N_{wire} N_{bundle} \quad (2.49)$$

Considering the length of each segment as fixed, three elements should be defined to size the cables: the number of wires, the rated temperature, and the size of the conductor section. The following equations will be introduced to design the cabling with the objective of reducing the wire size and the number of conductors in each bundle.

Since the variables playing a role are many, some additional considerations need to be introduced. The first one deals with the current loading percentage (L_I) on

each bundle. Since the sizing power considered is the maximum power managed by the distribution system, the loading percentage considered is 100%. This is one of the input variables, together with the number of wires, necessary to estimate the first derating factor introduced in Eq. (2.49) and shown in Fig. 2.12.

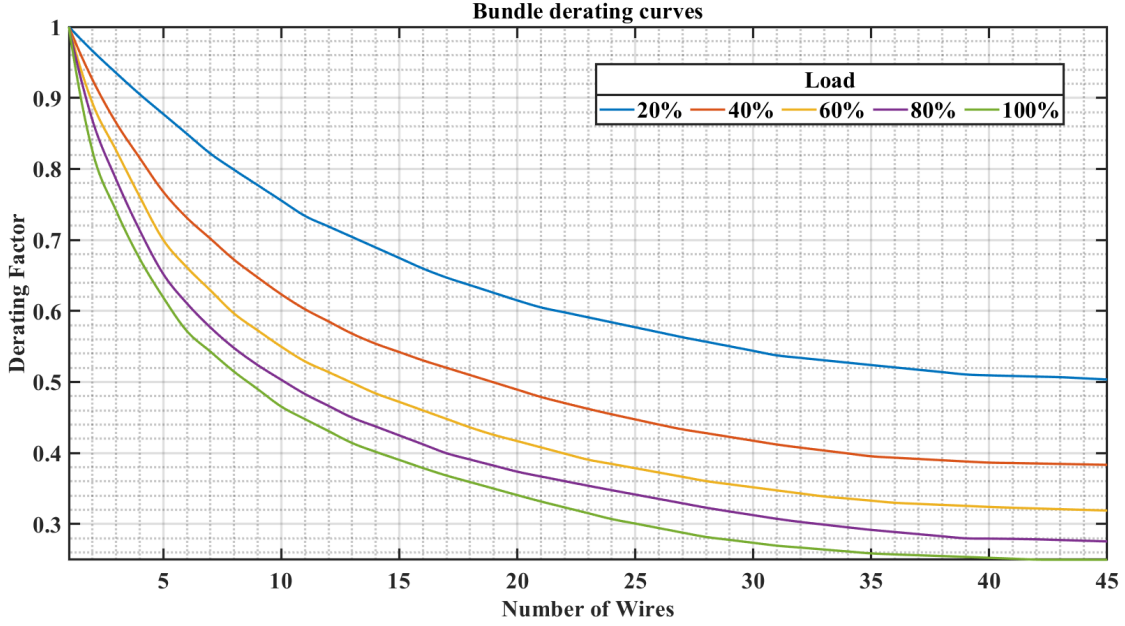


Figure 2.12: Derating factor related to the number of conductors in each bundle and the current load of the bundle.

The second derating factor depends on the altitude, which can be chosen between the ceiling and cruise altitudes to obtain the value from Fig. 2.13. Thus, chosen the reference altitude, this derating factor is automatically fixed.

Since the ampacity is a function of the wire size, as shown in Table (2.8), and the first derating factor presented depends on the number of wires, Eq. (2.49) is a function of these two variables. Assuming that the maximum bundle rated ampacity is equal to the required current, Eq. (2.49) is changed with the following Eq. (2.50), where the dependencies from the unknowns are made explicit.

$$I = K_1(N_{wire})K_2I_{wire}(AWG)N_{wire} \quad (2.50)$$

The maximum allowable voltage drop has been fixed to 2% of the nominal voltage. Since the length of each segment has been fixed, this constraint depends

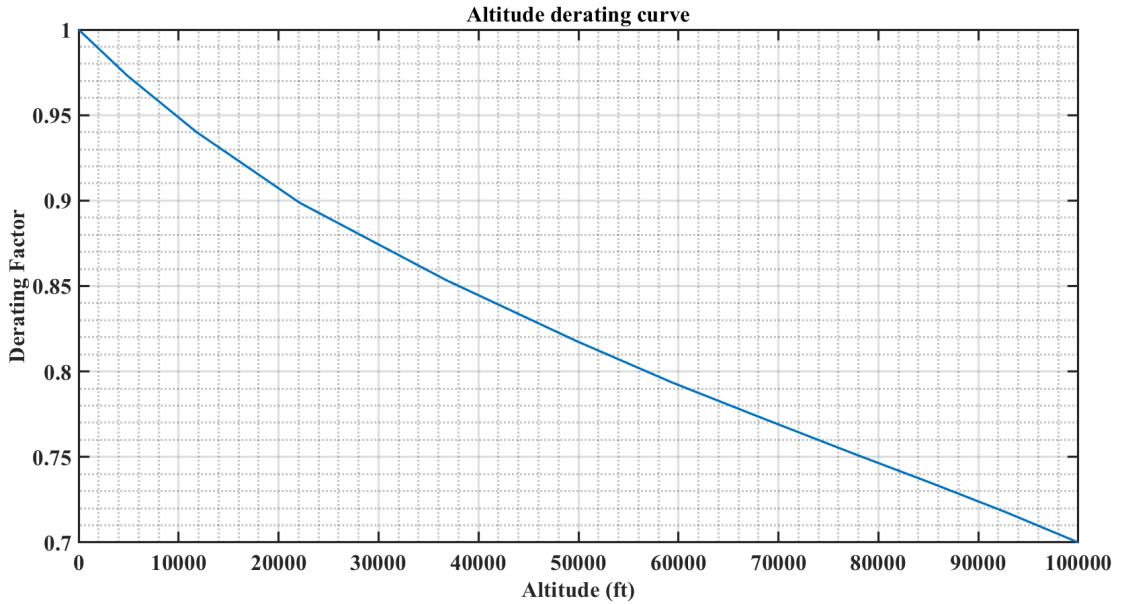


Figure 2.13: Derating factor related to the operating altitude.

on the resistivity (ρ_{Ω}) and the ampacity. The last equation of the system is Eq. (2.51), where the length l of the segment is fixed and the maximum voltage drop is calculated from the nominal voltage, but the ampacity and the resistivity are a function of the size, once the conductor material has been chosen.

$$V_{drop} = \rho_{\Omega}(AWG)lI(N_{wire}, AWG) \quad (2.51)$$

At constant size, wire ampacity increases with the difference between rated temperature and the operating temperature. Thus, this second one should be fixed to be the highest one along the mission profile or, in other words, the ambient temperature at take-off. On the other hand, the rated temperature is fixed by the designer, but cannot be lower than the indicated ambient temperature. The sizing procedure is thus the following:

- 1 The rated temperature of the wire is chosen.
- 2 The current loading percentage is chosen.
- 3 The number of bundles is chosen.
- 4 From the maximum operating altitude, the associated derating factor is calculated (Fig. 2.13).

- 5 A certain range of feasible AWG size is chosen, then, the associated values of resistivity (Table 2.7) and ampacity (Table 2.8 and Fig. 2.14) are calculated.
- 6 A certain range for the number of conductors in the cable is chosen and the associated derating factors (Fig. 2.12) are calculated.
- 7 From outputs obtained at previous steps, the matrix of possible bundle ampacity is calculated through Eq. (2.50). The values calculated depend on the range of possible size and number of wires chosen.
- 8 From the required current calculated through Eq. (2.48), the possible combination of size and number of conductors is reduced (Fig. 2.15).
- 9 Each cable dimensioned at the previous step is then checked for the maximum voltage drop (Eq. (2.51)).
- 10 From the remaining wire size compliant with the requirements, the minimum wire diameter is chosen.
- 11 The number of conductors is the minimum necessary to fulfil the requirements with the wire size frozen at the previous step.

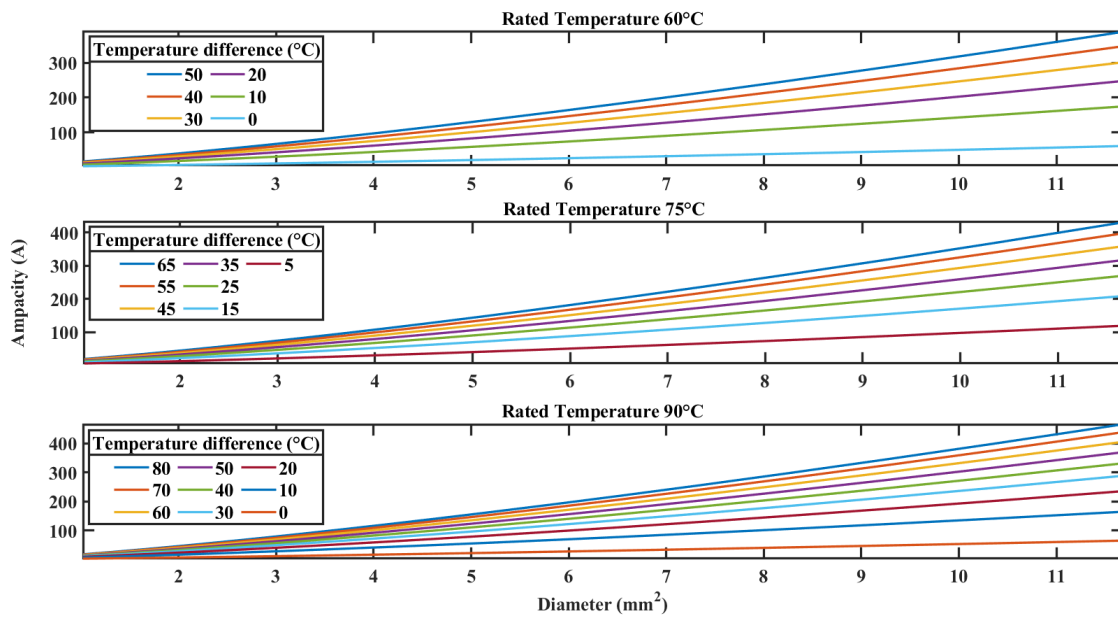


Figure 2.14: Ampacity in free air with respect to wire diameter at different rated and operating temperatures.

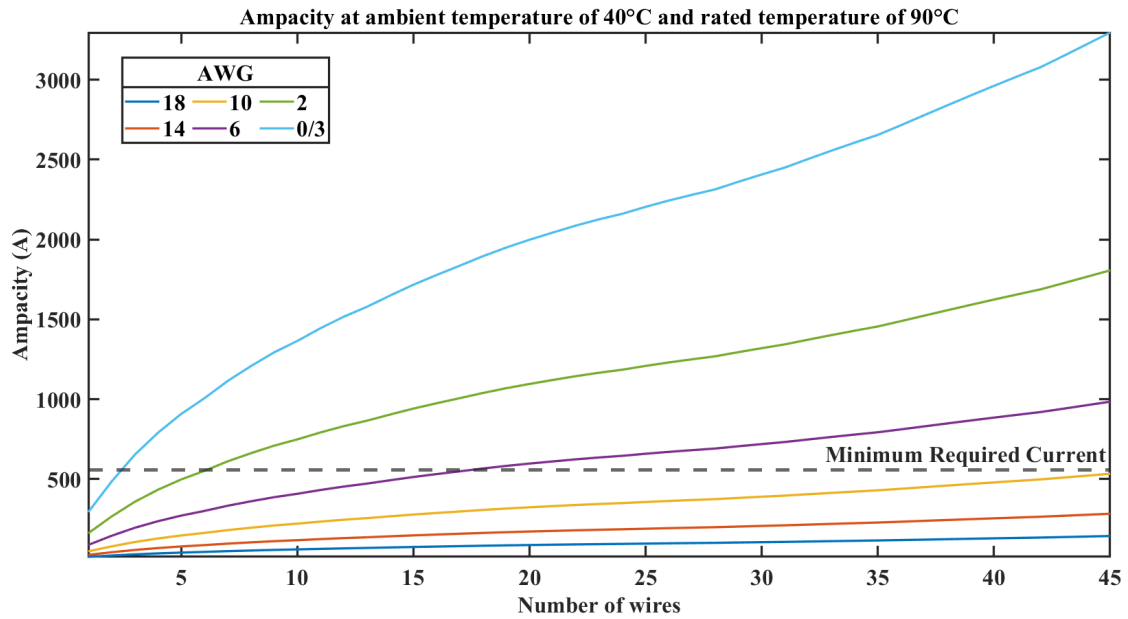


Figure 2.15: Ampacity of a cable considering different combinations of size and number of conductors. The minimum required current is 555 A (150 kW and 250 V DC).

2.1.6 Fuel Storage

The fuel system is designed to provide a continuous supply of fuel at the right temperature and pressure to the engines, the fuel cells, and the auxiliary power unit. As shown in Fig. 2.16, the fuel system can be divided in two different components [109]: one is deputed to the fuel storage and distribution, the other one monitors the environmental conditions and the fuel properties assuring that the variations of local pressure and temperature are within the tolerance range. The present work does not investigate the design of each single component composing the fuel system, focusing the attention only on the fuel storage and, in particular, on the differences between tanks designed to store conventional fuel and those designed to store hydrogen.

The hydrogen specific energy is approximatively 33.6 kWh/kg , making it one of the most promising alternatives to fuel. However, the density of the gaseous hydrogen is pretty low, tightening up the challenge of storing large quantities of fuel in reduced available space. This is the main issue when designing a storage unit, even for conventional fuel systems. The most common location used for fuel storage is within the wing structure typically between the two main spars. On the one

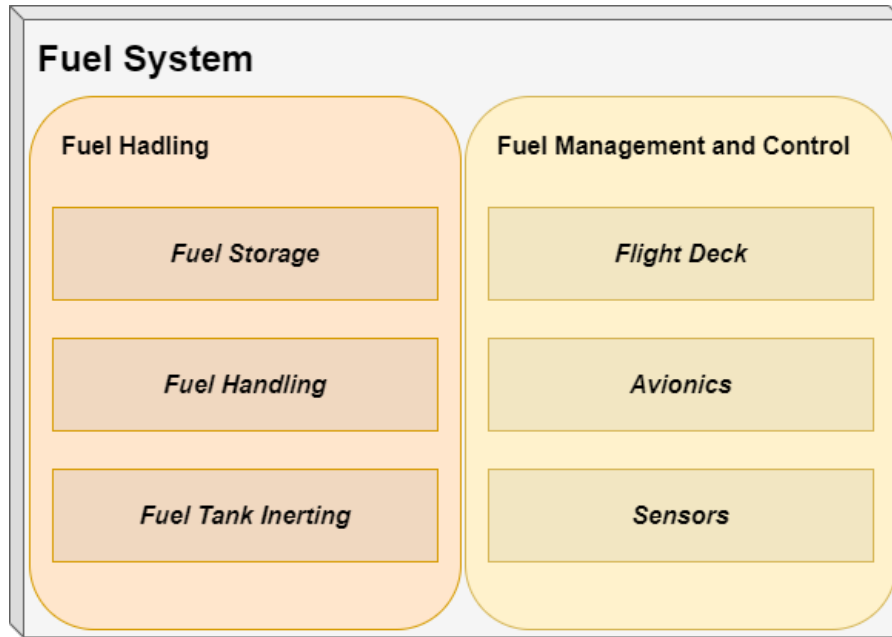


Figure 2.16: Conventional fuel system map.

hand, this allows load reduction over the wing, but, on the other hand, the available space is reduced for aerodynamics reasons and the proximity to engines could cause major damages in case of uncontained rotor burst. Hydrogen is generally stored as compressed gas or cryogenic liquid, requiring the design of tanks capable of facing the structural stress. For this reason, cylindrical or spherical geometries are the most suited for hydrogen storing, even if this would require greater dimensions making the fuselage tailcone a more suited space to locate the tanks [110,111]. The storing of hydrogen in gelled form, chemically bounded to other elements or contained in permeable structures is not suited to supply fuel cells [112] and will not be discussed in the present work.

The first requirement for tank sizing is the energy required to accomplish the mission profile. Fuel mass and volume are calculated from the energy requirement through the specific energy and the energy density, respectively. However, in case of hydrogen stored as compressed gas, under the hypothesis of ideal gas, the following method can be considered to calculate the necessary volume [113]. The necessary hydrogen volume is calculated as reported in Eq. (2.52) [113], where the gas constant R is equal to $4157.20 \frac{Nm}{Kkg}$, the hydrogen mass m_{H_2} is fixed by mission

requirements, the temperature T is the maximum value experienced at landing, the pressure P is the minimum internal pressure, and, finally, the compressibility factor Z is calculated through Eq. (2.53).

$$V_{H_2} = \frac{ZRm_{H_2}T}{P} \quad (2.52)$$

$$Z = 0.9970 + 6.4149e^{-9}P \quad (2.53)$$

Once the internal dimension is calculated, the thickness of the tank can be calculated assuming a certain material and the associated yield strength σ_y (410 MPa for aluminium 2014-T6). Eq. (2.54) and Eq. (2.55) are used to calculate the thickness of spherical and cylindrical tanks, respectively, with a certain safety margin $S.M.$. The dependence of the thickness from the tank radius r could require more iterations to optimize the geometry.

$$t_w = S.M. \cdot \frac{rP}{\sigma_y} \quad (2.54)$$

$$t_w = S.M. \cdot \frac{rP}{2\sigma_y} \quad (2.55)$$

From geometry and material density (2800 kg/m^3 for aluminium tanks), the mass of the storage unit can be calculated.

In case of liquid fuel, the design of the system requires additional considerations dealing with viscosity, freezing point, density, and vapour pressure [109, 114]. The first two characteristics listed dictate the requirements for the fuel handling system, although they are not critical parameters for hydrogen. The increment of viscosity at low temperatures can cause critical flow losses in the pipeline. In case of aviation fuel, this condition can be experienced in cold days at landing, when the remaining quantity of fuel is low and fuel bulk temperature and pressure approach the freezing point. In freezing conditions, the wax precipitates out of solution creating obstructions and blocking piping lines and filters. To lower the severity of these constraints, some additives are used in the solution.

In a broader context, density variations vary the quantity of fuel storable at constant volume, determining one of the sizing factors for the tank volume.

These variations are related to pressure and temperature fluctuations during the flight mission. Typically, regarding conventional fuel, the density at the highest temperature admissible during refuelling is chosen to size the aircraft tank. In the end, the density ρ_{Fuel} obtained and the fuel mass m_{fuel} required to accomplish the mission profile are used to calculate the tank volume, as shown in Eq. (2.56).

$$V_{Fuel} = \frac{m_{Fuel}}{\rho_{Fuel}} \quad (2.56)$$

On the other hand, liquid hydrogen requires cryogenic storage at a temperature T_{H_2} of about $-260^\circ C$ and pressurized at about $0.145 MPa$ [115]. Consequently, the density variation of liquid hydrogen is neglected assuming a fixed value ($\rho_{H_2} = 71 kg/m^3$). The resulting liquid volume is calculated by Eq. (2.57), where an additional safety margin V_i of about 7.2% has been accounted [113].

$$V_{H_2} = \frac{m_{H_2}(1 + V_i)}{\rho_{H_2}} \quad (2.57)$$

Based on the shape of the tank, Eq. (2.54) and Eq. (2.55) can be applied to measure the thickness of the internal layer required to face the structural stress. Once volume and thickness have been calculated, the mass is determined from the material density. However, as further discussed in this section, in case of cryogenic storage, the additional mass necessary for insulation should be calculated.

The vapour pressure is a limiting factor for the operational flight envelope of commercial aircraft. Inevitably, increasing altitude and Mach number, high evaporation rate, and even boil-off could occur. Moreover, the vapour pressure approaches the pressure at the ullage making it difficult to supply fuel to the engines. These issues require the introduction of open vent systems on commercial aircraft to increase the tank pressure above ambient conditions. Conversely, the hydrogen tank and lines must be sealed off from the atmosphere and, thus, a closed vent system is needed. Focusing on cryogenic hydrogen, the boil-off condition can cause an abrupt increment of pressure and, naturally, critical structural stress. With the purpose of avoiding an uncontrolled boil-off, the fuel tank is wrapped in an insulation layer. The estimation of insulation layer thickness is based on the

analysis of the heat transfer process by applying the energy balance. The heat flow between tank wall and insulation due to conduction is equal to the exiting flow rate due to radiation and convection. In literature [113], the relationship between the two heat flow is summarized by Eq. (2.58), where K is the thermal conductivity of the insulation layer, S_i is the thermal exchange surface, T_i and T_{H_2} are the temperature of the outer and internal surfaces of the insulation layer, respectively, t_i is the layer thickness, M is the boil-off mass rate, and h_{H_2} is the latent heat of vaporization of liquid hydrogen ($h_{H_2} = 446592 J/kg$).

$$KS_i(T_i - T_{H_2})/t_i = Mh_{H_2} \quad (2.58)$$

From the maximum allowed fraction of hydrogen mass boiling during a complete mission, the mass boil-off rate is determined. The hydrogen flow supplied to fuel cells must free enough space to balance the gaseous hydrogen volume produced according to the chosen boil-off rate, otherwise a higher volume is required or a lower boil-off rate must be assumed. In other words, the maximum allowed boil-off rate depends on the available volume created by the exit of the hydrogen from the tank. The other parameters depend on the insulation material chosen and the characteristics of liquid hydrogen stored. Finally, substituting the surface S_i value as a function of the insulation layer thickness, this last can be calculated. When the insulation material is chosen and the density determined, these data are used to weigh the layer.

The particular geometry of the hydrogen tank, necessary to minimize the tensile stress, requires a larger volume with respect to conventional fuel tanks. This is the reason why cryogenic and pressurized tanks are generally boarded in the fuselage. However, some issues are related to this integration. Firstly, the number of emergency exits for the evacuation protocol requires a certain clearance that cannot be compromised by the presence of the tank. For this reason, it is advisable to put the hydrogen tanks in the rear part of the fuselage. The dimensions of those sections of the fuselage are the main constraints to the tank volume. From this point of view, based on the required hydrogen mass calculated to accomplish the mission analysis, it could be necessary to redraw the fuselage and iterate the design process.

2.2 Aero-propulsive Interactions

The design of innovative concepts proposed in the present work requires a dedicated discussion about aero-propulsive interactions. With the objective of going further than classical methods, while designing concepts powered by innovative propulsive systems, the benefits related to the installation of the powertrain need to be measured from the early stages of the design process. Different methods are presented considering the maturity reached at each step of the conceptual design chain. Starting from the sizing activity, during which the study of new concepts is approached by dimensionless parameters, and ending with mission analysis, the aero-propulsive interactions are discussed in the present chapter considering mathematical models with different reliability levels. Technologies discussed in the present section are specifically designed to provide aerodynamic benefits while performing their primary propulsive function, thus, jet flaps will be excluded, whilst referring the reader to literature studies dealing with this topic [116].

2.2.1 Distributed Electric Propulsion (DEP)

In the case of high-lift propulsion or distributed electric propulsion, the aerodynamic effects of the propeller slipstream interacting with lifting surfaces are measured considering two different approaches: a simple approach [22] based on the momentum theory [117], and an alternative medium-level method based on the vortex-lattice method [118, 119].

The first method has been discussed in literature and applied to the early stages of the design process [41]. When the present method is applied to the sizing step of the design chain, dealing with point performance, it requires a dimensionless description of the geometry of the wing, as well as of the distributed propulsive architecture. The present work describes the procedure with minor differences from Ref. [41] and only for the case of point performance. The percentage of distributed thrust, that is the percentage of thrust provided by distributed electric propellers or fans, with respect to the total thrust is defined by the χ parameter. This parameter is related to the distributed propulsive system efficiency, or, in other words, the

efficiency of the propellers or the fans distributed on the wingspan, the efficiency of the primary propulsive system and the shaft power ratio ϕ , that is the percentage of distributed propulsive power with respect to the total propulsive power.

$$\phi = \frac{P_{s2}}{P_{s1} + P_{s2}} \quad (2.59)$$

$$\chi = \frac{1}{1 + \frac{\eta_{p1}}{\eta_{p2}} \left(\frac{\phi}{1 - \phi} \right)} \quad (2.60)$$

The interaction between the propeller slipstream and the lifting surface, on which the propulsive system is mounted, depends on the geometry of the two elements. The geometry of the powertrain architecture, shown in Fig. 2.17, is described in relation to the lifting surface geometry on which it is mounted. The dimensionless

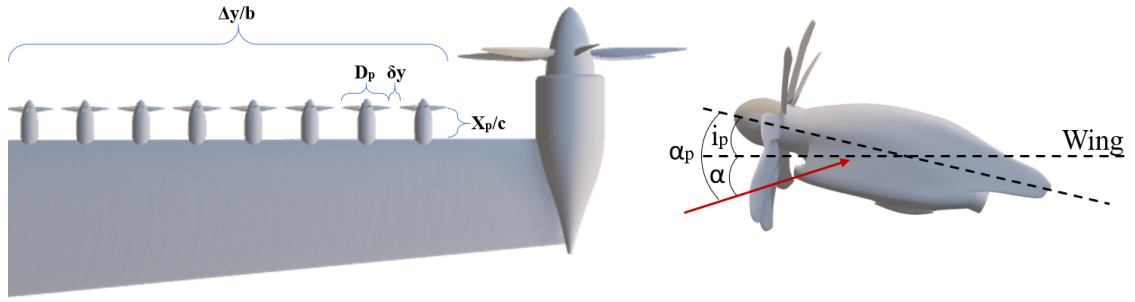


Figure 2.17: Geometric parameters of the distributed electric propulsive system.

diameter is described as a function of the wing loading, the fraction of wingspan covered by distributed propulsion, $\frac{\Delta y}{b}$, the number of propellers, N , and the distance between the propellers in fraction of propeller disk diameter δy .

$$\frac{D_p^2}{W} = \frac{\left(\frac{\Delta y}{b}\right)^2 AR}{N^2 (1 + \delta y)^2 W/S} \quad (2.61)$$

In the same way, the propeller radius can be expressed as reported in Eq. (2.62).

$$\frac{R_p}{c} = \frac{1}{2} \sqrt{\frac{D_p^2 W}{W S} AR} \quad (2.62)$$

The thrust to weight ratio of a single propeller can be written as in Eq. (2.63), where the thrust is provided in N and the weight is provided in kg .

$$\frac{T_p}{W} = \frac{T}{W} \frac{\chi}{N} \quad (2.63)$$

The actuator disk theory drives the estimation of the axial induction factor at the propeller disk as a function of thrust to weight ratio and the diameter of the propeller, Eq. (2.64).

$$a_p = \frac{1}{2} \left(\sqrt{1 + \frac{8}{\rho \pi V_\infty^2} \frac{T_p/W}{D_p^2/W}} - 1 \right) \quad (2.64)$$

The distance between the propeller and the vortex at 1/4 of the airfoil chord can be expressed as a function of the wing loading and the propeller diameter by combining Eq. (2.62) and (2.64), where x_p/c is the distance of the propeller from the leading edge in fraction of chord.

$$\frac{x_{p_{c/4}}}{R_p} = \frac{x_p/c + 1/4}{R_p/c} \quad (2.65)$$

Considering the contraction ratio of the slipstream at 1/4 of the airfoil chord as in Eq. (2.66).

$$\frac{R_{c/4}}{R_p} = \sqrt{\frac{1 + a_p}{1 + a_p \left(1 + \frac{x_{p_{c/4}}/R_p}{\sqrt{(x_{p_{c/4}}/R_p)^2 + 1}} \right)}} \quad (2.66)$$

The axial induction influencing the aerodynamic coefficients is expressed as in Eq. (2.67).

$$a_{c/4} = \frac{1 + a_p}{(R_{c/4}/R_p)^2} - 1 \quad (2.67)$$

The angle of attack of the propulsive system is the sum of the angle of attack, α , and the incidence of the system, i_p . The angle of attack can be estimated during the sizing activity from the value of the lifting surface lift coefficient, the Mach number, the sweep angle at half of the chord, $\Lambda_{c/2}$ and the aspect ratio.

$$\alpha = \frac{C_{L_{airframe}}}{2 \pi AR} \left[2 + \sqrt{AR^2 (1 - M^2) \left(1 + \frac{\tan \Lambda_{c/2}}{1 - M^2} + 4 \right)} \right] \quad (2.68)$$

From this step, it is necessary to introduce the finite-slipstream correction factor, β , which can be a crucial parameter when $R_{c/4}$ is little compared to the airfoil chord. Based on *CFD* analysis, a surrogate model has been proposed in literature,

Ref. [120], to estimate the value of this correction. The bidimensional lift coefficient increase due to aero-propulsive interactions is estimated by the following equation.

$$\begin{aligned} \Delta C_l = & \\ & 2\pi [(\sin(\alpha) - a_{c/4} \beta \sin(i_p)) \\ & \sqrt{(a_{c/4} \beta)^2 + 2 a_{c/4} \beta \cos(\alpha + i_p) + 1 - \sin(\alpha)}] \end{aligned} \quad (2.69)$$

The bidimensional drag coefficient variation is estimated by the sum of two different contribution: the induced drag coefficient variation and the skin friction dependent variation.

$$\Delta C_{d_i} = \frac{2 C_{L_{airframe}} \Delta C_l}{\pi AR} \quad (2.70)$$

$$\Delta C_{d_0} = a_{c/4}^2 C_f \quad (2.71)$$

In Eq. (2.71), the skin friction coefficient, C_f , is introduced. The three-dimensional coefficients are defined by multiplying the bidimensional coefficients by $\Delta y/b$, that is the ratio of wingspan covered by the slipstream of the distributed propellers.

One last consideration deals with the effect of high-lift propulsion on the lifting coefficient derivative with respect to the angle of attack (C_{L_α}). Assuming that the zero-lift angle of attack remains unchanged, the lift coefficient's curve slope is corrected for the contribution of distributed electric propulsion as reported in Eq. (2.72).

$$C_{L_{\alpha DEP}} = \frac{C_L + \Delta C_L}{C_L} C_{L_\alpha} \quad (2.72)$$

For the sake of completeness, one last contribution to airfoil aerodynamics deals with the increment in pitching moment [121]. Essentially, the airfoil pitching coefficient $C_{m_{ac}}$ with respect to the aerodynamic center x_{ac} of the airfoil is calculated by Eq. (2.73), where x_{cp} is the position of the pressure center and c is the chord length.

$$C_{m_{ac}} = C_l \frac{x_{ac} - x_{cp}}{c} \quad (2.73)$$

From Eq. (2.73), assuming that the aerodynamic center and the pressure center remain almost unchanged for subsonic flow [122], the contribution to the pitching moment due to propeller slipstream is calculated through Eq. (2.74).

$$\Delta C_{m_{ac}} = \frac{\Delta C_l}{C_l} C_{m_{ac}} \quad (2.74)$$

It is here explicitly noted that a negative pitching moment will remain negative when the lift coefficient increases.

As numerical method, the vortex lattice method (VLM) can provide additional information about the aero-propulsive interaction between the propeller (or the fan) slipstream and the lifting surface. VLMs describe the lifting surfaces by discretizing them in panels and modelling each panel as an infinitely thin vortex to compute its contribution to lift and induced drag. In Ref. [123], ring vortices are used to model wing panels and horseshoe vortices at the trailing edge are used to model wing wake. In Ref. [124], horseshoe vortices are placed on the wing plane using two pivotal points in the chordwise direction, and a cosine function distribution of panels for the spanwise direction. The present work does not discuss a specific formulation of the vortex lattice method, referring to literature for a baseline [118, 119, 123, 124]. VLM is based on some preliminary assumptions: flow field is incompressible, inviscid, and irrotational. These hypotheses limit the aero-propulsive effects measured to those on lift and induced drag. In most cases, the application of the aero-propulsive interaction to VLM is related to data that are not always available at the early stages of the design process (such as the rotational speed and angular direction). Moving from a common baseline [124], in Ref. [125–127] easy to implement aero-propulsive interactions are described. The method requires as inputs the propeller geometry, blade polars, and an aerodynamic database. The objective is to calculate the effective angle of attack by summing different contributions. The fundamental equation of the theory is the downwash integral (Eq. (2.75)) for a wing with given lift distribution as it is obtained by integrating the Euler equation of the motion [128].

$$\alpha_i = \frac{w_i}{V_\infty} = -\frac{1}{8\pi} \int \int \frac{lift(x_0, y_0)}{(y - y_0)^2} \left(1 + \frac{x - x_0}{\sqrt{(x - x_0)^2 + (y - y_0)^2}}\right) dx_0 dy_0 \quad (2.75)$$

The induced speed, w_i , at a certain point (x,y) of the lifting surface is related to lift by Eq. (2.75). The induced angle due to the propeller slipstream is calculated by Eq.2.76, where w_p is the vertical induced speed and u_p is the axial induced speed.

$$\alpha_p = \arctan \frac{w_p}{u_p + V_\infty} \quad (2.76)$$

The resulting angle of attack at a certain location is derived from the sum of induced angles and twist angle (ϵ) as suggested in Eq. (2.77).

$$\alpha_{eff}(y) = \alpha - \alpha_i + \alpha_p + \epsilon(y) \quad (2.77)$$

From Eq. (2.75), defining the dimensionless circulation as in Eq. (2.78) and the lift coefficient as in Eq. (2.79), it is possible to derive Eq. (2.80) relating the lift coefficient with the effective angle of attack.

$$\gamma = \frac{cC_l}{2b} = \frac{cC_{l_{alpha}}}{2b} \alpha_{eff} \quad (2.78)$$

$$C_l = C_{l_\alpha} \alpha_{eff} \quad (2.79)$$

$$C_L = \frac{\pi AR}{M+1} \sum_{n=1}^M \gamma_n \sin(\theta) \quad (2.80)$$

In Eq. (2.80), M is the number of spanwise stations and θ is calculated as in Eq. (2.81).

$$\theta = \frac{n\pi}{M+1} \quad (2.81)$$

The main problem related to the proposed approach is the high-level of details required to be implemented. Blade polars and aerodynamics characteristics are seldom frozen during the early stages of the conceptual design and it is always preferred to optimized propeller airfoils only when the concept is at its final assessment. When propellers are still modelled as actuator disks, the approach proposed cannot be considered. In this case, moving from the method proposed in literature [129], the propulsive effect on the lifting surface is modelled as increment speed due to axial induction in the propeller slipstream. From the above assumptions, the resulting flow field is conservative and, thus, describable by the sum of an asymptotic velocity field and a perturbation. The perturbation of each panel of the lifting surface is modelled by horseshoe vortex with a certain intensity, Γ . Considering a certain vortex of amplitude $[y_1, y_2]$ and positioned at 1/4 of the

panel chord (x_0, y_0) , the induced speed (w_{xy}) at a certain control point (x, y) , is reported in Eq. (2.82) (Eq. (2.83) for $x = x_0$).

$$w_{xy} = \frac{\Gamma}{4\pi} \left(\frac{1}{y - y_1} \left(1 + \frac{\sqrt{(x - x_0)^2 + (y - y_1)^2}}{x - x_0} \right) - \frac{1}{y - y_2} \left(1 + \frac{\sqrt{(x - x_0)^2 + (y - y_2)^2}}{x - x_0} \right) \right) \quad (2.82)$$

$$w_{xy} = \frac{\Gamma}{4\pi} \left(\frac{1}{y - y_1} - \frac{1}{y - y_2} \right) \quad (2.83)$$

Applying at each position (x_0, y_0) a Dirichlet boundary condition imposing a null normal velocity across the camber surface, the value of Γ at each control point can be calculated from Eq. (2.84), where A is the normalwash matrix.

$$A\Gamma = b \quad (2.84)$$

Each element a_{xy} of the matrix A is obtained by multiplying the normal vector positioned in each control point and the induced speed vector (Eq. (2.85)). The vector b is calculated as in Eq. (2.86).

$$a_{xy} = w_{xy} n_{xy} \quad (2.85)$$

$$b_{xy} = V_\infty [-\cos(\alpha) \cos(\beta), \sin(\beta), -\sin(\alpha) \cos(\beta)] n_{xy} \quad (2.86)$$

At a rough order of magnitude, the effect of the distributed propellers slipstream can be approximated by accounting for the induced speed (Eq. (2.67)) to modify V_∞ in Eq. (2.86) element by element, depending on the position of each panel with respect to the actuator disk. The resulting force acting on the lifting surface panel is calculated as in Eq. (2.87).

$$F_{xy} = \rho_\infty V_\infty \Gamma_{xy} \quad (2.87)$$

Panel by panel, the resulting force is decomposed in order to calculate drag and lift contributions of each panel. The additional information acquired by this numerical approach with respect to the semi-empirical method is the aerodynamics load distribution. Inertial and aerodynamics loads can vary due to propulsive lines distributed along the wingspan and this can be a crucial aspect when designing the structural components of the lifting surface.

2.2.2 Tip-Mounted Propeller

The main impact of propeller slipstream on wing performance is the increment of speed downstream of the propeller. The first simple assumption that can be done is that only the speed component normal to the propeller plane is increased, as modelled by the momentum theory, where the actuator disk substitutes the propeller. However, this model neglects the swirl in the propeller slipstream, whose interaction with the tip vortex of the wing causes a variation of induced drag, even more than the increment in axial speed. Thus, to consider the tangential induction in the propeller slipstream, the following considerations are based on the blade element momentum theory [130].

As shown in Fig. 2.18, the presence of the wing cause a decrease of the angle of attack related to the downwash speed induced. The induced angle of attack due to the wing, also called downwash angle, α_{i_w} , can be calculated as in Eq. (2.88).

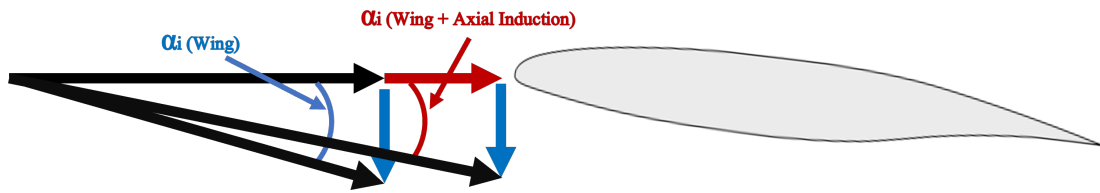


Figure 2.18: Induced speeds and angles.

$$\alpha_{i_w} = \frac{w}{V_\infty} = \frac{C_L}{\pi A R e} \quad (2.88)$$

In the same figure, the effect of the increase in axial speed due to the presence of the propeller is shown. The variation of the axial speed causes an upwash effect counteracting the downwash due to the wing. In a first approximation, it can be assumed that downwash due to the wing is equal to upwash due to the swirl in the propeller slipstream and that the only effect is related to the induced axial speed. Nevertheless, approaching a high angle of attack, the upwash can cause a premature stall from one side of the propeller, therefore upwash and downwash induced angles have to be estimated. In Fig. 2.19, the induced velocities considered in the present paragraph are shown. In order to estimate the upwash induced angle, the

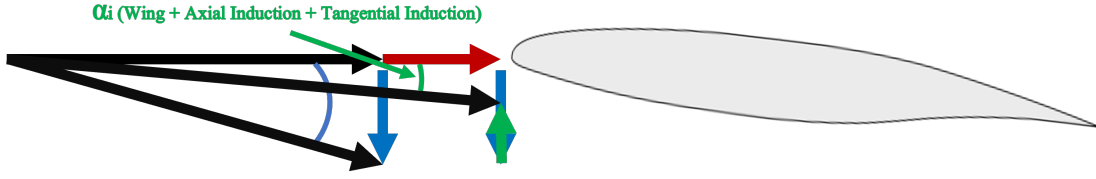


Figure 2.19: Induced speeds and angles.

tangential induction is introduced. The axial induction has been already introduced in Eq. (2.64) and, from that parameter, it is possible to calculate the increase in axial velocity. Differently from this parameter, the tangential induction is a measure of the ratio between the propeller angular speed, Ω , and the angular speed induced on the flow downstream of the propeller, ω , and it can be used to estimate the vertical speed. Eq. (2.89) is used to calculate the tangential induction due to the propeller.

$$a_{pt} = \frac{\omega}{2\Omega} = \frac{1}{2} - \sqrt{\frac{1}{4} - \frac{V^2}{\Omega^2 R_p^2} (1 + a_p) a_p} \quad (2.89)$$

Since the sizing activity does not move from a frozen geometry, some elements of the previous equation could not be surely determined at the early stages of the design chain. A necessary assumption should be made to relate the angular velocity of the propeller to its radius. The assumption is based on the fact that the maximum angular speed of the propeller should be such as to keep the tip Mach number lower than 0.7 to avoid aero-structural problems. Even if in the present work the chosen Mach number is equal to 0.7, more generally, it is a design parameter chosen by the propeller manufacturer. The tangential speed at propeller tip is calculated as the product of the angular speed Ω and R_p , but the same speed can be obtained imposing the propeller tip Mach number and the sound speed a related to that flight condition. Since the tip Mach number imposed is the maximum possible, the effect of the swirl is the highest possible as well. Thus, the previous equation can be written as follows:

$$a_{pt} = \frac{\omega}{2\Omega} = \frac{1}{2} - \sqrt{\frac{1}{4} - \frac{V^2}{(0.7a)^2} (1 + a_p) a_p} \quad (2.90)$$

The tangential speed, w_p , perceived in the propeller slipstream is a function of the tangential induction and the tangential speed of the tip of the propeller.

$$w_p = a_{pt}\Omega R_p \quad (2.91)$$

On the other hand, the axial speed induced in the propeller slipstream can be defined as in Eq. (2.92).

$$u_p = (1 + a_p)V_\infty \quad (2.92)$$

The total induced speed, V_p , on the wing due to the propeller can be found as a sum of the two aforementioned contributions.

The effective angle of attack due to the presence of the wing can be calculated as presented in Eq. (2.93).

$$\alpha_{eff} = \alpha - \alpha_{i_w} = \alpha - \frac{CL}{\pi ARe} \quad (2.93)$$

The angle of attack induced by the propeller slipstream, α_p , can be calculated as proposed in Eq. (2.94).

$$\alpha_{i_p} = \text{atan}\left(\frac{w_p}{u_p}\right) \quad (2.94)$$

Combining the effect of the wing and of the propeller, the variation of the induced drag coefficient can be expressed as reported in Eq. (2.95).

$$\Delta C_{D_i} = -\frac{\Delta y_b}{N-1} \frac{C_L^2}{\pi ARe} + \frac{\Delta y_b}{N-1} \left(\frac{V_p}{V_\infty}\right)^2 C_{L\alpha} (\alpha - \alpha_{i_p}) \left(\frac{C_L}{\pi ARe} - \alpha_{i_p}\right) \quad (2.95)$$

The resulting value of ΔC_{D_i} is based on the hypothesis that the propeller swirl is counter-rotating with respect to the wingtip vortex.

As discussed in 2.2.2, tip-mounted propellers effects can be simulated by introducing some correction to the vortex lattice method (VLM). Numerical methods calculate the induced drag as the sum of effects of the local inductions on each panel composing the lifting surface. The effective attitude perceived by panels behind the propeller disk is corrected to account for the induced angle from Eq. (2.94). The resulting angle of attack is used in Eq. (2.86) (α).

2.2.3 Validation of the Methods

The validation of the methods presented in 2.2 is carried out considering both medium and high-fidelity methods. The test campaign required a large number of computational fluid dynamics (CFD) analyses and involved the Italian Aerospace Research Center (CIRA) within the framework of the European project named *Innovative turbopROp configuration (IRON)* and the Italian project named *PROpulsione e Sistemi IBridi per velivoli ad ala fissa e rotante (PROSIB)*. In this context, the results discussed are limited to those produced by the University of Naples Federico II.

The high-fidelity analyses considered in this section are based on the Reynolds Averaged Navier-Stokes equations (RANs). The Spalart-Allmaras turbulence model has been chosen. In order to evaluate the correct parameters to set up the mesh, numerous analyses are carried out with the objective of choosing the proper mesh size balancing accuracy and calculation time. Associated with the size reduction, the number of cells increases as well, leading to more accurate results, but also to a higher computational time. In this context, increasing the number of cells, the consistency of the mesh is considered acceptable when the variation of the resulting aerodynamic coefficients is under 1%. The resulting number of cells for the test cases discussed in this section ranges from $5.75e + 6$ to $1.75e + 7$, depending on the geometry considered. The mesh box has been designed considering the semi-span as the reference dimension. Width and height are equal to 10 times the reference dimension, and the far-field length is 30 times the reference dimension.

When approaching the design of experiments to validate a method, a full-factorial matrix including a wide range of values for each design variable is the most suited approach. The present paragraph is based on some fundamental concepts of the statistical design of experiments that are not discussed in this work. Depending on the purpose, the analysis of the variance can be implemented to verify the hypothesis of sensitiveness of a test response from a factor or from a combination of factors. Through this approach, some design variables can be excluded in favour of others. The response variables considered in the present context are the variations

of the aerodynamic coefficients, namely ΔC_L , ΔC_{D_0} , and ΔC_{D_i} . Both the wing platform and the propulsive system influence the response variables. However, the analysis of the variance do not identify any stochastic correlation among the geometric characteristics of the wing and those of the propulsive system.

The first step is the definition of the case study or, in other words, the description of the wing geometry considered. The aerodynamic coefficients depend on the wing geometry, but it is necessary to exclude those variables that are not directly connected to the aero-propulsive interactions. The first variable excluded is the airfoil geometry. In fact, the methods discussed in 2.2 are sensible to the clean coefficients and not to the airfoil geometry. For the same reason, the interaction with the flap slot and the nacelle volume is neglected. Regarding the wing geometry, the design variables of interest are the local chord and the aspect ratio. The correlation between these parameters and the aero-propulsive effects is the key factor to determine the number of case studies necessary to validate the method.

The high-fidelity analyses are the benchmark for validating the aerodynamic coefficients calculated through the methods presented in this section. The results are considered reliable if the divergence is lower than 10%.

First Case Study

The first case study considered is the wing shown Fig. 2.20. The geometry is described in Table 2.9 and the characteristics of each section are described in Table 2.10.

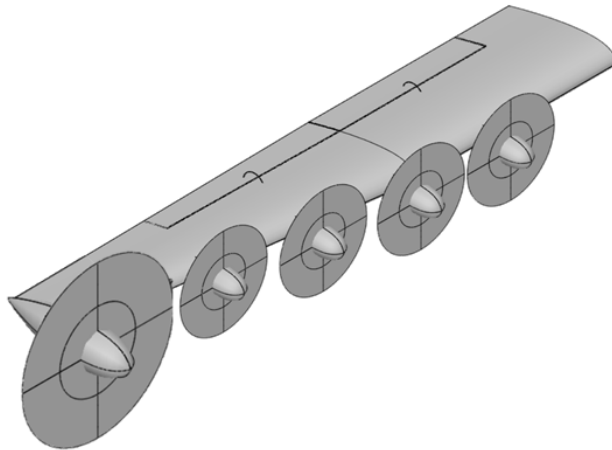


Figure 2.20: Wing geometry (semi-span) considered for the first study case.

	Value	Unit
Wingspan	24.57	<i>m</i>
Mean aerodynamic chord	2.28	<i>m</i>
Incidence angle	3.00	<i>deg</i>
Wing area	54.50	<i>m</i> ²
Aspect ratio	11.08	—

Table 2.9: Geometric characteristics of the wing in Fig. 2.20.

	Root	Kink	Tip
Airfoil	NACA 23015	NACA 23015	NACA 23018
Chord length (<i>m</i>)	2.57	2.57	1.41
Spanwise position (<i>m</i>)	0	4.75	12.29
Thickness ratio	0.15	0.15	0.18
Twist angle (<i>deg</i>)	0	0	1.50
Dihedral angle (<i>deg</i>)	0	0	1.92

Table 2.10: Geometric characteristics of the wing sections.

The two flaps of this lifting surface are described in Table 2.11.

	Inner flap	Outer flap
Inner position (<i>m</i>)	1.29	4.75
Outer position (<i>m</i>)	4.75	8.92
Flap chord fraction	0.3	0.3
Take-off deflection angle (<i>deg</i>)	15	15
Landing deflection angle (<i>deg</i>)	30	30

Table 2.11: Flaps geometric characteristics.

Concerning the design variables of interest, two different full-factorial test matrices have been designed to test the sensitiveness to the characteristics of the distributed propellers and the tip-mounted propeller. The design variables considered and the associated values are reported in Table 2.12.

As previously discussed, distributed propellers and tip-mounted propellers are propulsive architectures designed for different objectives. The former increases the lifting capability of the lifting surface at take-off and landing; the latter reduces the induced drag during climb and cruise. Consequently, the method presented in 2.2.1 is studied considering the stall speeds associated with three different flap deflections,

Distributed electric propulsion			
Number of propellers	8	12	16
Propeller diameter (m)	2.06	1.37	1.03
Distance between propellers (% of diameter)	1		
X position from L.E. (% of chord)	[10, 20, 50]		
Z position from L.E. (% of chord)	[-10, 0, +10]		
Thrust (N)	7500	5000	3750
Tip-mounted propeller			
RPM	[990, 1315, 1550, 1972]		
Propeller diameter (m)	[1.97, 2.50, 2.95, 3.93]		
Thrust (N)	[4003, 8006]		

Table 2.12: Design variables of interest associated with the study of the dependency of the aero-propulsive effects from the wing geometry.

labelled "clean", "take-off", and "landing" in Table 2.13. The method presented in 2.2.2 is verified under the "cruise" condition described in the same table.

Test case	Flap deflection angle (deg)	Speed (m/s)	Speed (m)
Clean	0	58.45	0
Take-off	15	49.85	0
Landing	30	44.99	0
Cruise	0	154.74	4544

Table 2.13: Operative conditions studied.

The first objective is to quantify the sensitiveness of the method in 2.2.1 to different numbers of distributed propellers in flapped and clean conditions. For this reason, the number of distributed propellers and their diameters are changed to measure the related variations of the aerodynamic coefficients. The distance from the leading edge of each propeller is constant (10% of the local chord). The vertical offset is null. The results are shown in Fig. 2.21, Fig. 2.22, and Fig. 2.23.

Assumed the conditions proposed in Table 2.14, the comparison highlights the capability of the method to quantify the increment of lift and drag associated with the different numbers of distributed propellers. However, a certain divergence of the results is detected in case of take-off configuration in the close proximity of the maximum lift coefficient. This phenomenon is due to the interaction between the propeller slipstream and the flap slot, which cannot be detected by the method. In

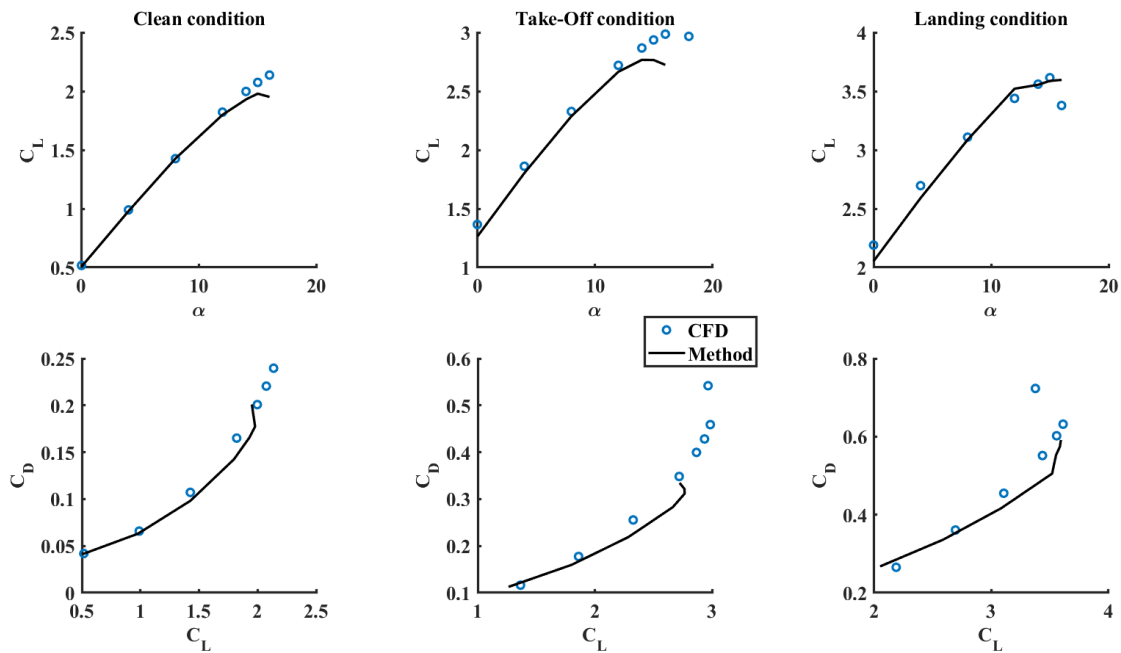


Figure 2.21: Comparison of the results for lift and drag coefficients for different flap configurations in case of 8 distributed propellers (test case 1-1).

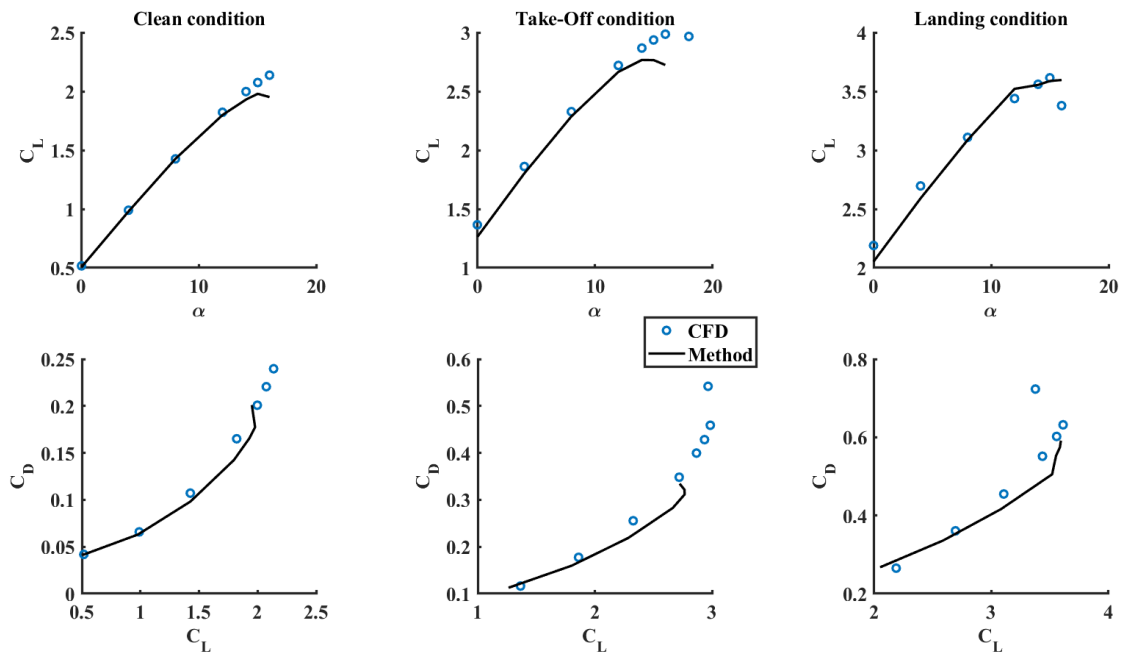


Figure 2.22: Comparison of the results for lift and drag coefficients for different flap configurations in case of 12 distributed propellers (test case 1-2).

Test Case ID	Number of propellers	Propellers diameter (m)	Thrust (N)	Flap deflection angle (deg)	Speed (m/s)
1-1 Clean	8	2.06	7500	0	58.45
1-1 Take-off	8	2.06	7500	15	49.85
1-1 Landing	8	2.06	7500	30	44.99
1-2 Clean	12	1.37	5000	0	58.45
1-2 Take-off	12	1.37	5000	15	49.85
1-2 Landing	12	1.37	5000	30	44.99
1-3 Clean	16	1.03	3750	0	58.45
1-3 Take-off	16	1.03	3750	15	49.85
1-3 Landing	16	1.03	3750	30	44.99

Table 2.14: Test cases considered to study the effect of different numbers of distributed propellers.

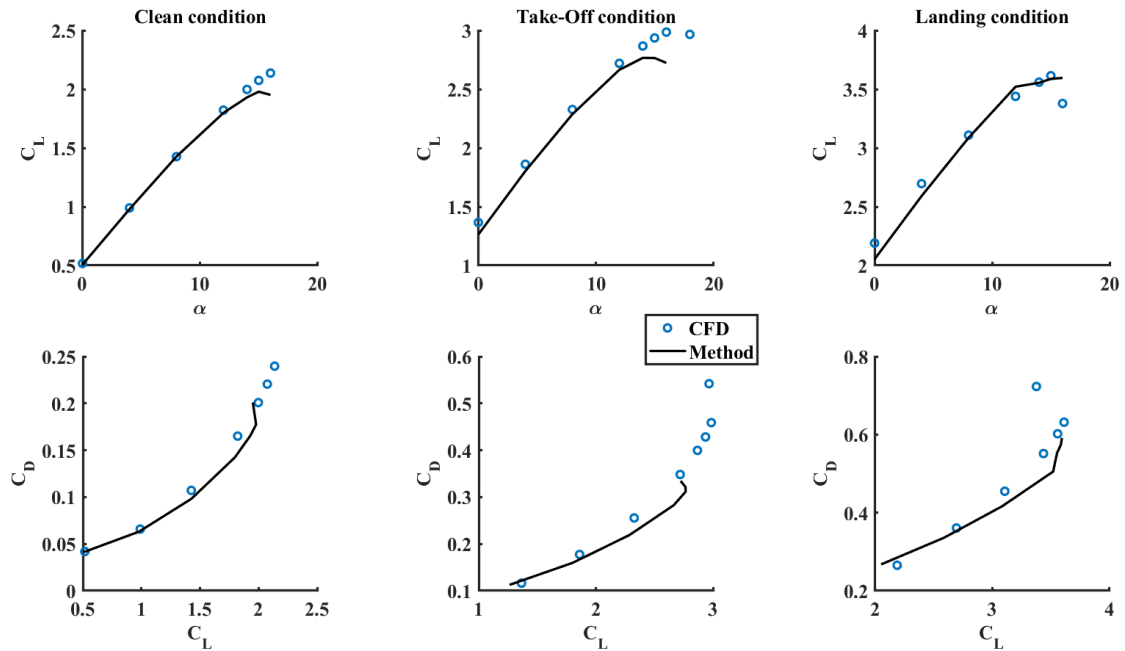


Figure 2.23: Comparison of the results for lift and drag coefficients for different flap configurations in case of 16 distributed propellers (test case 1-3).

fact, as shown by Fig. 2.24, the separation is delayed when the flow is energized by the propeller slipstream. However, increasing the flap deflection, this effect is lost and the maximum lift coefficient is reached at the same angle of attack of the case without propellers.

The interaction between the propeller slipstream and the flap is particularly sensible to the vertical offset. The methods discussed in this paragraph to measure the aero-propulsive interactions do not include this parameter as design variable. However, for small values of the vertical position of the propeller disk (between

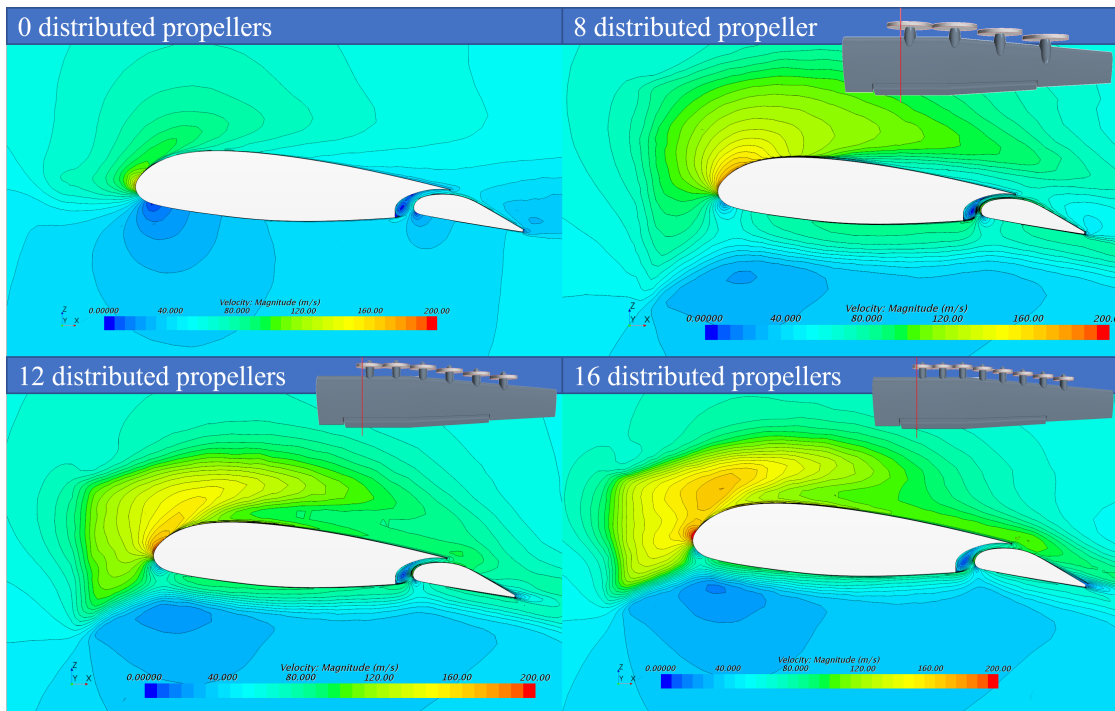


Figure 2.24: Particular of the wing section in take-off configuration at an angle of attack equal at 14 deg .

-10% and +10% of the local chord), the variations of the aerodynamic coefficients are of the same order of magnitude of the error measured comparing the CFD analysis with the low-fidelity methods, as shown in Fig. 2.25. It is here explicitly noted that the minimum divergence between the CFD analysis and the low-fidelity method is obtained for the null vertical offset.

Another variable of interest when studying the effect of distributed propulsion is the forward position of each propeller from the leading edge of the local chord. The method is sensitive to the relative positions of wing and propellers, but the reliability of the results is considered acceptable only up to an offset from the leading edge of about one chord length. This is because the method does not account for the curvature of the propeller slipstream with respect to the asymptotic airflow. Fig. 2.26 shows the lift coefficient at the angle of attack equal to 0 deg for different values of the forward position.

After validating the results concerning distributed propulsion, the following step deals with the interaction between tip-mounted propeller slipstream and wing-tip

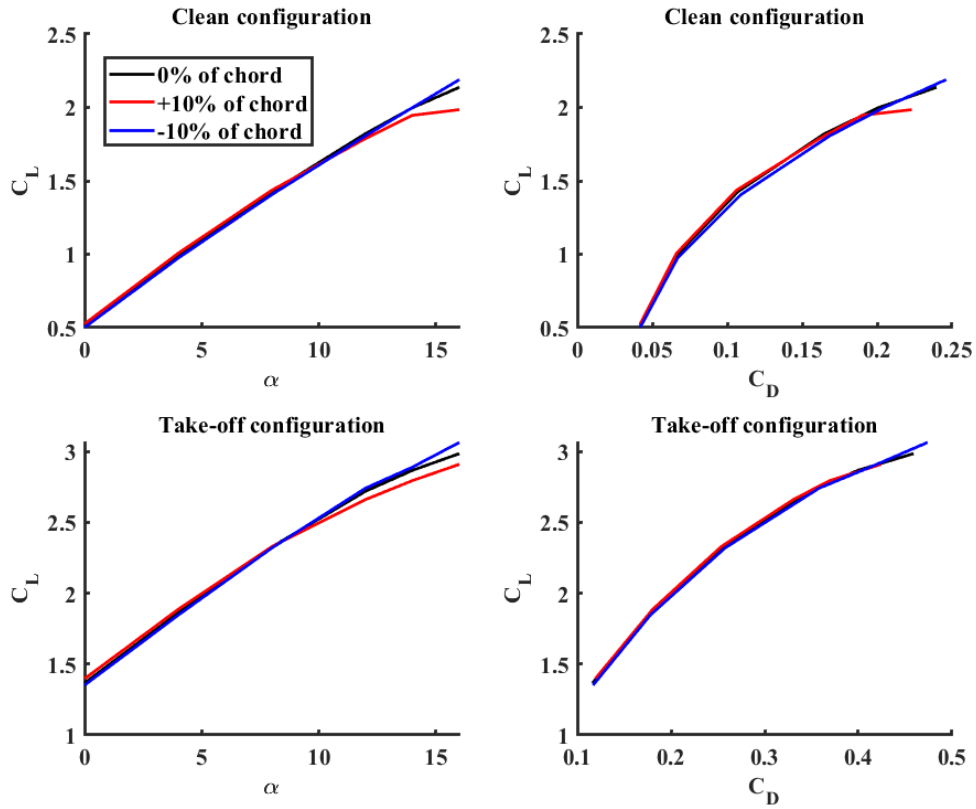


Figure 2.25: Lift and drag coefficients in clean and take-off configurations with 8 distributed propellers.

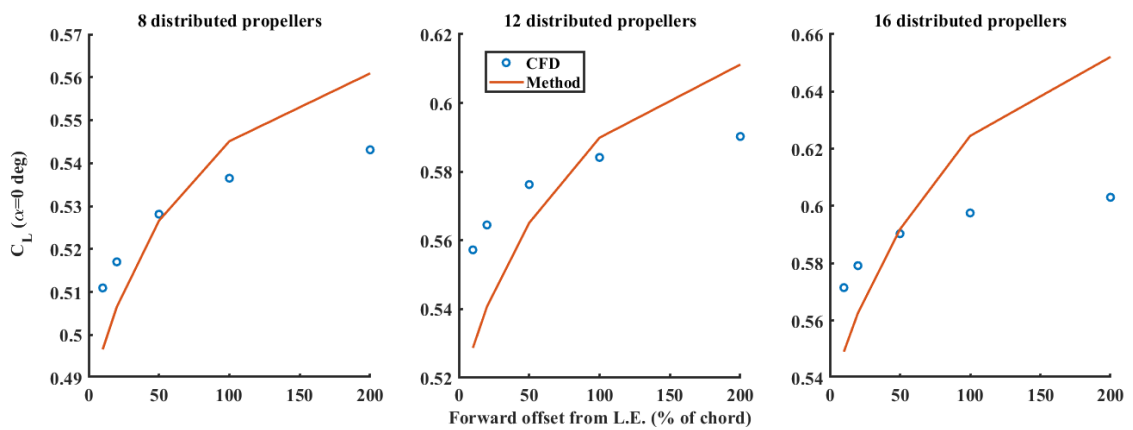


Figure 2.26: Effect of the forward offset of the propeller with respect to the leading edge.

vortex. The method proposed in 2.2.2 is sensitive to a different set of design variables: the rotational speed of the propeller, the thrust, and the propeller diameter. The values considered for each design variable are reported in Table 2.12 and the test conditions are reported in Table 2.13 labelled as "cruise". The comparison showed a good accordance of the high-fidelity and low fidelity methods in the range of angles of attack of interest (between -1 deg and 3 deg). On the contrary, at lower angles of attack, the difference is higher than 10%. The results shown in Fig. 2.27 support these conclusions.

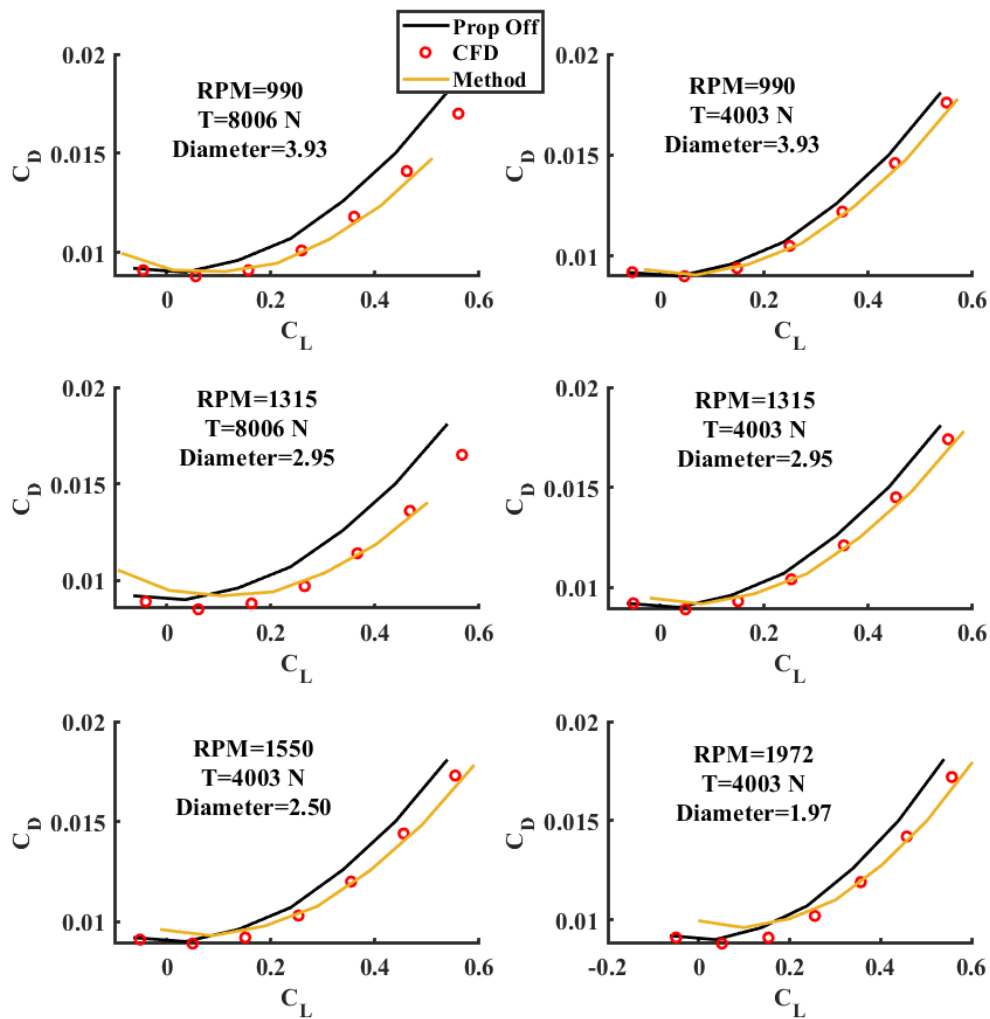


Figure 2.27: Drag polar variations associated to different characteristics of the tip-mounted propeller.

Before proceeding to the following step, one last issue remain unsolved. As previously stated, the type of correlation between the wing geometry and the aero-propulsive effects determines the number of necessary case studies. For this purpose, two additional wings have been designed by scaling the reference to 44 m^2 and 38 m^2 . By reducing the local chord of each section described in Table 2.10, the wing area is reduced at constant wingspan, consequently varying the aspect ratio. The tests carried out on the different lifting surfaces showed a linear correlation between the wing geometry and the aero-propulsive effects. For instance, the test case named *1-3 Clean* in Table 2.14 is showed in Fig. 2.28 applied to the three different wings. This

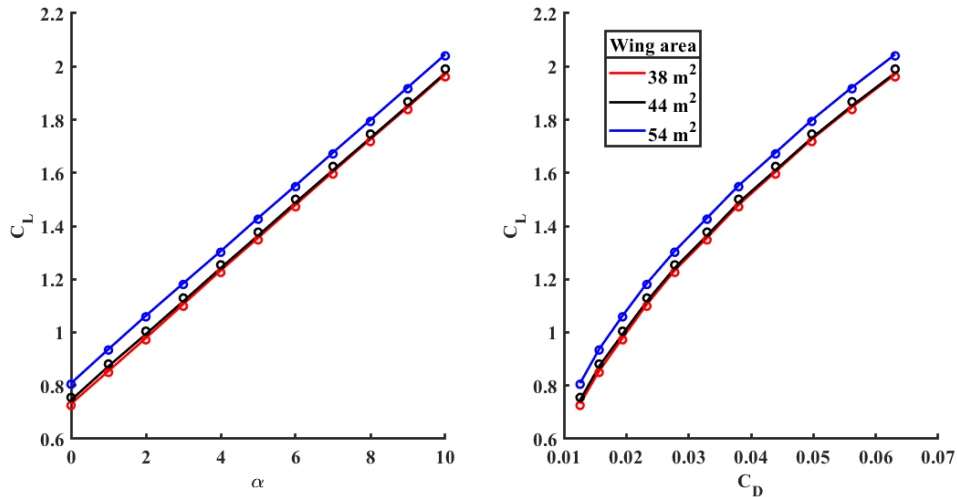


Figure 2.28: Comparison of the aerodynamic coefficients before and after the scaling at constant wingspan. The coefficients account for the aero-propulsive interaction with 16 distributed propellers. The values circled are calculated considering a linear regression.

correlation allows the reduction of the case studies required to validate the model to two. Thus, only one additional lifting surface will be described in the present section.

Second Case Study

The second model considered, shown in Fig. 2.29, is the subject of computational fluid dynamics (CFD) analysis and wind tunnel test campaign in the framework of the Italian project named *PROpulsione e Sistemi IBridi per velivoli ad ala fissa e rotante (PROSIB)*. The wing geometry is described in Table 2.15. The model has three distributed electric propellers and one tip-mounted propeller.

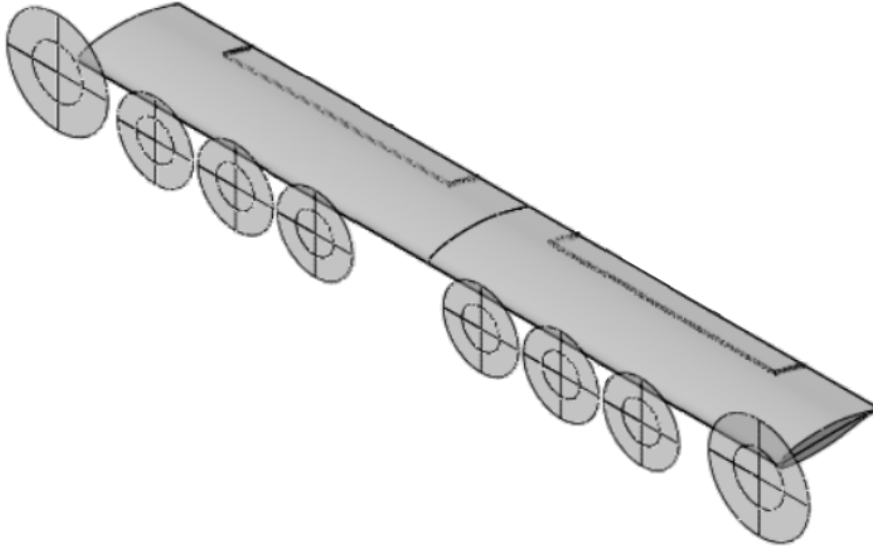


Figure 2.29: Wing geometry considered for the second case study.

	Value	Unit
Airfoil	GAW-1	—
Thickness ratio	0.17	—
Taper ratio	1.00	—
Wing span	2.80	m
Wing area	0.56	m^2
Aspect ratio	7.00	—
Chord	0.40	m
Flap chord ratio	0.30	—
Inner flap position	0.20	m
Outer flap position	1.10	m

Table 2.15: Geometric characteristics of the second model.

The objective of this study is to verify the validity of the methods and the sensitivity to the forward offset at low Reynolds number. Although the test campaign of the project assumed three different diameters for distributed electric propulsion, in the present context, a constant diameter of $0.3 m$ is fixed. Considering the body reference frame positioned at the leading edge of the root chord, three offset values are considered, as reported in Table 2.16, to test the capability of the method to quantify the sensitiveness to the parameter.

The test conditions are reported in Table 2.17, combined in four different test cases reported in the following list.

	Value	Unit
DEP RPM	7000	<i>rpm</i>
Tip RPM	2000	<i>rpm</i>
DEP thrust	6.87	<i>N</i>
Tip thrust	16.33	<i>N</i>
DEP diameter	0.3	<i>m</i>
Tip diameter	0.4	<i>m</i>
DEP spanwise positions	0.33/0.65/0.97	<i>m</i>
Tip spanwise position	1.4	<i>m</i>
DEP offset	-0.16/-0.12/-0.08	<i>m</i>

Table 2.16: Geometric characteristics of the propellers.

	Value	Unit
Angle of attack	0 to 20	<i>deg</i>
Mach number	0.059	-
Speed	20	<i>m/s</i>
Air density	1.225	<i>kg/m³</i>
Dynamic viscosity	1.79e-5	<i>Pas</i>
Reynolds number	5.47e+5	-
Temperature	288.15	<i>K</i>
Pressure	101325	<i>Pa</i>

Table 2.17: Test conditions.

- 2-0 Clean configuration of the wing and inoperative propulsive system.
- 2-1 Clean configuration of the wing, operative tip-mounted propeller, and inoperative distributed electric propulsion.
- 2-2 Clean configuration of the wing, inoperative tip-mounted propeller, and operative distributed electric propulsion.
- 2-3 Clean configuration of the wing and both tip-mounted propeller and distributed electric propulsion operative.

The first test case is necessary to define the aerodynamic coefficients of the isolated wing that are used to calculate the variations through the methods proposed in this work. The results of the isolated wing are reported in Fig. 2.30. The pitch coefficient reported is referred to the aerodynamic center of the mean aerodynamic chord.

The test case 2-1 is intended to verify the method used to measure the benefits of tip-mounted propellers. For this purpose, lift, drag, and pitch coefficients from high-fidelity methods and the method proposed in this work are compared, as

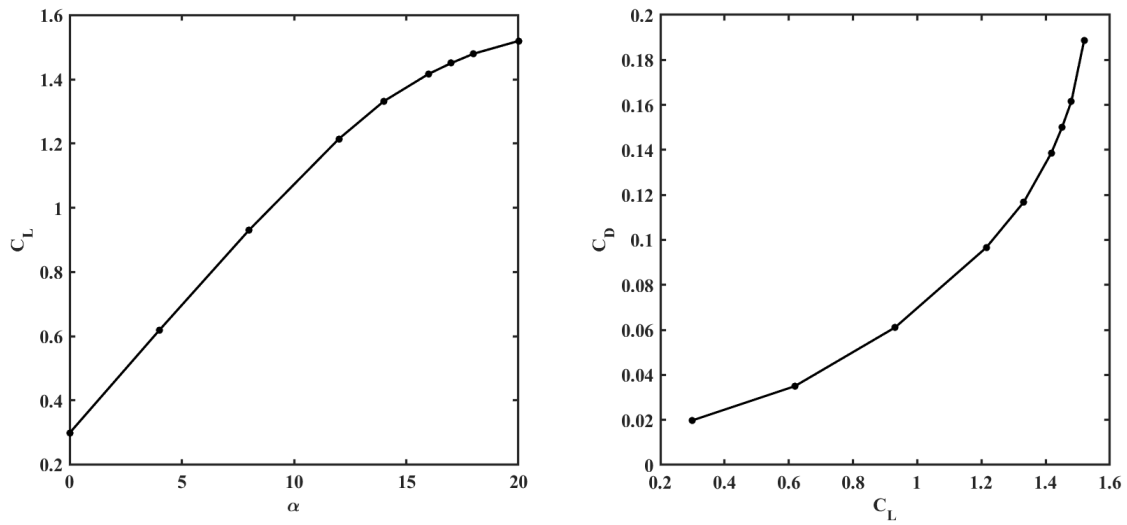


Figure 2.30: Lift curve and drag polar of the model in Fig. 2.29.

shown in Fig. 2.31. The method proposed in 2.2.2 provides a satisfactory match with CFD results, in particular when the time is a crucial aspect, as for the early stages of the design process.

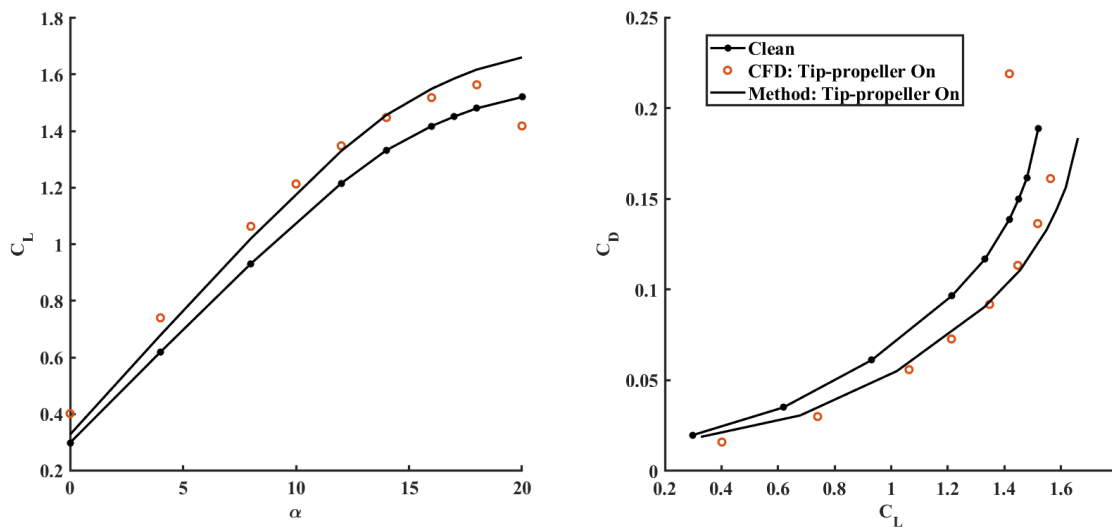


Figure 2.31: Lift curve and drag polar of the model in Fig. 2.29 with and without the effect of the tip-propellers.

The test case 2-2 includes the results associated to the three different offsets of the distributed propellers from the leading edge. A visual comparison of the results is proposed in Fig. 2.32.

The last test case on this model is aimed to verify the reliability of the results when the tip-mounted propellers and the distributed propulsion are coupled. What

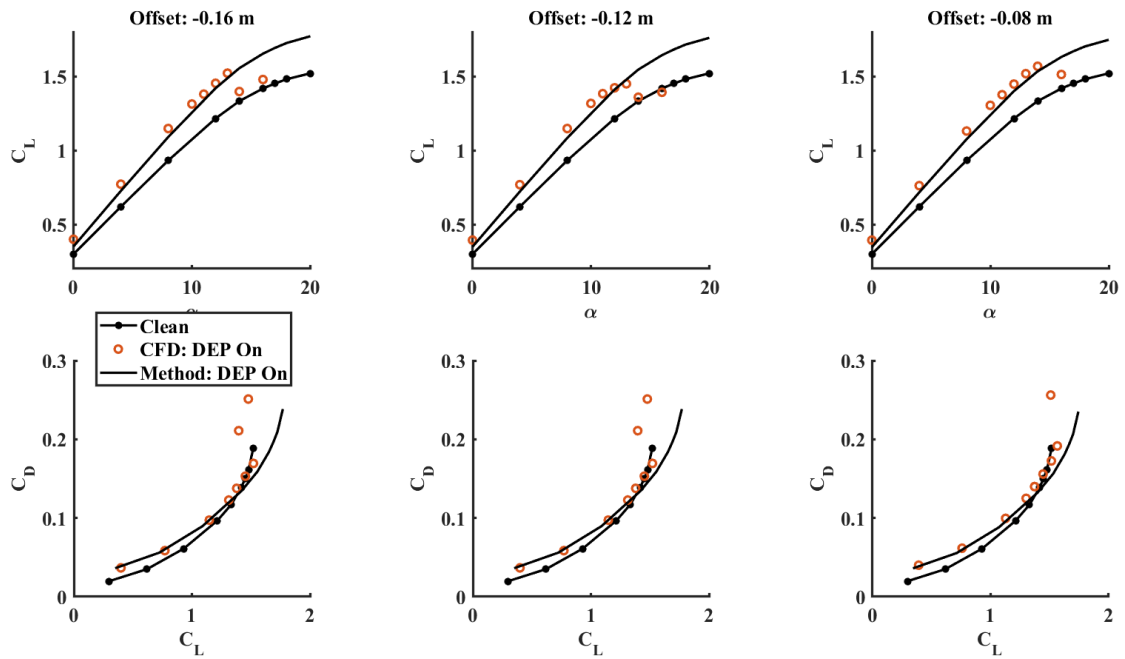


Figure 2.32: Lift curve and drag polar of the model in Fig. 2.29 with and without the effect of distributed propellers.

clearly emerges from Fig. 2.33 is the overestimation of the lift coefficient calculated with respect to the one obtained by CFD analysis.

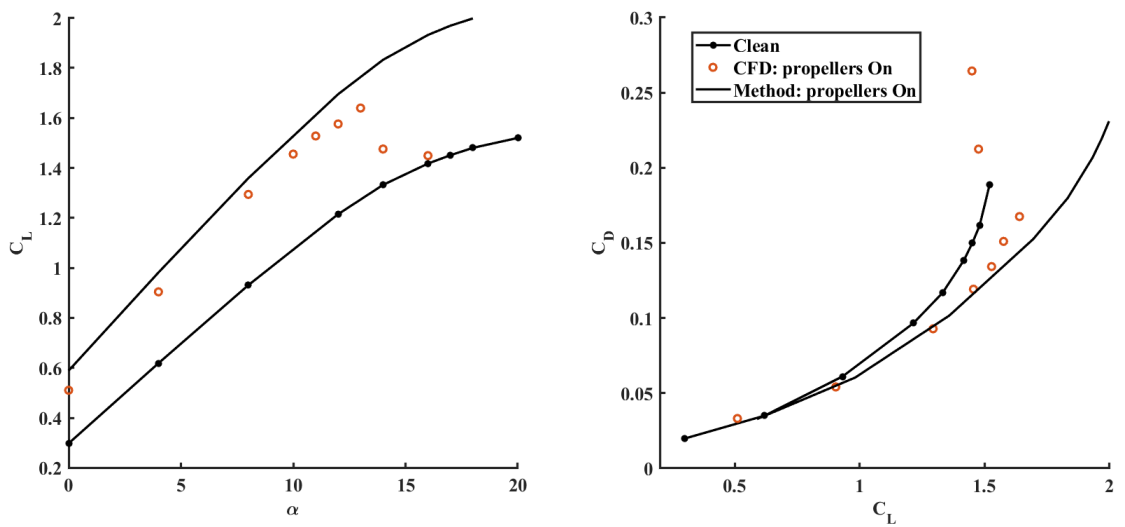


Figure 2.33: Lift curve and drag polar of the model in Fig. 2.29 with and without aero-propulsive effects.

In the end, results associated with the method proposed in 2.2 are in line with computational fluid dynamics analyses made by the *Design of Aircraft and*

Flight technologies (DAF) research group of the University of Naples "Federico II. Particularly at those angles of attack where the lift coefficient curve is linear, the accordance of the results is satisfactory, giving the opportunity to reliably measure the effect of these propulsive architectures on aerodynamics from the early stages of the design process. However, since high-lift propulsion is a technology specifically designed to increase the maximum lift coefficient, the difference between the CFD results and the values calculated at higher angles of attack requires further studies. The second test case highlights that the impact of the scale effects is particularly critical for the distributed propulsion. The pseudo-Reynolds number effects modify the characteristics of the propeller slipstream differently from what can be estimated by the low-fidelity method [131]. Additionally, the scale effects influence the boundary layer and the stall conditions making the methods inefficient under a certain value of the Reynolds number. The second case study highlights the necessity of defining a correction parameter for the Reynolds number. This task is left to future studies.

2.3 Airworthiness

Airworthiness is the possession of the necessary requirements for flying in safe conditions, within allowable limits [132, 133]. This definition introduces three main concepts: safety, the necessary requirements, and the allowable limits. The first concept is linked to the reduction of the risk factor to avoid conditions that could potentially cause accidents. Thus, the aircraft must fly in conditions assuring the safety of people, equipment, and properties. To permit this condition, the aircraft and any of its parts are designed according to regulation constraints aimed to mitigate or eliminate risk factors. Out of regulation constraints, the design of an aircraft is made within the limits of the flight envelope. The operating condition is established as allowable limits and exceeding those constraints can cause accidents.

2.3.1 One Engine Inoperative Condition (OEI)

Safety is one of the key drivers of powertrain system design: even if hybrid-electric propulsion is currently feasible from a technical point of view, these concepts will not take off until their safety will be proven. From a system point of view, the complexity of hybrid-electric powertrain is related to the high number of components and the variety of connections among them. These degrees of freedom need to be considered from the early stages of the design process since energetic requirements, performance, and weight depend on it. However, the lack of methods systematically supporting the early powertrain design is slowing the commercialization of hybrid-electric aircraft.

This section is dedicated to the fault tolerance analysis of the propulsive system, intended as the verification of the safety conditions and performance in the event of one failure. When designing a new aircraft, the designer must ensure its controllability in the most critical of probable situations, excluding only events whose estimated frequency is sufficiently lower than the operational life. Driving factors are the thrust provided by each propeller (or fan), the power management architecture making some propellers more reliable than others, or even the position itself with respect to the center of gravity, which is crucial when dimensioning the vertical tailplane. Conventionally, the One Engine Inoperative (OEI) condition stands for the loss of one of the engines and therefore, for twin-engine aircraft, half of the available thrust. A conventional aircraft must guarantee compliance with the constraints imposed by regulation [19, 20, 134] even in the worst-case scenario, corresponding to the loss of the critical engine. The latter is identified as the engine responsible for the greatest yaw moment, for example by virtue of its greater distance from the center of gravity of the aircraft or asymmetry in thrust. Also, tailplane sizing is primarily driven by this yaw moment [62]. The definition of OEI condition for hybrid-electric aircraft must be revised including other units. Depending on the mechanical or electrical interconnections between the components, the degree of hybridization, and the type of power sources, the failure of an element can have different consequences in terms of residual power and yaw moment. The analyst

may be interested in using two different criteria for determining the critical scenario: the minimum (residual) thrust criterion and the maximum yaw moment criterion.

The relation between system architecting for hybrid-electric aircraft and their intended fail-safe behaviour brings an interesting potential to combine the activities of designing and failure/fault tolerance analysis. In the early stages of the design process, the foresight of the designer is limited by many aspects. Firstly, the objective of meeting new market demands improving an original baseline. Secondly, the necessity of approaching a multidisciplinary design from different perspectives, typically involving informal or semi-formal representations or drawings of the concept. Finally, the inclusion of multiple tools created for the specific type of architecture, which could be a limiting factor in the case of wide design spaces. In the context of conceptual design, generative engineering is the most suited approach [135]. With generative engineering, the creative task of finding and selecting the right propulsive architecture is automatized.

Three main steps for the creation and selection of a safe architecture, in the context of hybrid-electric propulsion system design, are presented. The first step is the identification and description of the components composing the propulsive system, excluding cabling and power units that will be detailed after the architecture is chosen. The designer imposes at the beginning of the design process the presence or the absence of each of the seven components reported below.

- e-motor drives
- gearboxes
- propellers (or fans)
- thermal engines
- fuel cells
- battery packs
- P.M.A.D.

Moreover, the designer chooses the number of propulsive units (propellers and fans) and power sources (thermal engines, fuel cells, and battery packs). Each component is characterized by additional constraints related to the number and

the type of inputs, outputs, or input/output ports. Depending on the number of ports, each component can be linked to one or more elements in inputs and/or in outputs. The links between the elements are in turn constrained by the nature of the ports that can be electrical or mechanical.

The second step is the core of the creative task, related to the generation of all the possible architecture linking a fixed number of power sources with the fixed number of propulsive units. Generative engineering facilitates this step by automatically architecting and writing down the powertrain equations describing all the possible propulsive systems when appropriate physical conditions have been specified. On the other hand, for the application discussed in the present work, a wide set of possible architecture will be specified by the designer assuming a fixed number of elements.

At the end of the creative task, the last step is the analysis of the one-engine inoperative conditions. Depending on the mechanical or electrical interconnections between the components, the failure of a unit can have different impacts on the power distributed through the residual units. Furthermore, when dealing with electrically powered propellers, the power can be redirected to reduce the yawing moment generated by the failure. Additionally, as for the APR power rating of the thermal engines, fuel cells and batteries can provide additional power up to the peak power for which they have been designed. The possible critical conditions considered in the present work assumes the following possible failures:

- 1 one thermal engine if the number of installed gasturbine is lower than three, otherwise, an additional thermal engine failure is added;
- 2 one e-motor drive directly powering a propeller;
- 3 one generator transforming the mechanical power from the thermal engine to electrical power;
- 4 one battery pack;
- 5 one thermal engine and the associated e-motor drive powering one common propeller.

Considering the nine operating modes, the total number of possible failure scenarios is 45. In their classic formulation, powertrain equations consider the overall powers

of similar elements, meaning that the power of each isolated physical element must be obtainable by dividing the overall power by the number of units of the same type. Their validity is therefore subordinated to the hypothesis of homogeneously distributed power on similar parts and of symmetric distribution. The occurrence of a failure introduces an asymmetry in the propulsion system and the power distribution cannot be captured by equations previously discussed. When approaching the fault analysis, the propulsive system can no longer be considered as a unique assembly, but it is fundamental the identification of the subsystems composing it. This can be done by means of a user interface allowing the model based design of each subsystem or by automatically computing all the elements powered by the same power source or group of power sources. In this second case, for example, the tool starts considering the link between the thermal engine and the following element, then, from this to the following elements connected, and so on until the system of equations is closed. It is here explicitly highlighted that the procedure will automatically include in the same subsystem the power source powering the same propulsive elements. Given a certain number of subsystems, the same number of linear systems of equations is required, similar to Eq. (2.97).

For instance, considering a generic hybrid-electric powertrain, as the one in Fig. 2.34, two possible architectures are proposed depending on the link between the two P.M.A.D. units. Assumed that the propulsive system works in accordance with the first operating mode, Eq. (2.5) can describe the global power distribution when all the elements are operative. However, when the hypothesis of homogeneity and symmetry are not satisfied, the powertrain equations should be written accounting for each single element separately. In this context, the power referred to each single subsystem is addressed as a lower case p letter. With the purpose of describing the power distribution in case of failure, an additional parameter is introduced to describe the fraction of power delivered to each unit of the same category. Each element is powered by a fraction of the total power, referred to as α_{*i} , where the asterisk indicates a generic unit type and the single elements are referred to by the

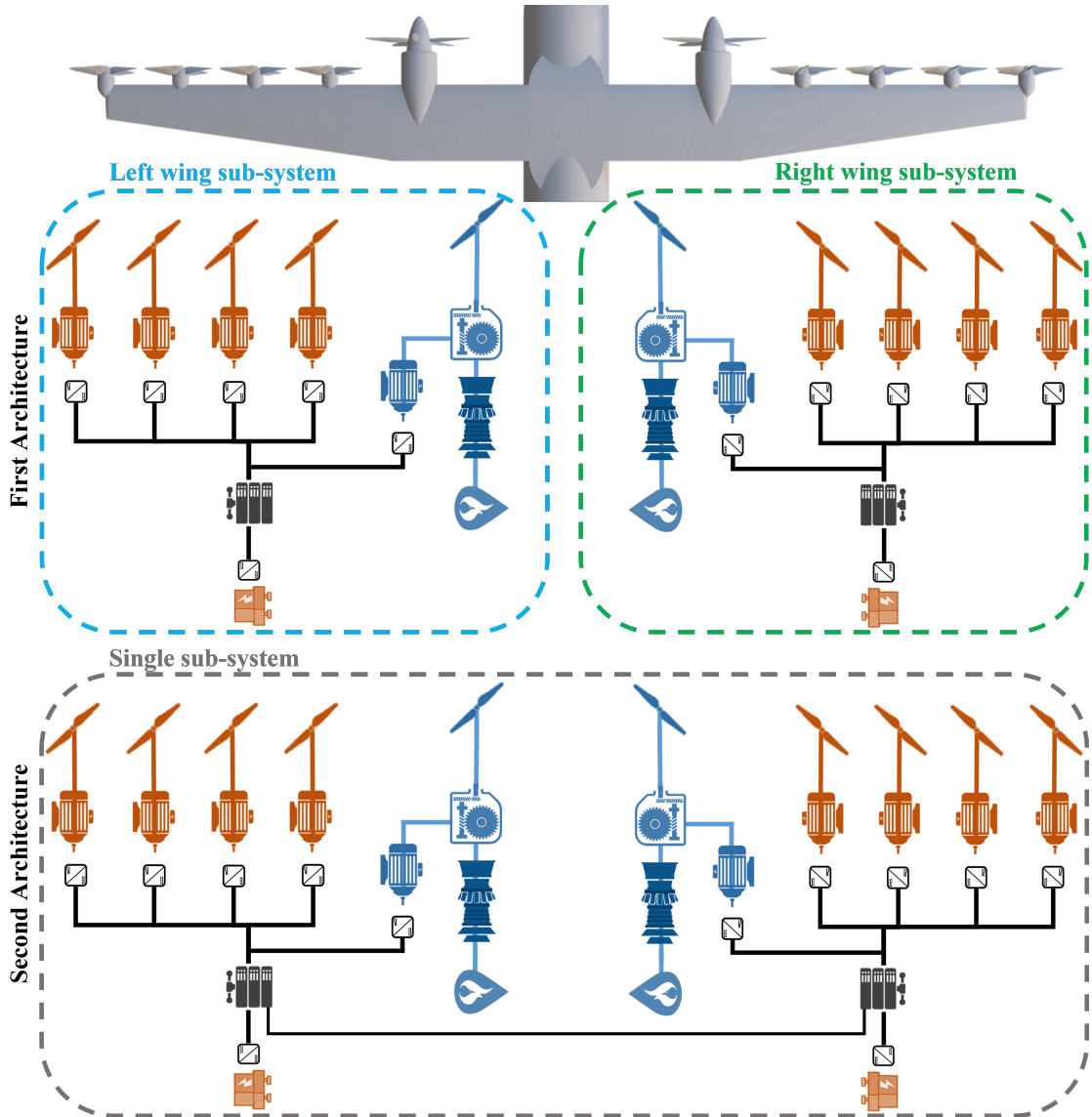


Figure 2.34: Propulsive subsystems for an hybrid-electric aircraft with distributed electric propulsion.

subscript i . At the occurrence of the failure, the fraction of total power delivered to a generic element (f_*) is calculated through Eq. (2.96).

$$f_* = \sum_i^{N_*} \alpha_{*i} - \alpha_{*_{failed}} \quad (2.96)$$

At the occurrence of the failure, the power supplied is kept constant, but the distribution is modified according to the new operating condition. Moreover, this would require a new estimation of the hybridization factors accounting for the remaining battery packs, e-motor drives, and thermal engines through the fraction

coefficients (Eq. (2.96)). Eq. (2.97) is suited to describe the power distribution among each subsystem of the two architectures proposed by way of example.

$$\begin{bmatrix} -\eta_{GT}f_{GT} & 0 & 0 & 0 & 0 & 0 & 0 & 0 & 0 & 0 \\ 0 & f_{EM1} & 1 & 0 & 0 & 0 & 0 & 0 & 0 & 0 \\ 0 & 0 & -\eta_{P1} & 0 & 0 & 0 & 0 & 1 & 0 & 0 \\ 0 & -\eta_{EM1}f_{EM1} & 0 & f_{EM1} & 0 & 0 & 0 & 0 & 0 & 0 \\ 0 & 0 & 0 & -\eta_{PM}f_{EM1} & -\eta_{PM}f_{BAT} & f_{EM2} & 0 & 0 & 0 & 0 \\ 0 & 0 & 0 & 0 & 0 & -\eta_{EM2}f_{EM2} & f_{EM2} & 0 & 0 & 0 \\ 0 & 0 & 0 & 0 & 0 & 0 & -\eta_{P2}f_{EM2} & 0 & f_{EM2} & 0 \\ \Phi f_{GT} & 0 & 0 & 0 & (\Phi - 1)f_{BAT} & 0 & 0 & 0 & 0 & 0 \\ 0 & 0 & \phi & 0 & 0 & 0 & (\phi - 1)f_{EM2} & 0 & 0 & 0 \\ 0 & 0 & 0 & 0 & 0 & 0 & 0 & 1 & f_{EM2} & -1 \end{bmatrix} \begin{bmatrix} p_{Fuel} \\ p_{GB} \\ p_{S1} \\ p_{EM1} \\ p_{BAT} \\ p_{EM2} \\ p_{S2} \\ p_{P1} \\ p_{P2} \\ p_P \end{bmatrix} = \begin{bmatrix} -p_{GT} \\ \eta_{GB}p_{GT} \\ 0 \\ 0 \\ 0 \\ 0 \\ 0 \\ 0 \\ 0 \\ 0 \end{bmatrix} \quad (2.97)$$

Considering the second architecture shown in Fig. 2.34, an implicit hypothesis is that the two power management and distribution units connected are considered as a unique element. Furthermore, the presence of two independent subsystems in the first architecture requires the resolution of as many independent systems of equations.

Once the mathematical model describing the powertrain system has been introduced, the procedure for the fault tolerance analysis starts from calculating the power at the occurrence of the failure through Eq. (2.97). Then, the single yawing moments due to the thrust provided by each propulsive element are evaluated, as shown in the following equations, where y is the distance from the center of gravity.

$$N_{P1_i} = \alpha_{P1_i} T_{P1} y_{P1_i} \quad (2.98)$$

$$N_{P2_i} = \alpha_{P2_i} T_{P2} y_{P2_i} \quad (2.99)$$

In this context, two different mitigation strategies are adopted dealing with the resulting thrust loss and the additional yawing moment. After the occurrence of the failure, the compliance with the required flight performance depends on the residual thrust. On the one hand, the regulation requires a minimum climb rate; on the other hand, flight performances are assigned as design requirements in terms of balanced field length and ceiling altitude. Starting from the power distribution at the occurrence of the failure, the power supplied by the power sources is increased until the requirements are met. Firstly, the power provided by the thermal engine is increased up to maximum continuous or APR power ratings. If this is not sufficient, the supplied power ratio is increased up to the peak power of the powertrain elements. Assumed that this procedure has successfully mitigated

the thrust loss, the re-distribution of the propulsive power aims at either minimizing the yawing moment arising from the asymmetric thrust distribution or reducing it below the control moment generated by the vertical tailplane. In the present work, the mitigation of the yawing moment is a systematic procedure starting from an appropriate estimation of the shaft power ratio ϕ of each subsystem. Once the subsystem generating the maximum yawing moment has been identified, considering each propulsive line as a single propulsive unit, the shaft power ratio is modified to lower the total yaw. With the new shaft power ratio, the new power distribution is calculated through Eq. (2.97). If the remaining moment is still higher than the control moment generated by the vertical tailplane, the procedure is repeated iteratively considering small variations of the shaft power ratio. When the shaft power ratio reaches its limit values, the fraction of power of each propulsive element (α_{P1_i} or α_{P2_i}) can be conveniently changed to further reduce the yawing moment.

One additional consideration may be appropriate. The failure of the e-storage unit is a condition that hardly occurs due to the low failure rate. However, even if the failure of one battery pack could be an unfortunate occurrence, the division of a large e-storage unit in battery packs assures higher fault tolerance by supplying additional power from the remaining battery packs. Furthermore, since the e-storage failure rate is related to degradation of the cells which is a function of the operative lifetime, the reliability modelling [136] could drive the choice of the minimum number of battery packs and their programmed maintenance.

2.3.2 Trim and Stability

The **trim** is an equilibrium condition characterized by a null total force acting on the aircraft. Trim requirements must be met and maintained without the movement of either the primary controls or their corresponding trim controls. Once the trim condition is met, the **stability** of the aircraft is the capacity of withstanding perturbation returning to the trimmed condition after a certain response time. Studying stability without taking into account the inertia forces leads to the concept of **static stability**. On the contrary, **dynamic stability** is the ability

of the system including inertia forces to remain in the original condition opposing perturbations. In the present work, the dynamic stability will be neglected focusing the attention on static stability. Three main equilibrium conditions are discussed in the present section: lateral, directional, and longitudinal trim. The main objective is understanding the effect of aero-propulsive interactions on trim requirements (*CS-25 §25.161* [20, 134] and *CS-23 §23.161* [19]). With the objective of assessing the impact of unconventional propulsive systems, trim and stability are modelled based on equations from literature [137–139].

The first trim condition discussed deals with the longitudinal equilibrium. The mathematical model discussed in the present section is the classical configuration with two lifting surfaces, wing, and horizontal tailplane, with non-reversible control surfaces. The longitudinal stability and controllability depend on the aircraft pitching moment, whose dimensionless coefficient is C_M , and its derivative with respect to the lift coefficient. The coefficient is considered positive when the aircraft has a nose-up moment. The axis passing through the center of gravity or the wing aerodynamic center and parallel to the y-axis of the aircraft will be considered to calculate the pitching moment. Moments related to the first axis will be characterized by the subscript *c.g.*, while the second axis is referenced as *ac_w*. Since the objective of the present discussion is the identification of the aero-propulsive effects, the first consideration deals with the pitching moment of the main lifting surface with respect to its aerodynamic center: C_{Mac_w} . Wing pitching moment is composed of two components (Eq. (2.100)): the first one is the integral of local pitching moment coefficients with respect to the aerodynamic center, the second one is the contribution of the basic load due to sweep and twist.

$$\begin{aligned}
 C_{Mac_w} = & \\
 & \frac{1}{S_w \bar{c}} \left[\int_{-b/2}^{b/2} [C_{mac}(y) c(y)^2] dy + \right. \\
 & \left. + \pi \int_{-b/2}^{b/2} C_{l_\alpha} [\alpha_{0L} - \epsilon_T(y) - \alpha_0(y)] c(y) x_1(y) dy \right] \quad (2.100)
 \end{aligned}$$

In Eq. (2.100), x_1 is the position of the aerodynamic center of each airfoil with respect to the aerodynamic center of the mean aerodynamic chord, α_0 is the zero-lift

angle of attack of each airfoil, α_{0_w} is the zero-lift angle of the whole wing and ϵ_T is the twist angle of each airfoil. The first contribution of aero-propulsive interaction and to the longitudinal equilibrium of the aircraft can be accounted by adding the increment calculated by Eq. (2.74). The second effect is quantified by Eq. (2.69) and, then, added to the lifting coefficient in the second integral of Eq. (2.100). It is here explicitly noted that the only technology discussed in the present work that contributes to the pitching moment is distributed electric propulsion.

The fuselage contribution to the pitching moment C_{M_f} can be calculated using different methods [137,140]. C_{M_f} is divided into two contributions: the first one does not depend on the angle of attack of the fuselage and the second one that depends on it. In the end, the pitching moment coefficient of the wing-body assembly is calculated using Eq. (2.101), where the attitude of the assembly is defined by the angle of attack (α_{wb}) with respect to the fuselage reference line.

$$C_{M_{wbacw}} = C_{M_{acw}} + C_{M_{f_0}} + C_{M_{f_\alpha}} \alpha_{wb} \quad (2.101)$$

Typically, $C_{M_{f_0}}$ and $C_{M_{acw}}$ are negative and $C_{M_{f_\alpha}}$ is positive. To sum up, since $C_{M_{acw}}$ is modified by the contribution calculated from Eq. (2.74), $C_{M_{wbacw}}$ is affected by the aero-propulsive interaction as well. The following step requires the calculation of the pitching moment at aircraft level to highlight the impact of

The pitching moment coefficient of the aircraft is calculated referring to the center of gravity (Fig. 2.35). The relative positions of the aerodynamic center of the wing, x_{ac} , and the center of gravity, $x_{c.g.}$, drive the longitudinal trim and determine if the aircraft is stable.

The pitching moment of the aircraft with respect to the center of gravity is calculated considering two different components. The first contribution ($C_{M_{c.g.0}}$) does not depend on the attitude, while the second one is a function of the angle of attack of the wing-body assembly (α_{wb}). Eq. (2.102) is used to calculate the

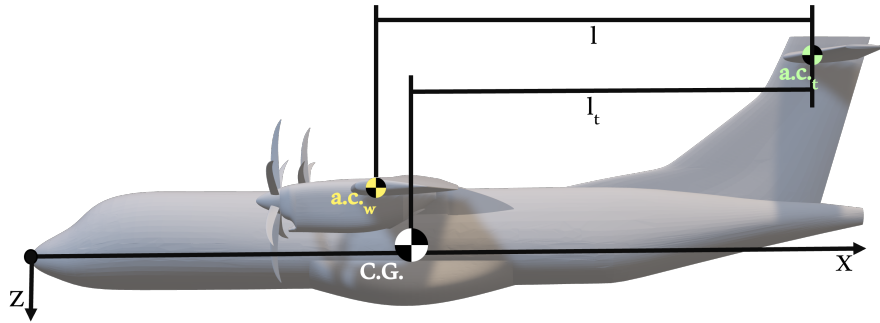


Figure 2.35: Body reference frame, position of the aerodynamic centers of the two lifting surfaces, and the center of gravity.

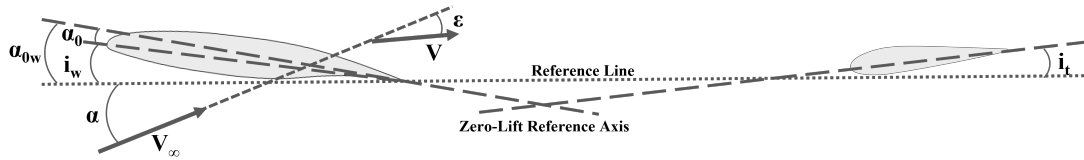


Figure 2.36: Characteristic angles.

pitching moment coefficient.

$$C_{M_{c.g.}} = C_{M_{c.g.-0}} + C_L \left[\frac{x_{ac} - x_{c.g.}}{\bar{c}} - \frac{C_{L\alpha_t}}{C_{L\alpha_{wb}}} \left[1 + \frac{C_{L\alpha_t}}{C_{L\alpha_{wb}}} \frac{S_t}{S_w} \eta_t \left(1 - \frac{d\epsilon}{d\alpha} \right) \right] \right] \eta_t \bar{V}_t \left(1 - \frac{d\epsilon}{d\alpha} \right) \quad (2.102)$$

As previously stated, the aero-propulsive effect on the pitching moment deals with the contribution of distributed electric propulsion. The lifting coefficient of the global aircraft C_L is affected by the increment of lift due to the interaction between propeller slipstream and the main lifting surface. The second element affected by propeller slipstream is the downwash derivative $\frac{d\epsilon}{d\alpha}$, whose mathematical model is not discussed in the present work. One last element modified is the derivative of the lifting coefficient of the aircraft with respect to the angle of attack ($C_{L\alpha_{wb}}$). The pressure ratio η_t is assumed to be independent of the blowing of the propulsive units. Furthermore, the tailplane lifting coefficient derivative with respect to the angle of attack ($C_{L\alpha_t}$) is considered constant. On the other hand, the component of the pitching moment coefficient that does not depend on the attitude, $C_{M_{c.g.-0}}$, is affected by the propeller slipstream through $C_{M_{wbacw}}$ and $C_{L\alpha_{wb}}$.

$$C_{M_{c.g.0}} = C_{M_{wbacw}} - \frac{C_{L\alpha_t}}{1 + \frac{C_{L\alpha_t} S_t}{C_{L\alpha_{wb}} S_w} \eta_t (1 - \frac{d\epsilon}{d\alpha})} (i_t - \alpha_{0_w}) \bar{V}_t \eta_t \quad (2.103)$$

The other parameters in the equations are geometrical characteristics: the incidence of the tailplane i_t , the volumetric ratio \bar{V}_t , the lifting surfaces areas (S_t and S_w), and the mean aerodynamic chord of the wing \bar{c} .

The static stability is assured when the derivative of the pitching moment coefficient with respect to the lift coefficient, or, in other words, the stick fixed **static stability margin**, is negative. From Eq. (2.104), it can be noted that longitudinal stability depends on $C_{L\alpha_{wb}}$, whose value increases when propellers blow on the main lifting surface. The increment of the lift coefficient derivative, due to the interaction with propeller slipstream, reduces the stability of the aircraft. Nevertheless, the lack of reliable mathematical models to account for the effect of distributed electric propulsion on dynamic pressure ratio and downwash requires further investigations at higher fidelity order.

$$\frac{\partial C_{M_{c.g.}}}{\partial C_L} = \frac{x_{ac} - x_{c.g.}}{\bar{c}} - \frac{C_{L\alpha_t}}{C_{L\alpha_{wb}} [1 + \frac{C_{L\alpha_t} S_t}{C_{L\alpha_{wb}} S_w} \eta_t (1 - \frac{d\epsilon}{d\alpha})]} \eta_t \bar{V}_t (1 - \frac{d\epsilon}{d\alpha}) \quad (2.104)$$

For an assigned flight condition, the longitudinal equilibrium is assured when the pitching moment coefficient and the total force in the xz plane (Fig. 2.35) are equal to zero. Thus, at a specific global lift coefficient C_L necessary to sustain the aircraft, an associated value of $C_{M_{c.g.0}}$ is necessary to equilibrate the pitching moment. However, $C_{M_{c.g.0}}$ appear to be constant as introduced in Eq. (2.103). With the objective of trimming the aircraft for a wide range of attitudes, the elevator, that is the control surface deputed to create the desired pitching moment, is introduced. The effect on the pitch coefficient is modelled substituting i_t in Eq. (2.103) with Eq. (2.105), where the value of the elevator deflection, δ_e , multiplied by the control surface efficiency τ is added to the tailplane incidence. Conventionally, the elevator deflection is considered positive when the elevator trailing edge goes down.

$$i_t = i_{t0} + \tau \delta_e \quad (2.105)$$

Assuming a certain necessary equilibrium lift coefficient (Eq. (2.106)), the associated lift coefficient of the tailplane is calculated through Eq. (2.107).

$$C_{L_e} = C_{L_w} \frac{l}{l_t} + C_{M_{wbacw}} \frac{\bar{c}}{l_t} \quad (2.106)$$

$$C_{L_{t_e}} = (C_{M_{wbacw}} + C_{L_e} \frac{x_{ac} - x_{c.g.}}{\bar{c}}) \frac{1}{\bar{V}_t \eta_t} \quad (2.107)$$

To provide the required tail lift, the elevator is deflected of an angle calculated as reported in the following equation.

$$\delta_{e_e} = \frac{\alpha_{0_w} - i_{t0}}{\tau} - \frac{C_{M_{wbacw}}}{-C_{L_{\alpha_t}} \bar{V}_t \eta_t \tau} - \frac{C_{M_{CL}}}{-C_{L_{\alpha_t}} \bar{V}_t \eta_t \tau} C_{L_e} \quad (2.108)$$

It is here explicitly noted that the effect of high-lift propellers requires a more negative deflection of the elevator to trim the aircraft [141].

The lateral-directional trim is studied considering the dimensionless coefficient C_{Σ} and C_N , respectively. As a matter of fact, the absence of general analytical methods to calculate the effect of propellers slipstream on the dynamic pressure ratio or the sidewash, make it difficult to assess the effect of the propulsive system on roll and yaw moments. However, the relevance of the lateral-directional trim is strongly related to the OEI condition in case of hybrid-electric propulsion and, thus, to the minimum control speed that will be discussed in the following section. In this context, lateral-directional trim conditions of the aircraft are assured by a total force in the yz plane equals zero and a null roll or yaw moment, respectively.

The lateral trim and stability are related to the rolling moment of the aircraft and the forces on the yz plane (Fig. 2.37).

Conventionally, the roll moment is assumed positive when the right wing goes down, according to the positive direction of the x-axis of the wind reference frame pointing in the opposite direction with respect to the body reference frame's x-axis (Fig. 2.38).

The control surface deputed to generate a control roll is the aileron, generally located in pair on the outboard panels of the wing. A positive ailerons deflection δ_{a_a} generates a negative roll. An additional effect of the aileron deflection is the adverse yaw, related to the asymmetric drag distribution and the roll rate of the

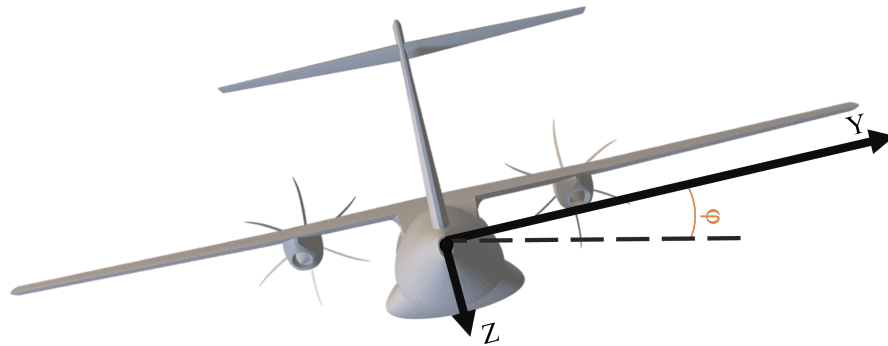


Figure 2.37: Body reference frame and bank angle (ϕ).

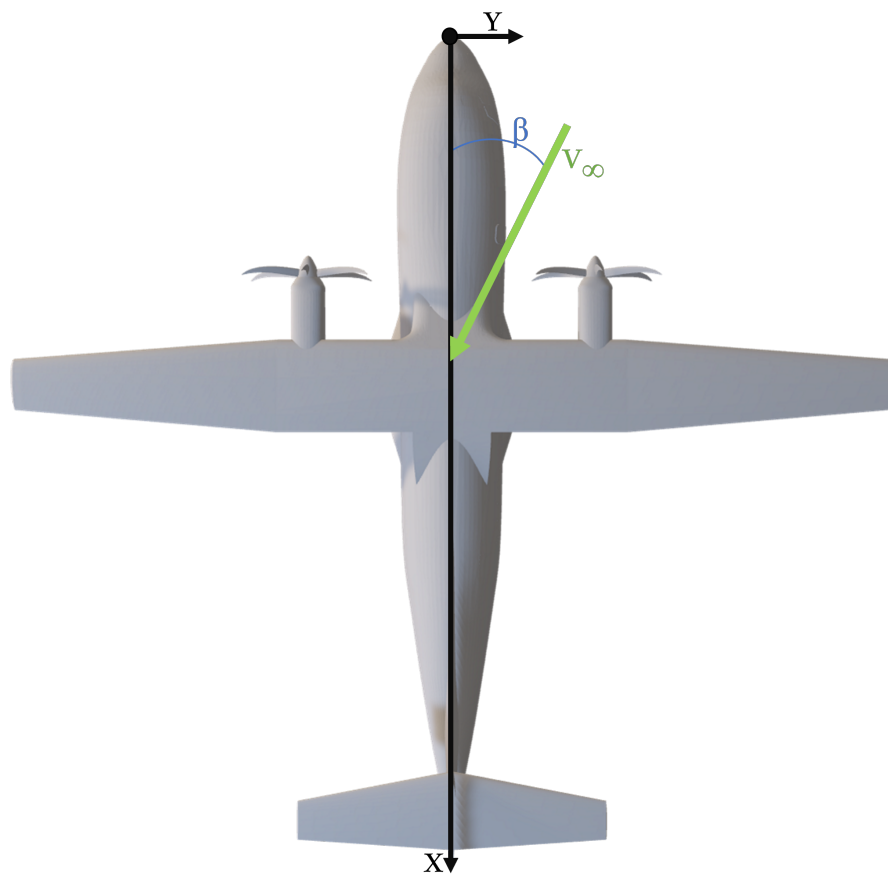


Figure 2.38: Body reference frame and sideslip angle (β).

aircraft, constituting one of the cross-effects of the lateral-directional trim. It is here explicitly noted that when the control surface is exposed to propellers slipstream, the effectiveness of the deflection increases due to the higher axial induction and, thus, the higher asymmetry in lift distribution, which generates the moment.

As for the previous case, directional trim requires the sum of forces in the yz plane to be null. On the other hand, directional trim also requires that the resulting yaw moment acting on the aircraft is zero. Yaw is assumed to be positive when the aircraft rotates clockwise. The rudder exercises directional control on the aircraft and it is generally located on the vertical tailplane for conventional configurations. Its positive deflection δ_r causes negative yaw. In case of rudder deflection, a cross-effect on the roll is induced by the decentralized force generated.

Without investigating the analytical models proposed in literature, the two moment coefficients are modelled as in Eq. (2.109) and Eq. (2.110). For the present work, the rolling moment coming from propeller slipstream or asymmetric elements is neglected. In case of lateral-directional stability, the capacity of withstanding perturbations of the sideslip angle β is related to the sign static stability derivative. On the one hand, for directional stability, C_{N_β} is required to be positive, on the other hand, lateral stability is assured by a negative C_{ξ_β} .

$$C_\xi = C_{\xi_\beta}\beta + C_{\xi_{\delta_a}}\delta_a + C_{\xi_{\delta_r}}\delta_r \quad (2.109)$$

$$C_N = C_{N_\beta}\beta + C_{N_{\delta_a}}\delta_a + C_{N_{\delta_r}}\delta_r \quad (2.110)$$

As previously stated, the equilibrium condition requires that the total force acting on the vehicle is equal to zero. In other words, lateral-directional stability requires the side force Y , or its coefficient C_Y , to be equal to zero. When a certain bank angle is introduced, as shown in Fig. 2.38, the side force accounts for the component of the total lift projected on the y -axis, as shown in Eq. (2.111).

$$C_Y = C_{Y_\beta}\beta + C_{Y_{\delta_a}}\delta_a + C_{Y_{\delta_r}}\delta_r + C_L \sin(\phi) \quad (2.111)$$

Based on the balance between lift and weight W , Eq. (2.111) is modified as reported below.

$$C_Y = C_{Y_\beta}\beta + C_{Y_{\delta_a}}\delta_a + C_{Y_{\delta_r}}\delta_r + \frac{2W}{\rho S_w V^2} \tan(\phi) \quad (2.112)$$

For a certain sideslip angle, the system composed by Eq. (2.110), Eq. (2.109), and Eq. (2.111) allows calculating the necessary bank angle, rudder, and ailerons deflection angles to trim the aircraft. The relationship between airspeed and side force coefficient shown in Eq. (2.112) is essential for the estimation of the minimum control speed, as discussed in the following section.

2.3.3 Stall Speed and Minimum Control Speed

The **stall speed** is defined as the minimum steady flight speed at which the aircraft is controllable, calculated at 1-g load factor. The reference stall speed is assigned by the manufacturer applying to the certification process and cannot be lower than the aforementioned one. Moreover, when a device for pitch control is installed, the reference stall speed cannot be less than 2 *kts* or the 2% of the speed at which the device operates. The manoeuvre to demonstrate the aircraft stall speed is described for each aircraft category in the associated regulation (*CS-25 §25.201* [20, 134] and *CS-23 §23.201* [19]).

Regarding the engine power rating, the regulation describes the stall speed certification procedure considering the engine idling. From the perspective of an unconventional aircraft with distributed electric propellers, devices specifically designed to alter the high-lift conditions, this severe constraint could undermine the competitiveness of the propulsive system whose benefits are strongly related to thrust. However, the Federal Aviation Administration (FAA) modified this constraint for small aircraft distinguishing the propulsive units designed to provide thrust from those designed to provide advantageous changes in aerodynamics due to aero-propulsive interaction [22]. In this new amendment, for each flight configuration, the stall speed or the minimum steady flight speed is determined considering the most adverse conditions with power sets at idle or zero thrust for

propulsion systems that are used primarily for thrust; and a nominal thrust for propulsion systems that are used for thrust, flight control, and high-lift systems. Moreover, as highlighted by authors in Ref. [22], the approach speed is not limited with explicit reference to stall speed, preferring the identification of the safety margin from landing performance. Previously, the approach speed was bounded by a safety margin of about 30% with respect to stall speed, which was in turn calculated in the condition of idling engines. In an operational setting, the aircraft will initially approach at a certain speed, decreasing continuously until touchdown, when it is close to stall speed. The variation of airspeed is associated with the increment of lift coefficient and the result is the approach profile. Regardless of the chosen operative procedure, the approach profile should be demonstrated to preserve a certain safety margin from the stall speed that can now be determined including the beneficial aero-propulsive interactions. High-lift propulsion generates additional lift from propellers blowing over the wing surface.

Differently from conventional aircraft, an aircraft with high-lift propellers can create additional lift at the same angle of attack by the efficient exploitation of propellers blowing. As stated, the contribution of high-lift propulsion is defined as an additional component that can be summed to the lift coefficient. Knowing the value of thrust, speed, and angle of attack, the associated increment can be calculated as discussed in 2.2.1. However, the increment in lift is not the only effect produced by the interaction between the propeller slipstream and the lifting surface. The additional increment in pitching moment should be accounted to calculate the longitudinal trim and, thus, the maximum total lift of the aircraft. At the early stages of the design process, when it is not possible to test the aircraft stalling, the stall speed can be calculated from Eq. (2.113), where C_L is the lift coefficient, S_w is the wing area, and W is the weight of the aircraft.

$$V_{stall} = \sqrt{\frac{2W}{\rho C_L S_w}} \quad (2.113)$$

However, when the objective is determining the stall speed when high-lift propulsion is operative, the calculation is repeated iteratively starting from the power-off condition. The aero-propulsive interaction has been related to the flying airspeed

and the thrust provided, which in turn depends on the airspeed as well. Thus, when the airspeed has to be determined, the process moves from the preliminary estimation of the aero-propulsive interaction at an airspeed close to stall speed.

In the definition of stall speed, controllability plays a major role. The longitudinal controllability of the aircraft requires the elevator to be still effective and the horizontal tailplane to withstand the tail equilibrium loads. Conversely, the directional controllability cannot disregard eventual asymmetry in the propulsive speed. Hence, the **minimum control speed** is introduced, that is the calibrated airspeed at which, when the critical engine is suddenly made inoperative, the aircraft is still controllable maintaining straight flight at the same speed with a bank angle ϕ not higher than 5 degrees [19, 20, 134]. In case of large aircraft with three or more engines, an additional engine made inoperative should be accounted for. The simulation of a thermal engine failure could be less critical for hybrid-electric aircraft than the failure of other elements.

Part 23 of the regulation requires that the minimum control speed of the aircraft must not exceed $1.20 V_{stall_1}$, where V_{stall_1} is the stall speed at maximum take-off weight. Similarly, Part 25 requires to not exceed $1.13 V_{stall_1}$. At this airspeed, the lateral, directional, and longitudinal controls must still be effective. This condition requires an appropriate deflection of ailerons and rudder to be maintained, thus, the maximum deflection angles of the control systems have a primary role in the determination of V_{MC} . The lateral-directional equilibrium discussed in 2.3.2 is not suited to model the one-engine inoperative condition. The failure of a critical propulsive element, regardless of the architecture chosen, generates direct and indirect effects of interest, both related to the asymmetric thrust. The direct effect is an additional yaw moment with respect to the center of gravity, that is the sum of the single yaw moments calculated as the product of the thrust vector of each propulsive unit and the distance from the center of gravity. The resulting yaw coefficient is calculated as shown in Eq. (2.114), where b_w is the wingspan, S_w is the wing area, and ρ is the air density.

$$C_{NOEI} = \sum_i \frac{2T_i y_i}{\rho S_w b_w V_{MC}^2} \quad (2.114)$$

The indirect effects deal with the yaw and roll caused by the asymmetric lift and drag related to the aero-propulsive interactions or the windmilling condition of one or more propulsive units. For these effects, the total drag will be addressed as D_{OEI} , assumed to be applied on the y-axis at a certain distance from the center of gravity ($y_{D_{OEI}}$), while the total lift is addressed as L_{OEI} , with a certain moment arm ($y_{L_{OEI}}$). The certification constraints should be verified in conditions of maximum take-off weight (W_{TO}), which allows calculating the lift coefficient as reported in the following equation.

$$C_{L_{OEI}} = \frac{2W_{TO}}{\rho S_w V_{MC}^2 \cos(\phi)} \quad (2.115)$$

In the end, the total yaw and roll moment coefficients due to drag and lift, respectively, can be calculated as follows.

$$C_{N_{D_{OEI}}} = \frac{2D_{OEI}y_{D_{OEI}}\cos(\beta)}{\rho S_w b_w V_{MC}^2} \quad (2.116)$$

$$C_{\xi_{L_{OEI}}} = \frac{2W_{TO}y_{L_{OEI}}}{\rho S_w b_w V_{MC}^2} \quad (2.117)$$

Thus, the set of equations necessary to estimate the minimum control speed is the following.

$$C_{\xi_{\beta}}\beta + C_{\xi_{\delta_a}}\delta_a + C_{\xi_{\delta_r}}\delta_r + \frac{2W_{TO}y_{L_{OEI}}}{\rho S_w b_w V_{MC}^2} = 0 \quad (2.118)$$

$$C_{N_{\beta}}\beta + C_{N_{\delta_a}}\delta_a + C_{N_{\delta_r}}\delta_r + \sum_i \frac{2T_i y_i}{\rho S_w b_w V_{MC}^2} + \frac{2D_{OEI}y_{D_{OEI}}\cos(\beta)}{\rho S_w b_w V_{MC}^2} = 0 \quad (2.119)$$

$$C_{Y_{\beta}}\beta + C_{Y_{\delta_a}}\delta_a + C_{Y_{\delta_r}}\delta_r + \frac{2W_{TO}}{\rho S_w V_{MC}^2} \tan(\phi) = 0 \quad (2.120)$$

Assuming small sideslip angles, the cosine of β is close to be of unitary value, which is conservative with respect to the effect of asymmetric drag on yaw moment. The resulting linear system is closed by two additional assumptions: ϕ is generally fixed to the maximum allowable, that is 5 degrees, and the δ_r is assumed to be the maximum deflection angle reachable. In the present work, some additional steps to this algorithm are considered when determining the minimum control speed. Firstly, the occurrence of the failure is simulated querying the engine deck at sea level, in

standard atmosphere conditions, and for airspeed close to stall speed, generally 20% higher. Once the electric power has been redistributed through the elements that are still working with the objective of ensuring the minimum thrust loss and the minimum additional yawing moment, the system of equations is solved considering rudder deflection and bank angle equal to the maximum allowable values. If, as likely, the resulting speed is different from the first attempt, the process is repeated querying the engine deck with the new airspeed. The algorithm is iterative until a certain sensibility margin between two consecutive calculation steps is reached.

This paragraph provides the necessary guidelines to extricate from ambiguities of the regulation when coming to innovative concepts. With the objective of clarifying the application of regulation constraints to hybrid-electric aircraft with innovative propulsive systems, a commuter aircraft is used as a benchmark. The aircraft has been designed in the framework of the European project named *ELectric Innovative Commuter Aircraft (ELICA)* (Fig. 2.39 and Table 2.18).



Figure 2.39: Hybrid-electric commuter aircraft.

The propulsive architecture considered is the same reported in Fig. 2.34, sized according to the rated powers reported in Table 2.19 for each element.

Table 2.20 lists the values of the aerodynamic derivatives necessary to calculate the V_{MC} through Eq. (2.120).

Assuming that any element could cause a critical thrust loss or residual yawing moment, each failure scenario is investigated separately. The critical aspects

Parameter	Value	Unit
Wing		
Wing surface	33.94	m^2
Wing span	22.58	m
Mean aerodynamic chord	1.78	m
Horizontal Tail		
Horizontal tail surface	10.60	m^2
Horizontal tail span	7.00	m
Mean aerodynamic chord	1.53	m
Distance from aft-most C.G.	7.89	m
Vertical Tail		
Vertical tail surface	8.63	m^2
Vertical tail span	3.76	m
Mean aerodynamic chord	2.46	m
Distance from aft-most C.G.	7.51	m
Fuselage		
Fuselage length	16.25	m
Cross section diameter	2.15	m
Propellers		
Number of primary propellers	2	-
Primary propeller diameter	2.54	m
Primary propeller no. 1 y-coordinate	-3.75	m
Primary propeller no. 2 y-coordinate	3.75	m
Number of secondary propellers (DEP)	8	-
Secondary propeller diameter	1.77	m
Secondary propeller no. 1 y-coordinate	-11.29	m
Secondary propeller no. 2 y-coordinate	-9.51	m
Secondary propeller no. 3 y-coordinate	-7.72	m
Secondary propeller no. 4 y-coordinate	-5.94	m
Secondary propeller no. 5 y-coordinate	5.94	m
Secondary propeller no. 6 y-coordinate	7.72	m
Secondary propeller no. 7 y-coordinate	9.51	m
Secondary propeller no. 8 y-coordinate	11.29	m

Table 2.18: Geometric parameters of a 19-passenger hybrid-electric concept.

Element	Power	Unit
Gasturbine	782.4	kW
Primary electric generator	645.8	kW
Secondary electric motor	184.5	kW
Battery pack	267.0	kW

Table 2.19: Reference power of single powerplant components.

Parameter	Value	Unit
$\delta_{r\text{Max}}$	30.0	<i>deg</i>
$\delta_{a\text{Max}}$	20.0	<i>deg</i>
$C_{\mathcal{L}\beta}$	-0.0033	<i>deg</i> ⁻¹
$C_{\mathcal{L}\delta_r}$	0.0043	<i>deg</i> ⁻¹
$C_{\mathcal{L}\delta_a}$	-0.0024	<i>deg</i> ⁻¹
$C_{N\beta}$	0.0030	<i>deg</i> ⁻¹
$C_{N\delta_r}$	-0.0011	<i>deg</i> ⁻¹
$C_{N\delta_a}$	0.0000	<i>deg</i> ⁻¹
$C_{Y\beta}$	-0.0162	<i>deg</i> ⁻¹
$C_{Y\delta_r}$	0.0043	<i>deg</i> ⁻¹
$C_{Y\delta_a}$	0.0000	<i>deg</i> ⁻¹

Table 2.20: Aerodynamic derivatives for the calculation of the minimum control speed.

associated to each simulation are reported in Table 2.21, both in terms of generated yaw moment and loss of propulsive power.

Failure case	Yawing moment (Nm)	Variation of the propulsive power (%)
Gas turbine no. 1	-54370.6	-41.6
Gas turbine no. 2	54370.6	-41.6
Primary electric generator no. 1	-26232.7	+4.1
Primary electric generator no. 2	26232.7	+4.1
Secondary electric motor no. 1	-27281.4	+4.1
Secondary electric motor no. 2	-26582.1	+4.1
Secondary electric motor no. 3	-25883.2	+4.1
Secondary electric motor no. 4	-25183.9	+4.1
Secondary electric motor no. 5	25183.9	+4.1
Secondary electric motor no. 6	25883.2	+4.1
Secondary electric motor no. 7	26582.1	+4.1
Secondary electric motor no. 8	27281.4	+4.1
Battery pack no. 1	-10123.2	-4.7
Battery pack no. 2	10123.2	-4.7

Table 2.21: Residual yawing moment and propulsive power loss at the occurrence of the failure of each possible scenario. Propulsive power before failure occurrence is 1255.5 kW.

The failure of a gasturbine visibly represents the most critical case, when considering the first operating mode in Table 2.1, because the malfunction entails a loss of power on both propulsive lines. Therefore, the minimum control speed must be deduced from the simulation of this scenario. Conversely, the low value of supplied power ratio makes the failure of one battery pack less critical. The case of failure of an electric machine is more complex. In principle, the yaw moment caused by the failure of a distributed electric motor drive could be critical because of the distance from the center of gravity. Nevertheless, the imbalance can be considerably

reduced by assuming that the power previously supplied to the failed element is automatically redistributed in the subsystem, or, in other words, that the failed electric element opens the circuit at the location where it is located. It is explicitly noted that the redistribution of power in the subsystem can sometimes increase the aerodynamic efficiency of the propellers causing a small increment of the propulsive power, as shown in Table 2.21. Similarly, when a generator is inoperative, where the output power from the gasturbine is completely directed to the primary propeller, increasing the global efficiency of the propulsive system.

In Fig. 2.40, the propulsive and aerodynamic yawing moments are reported as a function of the airspeed. The minimum control speed is identified by the intersection of the two curves. The aircraft stall speed, accounting for the aero-propulsive effects of high-lift propulsion, is 43.1 m/s , with a maximum take-off mass of about 7982 kg . At the occurrence of the failure, the yawing moment is higher than the aerodynamic moment, leading to a minimum control speed above the regulatory limit. However, when a cross-connection between the propulsive lines of the two semispan is present, as shown in Fig. 2.34, the power can be distributed among the propulsive elements to minimize the yaw moment. In Table 2.22, the results dealing with the simulation of the failure of the thermal engine on the left semispan are reported. The application of the procedure introduced in this section allows a significant reduction of both net yawing moment and minimum control speed.

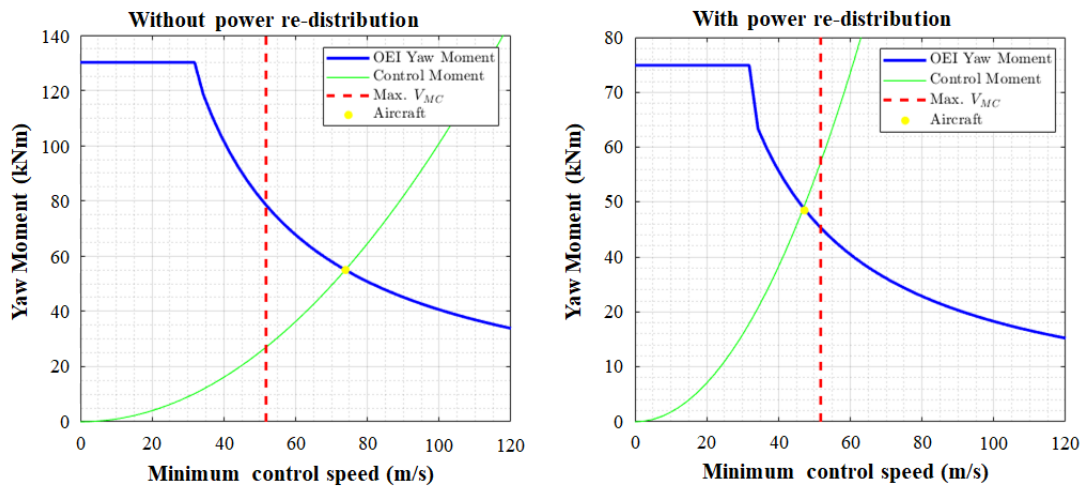


Figure 2.40: Minimum control speed calculated with and without power re-distribution.

Element	Unit	AEO conditions	Before redistribution	After redistribution
Primary propeller no. 1	<i>kW</i>	121.2	0.0	0.0
Primary propeller no. 2	<i>kW</i>	121.2	121.2	75.7
Primary electric generator no. 1	<i>kW</i>	632.1	0.0	0.0
Primary electric generator no. 2	<i>kW</i>	632.1	632.1	645.0
Secondary propellers no. 1–4	<i>kW</i>	126.6	21.9	34.2
Secondary propellers no. 5–8	<i>kW</i>	126.6	126.6	79.1
Secondary electric motors no. 1–4	<i>kW</i>	184.5	32.0	66.7
Secondary electric motors no. 5–8	<i>kW</i>	184.5	184.5	155.7
Battery pack no. 1	<i>kW</i>	127.9	127.9	267.0
Battery pack no. 2	<i>kW</i>	127.9	127.9	0.0

Table 2.22: Power distribution after the failure of gasturbine no. 1 (left half-wing).

The values of minimum control speed before and after redistribution are reported in Table 2.23.

Parameter	Unit	Without redistribution	With redistribution
Yawing moment	<i>Nm</i>	-54370.6	-38721.7
Propulsive power loss	%	-41.6	-42.1
Minimum control speed	<i>ms⁻¹</i>	74.7	47.2
Aileron deflection angle	<i>deg</i>	1.19	8.61
Sideslip angle	<i>deg</i>	4.29	-1.17
Bank angle	<i>deg</i>	-5.00	-5.00

Table 2.23: Results for the case of one inoperative gasturbine no. 1, with and without power redistribution.

Without any further power redistribution, at failure occurrence, V_{MC} would be higher than the limit established by regulation. However, one of the main advantages of a hybrid-electric propulsion architecture lies in its flexibility and it is appropriate to fully exploit it by redistributing the electric power. In this way, it is possible to prevent an unnecessary increment of the vertical tailplane area.

2.3.4 Flight Load Envelope

The term flight envelope is widely applied to the operative space in which the aircraft can fly assuring the required safety and performance. In general, the description of the operating limits is provided in terms of appropriate diagrams considering the flight level, the Mach number, and the normal load factor. Considering the body reference frame, the load factor (n) is the ratio of the net aerodynamic force acting normally to the longitudinal axis of the body reference frame with respect

to the weight of the aircraft, as shown by Eq. (2.121).

$$n = \frac{L \cos(\alpha_{WB}) + D \sin(\alpha_{WB})}{W} \tag{2.121}$$

The description of the flight envelope is carried out by two graphics representations: the doghouse plot (Fig. 2.41) [142] and the V-n diagram (Fig. 2.42) [143].

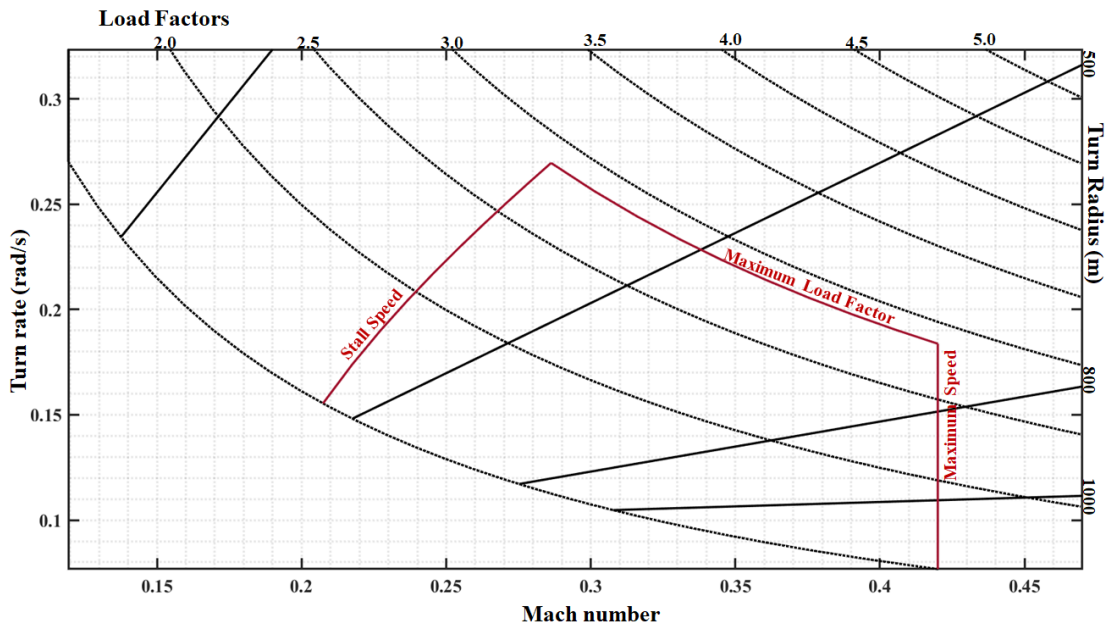


Figure 2.41: Doghouse plot of a commuter aircraft.

Doghouse plots are included in the aircraft handbook with the primary objective of describing the performance during combined turn-climb manoeuvres, completely defining the relationship between altitude, airspeed, turn radius and turn rate [142]. For the same operative purpose, but dealing with the longitudinal flight manoeuvres, the V-n diagram is included in the aircraft handbook. However, the main purpose of the V-n diagram is to determine the flight loads to which the aircraft’s structure should be designed. From this perspective, it is a design tool defining a set of limits within which the vehicle can safely operate. There are two sources of flight loads that need to be considered: aircraft manoeuvres and atmospheric gusts [143]. Each point of the loading diagram is described by airspeed and loading factor, fixed according to regulation constraints. More precisely, CS-23 §23.335 and CS-25 §25.335 indicate the equivalent airspeed values of the characteristic points, CS-23

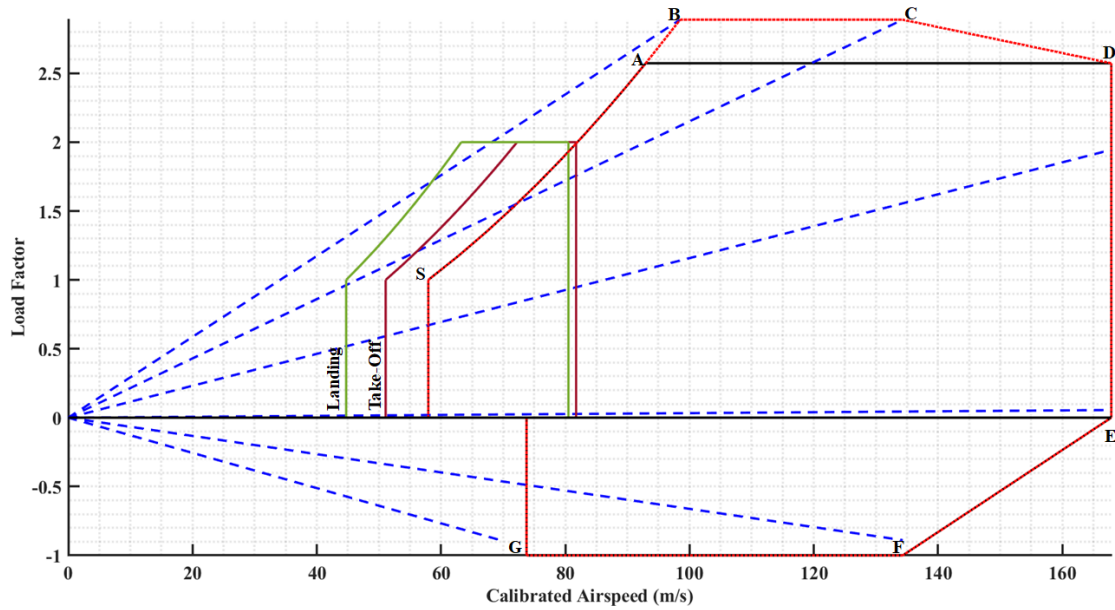


Figure 2.42: Manoeuvre diagram of a regional turboprop.

§23.337 and CS-25 §25.337 define the minimum load requirements associated with those points and, finally, section 341 of the two certification specifications guides the construction of the gust diagram [19, 20, 134].

Like any other design step discussed in the present work, the interest is motivated by the differences with respect to conventional concepts. The V-n diagram guides the structural sizing defining the strength requirements within the boundaries of the representative manoeuvring envelope. From this perspective, any aeropropulsive effect moving the boundaries of the flight envelope should be accounted to opportunely size the structure. The reduction of drag due to tip-mounted propellers has a negligible and beneficial impact on the normal load factor. Conversely, high-lift propulsion effects may be considered when dimensioning the limit load at stall condition. Three main considerations should be valued when designing a concept powered by distributed electric propellers. The first consideration deals with the objective of this kind of architecture, that is the wing area reduction. In fact, by reducing the wing area, the gust envelope is modified according to the new wing loading, also changing the dimensioning structural load. The second effect deals with the stall speed considered, which is influenced by the impact of distributed electric propulsion according to what has been discussed in 2.3.3. The last effect on the flight

envelope deals with the weight increment due to the hybridization of the propulsive system. This effect is in opposition to the others and it could mislead the designer.

In the present context, all the aspects will be discussed considering the effect of distributed electric propulsion on a regional turboprop similar to the *ATR-42*. The hybrid concept will be studied considering firstly the same maximum take-off mass of the conventional aircraft, then, assuming the mass calculated at the end of the conceptual design process, proposed in Table 2.24. In particular, the aircraft and its electric version are compared to highlight the role that aero-propulsive effects and electric powertrain play in the certification process for those aspects of interest during the conceptual design. The two aircraft have been designed in the framework of the Italian research project named *PROSIB*. The concept proposed in Fig. 2.43 is the conventional regional turboprop from which the electrification process has been carried out.

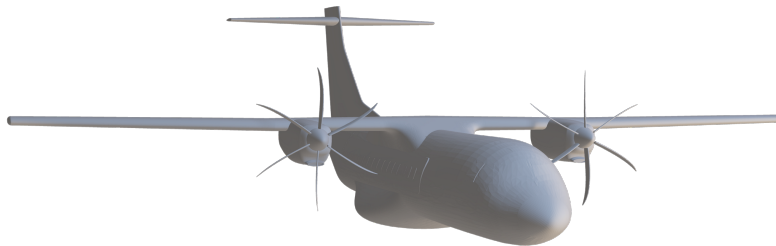


Figure 2.43: Geometry of the regional turboprop similar to ATR-42.

In Fig. 2.44, the geometry of the hybrid-electric concept is introduced. Besides the presence of distributed electric propulsion, the main difference between the two geometries is the wing area that is reduced with respect to the conventional platform.

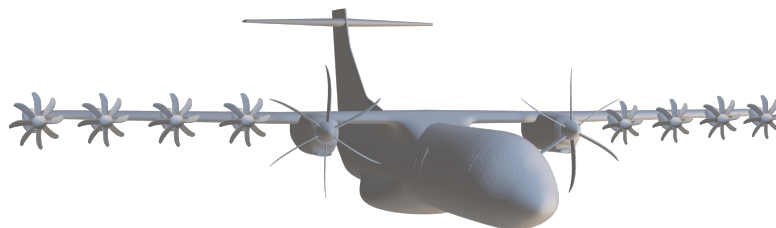


Figure 2.44: Geometry of the regional turboprop similar to ATR-42.

The hybrid-electric concept is powered by both fuel and e-storage, divided into two battery packs for safety reasons. The eight distributed electric propellers of this innovative concept allow the wing area reduction shown in Table 2.24, thanks to the increment of the lift coefficient. In the same table, the stall speeds are reported highlighting that the increment of the lift coefficient has to deal with the parallel effect of the mass on the stall speed.

	Conventional	Hybrid Electric
Mass		
Maximum Take-Off (kg)	18500	22455
Wing Geometry		
Area (m²)	54.5	44.7
Span (m)	24.6	24.6
Aspect ratio	11.1	13.5
Mean aerodynamic chord (m)	2.3	1.9
Horizontal Tail Geometry		
Area (m²)	11.7	11.7
Span (m)	6.9	6.9
Aspect ratio	4.1	4.1
Mean aerodynamic chord (m)	1.7	1.7
Vertical Tail Geometry		
Area (m²)	12.6	12.6
Span (m)	4.4	4.4
Aspect ratio	1.5	1.5
Mean aerodynamic chord (m)	2.9	2.9
Stall Speed		
Clean (m/s)	57.95	72.27
Take-Off (m/s)	51.09	58.63
Landing (m/s)	44.73	57.26

Table 2.24: Characteristics of the two concepts of interest.

Starting from a constant take-off weight of about 18500 *kg*, the two configurations are compared. In Fig. 2.45, the two V-n diagram of the conventional and hybrid-electric aircraft are reported.

At first glance, the difference in terms of maximum load factor is due to the gust envelope at sea level. The regulation prescribes a gust speed directly proportional to the flight altitude considered, which has been kept constant for the two configurations. The same goes for the cruise speed. The only difference influencing the gust load

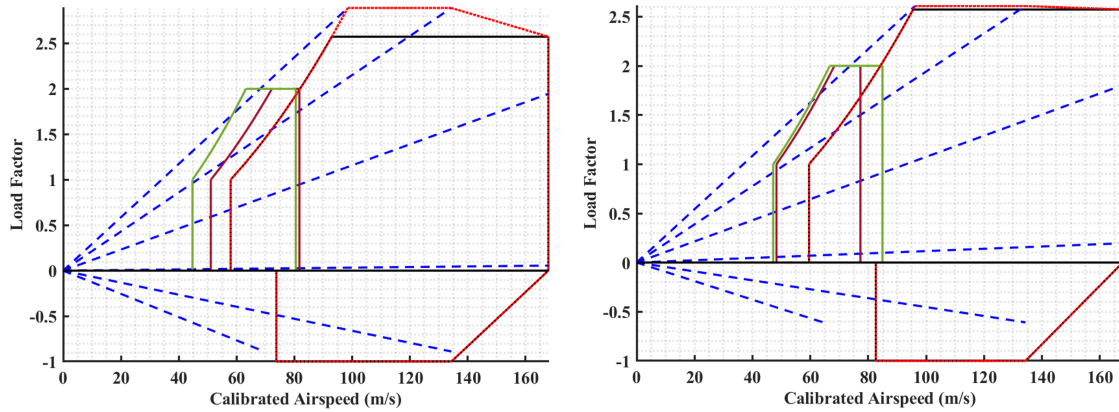


Figure 2.45: Manoeuvre diagrams of a regional turboprop similar to ATR-42 (left) and its hybrid-electric version (right) having the same maximum take-off weight (18500 kg).

factor is related to the wing load of the aircraft. The conventional aircraft has a wing load of about 339.45 kg/m^2 , while the hybrid-electric concept has a higher wing load (413.71 kg/m^2) because a lower wing area is required thanks to distributed electric propulsion. This is especially true when considering the maximum take-off masses reported in Table 2.24. Moreover, the effect on the stall speed reduces the boundaries of the flight envelope, as shown in Fig. 2.46.

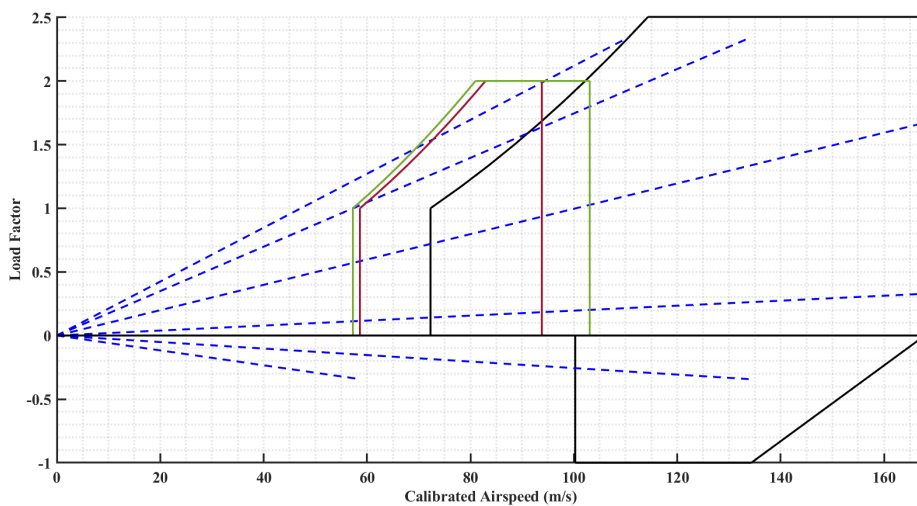


Figure 2.46: Manoeuvre diagrams of a hybrid-electric regional turboprop with a maximum take-off weight of 22455 kg.

The direct consequence of the different flight envelope is a reduction of the structural loads that should be considered when sizing the wing and the horizontal

tailplane. The tail load necessary to trim the limit conditions of the flight envelope are reported in Fig. 2.47.

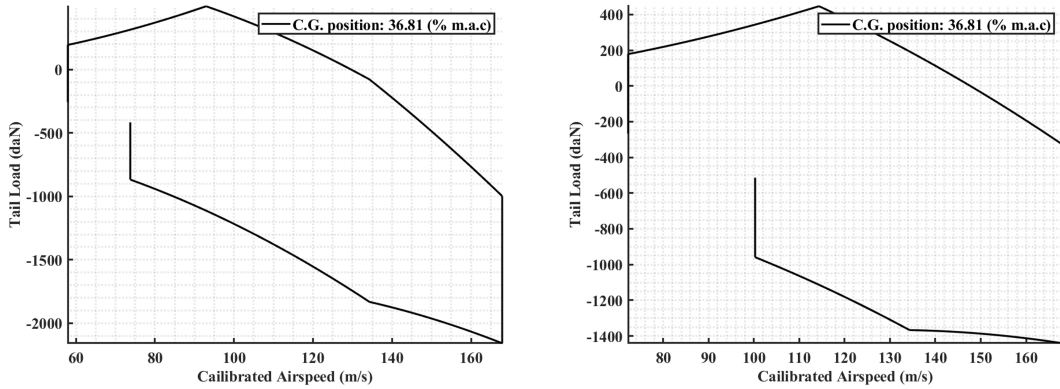


Figure 2.47: Tail load comparison a regional turboprop similar to ATR-42 (left) and its hybrid-electric version (right) (Table 2.24).

2.4 Weight estimation

The weight estimation is a key activity of each step of the design chain. From the sizing activity, up to the final assessment of flight performance, aircraft weight plays a major role in identifying the necessary aerodynamics characteristics of each lifting surface and the power demand. Methods are generally reported referring to different classes related to various fidelity levels. In the present work, three main classes are investigated.

- I Based on statistics, this method can be applied when the geometry is still not defined. This is the reason behind the success of low-fidelity methods for weight estimation at the early stages of the design process of hybrid-electric aircraft. The main drawback is the reliability of the method which lies in the right choice of the parameters (among the top-level requirements) by which the statistics are influenced.
- II This second level of reliability approaches the weight estimation at the system level considering some preliminary characteristics of geometry and power demand as driving factors of the weight estimation. Differently from the previous class, even if system weight is calculated from equations based on

statistics, the driving parameters are already known and frozen by the designer who created the method.

- III This last class of estimation is based on subsystem characteristics and concludes the weight estimation summing the masses of the single components. This is still not a detailed design method, but the refinement of the geometry and the major characteristics of the aircraft will permit a higher order of fidelity which is based on physics rather than statistics.

The first section of this paragraph describes the energetic method, which is a simplified mission analysis employed to measure fuel and electric energy requirements when an engine deck or a simulation based approach cannot be used. The three classes are presented in the following sections.

2.4.1 I Class Weight Estimation

The weight estimation proposed in literature for hybrid-electric aircraft is based on I class methods, which are generally based on statistical approaches related to the category of interest and, then, adapted to unconventional aircraft configurations. Ref. [41] proposes a modification of methods already discussed for conventional aircraft in Ref. [63, 64].

Without lacking of generality, two approaches are reported from literature to describe I class weight estimation methods. The first approach examined is based on a system of two different linear equations. The first equation is a linear regression relating the maximum take-off weight (MTOW) to the operative empty weight (OEW) of flying aircraft designed on similar TLAR. The second one describes the maximum take-off weight as the sum of operative empty weight, fuel weight, and payload weight (Eq. (2.122)).

$$MTOW = OEW + W_{fuel} + W_{payload} \quad (2.122)$$

Moving from TLAR about the passengers, the payload mass is estimated considering a certain weight per passenger. The fuel mass is estimated through the fuel fraction

method which moves from a preliminary knowledge (generally based on statistics) of the percentage of total fuel consumed during the flight phases, Eq. (2.123).

$$W_{fuel} = \frac{W_{fuel_{phase_2}}}{W_{fuel_{take-off}}} \frac{W_{fuel_{phase_3}}}{W_{fuel_{phase_2}}} \cdots \frac{W_{fuel_{phase_n}}}{W_{fuel_{phase_{n-1}}}} + W_{fuel_{reserve}} \quad (2.123)$$

Since no flying hybrid aircraft or innovative configurations can be considered for a statistical approach, this approach is not suited for unconventional aircraft. The second approach considered presents the main limit of moving from a well-educated guess on the MTOW and, then, correcting the value by an energetic estimation of the fuel and the e-storage required to accomplish the design mission. In classical methods, when the tank volume has not been fixed yet, the energy required to complete the design mission is estimated in order to calculate the fuel weight [61, 63]. Improvements to this method consist in the integration of the battery weight estimated considering the percentage of power (or energy) supplied to the powertrain by the two power sources [67].

$$MTOW = OEW + W_{fuel} + W_{payload} + W_{battery} \quad (2.124)$$

However, this approach underestimates the weight since it moves from a well-educated guess related to statistics based on conventional aircraft. In fact, the correlation between the operative empty weight and the maximum take-off weight can be strongly different because the introduction of new elements (electric motor drives, cables, power management units, etc.) increases the percentage of maximum take-off weight due to operative empty weight.

To overcome the limits of this second approach in case of hybrid-electric aircraft, in Ref. [41], a further breakdown of the operative empty weight has been suggested. At each step, moving from the OEW of a conventional platform, the powertrain and the wing masses are subtracted and the new values are summed, as shown in Eq. (2.125). It is here highlighted that the value of wing mass and powertrain mass should be calculated considering other methods than I class methods.

$$OEW = OEW_{ref} - W_{PT_{ref}} - W_{W_{ref}} + W_{PT} + W_W \quad (2.125)$$

As stated by the authors of Ref. [41], the update of powertrain and wing masses at each iteration of the sizing process is necessary to improve the accuracy of the weight estimation, even if, a better result can be achieved considering a II class method.

2.4.2 II Class Weight Estimation

The II class weight estimation aims to define the mass breakdown at system level. Methods proposed in literature are based on a preliminary knowledge of the geometric characteristics. In the present work, the main difference with classical methods deals with the evaluation of the propulsive system mass breakdown. For the remaining subsystems, the estimation is conducted without proposing any equation for the estimation of the specific masses of the components, leaving the free choice of the method to the designer among those proposed in literature [63, 64, 144]. Independently from the choice of the II class method, some common aspects are the dependence of weight breakdown from the geometric characteristics of the lifting surfaces or the maximum zero fuel mass. These elements are repetitively updated in a convergence loop and calculated with classical methods. However, in order to be compliant with hybrid-electric architectures, II class methods require the integration of new approaches to estimate the weight of the additional components of the propulsive system.

The first mass estimated is the engine dry mass, which can be related to thermal engine characteristics by regression laws. The turbofan engine dry mass is related to thrust by Eq. (2.126), which is a valid alternative to the outdated relationship proposed in literature [145].

$$W_{dry\ engine}(kg) = 0.0163Thrust(N) + 309 \quad (2.126)$$

$$W_{dry\ engine}(lbm) = 0.1596Thrust(lbf) + 681 \quad (2.127)$$

In case of turboprop engines, the dry mass can be estimated considering the following equation.

$$W_{dry\ engine}(kg) = 0.2266Power(kW) + 17.25 \quad (2.128)$$

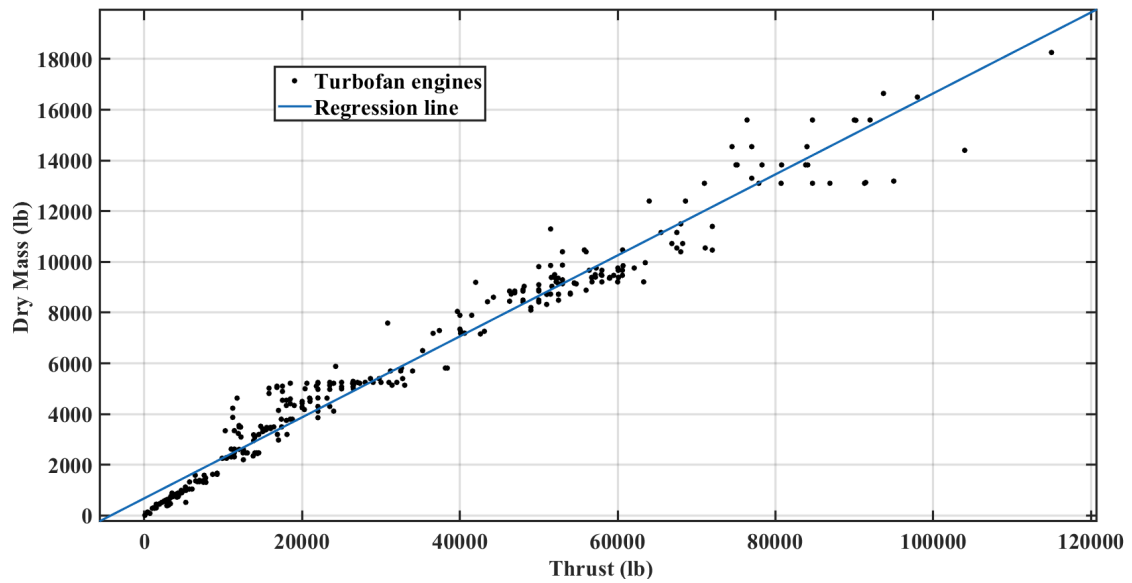


Figure 2.48: Turbofan engine dry mass vs thrust.

$$W_{dry\ engine}(lbm) = 0.3726SHP + 38.03 \quad (2.129)$$

Similar regression law can be drawn for the engine dry mass estimation considering

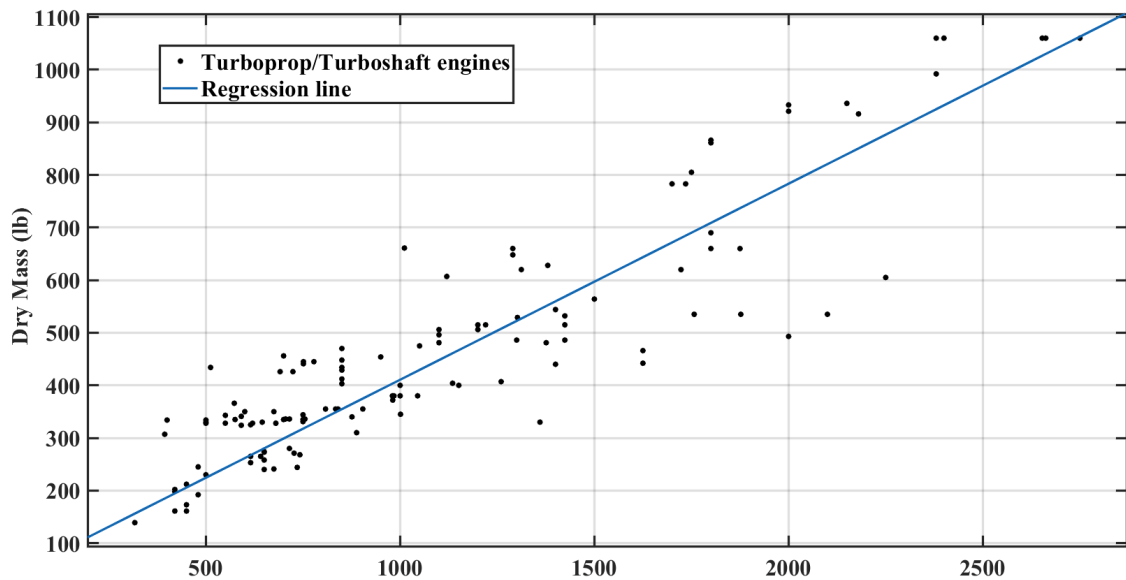


Figure 2.49: Turboprop engine dry mass vs shaft horse power.

different engine types based on data available in literature. The value of the engine dry mass estimated in this way is not affected by the presence of the electric components.

A different approach is suggested in case of propulsive systems designed for

boundary layer ingestion. In Ref. [69], the authors propose a preliminary design of these propulsive systems which is based on flow conditions, inlet dimension, and thrust required. In the same work, a preliminary weight estimation method is presented (Eq. (2.130)), where D_{fan} is the inlet diameter.

$$W_{dry\ engine}(lb) = 2.652(1.81D_{fan}^3(ft) - 19.80D_{fan}^2(ft))^{0.5833} \quad (2.130)$$

In case of hybrid-electric propulsive systems, the engine dry mass alone is not sufficient to describe the powerplant mass breakdown. Each component of the propulsive system is weighed by multiplying the dimensioning power of the component with the inverse of its own specific power (Eq. (2.131)).

$$W = \frac{P}{Specific\ Power} \quad (2.131)$$

In the same way, when the gasturbine is substituted by a fuel-cell, the mass of the fuel-cell is calculated by considering the specific power and the sizing power.

The power sources considered are dimensioned considering the energy requirements to accomplish the design mission or to fly the maximum range. Regardless of the type of chemical power source, Eq. (2.132) is a valid equation to estimate the mass.

$$W_{Fuel} = \frac{E_{Fuel}}{Specific\ Energy} \quad (2.132)$$

On the other hand, the battery mass is dimensioned considering the most demanding requirement between power and energy (Eq. (2.133)).

$$W_{BAT} = \max\left(\frac{E_{BAT}}{Specific\ Energy}, \frac{P_{BAT}}{Specific\ Power}\right) \quad (2.133)$$

The mass breakdown proposed in the present section is the result of traditional methods to estimate conventional aircraft masses and new methods to include the additional elements of hybrid-electric concepts.

2.4.3 III Class Weight Estimation

The III class weight estimation is carried out at subsystem level. As discussed in previous sections, methods proposed in literature can be applied to all those components that are not modified by the electrification process. Thus, in the present work, the discussion of weight estimation is limited to those elements composing the hybrid-electric powertrain and the structural mass of the wing, which is in turn influenced by the presence of different load distribution in case of these concepts.

The semi-empirical laws have been designed according to a unique procedure. The weights of the single components are the response variables of interest. The independent variables have been identified thanks to the analysis of the variance (ANOVA) in order to exclude those that are correlated. The semi-empirical equations have been chosen investigating the different possibilities that could maximize the coefficient of determination (R^2). A threshold value of 0.95 has been fixed to determine the compliance of the regression law with the experimental data. Since the data has been partially provided by industrial partners, the coefficients of determination associated with each semi-empirical law are not provided. On the other hand, the validity of these equations is limited by the data collected and these limits are reported in terms of valid ranges of the input variables at the end of each sub-section.

Gearboxes

Gearboxes are mechanical units composed of gears and gear trains with the specific aim of transmitting the mechanical power between two elements assuring a certain ratio between the input rotational speed and torque and the output values. The mass of these components strongly depends on two different parameters: the input torque and the gear ratio. In other words, fixed the input torque and the desired output, the mass value can be estimated by Eq. (2.134).

$$W_{Gearbox}(kg) = aTorque(Nm)^3 + bTorque(Nm)^2 + cTorque(Nm) + d \quad (2.134)$$

The coefficients reported can be calculated as a function of the gear ratios. The following equations allow calculating these coefficients considering the MKS system of units, or, in other words, when the mass is estimated in kilos and the torque in Nm .

$$\begin{aligned}
 a = & \\
 & 3.78e^{-9} * (Gear\ Ratio)^2 - 2.43e^{-8} * (Gear\ Ratio) + \\
 & + 4.21e^{-8} \qquad \qquad \qquad (2.135)
 \end{aligned}$$

$$\begin{aligned}
 b = & \\
 & - 2.32e^{-6} * (Gear\ Ratio)^2 - 7.32e^{-6} * (Gear\ Ratio) + \\
 & + 2.74e^{-5} \qquad \qquad \qquad (2.136)
 \end{aligned}$$

$$c = -0.01(Gear\ Ratio)^2 + 0.08(Gear\ Ratio) - 0.15 \qquad (2.137)$$

$$d = -0.06(Gear\ Ratio)^2 + 1.36(Gear\ Ratio) - 0.68 \qquad (2.138)$$

The equations have specific limits of validity. The gear ratios considered range from 2 to 7 and the maximum torque value admitted is 2000 Nm .

E-Motor Drives

The e-motor drive aims to transform electric power into mechanical power and vice versa. This transformation has the specific objective of transforming the electric energy to move the propellers or producing electric power from the mechanical power provided by the thermal engine shaft. The mass of these units is estimated, regardless of the direction of the power transformation, applying Eq. (2.139).

$$W_{E-Motor}(kg) = \alpha RPM^\beta + \gamma \qquad (2.139)$$

The coefficients reported in the previous equation are a function of the sizing power that can be based on statistical data available from manufacturers. Results discussed in the present work are derived from the following functions when the mass is in kilos and the power in kW.

$$\alpha = 166Power(kW) + 8469 \qquad (2.140)$$

$$\beta = 8.00e^{-5}Power(kW) - 1.07 \quad (2.141)$$

$$\gamma = 0.06Power(kW) - 3.08 \quad (2.142)$$

The validity of this semi-empirical law is constrained in terms of power and rotational speed. In other words, it is valid up to a maximum value of RPM equal to 50000 and a maximum rated power of about 1500 kW.

Power Electronics, Distribution and Management

Power electronics play a key role in power distribution and conversion, including both power management and distribution unit (PMAD) and converters/inverters. While the first is responsible for the direct control of the power distribution assuring the safety of the propulsive system and the risk management in case of failure, the seconds are responsible for switching direct current and alternating current in a power grid where units powered with direct current are connected by alternating current cabling. Mass estimation of converters, choppers, and inverters is managed with good reliability as reported in Eq. (2.131). Specific power for silicon-based power electronics systems today is approximately 2.2 kW/kg for aircraft applications, and their use for circuit protection is limited to 25 A at 270 VDC (7 kW). Highly powered circuit protection is provided by mechanical breakers and relays up to about 500 A at 270 VDC (135 kW) using state-of-the-art equipment.

However, in the present section a different approach to mass estimation is suggested in Eq. (2.143).

$$W_{Power Units}(kg) = KPower(kW) + 1.25 \quad (2.143)$$

The coefficient K reported is calculated by a function of the voltage (V) as reported in Eq. (2.144) when the power in Eq. (2.143) is in kW and the mass in kilos.

$$K = \frac{0.48}{Volt(V)} \quad (2.144)$$

The equation can be considered reliable if the values are within the range of data collected. Thus, it is advisable to use these equations when the rated power is lower than 1500 kW and the voltage is between 270 V and 850 V.

E-Storage Unit

The electric energy is stored in specific units designed to supply the necessary power along the flight mission. The design of these elements, discussed in the section dedicated to battery modelling (2.1.4), is driven by power and energy requirements. For this reason, the choice of specific power and energy is a crucial technological parameter for mass estimation, as seen in Eq. (2.133) for the case of Li-ion batteries. The relationship between the specific power of the battery and its specific energy is described by the following equation.

$$\text{Specific Energy}(Wh/kg) = f(\text{Year})(\text{Specific Power}(W/kg))^{-0.38} \quad (2.145)$$

The multiplying coefficient depends on the reference year of entrance in service which is considered the driving factor for the technological level reached. Based on data available in literature and from manufacturers [146–150], considering a realistic prediction for the battery technological innovation trend, the function can be defined by Eq. (2.146), when the specific power is in watt per kilogram and the specific energy is expressed in watt-hour per kilogram.

$$f(\text{Year}) = 100\text{Year} - 200000 \quad (2.146)$$

Data collected covers a wide range of years of service entry, allowing the estimation of the weight between the year 2020 and the year 2050.

Cabling

The distribution system has been designed starting from the conductor component in each cable. The number of wires N_{wires} and the section A_{wire} of each one is calculated starting from the required ampacity, while the position of the powertrain elements imposes the cable length l_{wire} . From these parameters, the cable mass can be calculated by summing the contribution of each segment.

$$W_{Cable} = \sum_i^{N_{cables}} N_{wires_i} l_{wire_i} A_{wire_i} \quad (2.147)$$

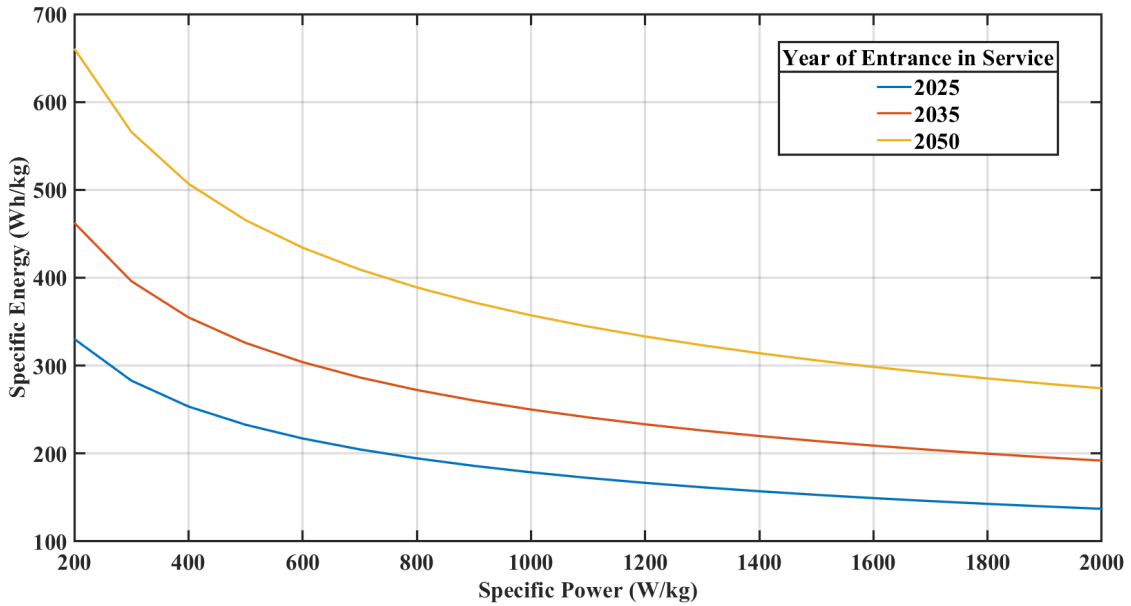


Figure 2.50: The curves of power density (W/kg) with respect to energy density (Wh/kg) are reported for three different technological levels associated with as many years of entrance in service.

Wing Structure

This section suggests a comprehensive mass estimation method for the lifting surfaces of unconventional hybrid-electric aircraft architectures. Determining the mass of a lifting surface with distributed propulsion via semi-empirical methods capable of accounting for the unconventional aspects of the propulsive system is necessary to increase the optimization capabilities.

The wing is considered here as a structural test case for the weight estimation method proposed and each component is designed according to specific criteria. The structure is broken down into primary and secondary structures. The load-carrying components are sized considering the minimum mass needed to withstand the prescribed static load. Then, the mass of each component is estimated considering semi-empirical approaches along with the compensation of dynamic loads. Since the main interest is in the effect that the propulsive system has on the wing weight, an important issue is related to its components (e.g.: battery pack, fuel cell, distributed propellers) positions and masses.

The **primary structure** mass computation is the core activity presented in

this section due to the effect that the mass distribution has on it. The primary structure consists of various elements. If the wing is stressed, all the components withstand the loads, but each of them has a specific task. From this perspective, a simplifying hypothesis is necessary. The assumption made is that the wing box is a statically determined equivalent system where each component bears a certain type of solicitation:

- the web of the front and back spars sustains the vertical shear forces;
- the caps of the spars are sized to withstand the bending moment;
- the covering skin of the wing bears the torsion moment;
- the ribs support the wing panels against buckling, preserving the airfoil shape.

Two main hypotheses have been adopted for the primary structure. Firstly, the aerodynamic load distribution is estimated assuming a constant lift distribution, in favour of a safety margin. Secondly, the propeller slipstream increases lift, but this aspect will be taken into account in a second step by introducing an iterative loop. Finally, torque and torsion due to thrust are not considered since the effect is negligible.

When estimating the mass of the primary structure, the first step is determining the distribution of internal solicitation over the wingspan. Firstly, the shear stress distribution is calculated considering the effect of lift and weights, including those of powertrain elements. After obtaining the shear distribution, the bending moment distribution over the wingspan is calculated. Finally, the twist moment is calculated assuming that the lift generated by each airfoil is applied in its focal point. Each component of the primary structure is sized considering the three loads introduced [151]. In the present context, the methods proposed in Ref. [61, 151] are considered for the estimation of the primary structure, whose theory is rapidly presented below. However, regardless of the method chosen, the aero-elastic effect related to the engines and e-motor drives distributed along the wingspan is not considered and requires a further correction that is the main topic of the present section.

As anticipated, at conceptual design level, *webs* are sized to bear the vertical shear stresses due to aerodynamic and inertial loads. The structure is sized to

withstand the maximum admissible stress, which must not be less than the static stress at maximum load factor and fatigue rupture stress at unitary load factor. Specifically, the webs are sized according to the Von Mises criterion [152]. Shear force distribution ($S(y)$) is measured through Eq. (2.148).

$$S(y) = n(W_{TO} - W_{wing} - W_{eng}) \quad (2.148)$$

In Eq. (2.148), the maximum take-off weight (W_{TO}) multiplied by the limit load factor (n) is the maximum load to withstand, while the masses of the wing and the propulsive system components alleviate the shear stress. The mass distribution along the wingspan allows to calculate the shear load at each chord. In particular, the distribution of nW_{TO} fits the lift distribution. Then, the required web surface (A_{web}) is calculated as shown in Eq. (2.149).

$$S(y) \leq \tau_{max} A_{web} \quad (2.149)$$

Finally, the required mass is obtained by integrating the surface along the wing elastic axis. It is here remarked that the value of the load factor in Eq. (2.148) depends on the sizing criterion.

When calculating the mass of spar *caps*, the flanges can be dimensioned considering two approaches based on stress and deformation. Considering the first one, the flanges are sized to sustain the stress caused by the bending moment at the limit load factor, without any permanent deformation or rupture. Similarly to spar webs, caps are sized to stress calculating the necessary area. Aiming at minimizing the mass required, two limitations are considered. On the one hand, the maximum stress is assumed to be equal to the ultimate rupture stress (σ_{max}). On the other hand, the load factor is assumed to be equal to the maximum load factor. The stress caused by the bending moment affecting upper and lower caps is calculated through Eq. (2.150).

$$\sigma = \frac{M_{bend}}{I_y} z \quad (2.150)$$

The equation reveals that the stress increases with the distance (z) from the neutral axis. In other words, once the airfoil has been chosen and the wing box geometry

has been fixed, the minimal required area of the caps is computed to assure the necessary moment of inertia (I_z). The inertial relief caused by the masses distributed along the wingspan should be considered when measuring the total bending moment (M_{bend}). From this perspective, some assumptions are necessary. Firstly, the wing mass distribution is assumed to be triangular while the tank is considered empty (conservative case). Secondly, the wing-mounted engines are modelled as mass points.

The *skin* covering the wing box absorbs the torsional load. This is the heaviest component of the primary structure, which means that it has to be sized accurately to achieve a reasonable prediction of the wing mass. Since the skin thickness (t_{skin}) is sized to withstand the torsion (T), Bredt theory can be applied to obtain Eq. (2.151), where A_{box} is the Bredt area [151].

$$\tau t_{skin} = \frac{T}{2A_{box}} \quad (2.151)$$

The thickness depends on the Bredt area, which is related to the wing box configuration. In addition to that, the coating must be sized to guarantee a certain minimum efficiency of the lateral control surfaces. Since the wing is flexible and deformable, the steering of the ailerons causes an additional torsional deformation negatively influencing the lateral manoeuvrability. Similarly to the spar caps, two dimensioning approaches can be used: the non-rupture criterion and the deformation criterion. According to the first one, the covering skin is sized to withstand critical loads, but this does not ensure the efficiency of the control surfaces. On the other hand, the deformation criterion is aimed to limit the torsional deformation caused by the commanded manoeuvre, satisfying the efficiency requirement (CS-25 §25.349 [20, 134] and CS-23 §23.349 [19]). Generally, both methods are considered so that the maximum thickness is taken into account to estimate the skin mass.

The analytical estimation of *ribs* mass would require detailed information on the wing design. Thus, this mass is calculated based on two assumptions. The first one is that ribs have all the same thickness, which is equal to the minimum value required to avoid instability. The second one is that the ribs are a fraction (f_{rib})

of the Bredt area A_{box} . The mass of a generic rib is calculated as in Eq. (2.152), where the rib volume is multiplied by the material density ρ_{rib} .

$$W_{rib} = t_{rib}A_{box}f_{rib}\rho_{rib} \quad (2.152)$$

The mass of the primary structure estimated must be corrected to account for the following contributions:

- mountings and connections;
- aeroelastic corrections;
- penalties due to loads and stiffness requirements;
- thickness variations, joints, and large cut-outs.

It is not trivial to estimate the mass correction in an analytical way. This difficulty can be resolved by simply increasing the primary mass of a certain percentage. However, this method could lead to results that are not consistent with the real value. Thus, alternatives methods from literature are suggested, as those proposed in Ref. [153]. However, the aero-elastic correction proposed by the latter method does not account for the effect of engines arbitrarily located along the wing.

As previously stated, the objective of the present section is the estimation of the necessary corrections necessary to account for the aero-elastic effect on the wing mass caused by the weight of the unconventional propulsive system. Hence, once the definition of the primary mass is obtained according to the methods chosen by the designer, the following procedure is suggested to evaluate this variation ($\Delta W_{aero|eng}$). In literature, aero-elastic issues in wing design including the effect of distributed electric propulsion have been studied for the case of NASA X-57 [154]. In that case, several adjustments were carried out to account for both wing and whirl flutters. In the present work, only the wing flutter is valued.

Placing engines, modelled as concentrated masses, along the wingspan and the airfoil chord has an immediate effect on the static loads. Instead, it is neither obvious nor easy to measure the effects on the structural dynamics. The former contribution is estimated by introducing the engine weight and position within the flexural beam approach adopted to estimate the load carried by each airfoil section.

Basically, by moving the engine outward along the wingspan the bending moment is mitigated. On the other hand, the evaluation of the aero-elastic effect induced by the engine is a challenging matter. A relatively small number of papers deals with this topic [154, 155]. Additionally, the effect may be strongly non-linear, due to the non-linear nature of the problem. Basically, the engine position affects the flutter speed and the available literature demonstrated that moving the engine outward along the wingspan or adding a new tip-mounted engine is a big issue resulting in a non-linear flutter speed distribution versus engine position. For instance, moving the only engine mounted from root to tip causes an increment of the flutter speed around 60% of the wingspan, followed by a sudden decrease, even below the reference value. However, the flutter speed is an important design parameter that cannot be decreased. To accommodate the flutter speed reduction, a weight penalty is calculated using the semi-empirical formulation proposed in Ref. [156]. However, before quantifying the mass penalty needed on the primary structure, the flutter speed variation must be quantified. For example, the presence of tip-mounted propellers is expected to generate dynamic instability strongly reducing the flutter velocity. However, in Ref. [157], it has been demonstrated that placing the engine at certain locations, the flutter speed can be even increased. This phenomenon may be induced in two ways. The first way is locating the engine where lower frequency flutter mode is relegated to a higher frequency. The other method is positioning the engine where the interaction between fluid and structure is decreased. In other words, both criteria could be met at the section of the minimum kinetic energy of the mode [155]. Moreover, in case of wings characterized by high-aspect ratios, as those designed thanks to the contribution of distributed electric propellers, the areas of minimum kinetic energy related to bending and torsional modes may be different. For example, the first bending mode has a minimum value at the root, the second bending mode shows the minimum kinetic energy density outboard of the 85% of the wingspan. This result reported in Ref. [155] opens a new challenge that deals with the aero-elastic tailoring of the wing.

The objective of aero-elastic tailoring is to keep the value of flutter speed constant while introducing the weight of the propulsive elements. However, at conceptual design level, the evaluation of the dynamic modes could be difficult and semi-empirical methods should be preferred. From this perspective, based on the semi-empirical approach suggested in Ref. [156], Eq. (2.153) links flutter speed and wing mass distribution through the parameter C , calculated as reported in Eq. (2.154).

$$V_{Fl} = C\sqrt{\omega_T^2 - \omega_B^2} \quad (2.153)$$

$$C = \sqrt{\frac{d_3 W_{wing} k^2}{\rho_0 C_{L_\alpha} y}} \quad (2.154)$$

In Eq. (2.153), ω_T is the angular frequency of wing torsional mode and ω_B is the angular frequency of the bending mode. In Eq. (2.154), d_3 is the semi-empirical parameter depending on the taper ratio, W_{wing} is the wing mass over the wingspan, k is the ratio between the average radius of gyration of the wing section (normal to the section at the shear center) and the wind chord, ρ_0 is the air density at sea level, y is the distance between wing section shear center and aerodynamic center. Assigning the apex ' to the flutter speed of the isolated wing and the apex '' for the case with distributed electric propellers, Eq. (2.153) and Eq. (2.154) can be combined in Eq. (2.155) to calculate the necessary additional mass.

$$\left(\frac{V'_{Fl}}{V''_{Fl}}\right)^2 = \frac{W''_{wing}}{W'_{wing}} \quad (2.155)$$

At conceptual design level, the parameters required in Eq. (2.153) are not always available. Thus, a different approach is used to calculate the ratio between the two flutter speeds on the left of Eq. (2.155). Based on the results in Ref. [158], a semi-empirical relationship between the engine location and the variation of flutter speed has been determined, as shown in Fig.2.51.

After the effect related to the single component of the propulsive system is measured, the effect is scaled by a ratio f_{eng} , where W_i is the mass of the specific element and W_{tot} is the total mass of the propulsive elements mounted on the wing.

$$f_{eng} = \frac{W_i}{W_{tot}} \quad (2.156)$$

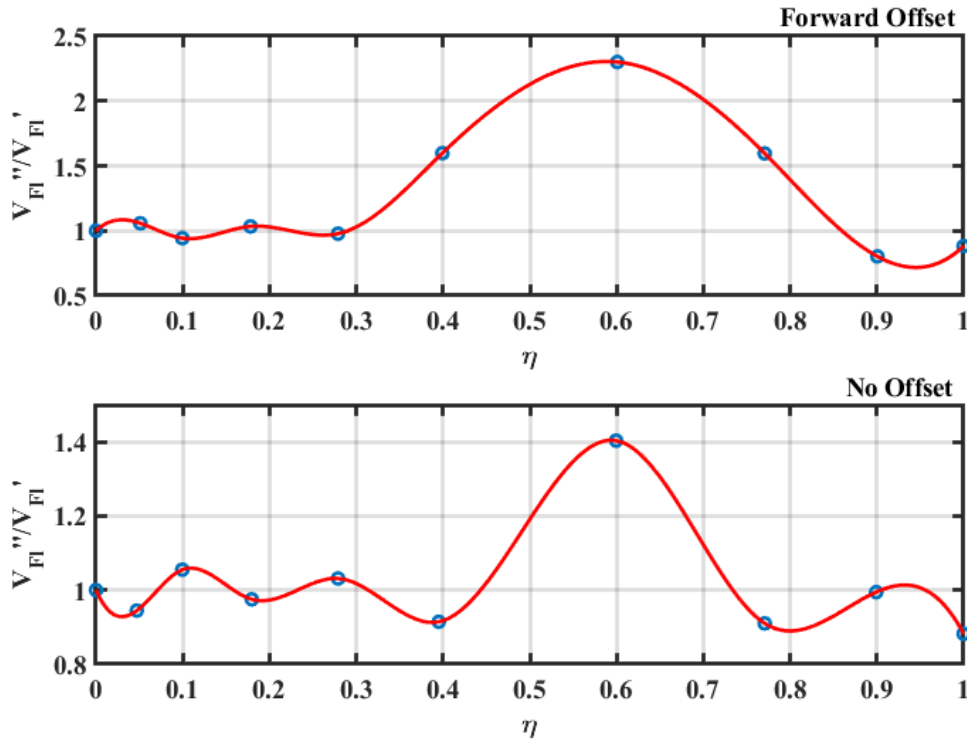


Figure 2.51: Flutter speed variation with respect to the dimensionless location of the engine along the wingspan (η) for the case of an engine mass concentrated on the elastic axis or forward from it up to the order of a mean aerodynamic chord.

Finally, the aeroelastic penalty is calculated with respect to the total wing mass, as shown in Eq. (2.157).

$$\Delta W_{aero|eng}(\%) = 0.45 \left(\frac{V_{Fl}^{\prime 2}}{V_{Fl}^{\prime 2}} - 1 \right) f_{eng} 100 \quad (2.157)$$

In Eq. (2.157), the coefficient 0.45 has been introduced to account for the percentage (45%) of the primary structure providing bending and torsional stiffness.

The validation of this approach required the comparison with the results obtained by the finite element method applied on the same wing, as shown in Fig. 2.52. The results are detailed in Ref. [159] and Ref. [160].

Finally, the **secondary structure** must be weighted and its contribution added to the total mass. The secondary structure includes fixed leading and trailing edges, control surfaces and high-lift devices, whose weights are estimated with statistical methods depending on the geometry of the different components. The secondary mass is about 30% of the total wing mass, so it has an important effect on the

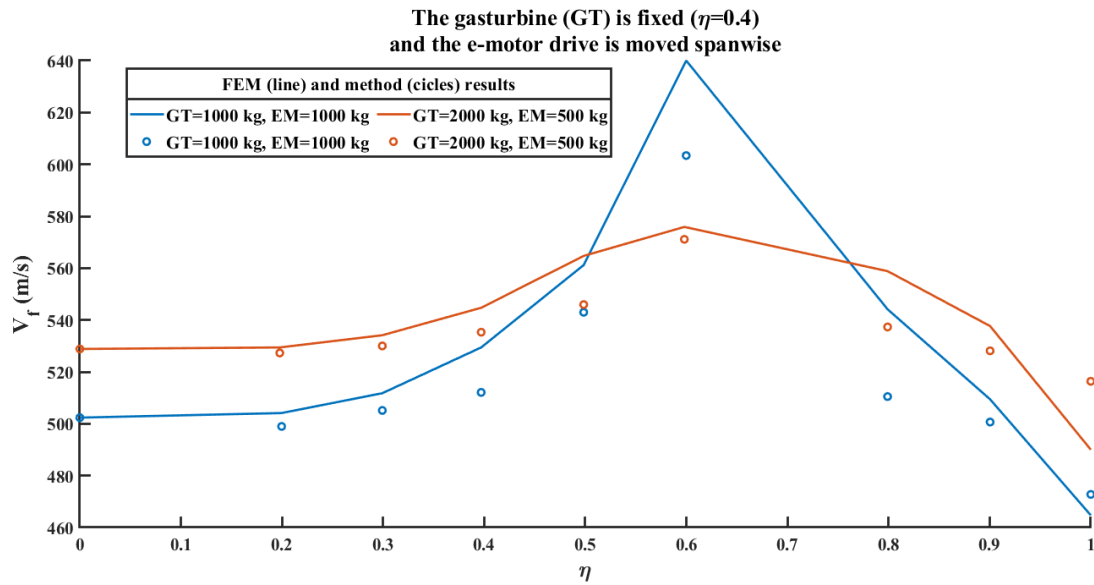


Figure 2.52: Variation of the flutter speed calculated through finite element method and semi-empirical approach.

inertial relief. Due to the complexity of the different components, a statistical approach appears necessary at this stage of the design chain. The semi-empirical equations proposed in Ref. [61] seem to be well suited for the estimation of the secondary mass contribution when the necessary details are available.

When the designer approaches his desk with the will of designing innovative aircraft, he will suffer the lack of methods.

— Salvatore Corcione

3

Point Performance of the Aircraft

Contents

3.1	Introduction	148
3.2	Performance and Regulation Constraints	153
3.2.1	Take-Off Constraints (FAR-23 or CS-23)	153
3.2.2	Take-Off Constraints (FAR-25 or CS-25)	154
3.2.3	Take-Off Constraints: alternative method	156
3.2.4	Landing Constraints (FAR-23 or CS-23)	158
3.2.5	Landing Constraints (FAR-25 or CS-25)	159
3.2.6	Landing Constraints: alternative method	161
3.2.7	Climb Constraints (FAR-23 or CS-23)	164
3.2.8	Climb Constraints (FAR-25 or CS-25)	167
3.2.9	Cruise Constraints	173
3.3	Preliminary Weight Assessment	174
3.4	Validation and Sensitivity Analysis	178
3.4.1	FAR-23 or CS-23	181
3.4.2	FAR-25 or CS-25	191

3.1 Introduction

Aircraft **Sizing** is a preliminary activity necessary to estimate the point performance in terms of power loading and wing loading to be compliant with Top Level Aircraft Requirements (TLAR) and certifications requirements. Led by the estimated wing loading and power loading the preliminary sizing ends with a

preliminary estimation of masses and geometries. The present work moves from the consideration that the market opportunities are diversifying by the introduction of innovative concepts and hybrid-electric propulsive systems, thus, it cannot prescind from the objective to take into account the different impacts of these technologies on the design space in a simple and loose way. In particular, since the sizing activity defines the boundaries of the design space, the introduction of the aero-propulsive effects (e.g.: distributed electric propulsion or tip-mounted propellers) can enlarge the design space leading to new concepts (as proposed in Ref. [41,67,161,162]).

When approaching this activity outlining a new design procedure, it is necessary to measure the outcomes with respect to methods already commonly used [41,64].

Two differences can be underlined among referenced methods:

- The **power loading** at which the sizing procedure refers can be the propulsive power loading or the installed power loading depending on the sizing methods considered. In the present work, the power loading ($\frac{W}{P}$) considered will be the propulsive power loading.
- Method proposed in Ref. [64] does not take into account for the **aero-propulsive interactions** between propeller slipstream, which has a high impact on the design space when the distributed electric propulsion is integrated [41].

The sizing activity presented in the following sections can be applied to both hybrid-electric, full-electric, turbo-electric, and conventional aircraft employing or not distributed electric propulsion, boundary layer ingestion, and/or tip-mounted propellers. For the present case, the method will be presented considering distributed electric propulsion and tip-mounted propellers interacting with the airframe. In the most general case, the aero-propulsive effects depend on the geometry of the propulsive system, which is described by dimensionless parameters at this level of the design process, on the wing loading and the propulsive power loading or the thrust to weight ratio. It is noted that referring to propulsive power loading, this method is applicable even at aircraft propelled by turbofan or turbojet engines when classical methods prefer the estimation of the thrust to weight ratio. In

order to define the design space, the sizing activity integrates the top-level aircraft requirements and the regulation constraints to delimit the sizing curves of the sizing plot. In the end, the sizing point of the aircraft, which is a combination of wing loading and power loading within the design space, is chosen.

When propulsive power loading and wing loading are estimated, the geometry of the aircraft and the aerodynamic characteristics are refined to be compliant with the design requirements and parameters. The present work moves from a simple geometry of the aircraft based on statistical data collected by the University of Naples "Federico II" and semi-empirical laws publicly available in literature. The preliminary geometry is defined in a specific workflow called **Pre-Design** in the present work. However, since the geometry of the aircraft can be defined and modified freely at this level by the designer without affecting in a significant way the point performance, the Pre-Design is not discussed in the present work. The attention of the author has been focused on the development of a precise method to evaluate the masses of the macro-components of the aircraft system, integrating methods available in literature with considerations focused on innovative propulsive systems and configurations. The dependence of the aero-propulsive interaction from the characteristics of both the lifting surface and the propulsive system leads to a way of thinking about the sizing activity as an iterative process of nested loops (Figure 3.1). The percentage of wing area covered by distributed propellers and the characteristics of the propulsive system, for example, can be considered a design parameter chosen by the designer, however, after a preliminary sizing, when the point performance is determined and the weights are estimated, the aero-propulsive interaction considered during the estimation of the point performance can be refined considering the new propeller efficiencies. Thus, more iterations of the workflow proposed are required in order to obtain a reliable result.

The design of a flying machine is strictly dependent on the regulations on which it must be certified to be operative. Airworthiness codes are constantly updated, and they must be able to merge technological improvements with an increasing level of safety. Researchers push towards disruptive concepts in aircraft design,

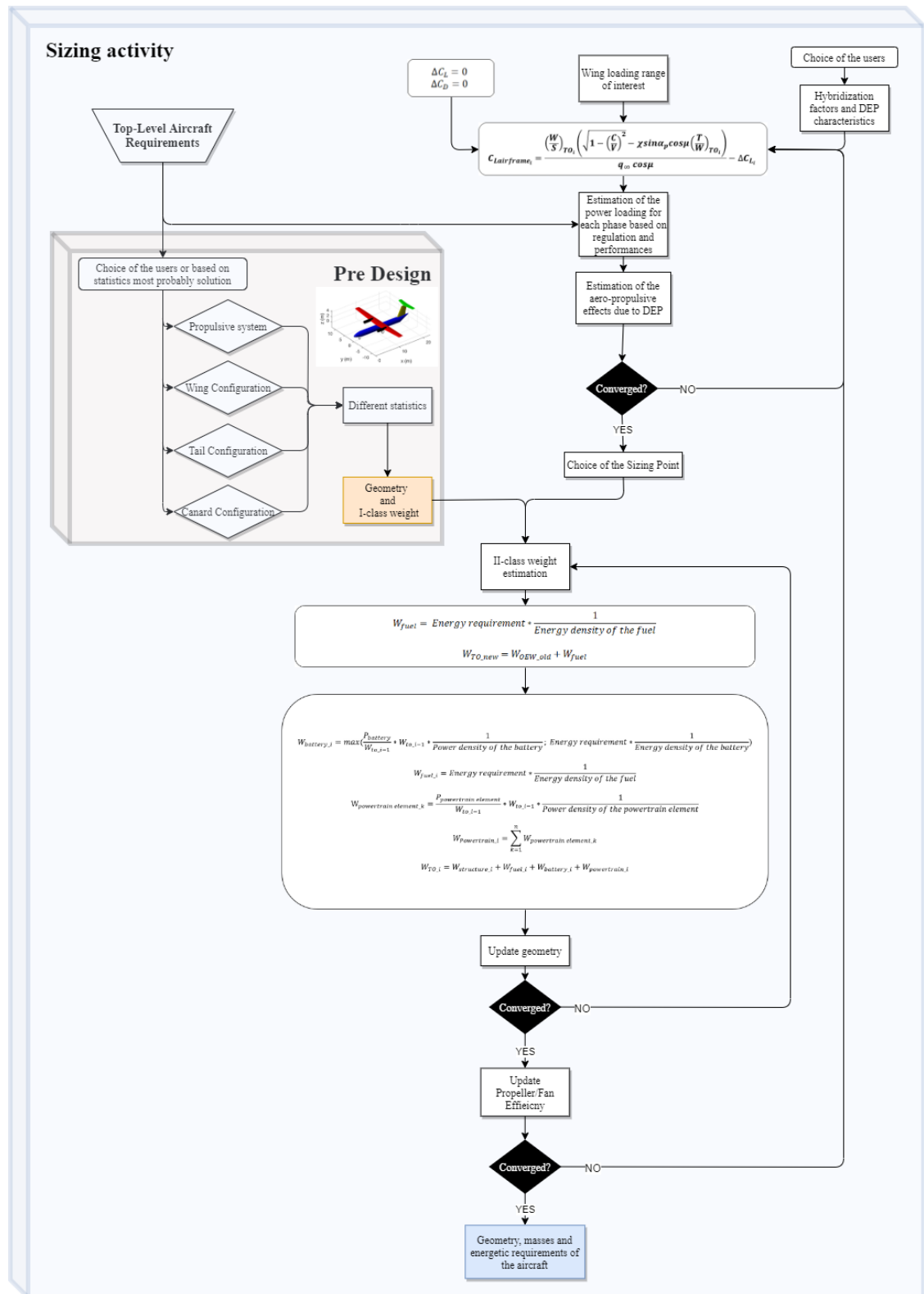


Figure 3.1: Conceptual Design process as proposed by the author and integrated in the design tool HEAD.

which must be compliant with current regulations. On the other side, the aviation safety agencies draw ideas from such unconventional configurations, amending and making modifications to existing codes. Transport aircraft are mainly regulated by Part 23 [19], "Certification Specifications for Normal, Utility, Aerobatic, and Commuter Category Aeroplanes", and Part 25 [20] "Certification Specifications for Large Aeroplanes". According to Subpart A of CS-23 §23.1, Applicability, CS-23 airworthiness code is applicable to "(1) Aeroplanes in the normal, utility and aerobatic categories that have a seating configuration, excluding the pilot seat(s), of nine or fewer and a maximum certificated take-off weight of 5670 kg (12500 lb) or less; and (2) Propeller-driven twin-engined aeroplanes in the commuter category that have a seating configuration, excluding the pilot seat(s), of nineteen or fewer and a maximum certificated take-off weight of 8618 kg (19000 lb)". The CS-25 §25.1 states "this Airworthiness Code is applicable to turbine powered Large Aeroplanes" and it is applicable for a generic weight and aircraft size. FAR are perfectly equivalent to CS.

In the next sections of this chapter, the point performance is investigated considering the equations proposed in 3.2 and integrating the aero-propulsive effects estimated as discussed in 2.2. The applications of the design process are shown in 3.4 considering the weight estimation process proposed in 2.4.

3.2 Performance and Regulation Constraints

The evaluation of point performance is aimed to define the boundaries of the design space in terms of possible wing loading and power loading. It ends with the choice by the designer of the *sizing point*, that is the couple of wing loading and propulsive power loading of the aircraft. In order to make this choice compliant with the prescribed TLAR and certification requirements, constraints relationships are defined among the two parameters describing the sizing point. These constraints, whose graphic presentations are called *constraints curves*, are then coupled to bound the area of the *sizing plot*, also called *constraints plot*, where the designer can choose the sizing point, that is the design space.

3.2.1 Take-Off Constraints (FAR-23 or CS-23)

The take-off constraints in case of *FAR-23* (or *CS-23*) certified aircraft can be related to take-off ground length. In fact, a statistical correlation links the take-off parameter for *FAR-23* (or *CS-23*) certified aircraft to the ground length.

$$S_{TO_{ground}} = 4.9 TOP_{23} + 0.009 TOP_{23}^2 \quad (3.1)$$

The ground length can be estimated through a semi-empirical law based on the total take-off length, which is commonly assigned as top-level aircraft requirement (or, alternatively, when the take-off field length S_{TOFL} is assigned, $S_{TO} = S_{TOFL}/1.15$):

$$S_{TO_{ground}} = \frac{S_{TO}}{1.66} \quad (3.2)$$

By definition, the take-off *FAR-23* (or *CS-23*) parameter is related to wing loading and propulsive power loading, as shown in Eq. (3.3), where η_{pTO} is the propeller aerodynamic efficiency at take-off and σ is the relative density ratio.

$$TOP_{23} = \frac{(\frac{W}{S})_{TO} (\frac{W}{P})_{TO}}{\eta_{pTO} \sigma C_{L_{max_{to}}}} \quad (3.3)$$

From Eq. (3.3), it is possible to define a correlation between wing loading and power loading.

The lift coefficient at take-off is fixed by the designer as design objective, but

it does not consider the aero-propulsive effect. Thus, an appropriate form of Eq. (3.3) is the following one.

$$\left(\frac{W}{P}\right)_{TO} = \frac{TOP_{23} \sigma (C_{L_{max_{to}}} + \Delta C_L)}{\left(\frac{W}{S}\right)_{TO} \eta_{pTO}} \quad (3.4)$$

The estimation of ΔC_L , which is the increase due to aero-propulsive interactions, requires an iterative approach whose first attempt is $\Delta C_L = 0$.

The iterative estimation of the take-off sizing constraint is described for an arbitrary value of the wing loading, but the same process has to be repeated point by point. Firstly, a certain range of interest for the independent variable, the wing loading, is chosen. Considering a certain value of wing loading, the corresponding propulsive power loading is estimated through Eq. (3.4). From these power loading and wing loading, the increment in lift coefficient is estimated. The new lift coefficient estimated, which is a sum of the airframe lift coefficient and the Δ term, leads to a new value of propulsive power loading for the same wing loading. Thus, it will be necessary to estimate the ΔC_L for the case of this new propulsive power loading. The final value of propulsive power will be reached when the process converges on a ΔC_L with a certain accuracy.

3.2.2 Take-Off Constraints (FAR-25 or CS-25)

The take-off certification requirement of a *FAR-25* or *CS-25* certified conventional aircraft is related to the choice of take-off field length, S_{TOFL} , one of the top-level aircraft requirements. The choice of S_{TOFL} cannot prescind an appropriate take-off maximum lift coefficient, $C_{L_{max_{to}}}$. Classical methods assure the compliance with the take-off distance constraint is achieved through the statistical correlation between S_{TOFL} to the take-off parameter for *FAR-25* or *CS-25* certified aircraft (TOP_{25}):

$$S_{TOFL} = 37.5 TOP_{25} \quad (3.5)$$

The correlation between TOP_{25} and S_{TOFL} requires the dimensions of these two parameters to be lb/ft and ft respectively. By definition, TOP_{25} can be defined as follows:

$$TOP_{25} = \frac{(\frac{W}{S})_{TO}}{\sigma C_{L_{max_{to}}} (\frac{T}{W})_{TO}} \quad (3.6)$$

Where σ is the relative density ratio. The statistical correlation between installed power and thrust is a simple proportion: $T = 2.8P$. However, differently from classical methods, it is here necessary a correlation with the propulsive power:

$$T = 2.8 \eta_{p_{TO}} P \quad (3.7)$$

Combining Eqs. (3.6), (3.5) and (3.7) the following relation between wing loading and propulsive power loading is obtained:

$$(\frac{W}{P})_{TO} = \frac{2.8 \eta_{p_{TO}} \sigma C_{L_{max_{to}}} S_{TOFL}}{37.5 (\frac{W}{S})_{TO}} \quad (3.8)$$

The lift coefficient considered up to now does not take into account for the aero-propulsive interactions. Thus, it is better to substitute $C_{L_{max_{to}}}$ in the previous equations with $C_{L_{max_{to}}} + \Delta C_L$. The determination of ΔC_L requires an iterative approach whose first attempt is $\Delta C_L = 0$.

Firstly, a certain range of interest for the independent variable, the wing loading, is chosen. The iterative estimation of the take-off sizing constraint when aero-propulsive interaction will be described for an arbitrary value of the wing loading, but the same process has to be repeated point by point. Considering a certain value of wing loading, the corresponding propulsive power loading is estimated through Eq. (3.8). From these power loading and wing loading, it is possible to estimate the increment in lift coefficient related to the aero-propulsive effects. The new lift coefficient estimated, which is a sum of the previous lift coefficient and the Δ term, leads to a new value of propulsive power loading for the same wing loading. Thus, it will be necessary to estimate again the ΔC_L for the case of this new propulsive power loading. The final value of propulsive power will be reached when the process

converges on a ΔC_L with a certain accuracy. In case of distributed propulsion, a suitable model is presented in Ref. [42], for tip-mounted propellers, Ref. [70] provides the necessary guidelines to model the effect, while in case of boundary layer ingestion, a design method is presented in Ref. [163].

3.2.3 Take-Off Constraints: alternative method

When approaching the sizing activity of the design process, the major limit is the statistics linking the TLARs to the aircraft performance. In particular, this is a problem emerging in case of take-off and landing phases, where the distances and the speed are related through statistical relationships based on conventional aircraft and that cannot be safely applied to modern aircraft or hybrid-electric concepts. In case of take-off phase, the take-off parameter (TOP_{23} or TOP_{25}), which is based on a statistical law, plays a major role in the sizing curve. To avoid the introduction of this parameter based on statistics, an alternative procedure is suggested in the present paragraph. Firstly the relationship between the take-off field length and the take-off distance is introduced (Ref. [138]).

$$S_{TOFL} = 1.15 S_{TO} \quad (3.9)$$

The value of the take-off distance, calculated from the take-off field length, can be used to relate the required thrust to weight ratio and wing loading. The take-off distance, S_{TO} , can be related to the ground distance, $S_{TO_{ground}} = S_{TO}/1.66$, however, since the main objective is to avoid any statics or semi-empirical law, a different approach is suggested to calculate the take-off ground distance. Firstly, it is necessary to calculate the airborne distance, $S_{TO_{air}}$, which depends on the stall speed at take-off that can be assigned as TLAR or calculated from the assigned value of maximum lift coefficient at take-off. Independently from the method chosen to calculate the stall speed, the airborne distance can be calculated as follows in Eq. (3.10).

$$S_{TO_{air}} = R \sin(\gamma) \quad (3.10)$$

Where the radius of the pull-up manoeuvre can be calculated from the stall speed, as in Eq. (3.11).

$$R = \frac{(1.15 V_{stall})^2}{g \cdot 0.19} \quad (3.11)$$

The angle covered by the airborne phase can be obtained as in Eq. (3.12), where h is 35 ft in case of FAR-25 certified aircraft and 50 ft in case of FAR-23 certified aircraft.

$$\gamma = \arccos\left(1 - \frac{h}{R}\right) \quad (3.12)$$

Since the take-off run is a sum of the airborne distance and the ground distance, as shown in Fig. 3.2, the obtained value of the airborne distance is used to calculate the ground run and included in the following relationship linking the thrust to weight ratio to the wing loading.

$$\left(\frac{T}{W}\right)_{TO} = \left(\frac{W}{S}\right)_{TO} \frac{1.21}{S_{TO_{ground}} \rho g (C_{L_{max_{to}}} + \Delta C_L)}; \quad (3.13)$$

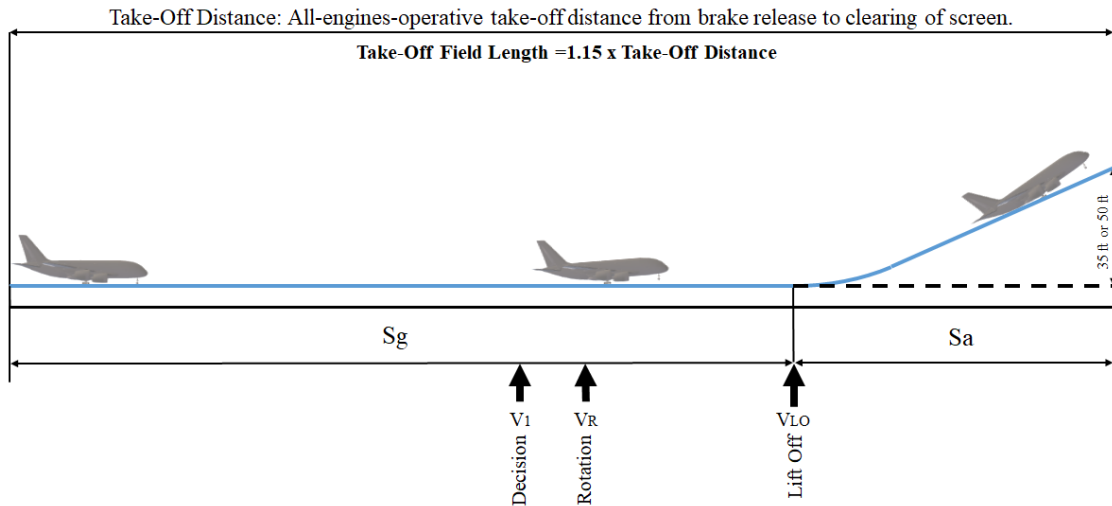


Figure 3.2: Take-off distance breakdown, Ref. [138].

3.2.4 Landing Constraints (FAR-23 or CS-23)

In case of *FAR-23* or *CS-23* certified conventional aircraft, constraints deals with the S_{LANDFL} and, at the same time, the required $C_{L_{max_{land}}}$. Statistical correlations link the landing distance S_{LAND} , related to the landing field length by $S_{LAND} = 0.6 S_{LANDFL}$, with the ground distance and this last one with the stall speed.

$$S_{ground} = \frac{S_{LAND}}{1.938} \quad (3.14)$$

$$S_{ground} = 0.265 V_s^2 \quad (3.15)$$

Combining Eqs. (3.14) and (3.15), as well as the definition of the stall speed, the landing limit for the wing loading is obtained.

$$\left(\frac{W}{S}\right)_{LAND} = \frac{S_{LANDFL} \rho C_{L_{max_{land}}}}{0.265 \cdot 1.938 \cdot 2} \quad (3.16)$$

Since the design space is usually referred to the maximum take-off weight, the sizing plot curve for the landing constraint will take into account the ratio of the landing weight with respect to the take-off weight.

$$\left(\frac{W}{S}\right)_{TO} = \frac{S_{LANDFL} \rho C_{L_{max_{land}}}}{0.265 \cdot 1.938 \cdot 2 \frac{W_{LAND}}{W_{TO}}} \quad (3.17)$$

Considering the influence of aero-propulsive interaction on the lift coefficient, in case of positive ΔC_L , the design space will be enlarged because of the maximum wing loading increment for landing. Since the landing constraint does not couple the wing loading and the power loading, to estimate the power loading necessary to aero-propulsive mathematical models, the equilibrium condition along x-axis and z-axis with respect to the wind reference frame (Fig. 3.3) is estimated. The thrust to weight ratio and thus, the power loading, is estimated by Eq. (3.18), where at the first step the contributions to lift and drag due to aero-propulsive interactions are null, e is the Oswald factor, AR is the aspect ratio, χ is the percentage of thrust provided by the propulsive system generating aero-propulsive

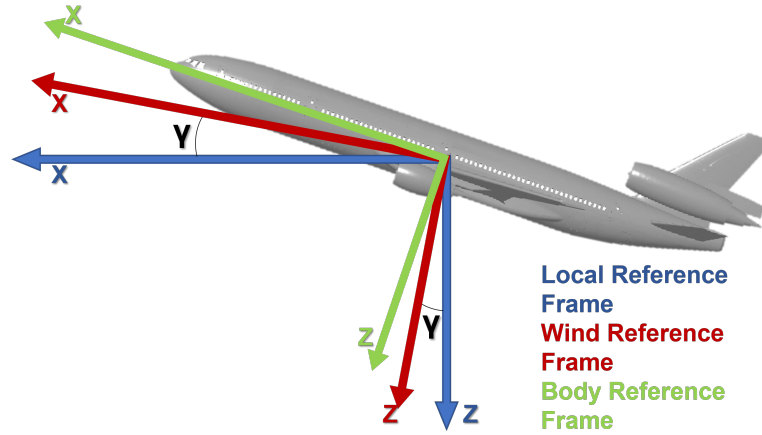


Figure 3.3: x-axis and z-axis in different reference frames.

interactions with the airframe, α_p is the angle of attack of the same propulsive system and g is the gravitational acceleration.

$$\left(\frac{T}{W}\right)_{TO} = \frac{1}{1 - \chi (1 - \cos(\alpha_p))} \left[\frac{q_\infty}{(W/S)_{TO}} (C_{D_{0_{land}}} + \Delta C_{D_0} + \frac{C_{L_{max_{land}}}^2}{\pi AR e} + \Delta C_{D_i}) + \frac{c}{V_A} + \frac{1}{g} \frac{dV}{dt} \right] \quad (3.18)$$

From this thrust to weight ratio and the corresponding wing loading, the aerodynamic contribution in terms of ΔC_L is estimated. This will drive a new estimation of the required wing loading and from the new value of wing loading the iterative process will restart.

3.2.5 Landing Constraints (FAR-25 or CS-25)

The landing requirement of a *FAR-25* or *CS-25* certified conventional aircraft is related to the choice of the landing field length, S_{LANDFL} . At the same time, the requirement in terms of landing field length should be compliant with the maximum lift coefficient in that phase, $C_{L_{max_{land}}}$, and, thus, to the associated stall speed.

A statistical correlation links the landing field length to the square value of the approach speed, V_A^2 , when the first is measured in *ft* and the second one is measured in *kts*. Since the approach speed is related to the stall speed, $V_A = 1.3V_s$, the

correlation can be expressed in terms of stall speed (V_s).

$$S_{LANDFL} = 0.3 \cdot 1.3^2 V_s^2 \quad (3.19)$$

The dependency of the stall speed on the wing loading can be used to estimate the wing loading necessary to be compliant with the landing requirements described by Eq. (3.19). The result is the following equation:

$$\left(\frac{W}{S}\right)_{LAND} = \frac{S_{LANDFL} \rho C_{L_{max_{land}}}}{0.3 \cdot 1.3^2 \cdot 2} \quad (3.20)$$

However, since the design space is usually referred to the maximum take-off weight, a further modification is required to introduce the ratio between the landing weight and the take-off weight:

$$\left(\frac{W}{S}\right)_{TO} = \frac{S_{LANDFL} \rho C_{L_{max_{land}}}}{0.3 \cdot 1.3^2 \cdot 2 \frac{W_{LAND}}{W_{TO}}} \quad (3.21)$$

The lift coefficient presented so far does not take into account the aero-propulsive interaction. In order to consider the increase due to the aero-propulsive interaction between the airframe and the propulsive system inflow and/or slipstream, it is necessary to formulate the lift coefficient as the sum of two components: the airframe contribution and the increase due to aero-propulsive effects.

Differently from the take-off constraint, in case of landing, there is no coupling between propulsive power loading and wing loading. Thus, it is necessary to impose the equilibrium condition along x-axis and z-axis with respect to the wind reference frame (Fig. 3.3). The wing loading estimated by Eq. (3.21), where ΔC_L is imposed equal to zero, is used to estimate the thrust to weight ratio by Eq. (3.22), where at the first step lift and drag contributions due to aero-propulsive interactions are neglected, e is the Oswald factor, AR is the aspect ratio, χ is the percentage of thrust provided by the propulsive system generating aero-propulsive interactions with the airframe, α_p is the angle of attack of the same propulsive system and

g is the gravitational acceleration.

$$\left(\frac{T}{W}\right)_{TO} = \frac{1}{1 - \chi (1 - \cos(\alpha_p))} \left[\frac{q_\infty}{(W/S)_{TO}} (C_{D_{0_{land}}} + \Delta C_{D_0} + \frac{C_{L_{max_{land}}}^2}{\pi AR e} + \Delta C_{D_i}) + \frac{c}{V_A} + \frac{1}{g} \frac{dV}{dt} \right] \quad (3.22)$$

The value of the increase in lift coefficient is used to estimate the new wing loading associated.

$$\left(\frac{W}{S}\right)_{TO} = \frac{S_{LANDFL} \rho (C_{L_{max_{land}}} + \Delta C_L)}{0.3 \cdot 1.3^2 \cdot 2 \frac{W_{LAND}}{W_{TO}}} \quad (3.23)$$

Moving from the new wing loading a different thrust to weight ratio will be estimated and, thus, a new ΔC_L . The same calculation is iteratively made until the convergence criterion on ΔC_L is reached.

3.2.6 Landing Constraints: alternative method

As stated in case of take-off, the landing phase is generally considered during the sizing activity from a statistical point of view relating the landing distance to the aircraft performance. However, in case of hybrid-electric and modern concepts, this approach is not reliable. Moreover, the classical sizing methods are focused on the approach phase and generally relate the wing loading to any value of the thrust to weight ratio of the sizing plot for that particular phase. Considering that the approach angle and the flare angle strongly depend on the thrust to weight ratio, this cannot be considered a valid approach.

The landing distance assigned as top-level requirement in case of FAR-25 (or CS-25) aircraft is the landing field length, generally related to the actual landing distance by the simple semi-empirical law expressed in Eq. (3.24).

$$S_{LAND} = 0.6 S_{LANDFL} \quad (3.24)$$

The landing distance can be decomposed in two different phases, the airborne phase and the ground run, as shown in Fig. 3.4. In particular, the airborne phase can be

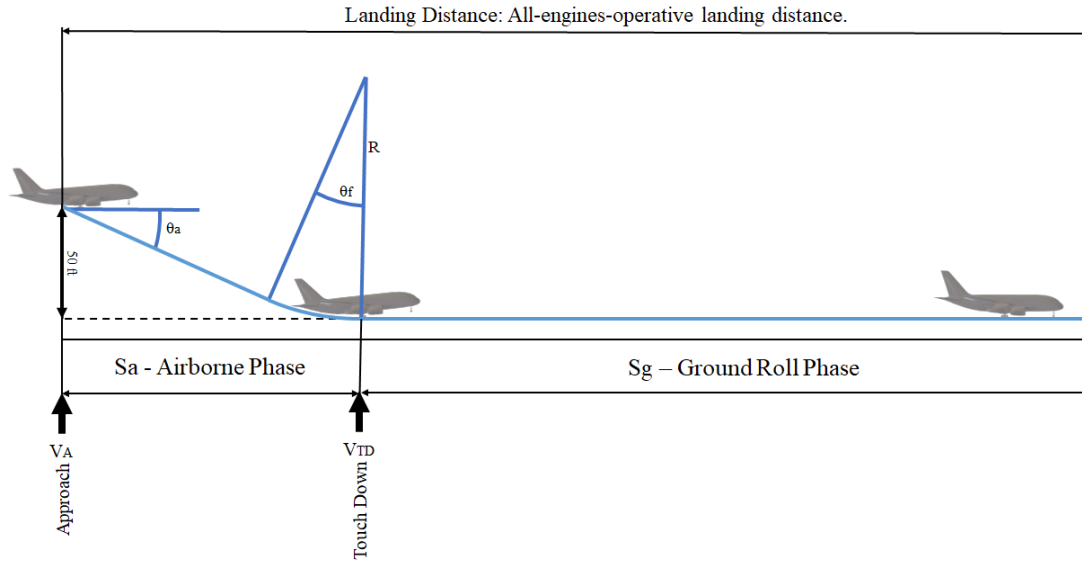


Figure 3.4: Landing distance breakdown, Ref. [138].

further divided into two different manoeuvre: approach and flare. Considering the fact that the sizing plot moves from a value of the power loading equal to zero, this would mean to have an infinite thrust or a null value of the weight resulting in an approach angle making the landing impossible, as calculated from Eq. (3.25).

$$\theta_a = \arcsin\left(\frac{D}{L} - \frac{T}{W}\right) \quad (3.25)$$

To avoid this problem, a different approach is suggested taking into account the typical relationship between the total field length and the ground length.

$$S_{LAND} = 1.938 S_{LAND_{ground}} \quad (3.26)$$

Moving from the estimated value of the ground run, the value of the necessary wing loading can be estimated. Actually, if the percentage of reverse thrust with respect to take-off thrust is known, it could be possible to estimate the wing loading related to each value of the power loading of the sizing plot. However, it is here suggested to be conservative to consider a null value of reverse thrust. This assumption will avoid also a wrong assumption in those cases where the distributed electric propulsion is employed to increase the lift and drag coefficients. In fact, since no experience has been matured on these concepts, a safe assumption would consider

the case of total net thrust equal to zero. In this case, considering the simplified relation between the ground distance and the wing loading expressed in Eq. (3.27), the resulting value of wing loading can be calculated as in Eq. (3.28), where μ_g is the brake friction, the subscript TD is used to indicate the *Touch Down* condition and the subscript g is used to indicate the ground roll attitude.

$$S_{LAND_{ground}} = 1.5^2 \frac{W}{S} \frac{1}{g \rho C_{L_{max_{land}}} [D/W + \mu_g (1 - L/W)]_{0.7V_{TD}}} \quad (3.27)$$

$$\begin{aligned} \left(\frac{W}{S}\right)_{TO} = & \frac{1}{2} \frac{W_{TO}}{W_{LAND}} \frac{\mu_g (C_{L_{max_{land}}} + \Delta C_L) g \rho S_{LAND_{ground}}}{1.5^2} + \\ & + \sqrt{\left(\frac{\mu_g (C_{L_{max_{land}}} + \Delta C_L) g \rho S_{LAND_{ground}}}{1.5^2}\right)^2 +} \\ & + \sqrt{4 \left(\frac{S_{LAND_{ground}}}{1.5^2} \rho g \frac{1}{2} \rho (0.7V_{TD})^2 (C_{D_g} + \mu_g C_{L_g})\right)} \end{aligned} \quad (3.28)$$

This wing loading should be considered as a limit value for the x-axis of the sizing plot, in fact, neglecting the reverse thrust and the aero-propulsive interactions, the ground run only depends on the wing loading without any relationship with the required power loading. When the aero-propulsive interactions are taken into account, the value of the aerodynamic Δ must be calculated for each value of the power loading in the sizing plot and an iterative approach is necessary to estimate the corresponding value of wing loading.

3.2.7 Climb Constraints (FAR-23 or CS-23)

The constraints commonly addressed as *climb phase constraints* are generally referred to flight phases immediately after the take-off phase or before the touch down of the landing phase. Regulation constraints dealing with altitude, landing gear configuration, number of operative engines, climb gradient or rate of climb and operating speed are coupled to give a set of limiting conditions. *FAR-23* (or *CS-23*) certified aircraft are compliant with a set of constraints which can be summarized in four different flight conditions, as reported in Table 3.1. It is here highlighted that in *one engine inoperative* condition, classical methods suggest to scale the propulsive power by a factor which is the ratio between the number of engines minus one and the total number of thermal engines. However, in case of distributed propellers or when the electric drives are powered by a unique power line, the definition of this factor is not univocally defined. In the present case, it is suggested to define the OEI_{factor} depending on the propulsive system chosen and the power line architecture (for example, basing the choice on the redundancies which are a major factor of risk for this category).

The four different flying conditions are described on the sizing plot by four different constraint curves. Since wing loading and power loading can be related to the **rate of climb parameter (RCP)**, the certification limits on the rate of climb are converted to rate of climb parameter constraints: $RCP = RC / 33000$. through The first constraint curve, dealing with *FAR-23* §23.65 condition, is described by Eq. (3.29), Eq. (3.30), and Eq. (3.31), where ΔC_{D_0} , ΔC_{D_i} and ΔC_L are the effects on aerodynamic coefficients due to aero-propulsive interactions.

$$C_{L_{climb\ 1}} = C_{L_{max_{to}}} + \Delta C_L \quad (3.29)$$

$$C_{D_{climb\ 1}} = C_{D_0} + \frac{C_{L_{max_{to}}}^2}{\pi AR e} + \Delta C_{D_0} + \Delta C_{D_i} + \Delta C_{D_{0_{flap}}} \quad (3.30)$$

FAR 23	Description
§23.65	<ol style="list-style-type: none"> 1. <i>Rate of climb</i> ≥ 300 ft/min 2. All engine operative (AEO) 3. Landing gears retracted 4. High-lift devices in take-off condition 5. Maximum thrust or power continuous 6. Sea level
§23.65	<ol style="list-style-type: none"> 1. <i>Climb Gradient</i> $\geq 1/12$ rad 2. All engine operative (AEO) 3. Landing gears retracted 4. High-lift devices in take-off condition 5. Maximum thrust or power continuous 6. Sea level
§23.67	<ol style="list-style-type: none"> 1. <i>Rate of climb</i> $\geq 0.027 V_{stall}$ ft/min 2. One engine inoperative (OEI) 3. Landing gears retracted 4. High-lift devices at their best condition 5. Maximum take-off thrust or power 6. 5000 ft of altitude
§23.77	<ol style="list-style-type: none"> 1. <i>Climb Gradient</i> $\geq 1/12$ rad 2. All engine operative (AEO) 3. Landing gears extended 4. High-lift devices in landing condition 5. Maximum take-off thrust or power 6. Sea level

Table 3.1: Constraints about climb phase - *FAR-23* (or *CS-23*)

$$\left(\frac{W}{P}\right)_{TO} = \frac{1}{RCP(\text{climb } 1) + \frac{(W/S)_{TO}^{1/2}}{19 \frac{C_{L_{climb 1}}}{C_{D_{climb 1}}} \sigma^{1/2}}} \frac{P_{max}}{P_{TO}} \quad (3.31)$$

As for the case of the take-off constraint curve, the iterative process moves from a null value of the " Δ terms", then, from the estimated power loading and the chosen wing loading, the associated aero-propulsive effects are estimated.

The second flight condition described in Table 3.1 leads to the following system of equations.

$$C_{L_{climb 2}} = C_{L_{max_{to}}} + \Delta C_L \quad (3.32)$$

$$C_{D_{climb\ 2}} = C_{D_0} + \frac{C_{L_{max_{to}}^2}{\pi AR e} + \Delta C_{D_0} + \Delta C_{D_i} + \Delta C_{D_{0_{flap}}} \quad (3.33)$$

$$\begin{aligned} \left(\frac{W}{P}\right)_{TO} = & \\ & 18.97 \frac{(C_{L_{climb\ 2}})^{0.5}}{CGR(climb\ 2) + C_{D_{climb\ 2}}/C_{L_{climb\ 2}}} \\ & \frac{1}{(W/S)_{TO}^{0.5}} \frac{P_{max}}{P_{TO}} \end{aligned} \quad (3.34)$$

The same consideration made for the iterative process dealing with Eq. (3.29), Eq. (3.30), and Eq. (3.31) can be applied for the present constraint.

The third flight condition is described by the following equations.

$$C_{L_{climb\ 3}} = C_{L_{max_{best}}} + \Delta C_L \quad (3.35)$$

$$\begin{aligned} C_{D_{climb\ 3}} = & \\ & C_{D_0} + \frac{C_{L_{max_{best}}^2}{\pi AR e} + \Delta C_{D_0} + \Delta C_{D_i} + \Delta C_{D_{0_{flap}}} + \\ & + \Delta C_{D_{0_{OEI}}} \end{aligned} \quad (3.36)$$

$$\left(\frac{W}{P}\right)_{TO} = OEI_{factor} \frac{1}{RCP(climb\ 3) + \frac{((\frac{W}{S})_{TO} \frac{W_{TO}}{W_{LAND_{OEI}}})^{1/2}}{\frac{C^{3/2}}{19} \frac{C_{L_{climb\ 3}}}{C_{D_{climb\ 3}}} \sigma^{1/2}}} \frac{P_{max}}{P_{TO}} \quad (3.37)$$

It is here remarked that as for the previous constraints, the same iterative process should be performed in case of Eq. (3.37).

The last limiting condition presented in Table 3.1 is described by Eq. (3.40).

$$C_{L_{climb\ 4}} = C_{L_{max_{to}}} + \Delta C_L \quad (3.38)$$

$$\begin{aligned}
C_{D_{climb\ 4}} = & \\
& C_{D_0} + \frac{C_{L_{max\ to}}^2}{\pi AR e} + \Delta C_{D_0} + \Delta C_{D_i} + \Delta C_{D_{0_{flap}}} + \\
& + \Delta C_{D_{0_{landing\ gears}}}
\end{aligned} \tag{3.39}$$

$$\begin{aligned}
\left(\frac{W}{P}\right)_{TO} = & \\
& 18.97 \frac{(C_{L_{climb\ 2}})^{0.5}}{CGR(climb\ 4) + C_{D_{climb\ 4}}/C_{L_{climb\ 4}}} \\
& \frac{1}{\left(\left(\frac{W}{S}\right)_{TO} \frac{W_{TO}}{W_{LANDAEO}}\right)^{0.5}} \frac{P_{max}}{P_{TO}}
\end{aligned} \tag{3.40}$$

The same iterative process applied to previous climb constraints is performed for the present one.

3.2.8 Climb Constraints (FAR-25 or CS-25)

The constraints addressed as *climb phase constraints* in classical sizing methods deal with flight phases immediately after take-off or before landing touch down. *FAR-25* or *CS-25* regulation constraints dealing with altitude, landing gear configuration, number of operative engines, climb gradient or rate of climb, and operating speed are coupled to give a set of limiting conditions (Table 3.2). Among the power requirements, the *one engine inoperative* condition is one of the sizing demands. For this condition, classical methods suggest reducing the propulsive power by a multiplying factor defined as the ratio between the number of engines minus one and the total number of thermal engines. In Ref. [23], it is suggested to consider the OEI condition as a matter of probability analysis of one or more engine failures. The probability of engine failure is based on statistical measures of failure per flight hour. Considering the number of possible engine failures (m), the probability of the m^{th} engine fault ($P^{m^{th}}$) and the total number of engines (N), the probability

of that condition (P_m) is defined as in Eq. (3.41). The first condition above the probability threshold defines the OEI condition.

$$P_m = P^{m^{th}} \binom{N}{m} \quad (3.41)$$

However, this is not applicable to any powertrain architecture (e.g.: turbo-electric concept where probability are not statistically independent). In general, it is suggested to define the OEI_{factor} depending on the propulsive system chosen and the power line architecture (for example, basing the choice on the redundancies).

FAR 25	Description	FAR 25	Description
§25.111	<p>1. <i>Climb gradient</i></p> <ul style="list-style-type: none"> • $\geq 0.012 \text{ rad}$ - twin engine • $\geq 0.015 \text{ rad}$ - three engines • $\geq 0.017 \text{ rad}$ - four or more engines <p>2. One engine inoperative (OEI))</p> <p>3. Landing gears retracted</p> <p>4. High-lift devices in take-off condition</p> <p>5. Maximum thrust or power continuous</p> <p>6. $V = 1.2 V_{stall_{TO}}$</p> <p>7. Sea level and ground effect</p>	§25.121	<p>1. <i>Climb gradient</i></p> <ul style="list-style-type: none"> • $\geq 0.000 \text{ rad}$ - twin engine • $\geq 0.003 \text{ rad}$ - three engines • $\geq 0.005 \text{ rad}$ - four or more engines <p>2. One engine inoperative (OEI))</p> <p>3. Landing gears extended</p> <p>4. High-lift devices in take-off condition</p> <p>5. Maximum thrust or power continuous</p> <p>6. $V_{lift-off} < V < 1.2 V_{stall_{TO}}$</p> <p>7. Sea level and ground effect</p>
§25.121	<p>1. <i>Climb gradient</i></p> <ul style="list-style-type: none"> • $\geq 0.024 \text{ rad}$ - twin engine • $\geq 0.027 \text{ rad}$ - three engines • $\geq 0.030 \text{ rad}$ - four or more engines <p>2. One engine inoperative (OEI))</p> <p>3. Landing gears retracted</p> <p>4. High-lift devices in take-off condition</p> <p>5. Maximum thrust or power continuous</p> <p>6. $V = 1.2 V_{stall_{TO}}$</p>	§25.121	<p>1. <i>Climb gradient</i></p> <ul style="list-style-type: none"> • $\geq 0.011 \text{ rad}$ - twin engine • $\geq 0.014 \text{ rad}$ - three engines • $\geq 0.016 \text{ rad}$ - four or more engines <p>2. One engine inoperative (OEI))</p> <p>3. Landing gears retracted</p> <p>4. High-lift devices retracted</p> <p>5. Maximum thrust or power continuous</p> <p>6. $V = 1.25 V_{stall_{clean}}$</p>
§25.119	<p>1. <i>Climb Gradient</i> $\geq 0.032 \text{ rad}$</p> <p>2. All engine operative (AEO)</p> <p>3. Landing gears extended</p> <p>4. High-lift devices in landing condition</p> <p>5. Maximum landing weight</p> <p>6. $V = 1.3 V_{stall_{LAND}}$</p>	§25.121	<p>1. <i>Climb gradient</i></p> <ul style="list-style-type: none"> • $\geq 0.021 \text{ rad}$ - twin engine • $\geq 0.024 \text{ rad}$ - three engines • $\geq 0.027 \text{ rad}$ - four or more engines <p>2. One engine inoperative (OEI))</p> <p>3. Landing gears extended</p> <p>4. High-lift devices in approach condition</p> <p>5. Maximum thrust or power continuous</p> <p>6. $V \leq 1.40 V_{stall_{approach}}$</p> <p>7. Maximum landing weight</p>

Table 3.2: Constraints about climb phase - FAR-25 or CS-25

In case of *FAR-25* or *CS-25* certified aircraft, an important role plays the climb limitation which is a limiting factor for the propulsive power loading, together with the take-off constraint. Six climb curves are defined on the sizing plot dealing with the six different limiting flight conditions in Table 3.2. The first flight phase is described by the system of equations composed by Eq. (3.42), Eq. (3.43), and Eq. (3.44), where $\frac{P_{50°F}}{P_{TO}}$ is the temperature correction which relates the maximum take-off power to the maximum take-off power in case of *hot and dry* weather conditions.

$$C_{L_{climb\ 1}} = C_{L_{max_{to}}}/1.20^2 + \Delta C_L \quad (3.42)$$

$$\begin{aligned} C_{D_{climb\ 1}} = & \\ & C_{D_0} + \frac{(C_{L_{max_{to}}}/1.2)^2}{\pi AR e} + \Delta C_{D_0} + \Delta C_{D_i} + \\ & + \Delta C_{D_{0_{flap}}} + \Delta C_{D_{0_{OEI}}} \end{aligned} \quad (3.43)$$

$$\left(\frac{W}{P}\right)_{TO} = \frac{\frac{P_{50°F}}{P_{TO}} OEI_{factor} 18.97 \sigma^{0.5} C_{L_{climb\ 1}}^{0.5}}{\left(\frac{W}{S}\right)_{TO}^{0.5} CGR(climb\ 1) + (C_{D_{climb\ 1}}/C_{L_{climb\ 1}})} \quad (3.44)$$

As for the following equations describing the other climb constraints, the first attempt of the iterative sizing process requires Δ terms describing the aero-propulsive effects to be equal to zero. Moving from the values of wing loading and power loading related by Eq. (3.44), after estimating the thrust to weight ratio, if necessary to the aero-propulsive interaction model, the variations of the aerodynamic coefficients are estimated. A new power loading is calculated after adding the estimated Δ terms to the aerodynamic coefficients, then the process moves to the next step. The same iterative process is followed for all the equations describing the flight condition in Tab. 3.2.

The remaining flight conditions in Tab. 3.2 are described by Eqs. (3.47), (3.50), (3.53), (3.56), and (3.59). For each condition, the aerodynamic coefficients can be calculated as reported in the associated equations.

$$C_{L_{climb\ 2}} = C_{L_{max_{to}}}/1.15^2 + \Delta C_L \quad (3.45)$$

$$\begin{aligned} C_{D_{climb\ 2}} = & \\ & C_{D_0} + \frac{(C_{L_{max_{to}}}/1.15)^2}{\pi AR e} + \Delta C_{D_0} + \Delta C_{D_i} + \\ & + \Delta C_{D_{D_0_{flap}}} + \Delta C_{D_{D_0_{OEI}}} + \Delta C_{D_{D_0_{landinggears}}} \end{aligned} \quad (3.46)$$

$$\left(\frac{W}{P}\right)_{TO} = \frac{\frac{P_{50\%F}}{P_{TO}} OEI_{factor} 18.97 \sigma^{0.5} C_{L_{climb\ 2}}^{0.5}}{\left(\frac{W}{S}\right)_{TO}^{0.5} CGR(climb\ 2) + (C_{D_{climb\ 2}}/C_{L_{climb\ 2}})} \quad (3.47)$$

$$C_{L_{climb\ 3}} = C_{L_{max_{to}}}/1.20^2 + \Delta C_L \quad (3.48)$$

$$\begin{aligned} C_{D_{climb\ 3}} = & \\ & C_{D_0} + \frac{(C_{L_{max_{to}}}/1.20)^2}{\pi AR e} + \Delta C_{D_0} + \Delta C_{D_i} + \\ & + \Delta C_{D_{D_0_{flap}}} + \Delta C_{D_{D_0_{OEI}}} \end{aligned} \quad (3.49)$$

$$\left(\frac{W}{P}\right)_{TO} = \frac{\frac{P_{50\%F}}{P_{TO}} OEI_{factor} 18.97 \sigma^{0.5} C_{L_{climb\ 3}}^{0.5}}{\left(\frac{W}{S}\right)_{TO}^{0.5} CGR(climb\ 3) + (C_{D_{climb\ 3}}/C_{L_{climb\ 3}})} \quad (3.50)$$

$$C_{L_{climb\ 4}} = C_{L_{max_{to}}}/1.25^2 + \Delta C_L \quad (3.51)$$

$$\begin{aligned} C_{D_{climb\ 4}} = & \\ & C_{D_0} + \frac{(C_{L_{max_{to}}}/1.25)^2}{\pi AR e} + \Delta C_{D_0} + \Delta C_{D_i} + \\ & + \Delta C_{D_{D_0_{OEI}}} \end{aligned} \quad (3.52)$$

$$\left(\frac{W}{P}\right)_{TO} = \frac{\frac{P_{50\%F}}{P_{TO}} OEI_{factor} 18.97 \sigma^{0.5} C_{L_{climb\ 4}}^{0.5}}{\left(\frac{W}{S}\right)_{TO}^{0.5} CGR(climb\ 4) + (C_{D_{climb\ 4}}/C_{L_{climb\ 4}})} \quad (3.53)$$

$$C_{L_{climb\ 5}} = C_{L_{max_{to}}}/1.25^2 + \Delta C_L \quad (3.54)$$

$$\begin{aligned} C_{D_{climb\ 5}} = & \\ & C_{D_0} + \frac{(C_{L_{max_{to}}}/1.25)^2}{\pi AR e} + \Delta C_{D_0} + \Delta C_{D_i} + \\ & + \Delta C_{D_{0_{flap}}} + \Delta C_{D_{0_{landinggears}}} \end{aligned} \quad (3.55)$$

$$\left(\frac{W}{P}\right)_{TO} = \frac{W_{TO}}{W_{Land}} \frac{\frac{P_{50\%F}}{P_{TO}} OEI_{factor} 18.97 \sigma^{0.5} C_{L_{climb\ 5}}^{0.5}}{\left(\frac{W}{S}\right)_{TO}^{0.5} CGR(climb\ 5) + (C_{D_{climb\ 5}}/C_{L_{climb\ 5}})} \quad (3.56)$$

$$C_{L_{climb\ 6}} = C_{L_{max_{to}}}/1.30^2 + \Delta C_L \quad (3.57)$$

$$\begin{aligned} C_{D_{climb\ 6}} = & \\ & C_{D_0} + \frac{(C_{L_{max_{to}}}/1.30)^2}{\pi AR e} + \Delta C_{D_0} + \Delta C_{D_i} + \\ & + \Delta C_{D_{0_{flap}}} + \Delta C_{D_{0_{OEI}}} + \Delta C_{D_{0_{landinggears}}} \end{aligned} \quad (3.58)$$

$$\left(\frac{W}{P}\right)_{TO} = \frac{W_{TO}}{W_{Land}} \frac{\frac{P_{50\%F}}{P_{TO}} OEI_{factor} 18.97 \sigma^{0.5} C_{L_{climb\ 6}}^{0.5}}{\left(\frac{W}{S}\right)_{TO}^{0.5} CGR(climb\ 5) + (C_{D_{climb\ 6}}/C_{L_{climb\ 6}})} \quad (3.59)$$

3.2.9 Cruise Constraints

The cruise condition limits are estimated by classical methods [64] based on the power index (I_p), which relates the installed power loading to the wing loading through Eq. (3.60).

$$I_p = \sqrt[3]{\frac{W/S}{\sigma W/P}} \quad (3.60)$$

In the present case, where the propulsive power loading is of interest, the relationship between power loading and wing loading is based on the equilibrium along the x-axis and the z-axis of the wind reference frame. For each wing loading considered on the sizing plot, the associated thrust to weight ratio related to the wing loading is defined by the equilibrium conditions presented in Eq. (3.61). In particular, the equilibrium along the z-axis defines the relationship between the required lift coefficient and the assigned wing loading, while the equilibrium condition along the x-axis relates the thrust to weight ratio to the lift coefficient.

$$C_L = \frac{(\frac{W}{S})_{TO} \frac{W_{cruise}}{W_{TO}}}{(1/2 \rho_{cruise} V_{cruise}^2)} - \Delta C_L \quad (3.61)$$

$$\left(\frac{T}{W}\right)_{cruise} = \frac{(C_{D_0} + \Delta C_{D_0} + \frac{C_L^2}{\pi AR e} + \Delta C_{D_i})}{C_L + \Delta C_L}$$

The process starts from a chosen wing loading and neglecting the aero-propulsive interactions. The aero-propulsive interaction depends on wing loading, propulsive power loading, and the characteristics of the propulsive system, depending on the theoretical model considered, thus, after a first estimation of the propulsive power loading, the variations of the aerodynamic coefficients are evaluated. Including the estimated Δ in Eq. (3.61), a new thrust to weight ratio is obtained. When the iterative process converges to a value of the aerodynamic increment of lift coefficient and drag coefficient, the propulsive power loading associated with the wing loading is obtained by Eq. (3.62), where eventual unit conversion multiplying factors are not reported.

$$\left(\frac{W}{P}\right)_{TO} = \frac{1}{\left(\frac{T}{W}\right)_{cruise}} \frac{1}{\frac{W_{cruise}}{W_{TO}}} \quad (3.62)$$

Actually, the same approach considered to evaluate cruise constraints can be considered for the climb, even if in this second case the equilibrium condition should take into account the regulation constraints on the climb gradient which is considered null in case of cruise. This approach requires a more general formulation of the equilibrium along the x and z axis, as expressed in Eq. (3.63), where ϕ is the bank angle and CGR is the climb gradient ratio.

$$\frac{T}{W} = \frac{\frac{q_\infty}{W/S} [C_{D_0} + \Delta C_{D_0} + \frac{C_L^2}{\pi e AR} + \Delta C_{D_i}] + CGR + \frac{1}{V} \frac{dV}{dt}}{1 + \chi (1 - \cos(\alpha_p))} \quad (3.63)$$

$$\frac{W}{S} = \frac{q_\infty \cos(\phi) [C_L + \Delta C_L]}{\sqrt{1 - CGR^2 - \chi \sin(\alpha_p) \cos(\phi)} \frac{T}{W}}$$

3.3 Preliminary Weight Assessment

The early stages of the design process lack a defined geometry and this would discourage the use of II class weight estimation or higher, making the success of low-fidelity methods based on statistics. This is the case of design methods for hybrid-electric aircraft proposed in literature which are based on preliminary information about wing loading and power loading from the sizing activity. In the present work, a different approach is suggested. In the end, the sizing activity provides point performance of the aircraft, while preliminary information about geometry and masses are obtained in classical methods after further and more detailed design steps. However, the sizing activity of hybrid-electric aircraft strongly depends on the hybridization factors (*shaft power ratio* and *supplied power ratio*), the aerodynamics requirements, the number of distributed propellers, and many others. Proceeding to higher design stages without a deep understanding of their influence on the chosen configuration would result in high severity risks at project level. For this reason, the sizing activity should be repeated on more platforms to chose the most performing compromise of hybridization factors and top-level requirements. The comparison requires a conventional starting point, defined by the designer or on statistics, which is modified based on the preliminary information at this level.

The sizing activity proposed in the present work is iterative and inside each loop, there are two additional iterative processes: the first one is the sizing plot

definition, described previously, and the second one is the weight estimation. Each aircraft starts from a preliminary geometry, defined statistically and based on the TLAR. Depending exclusively on TLAR, at the beginning of the sizing process, the same geometry is defined for both conventional and hybrid-electric platforms, starting from the same requirements. However, the different design space due to aero-propulsive interactions and the different weights of the propulsive systems drive the update of the geometry while keeping constant some parameters. At each step of the weight estimation loop, geometry is updated, while keeping constant the following parameters:

- the wing loading chosen;
- the wing aspect ratio;
- the volumetric ratio of the tailplanes;
- the percentage of wing covered by distributed propellers;
- the propeller diameter of the primary propulsive line.

The update of the geometry is necessary since the estimation of the weight, at equal wing loading, drives the change of the wing area. This, at constant aspect ratio, requires the update of the wingspan. In the end, keeping constant the percentage of wing covered by distributed propellers, the diameter of these will be different and, thus, a different propulsive efficiency is estimated. In alternative to the aspect ratio, wingspan and propellers diameters can be kept constant. The different propulsive efficiency (or the different chord length in case of constant wingspan) changes the magnitude of the aero-propulsive interactions making necessary more iterations of the whole sizing process.

The first step of the preliminary weight estimation starts from point performance defined at aircraft level. However, the power loading calculated refers to the maximum propulsive power in the most power-demanding flight condition. Since each flight phase is characterized by different power management conditions in terms of operating modes, efficiencies, and hybridization levels, the resulting sizing power of each element of the propulsive system is differently constrained. In other words, different flight phases can be sizing conditions for different powertrain elements.

Thus, the first step of the preliminary assessment is the estimation of the power requirements of each element of the powertrain. Two procedures can be considered for this. The first procedure apply the powertrain equations at each couple of wing loading and propulsive power loading from the sizing plot of the aircraft, to obtain the sizing plot of each element of the powertrain (Fig. 3.5). From the sizing plot

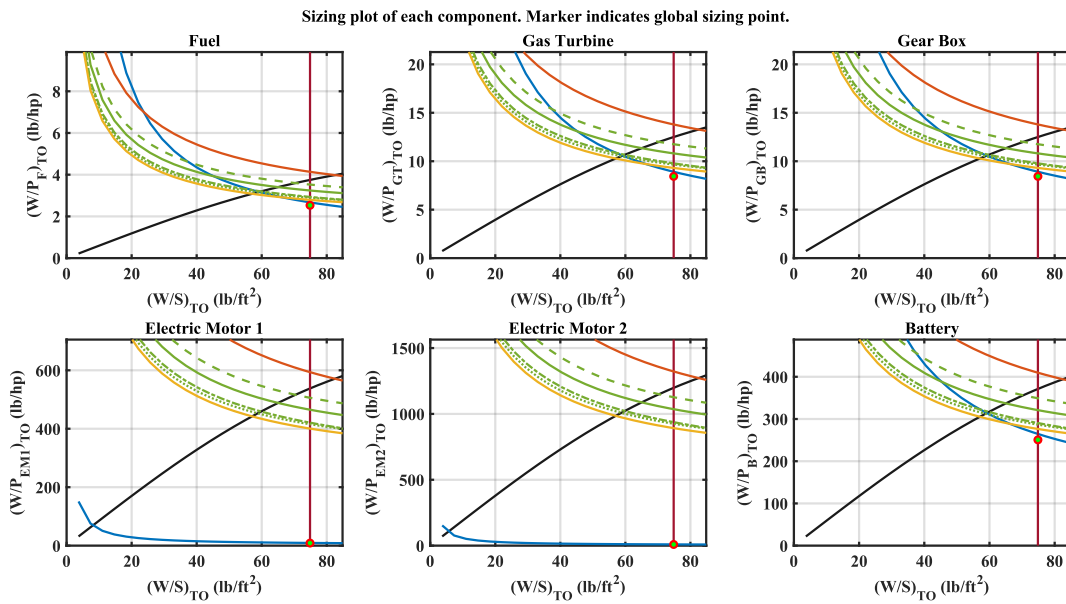


Figure 3.5: Sizing Plot of each component of the propulsive system.

obtained, the sizing points of each component of the propulsive system are fixed. The second procedure moves from the propulsive power loading associated with the sizing point. The inverse of this power loading is used to calculate the entering power of each component through Eq. (2.3) for each flight condition. The highest values obtained for each element along the flight mission are the sizing ones.

However, the estimation of the dimensioning power is only one of the requirements for the preliminary estimation of the masses. The second energetic requirement evaluated deals with the energy supplied by the power sources. The evaluation of the energy required to accomplish the mission profile is based on low fidelity methods, such as the Breguet equations [68]. In the present work, the thrust to weight ratio is calculated point by point of the flight path through Eqs. 3.63. The corresponding power loading at aircraft level for each flight phase is calculated by

multiplying the thrust to weight ratio by the speed corresponding to that flight segment. From the resulting propulsive power loading and Eq. (2.3), the power loadings of e-storage and fuel are estimated. Integrating in time, the corresponding energy divided by the max take-off weight is obtained for each step of the mission profile. The sum of these values, multiplied by the maximum take-off weight, provides the energy requirements for the two power sources.

Since the maximum take-off weight is not known at this level of the design process, a well educated guess is necessary. The I class weight estimation discussed in 2.4.1 can be applied for this purpose. From maximum take-off weight and maximum zero fuel weight estimated with I class methods, the energy requirements discussed previously, and the geometry from statistics or designer choices, the II class weight estimation method can be applied. Considering the preliminary information available the fuel mass is estimated in terms of supplied energy by Eq. (3.64). It is here explicitly remarked that the same process can be applied to the hydrogen necessary to fuel cells.

$$W_{Fuel} = \frac{E_{Fuel}}{Specific\ Energy} \quad (3.64)$$

In case of e-storage units, such as batteries, the main example of the present work, the dimensioning condition is the limiting one among power and energy. Thus, after fixing the specific power and energy of the battery, as well as the specific energy of the fuel, the weight of the power sources is preliminarily estimated as follows.

$$W_{BAT} = \max\left(\frac{E_{BAT}}{Specific\ Energy}, \frac{P_{BAT}}{Specific\ Power}\right) \quad (3.65)$$

Once the weight of each element is estimated, the geometry is updated as discussed previously and a new weight estimation loop is initialized with the new maximum take-off weight and the new maximum zero fuel weight. After convergence, the new sizing loop is initialized considering the updated propeller efficiency, if necessary.

3.4 Validation and Sensitivity Analysis

The present section aims to illustrate two different applications of the sizing process proposed dealing with two different categories: *FAR-23* (or *CS-23*) and *FAR-25* or *CS-25*. In both cases the aero-propulsive interactions considered will be related to a propulsive architecture employing distributed electric propellers and tip-mounted propellers. The difference between conventional architecture and hybrid-electric concept employing distributed electric propulsion is highlighted through the response surfaces comparing the maximum take-off weight and the fuel saving percentage.

Before discussing the results, some considerations are needed. In general, once the top-level requirements are provided by the stakeholders, the designer chooses the target values of the maximum lift coefficients at take-off and landing and freezes some characteristics of the propulsive system. The first step is aimed to choose the sizing point and the procedure is similar to the one proposed in Ref. [41]. The choice is performed within the design space, which is defined as the non-negative area of the sizing plot bounded from above by the minimum required power, or, in other words, the maximum power loading required to satisfy the constraints, from the right by the maximum wing loading, or, in other words, the minimum wing area. For the present examples, the maximum wing loading criterion drives the choice. However, the sizing point provides only information dealing with the effect of the aero-propulsive interactions on the boundaries of the design space, constrained as discussed in 3.2.

From this point, entering the substance of the weight estimation loop, geometry plays a role in the estimation of the performance. Differently from literature studies, in this work, the weight is calculated considering II-class methods to determine the effect of weight variations on each subsystem. The main issue is that II-class methods are based on semi-empirical laws requiring a certain maturity of the geometry that is not achieved at this stage. Nevertheless, the geometry provided by the Pre-Design tool is based on aircraft designed on similar TLAR and can be assumed for the sensitivity analysis without loss of generality. In fact, considering as starting points

different geometries based on similar TLAR, the results in terms of fuel saving percentages presents minimal variations, lower than 2%. Once the maximum take-off weight is estimated, the wing area is updated according to the sizing point chosen. As already stated in 3.3, the weight estimation is an iterative process requiring some preliminary hypothesis about the geometric parameters kept constant. Among the others, the choice of keeping constant the aspect ratio is conservative, since this parameter has a strong impact on both the structural weight and the induced drag.

The validation of the method is proposed in Ref. [164] by comparing different weight estimation methods applied to the case of DO-228NG with the design process proposed in the present work. The comparison of the sizing activity discussed in this chapter with the methods proposed in Ref. [165], developed at FH Aachen and TU Delft, is necessary to assess the reliability of the results in a context where flying platforms do not exist yet. The design procedures developed by FH Aachen and TU Delft are addressed in the following comparison as *Method B* and *Method C*, respectively. In Table 3.3, the first step of the validation assess the reliability of the results for the conventional aircraft chosen. The sizing activity discussed in this chapter is addressed as *Method C*.

	Method A	Error	Method B	Error	Method C	Error	DO-228NG
Geometry							
Wing area (m^2)	32.3	0.31%	32.2	0.00%	32.15	-0.16%	32.2
Weight breakdown (kg)							
Max take-off mass	6641	3.77%	6416	0.25%	6471	1.11%	6400
Zero fuel mass	6026	2.83%	5825	-0.60%	5924	1.09%	5860
Operative empty mass	3866	-0.97%	3865	-1.00%	3964	1.54%	3904
Fuel mass	615	13.89%	591	9.44%	547	1.30%	540
Engine dry mass	356	1.71%	354	1.14%	350	0.00%	350
Payload mass	1960	0.00%	1960	0.00%	1960	0.00%	1960
Sizing Point							
Wing Loading (N/m^2)	1957	-0.25%	1958	-0.20%	1974	0.64%	1962
Power to Weight (W/N)	18.65	1.14%	18.63	1.03%	18.61	0.92%	18.44

Table 3.3: Comparison of the sizing activity of the three methods with respect to the same reference aircraft (DO-228NG).

The similarity of the results regarding the conventional aircraft chosen as baseline for the comparison is satisfactory. However, since the main objective of the workflow is the analysis of point performance regarding hybrid-electric aircraft, the comparison of the methods is carried out on two additional concepts: a parallel

hybrid-electric concept and a full electric concept. The reliability of the methods can only be assessed through the comparison, due to the lack of information regarding hybrid-electric prototypes (TRL 7 or higher). In the present case, the comparison is based on the payload-range energy efficiency ($PREE$), which is the product of range and payload divided by the energy required to complete the mission. The parameter has been chosen considering that the main objective of the sizing activity is quantifying the effect of the design parameters on the emissions. The technological level considered is the same reported in Ref. [165]. The following figures (Fig. 3.6 and Fig. 3.7) provide the comparison of the methods presented in terms of $PREE$ while varying range and supplied power ratio.

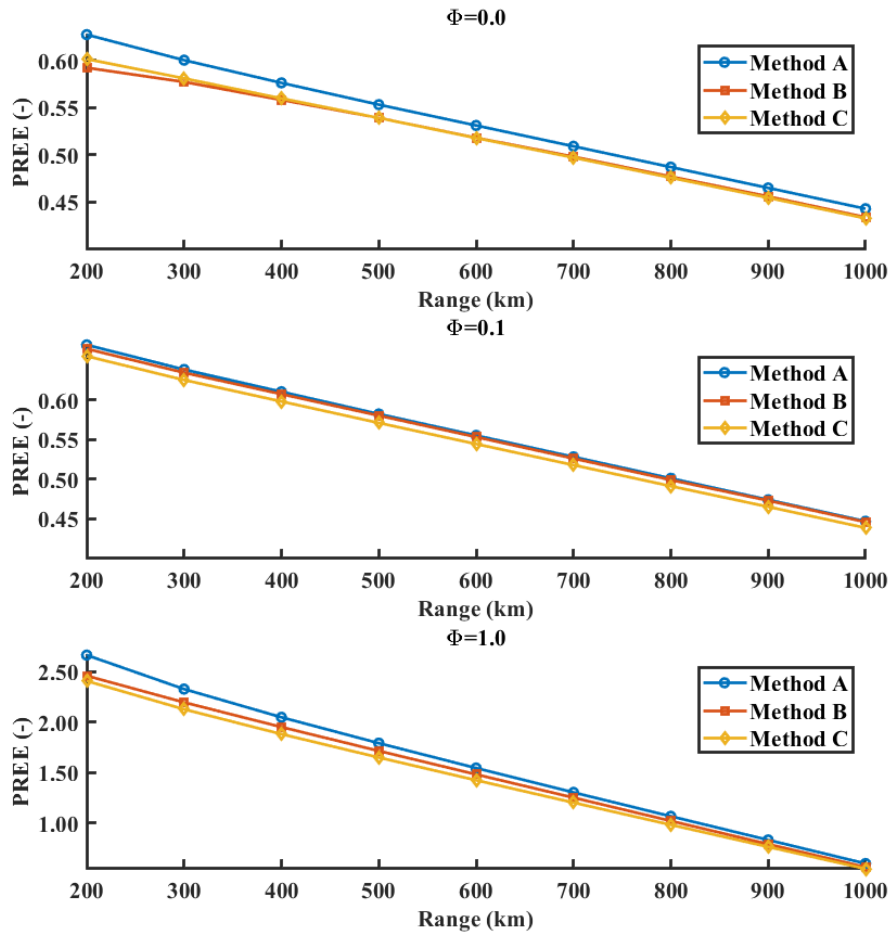


Figure 3.6: Comparison of the results in terms of $PREE$ associated to different values of the supplied power ratio and design range.

The trends shown in both figures highlight that increasing the range or the

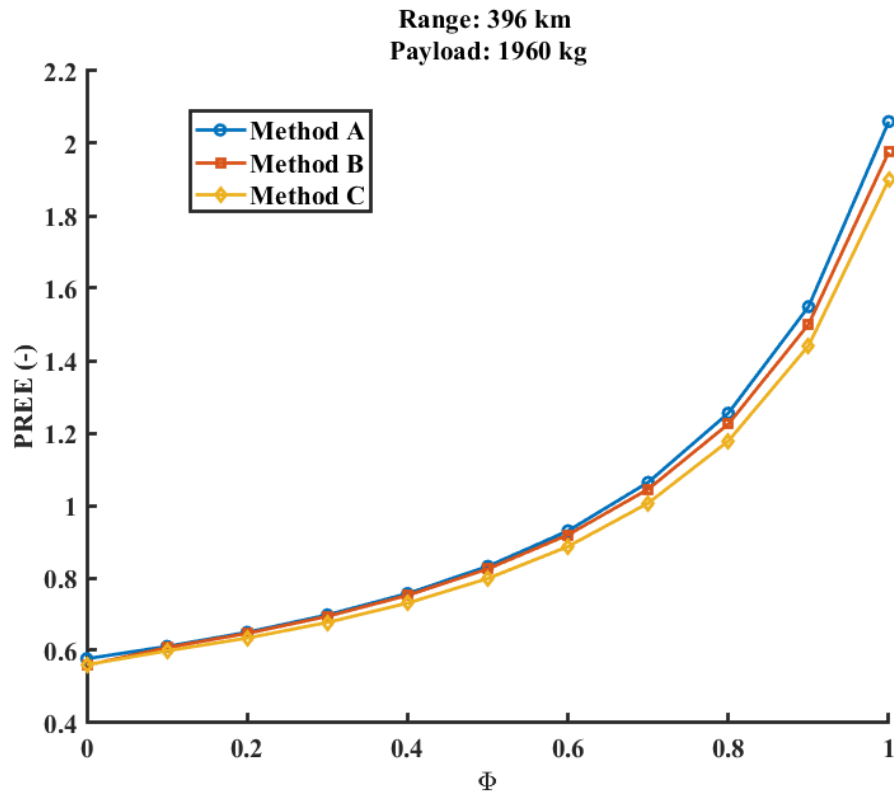


Figure 3.7: Comparison of the results in terms of PREE associated to different values of the supplied power ratio for a design range of 396 km and a maximum payload mass of about 1960 kg.

supplied power ratio, the Method C provides a smaller *PREE*. This phenomenon is related to the use of II-class methods for the estimation of the masses. In general, increasing the battery mass stored on board, the operative empty weight increases and the same goes for the energy required to complete the mission. However, in case of II-level methods, the masses of certain components, such as undercarriage or wing, depend on the maximum zero-fuel mass, causing a more rapid increase of the total weight of the aircraft. This effect becomes more critical considering a higher range or a lower specific energy value for the battery. Table 3.4 and Table 3.5 show the details of this comparison.

3.4.1 FAR-23 or CS-23

The present application is focused on the design space commuter aircraft with the distributed propellers along the wingspan and two main tip-mounted propellers.

Φ	Range (km)	Method A		Method B		Method C	
		MTOW (kg)	PREE	MTOW (kg)	PREE	MTOW (kg)	PREE
0.00	100	5576	0.67			5629	0.66
0.00	200	5777	0.63	5812	0.59	5850	0.60
0.00	300	5993	0.60	6030	0.58	6069	0.58
0.00	400	6225	0.58	6267	0.56	6306	0.56
0.00	500	6476	0.55	6521	0.54	6561	0.54
0.00	600	6747	0.53	6798	0.52	6837	0.52
0.00	700	7041	0.51	7098	0.50	7137	0.50
0.00	800	7362	0.49	7426	0.48	7465	0.48
0.00	900	7713	0.47	7785	0.46	7823	0.45
0.00	1000	8099	0.44	8179	0.43	8217	0.43
0.10	100	5619	0.70			5673	0.69
0.10	200	5850	0.67	5871	0.66	5917	0.65
0.10	300	6100	0.64	6122	0.63	6169	0.62
0.10	400	6372	0.61	6397	0.61	6446	0.60
0.10	500	6669	0.58	6696	0.58	6746	0.57
0.10	600	6994	0.56	7025	0.55	7077	0.54
0.10	700	7353	0.53	7386	0.53	7440	0.52
0.10	800	7739	0.50	7786	0.50	7837	0.49
0.10	900	8190	0.47	8231	0.47	8289	0.47
0.10	1000	8730	0.45	8730	0.45	8813	0.44
1.00	100	6080	2.28			6138	2.15
1.00	200	6654	2.67	6733	2.46	6758	2.41
1.00	300	7349	2.33	7445	2.20	7468	2.13
1.00	400	8206	2.05	8327	1.95	8346	1.88
1.00	500	9289	1.79	9443	1.72	9456	1.65
1.00	600	10701	1.55	10907	1.48	10907	1.42
1.00	700	12620	1.30	12905	1.25	12885	1.20
1.00	800	15377	1.07	15801	1.02	15738	0.98
1.00	900	19675	0.83	20372	0.79	20215	0.76
1.00	1000	27309	0.60	28669	0.56	28257	0.54

Table 3.4: Comparison of the sizing activity of the three methods varying both the supplied power ratio and the range at constant payload mass (1960 kg).

Φ	Method A		Method B		Method C	
	MTOW (kg)	PREE	MTOW (kg)	PREE	MTOW (kg)	PREE
0.00	6216	0.58	6258	0.56	6297	0.56
0.10	6361	0.61	6386	0.61	6434	0.60
0.20	6515	0.65	6552	0.65	6596	0.63
0.30	6679	0.70	6727	0.69	6767	0.68
0.40	6855	0.76	6912	0.75	6949	0.73
0.50	7042	0.83	7109	0.83	7143	0.80
0.60	7241	0.93	7318	0.92	7349	0.89
0.70	7452	1.06	7540	1.05	7568	1.01
0.80	7676	1.26	7774	1.23	7799	1.18
0.90	7914	1.55	8019	1.50	8043	1.44
1.00	8168	2.06	8269	1.98	8297	1.90

Table 3.5: Comparison of the sizing activity of the three methods varying the supplied power ratio at constant range (396 km) and payload mass (1960 kg).

The aero-propulsive interactions are based on aerodynamic models presented in 2.2. From the perspective of *FAR-23* (or *CS-23*) certified aircraft, the results are constrained by the MTOW, which should not exceed 19000 *lb*, that is a limiting factor for the battery mass and, thus, for the electric energy. Compliant with this limit, the sizing activity investigates the combination of parameters that results in the highest fuel saving percentage. The number of distributed propellers, the enabling strategy for DEP during the flight mission, and the specific energy of the battery are compared with the precise objective of maximizing the fuel percentage saved with respect to the conventional propulsed platform. In general, the design of a completely new aircraft moves from a set of top-level aircraft requirements (TLAR) which can be fixed in relation to new market demands or proposed by stakeholders. Some requirements, as take-off and landing field lengths, are based on a statistical approach relating the payload and/or the category with the market requirements. In other words, the requirements are chosen so that the same performance of nowadays flying aircraft are guaranteed. The commuter aircraft category shows a range average of around 800 *nmi*, Fig. 3.8, slightly reducing when increasing the number of passengers. Differently from the design range, the other TLAR have been chosen considering the typical values of nowadays aircraft.

The requirements are reported in Table 3.6 with some design parameters that guide the investigation.

Variable	Value	Unit
Number of passengers	19	—
Number of thermal engines	2	—
Number of e-motor drives	From 8 to 20	—
Design range	From 100 to 600	<i>nmi</i>
Take-off field length	700	<i>m</i>
Landing field length	720	<i>m</i>
Cruise Mach number	0.26	—
Cruise altitude	10000	<i>ft</i>

Table 3.6: Top Level Aircraft Requirements - *FAR-23* (or *CS-23*)

When approaching an innovative configuration, some requirements are driving factors for the design choices more than others and the identification of the formers

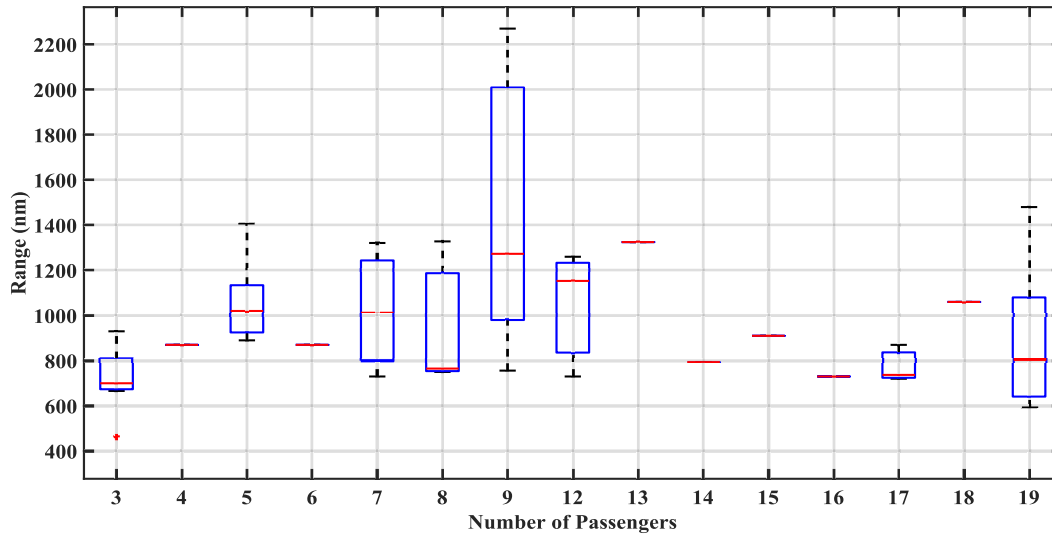


Figure 3.8: Boxplot of design range against number of passengers for FAR-23 certified aircraft. The central mark indicates the median, the bottom and top edges of the box indicate the 25th and 75th percentiles, respectively and the whiskers extend to the most extreme data points not considered outliers. The median for a 19 passenger is about 800 *nmi*.

is the main objective of this section. The sizing plot shown in Fig. 3.9 is the tool used for this preliminary study. This type of analysis has been already discussed in literature considering the effects related to distributed electric propulsion. The application of this technology to increase the lifting capability at take-off and landing has a different impact depending on the number of distributed propellers used. As shown in Table 3.7, the number of distributed propellers at constant wingspan causes an increment of the disk load affecting both lift and drag coefficients.

$V = 35 \text{ m/s}$	Take-Off Condition $C_L = 1.95$			Landing Condition $C_L = 2.20$			
	no. DEP	ΔC_L	ΔC_{D_0}	ΔC_{D_i}	ΔC_L	ΔC_{D_0}	ΔC_{D_i}
	8	+0.75	+0.0003	+0.0776	+0.83	+0.0003	+0.0971
	12	+0.92	+0.0006	+0.0957	+1.03	+0.0006	+0.1199
	16	+1.03	+0.0010	+0.1063	+1.14	+0.0010	+0.1332
	20	+1.09	+0.0014	+0.1128	+1.21	+0.0014	+0.1415

Table 3.7: Lift coefficient increment associated to distributed electric propulsion ($T_0 = 23130 \text{ N}$, $\phi = 1$ and 62% of the wing covered by DEP).

The effects reported in Table 3.7 affect the design space as shown in Fig. 3.10.

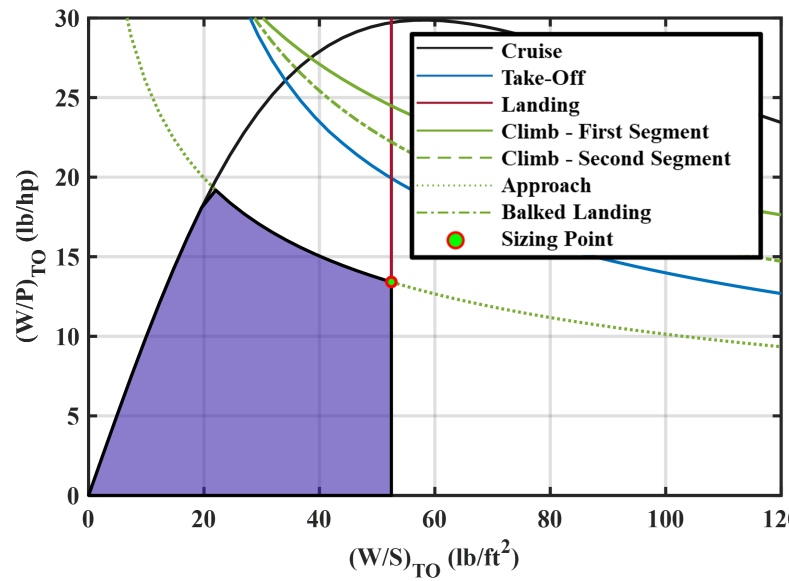


Figure 3.9: Sizing plot.

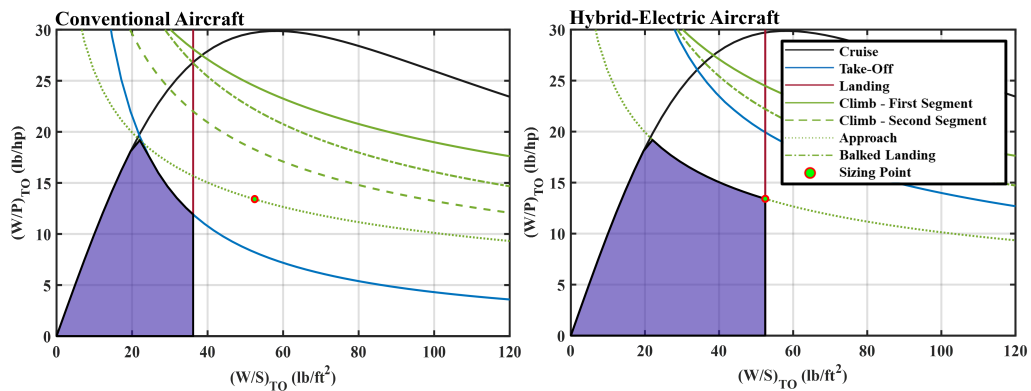


Figure 3.10: Sizing plots of turbo-electric and conventional concepts. The sizing points are both referred to the same turbo-electric aircraft.

However, as shown by Fig. 3.11, a larger design space does not necessarily mean a lower wing surface. In fact, when coming to hybrid-electric concepts, the impact on take-off and landing of weight increment related to batteries could be mitigated, but not nullified by distributed propulsion.

When approaching a new concept integrating innovative technologies, the effects of each one of these technologies must be investigated judging the results from the point of view of the requirements. For the present application, a maximum take-off weight lower than 19000 lb and a high fuel-saving percentage are the two criteria of judgement. The technological level, the DEP enabling strategy, and the number

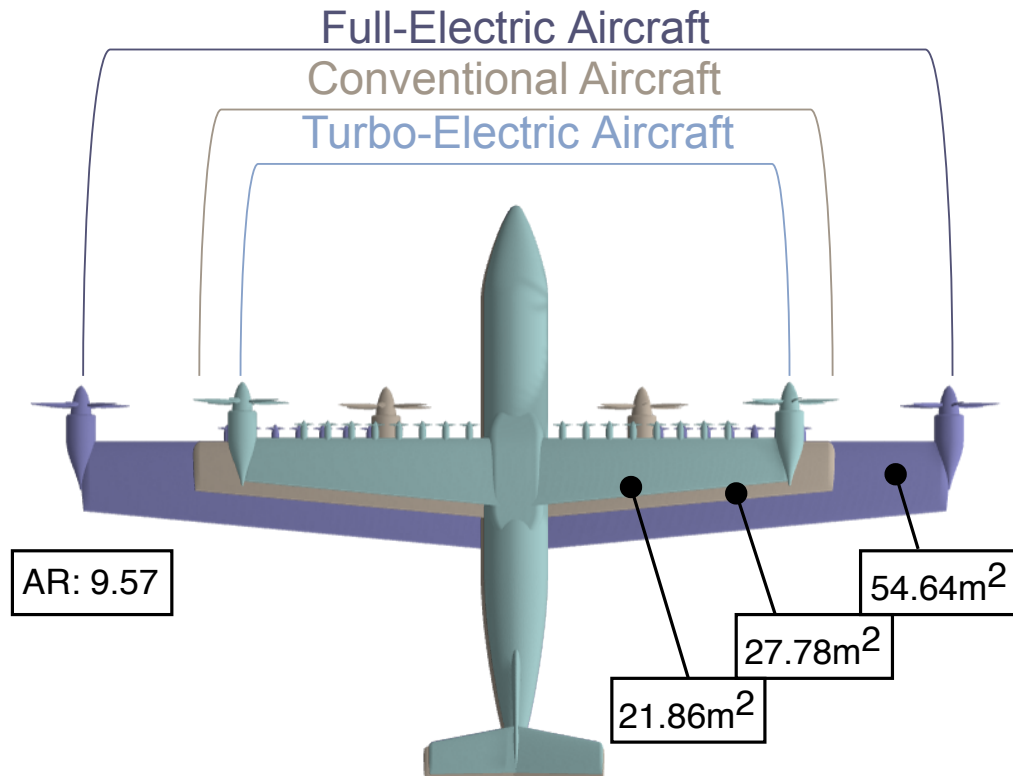


Figure 3.11: Comparison of three different commuter aircraft designed on a range of 400 *nmi* ($\phi = 0.90$ and 16 distributed propellers).

of distributed propellers are the parameters considered for this investigation. The DEP enabling strategy, that is the different use of the distributed propulsion phase by phase, or, in other words, the different shaft power ratio considered phase by phase, has been discussed in Ref. [164], where the most promising strategy has been identified in the use of distributed propulsion during take-off, landing and climb. The maturity of the enabling technologies, or, in other words, the technological level, is measured by some characteristics of the powertrain components considered. For the present case, considering the impact of the battery mass on the whole aircraft performance, the specific energy of the battery is the parameter considered. In fact, since the battery is dimensioned by energy and not by power, this parameter has a major impact on the design process results. On the other hand, a minor impact results in the specific power of the e-motor drives, which is kept constant. The value considered have been reported in Tab. 3.8.

Variable	Value	Unit
E-storage specific energy	250/350/500	Wh/kg
E-storage specific power	1	kW/kg
E-storage energy density	800	Wh/l
E-motor drive specific power	7.7	kW/kg

Table 3.8: Technological level

To make a fair comparison between the three different specific energy of the e-storage, the mission compared does not include the reserves (loiter and alternate) whose ranges summed could be even higher than 100 *nmi*, which is the shortest design range considered. Only 5% of fuel reserve is considered. In Fig. 3.12, the comparison of the different percentages of fuel saving is shown when the 10% of the power supplied at each phase to the propulsive system is provided by e-storage. The detail of Fig. 3.12 highlights the impact on fuel consumption of specific energy for a design range equal to 200 *nmi*. However, even if the specific energy influence at short design range results in a different fuel saving percentage, increasing the range, the hybridization of the platform could results in higher fuel consumption with respect to the baseline depending on the specific energy considered.

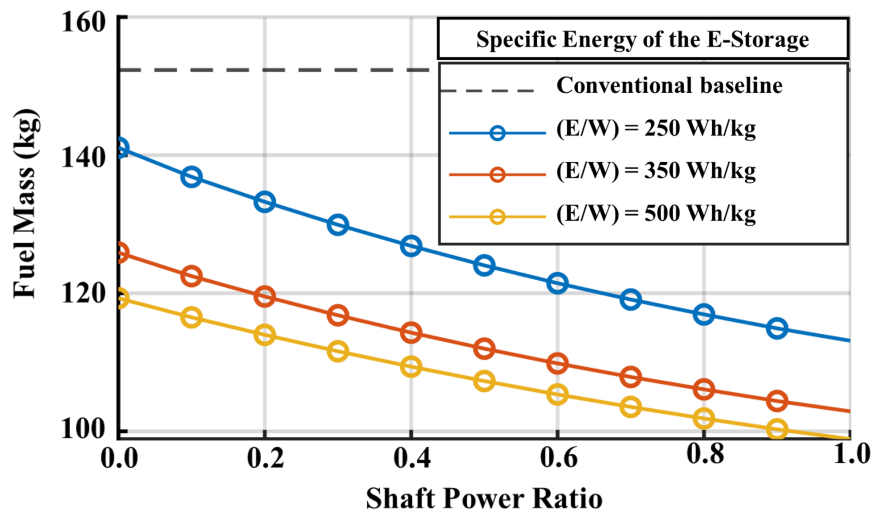


Figure 3.12: Fuel saving against shaft power ratio for three different values of battery specific energy, at constant design range (200 *nmi*) with 10% of power supplied by the e-storage in all phases and 20 distributed electric propellers enabled at take-off, landing and climb.

The different fuel saving percentage is maybe one of the major outcomes in case

of different technological levels. However, when approaching this aircraft category, one of the major interests is the design of a full-electric platform. The interest in full-electric commuter aircraft is related to the opportunity of employing on short ranges the small air transports, reducing both the pollutants emitted by aviation and urban transports. However, a suitable range for this category would be at least 400 *nmi*. In Fig. 3.13, the comparison of different maximum take-off weights with respect to the regulation constraint of 19000 *lb* shows that increasing the battery specific energy, the maximum design range achievable with a CS-23 (or FAR-23) certified aircraft increases. From 100 *nmi* with 250 *Wh/kg*, the maximum design range reaches 300 *nmi* when the specific energy double (500 *Wh/kg*).

In the following steps, the specific energy value fixed is 500 *Wh/kg*.

The following parameter analysed, which affects the fuel saving percentage, is the number of distributed propellers. In Fig. 3.14, the comparison among 8 and 12 propellers highlights the importance of a higher number of distributed propellers to maximize the fuel saving percentage. However, increasing the number of propellers the favourable effects on wing area reduction and fuel saving can be perceived only up to a certain point, after which, the high disk loading causes a drop of propulsive efficiency. Moreover, the increasing number of propellers can have a major impact on maintenance costs than on fuel saving. Moreover, as shown by the second row of Fig. 3.14, the effect on fuel saving of the increasing number of propellers is negligible for this aircraft category when approaching a high supplied power ratio.

The present section proposes an overview of many feasible concepts compared considering the fuel saving percentage as criterion. However, some considerations should be highlighted when coming to the number of distributed propellers. A higher number of e-motor drives and propellers would result in higher acquisition, installation, and maintenance costs. Moreover, the reduced propeller diameter would result in a troubling design to maintain high efficiency. These considerations are often not investigated by research teams but can make a feasible concept not economically profitable. The collaboration with the advisory board of ELICA project, one of the European projects funded by the Clean Sky 2 research framework,

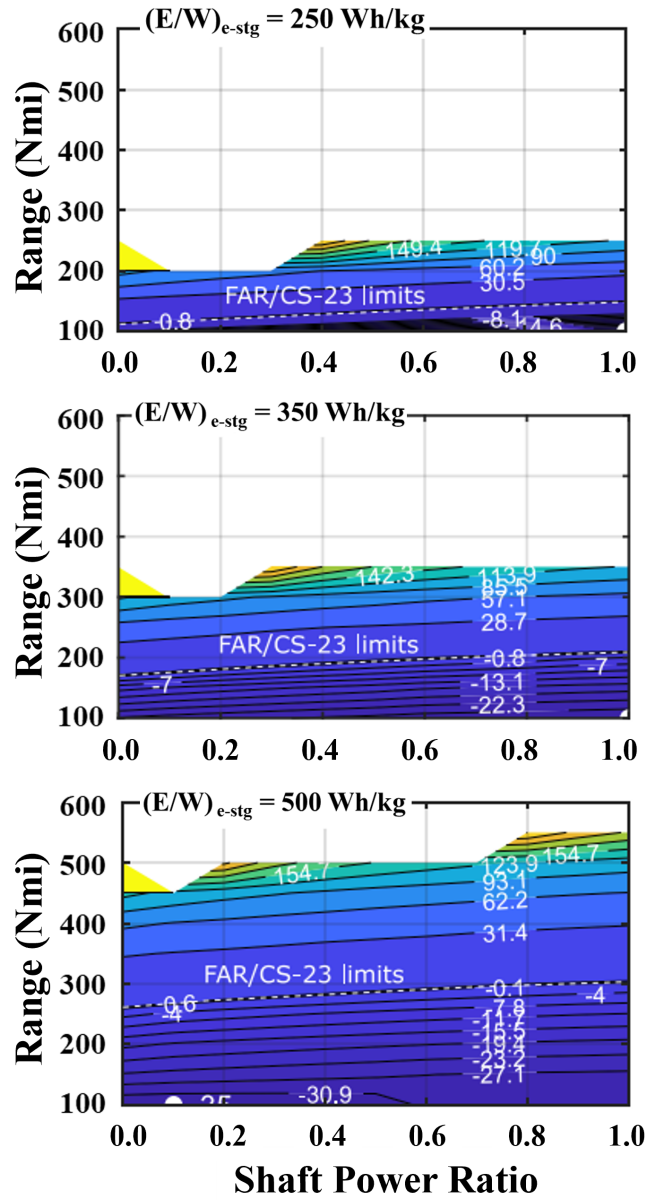


Figure 3.13: Comparison of MTOW increments with respect to CS-23 regulation constraint against range and shaft power ratio for three different values of battery specific energy. The white area refers to diverged mass estimations.

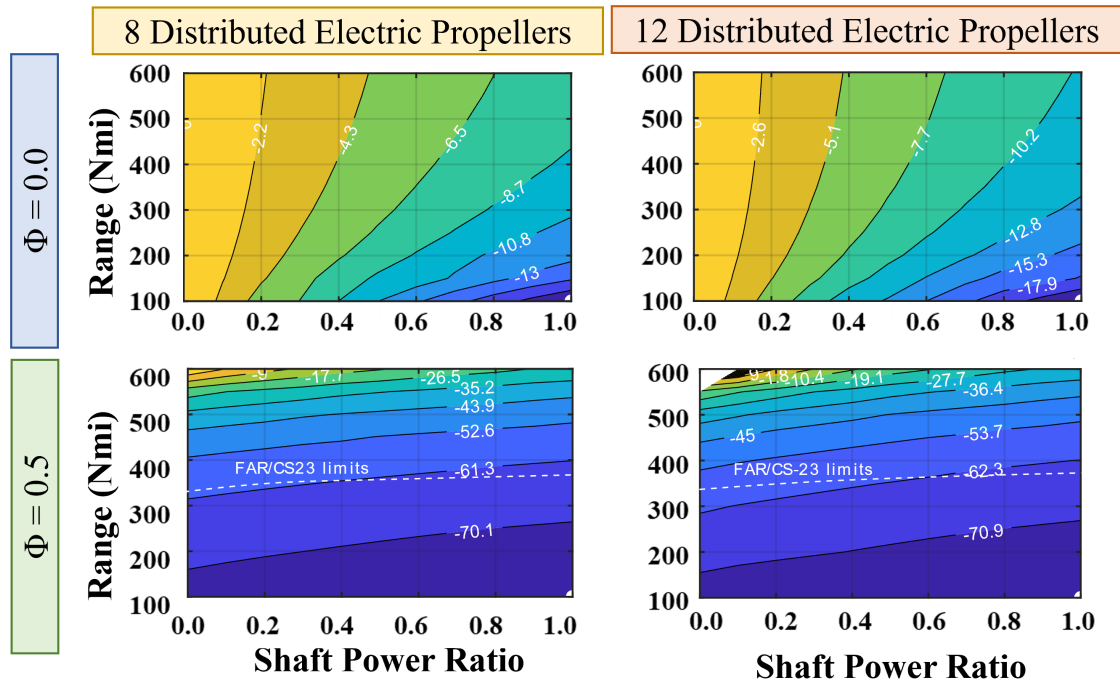


Figure 3.14: Comparison of fuel saving percentage against range and shaft power ratio for two different numbers of distributed propellers (8 and 12) and supplied power ratios (0 and 0.5).

highlighted the willingness of the industrial designers to a number of distributed propellers between 8 and 12.

3.4.2 FAR-25 or CS-25

The sizing activity for the conceptual design of a *FAR-25* or *CS-25* certified aircraft is here presented. In Tab. 3.9, the top-level aircraft requirements of the regional turboprop considered in the present section are introduced.

Variable	Value	Unit
Number of passengers	40	—
Number of thermal engines	2	—
Number of e-motor drives	From 8 to 20	—
Design range	From 100 to 700	<i>nmi</i>
Alternate range	100	<i>nmi</i>
Take-Off field length	1000	<i>m</i>
Landing field length	1100	<i>m</i>
Cruise Mach number	0.47	—
Alternate Mach number	0.30	—
Loiter Mach number	0.27	—
Cruise altitude	17000	<i>ft</i>
Alternate altitude	10000	<i>ft</i>
Loiter time	30	<i>min</i>

Table 3.9: Top Level Aircraft Requirements - *FAR-25* or *CS-25*

Approaching this category, not all the considerations made in the previous section are still valid, as can be derived by comparing conclusions of Ref. [42] and Ref. [164]. In Fig. 3.15, the impact of distributed propulsion activation during take-off and landing or during take-off, landing and climb is shown. For *CS-25* (or *FAR-25*) certified aircraft the use of DEP during the climb phase has a negative impact on fuel consumption due to the increment of power required and, thus, weight. The increase in fuel saved with range for the turbo-electric configuration proposed in Fig. 3.15, is related to the reduction of the wing area which has a major impact on cruise. Thus, having a lower wing area (and drag) with respect to the conventional aircraft, the percentage of fuel saved on the whole mission increases while increasing the cruise range. However, this effect is mitigated by weight increase for ranges higher than 700 *nmi*.

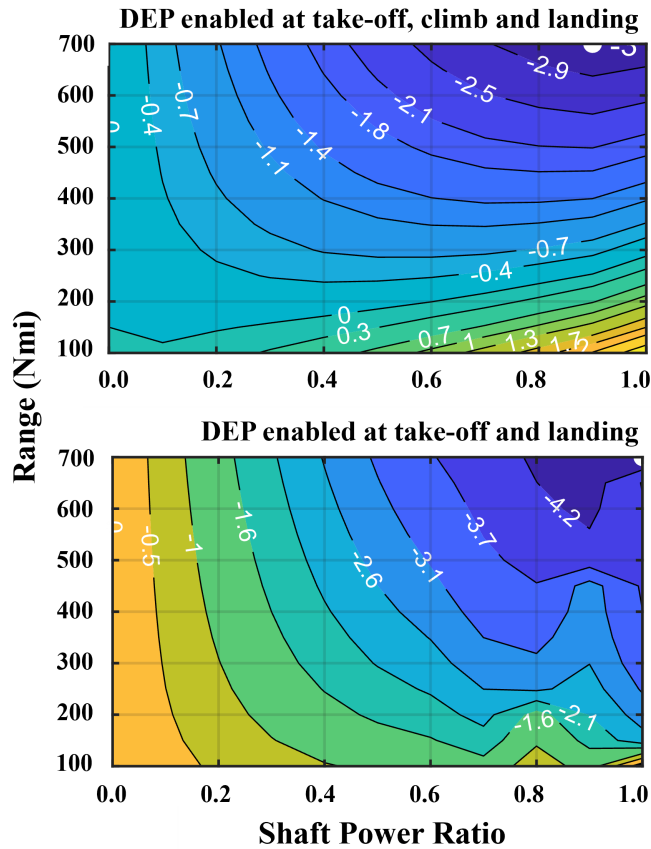


Figure 3.15: Fuel saving percentage against range and shaft power ratio referred to two different enabling strategies of 12 distributed electric propellers mounted on a turbo-electric regional turboprop.

As shown in Fig. 3.16, the impact on fuel saving percentage related to the specific energy of the e-storage is similar to the one discussed for the case of CS-23 (or FAR-23) certified aircraft. The only difference is that the MTOW is not limited. In the present case, considering the high efficiency of thermal engines during cruise and to mitigate the increment of weight, the battery provides energy in all flight phases except during cruise. This makes possible a profitable hybridization even for long ranges, as discussed in Ref. [42].

Distributed electric propulsion is proposed, for the present application, as a method to further increase the maximum lift coefficient during take-off and landing with the objective of reducing the wing area, as shown in Table 3.10.

Reducing the necessary wing area and, thus, enlarging the design space, lower fuel consumption can be achieved. For the following analysis, the distributed electric

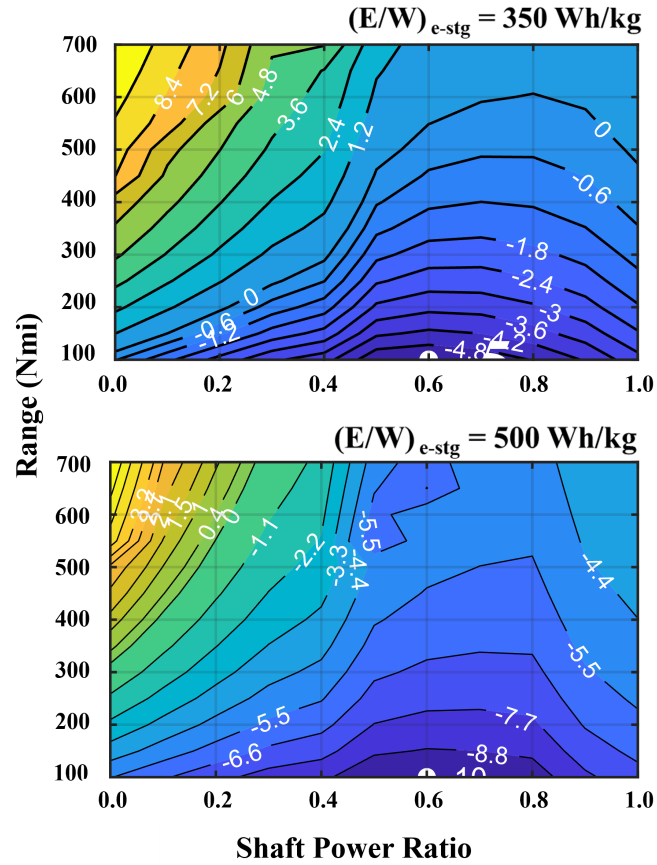


Figure 3.16: Fuel saving percentage against range and shaft power ratio for two different values of battery specific energy.

$V = 60 \text{ m/s}$	Take-Off Condition $C_L = 2.10$			Landing Condition $C_L = 2.70$		
	no. DEP	ΔC_L	ΔC_{D_0}	ΔC_{D_i}	ΔC_L	ΔC_{D_0}
8	+0.61	+0.0001	+0.0743	+0.75	+0.0001	+0.1167
12	+0.78	+0.0002	+0.0945	+0.96	+0.0002	+0.1489
16	+0.89	+0.0004	+0.1075	+1.09	+0.0004	+0.1697
20	+0.97	+0.0006	+0.1166	+1.19	+0.0006	+0.1842

Table 3.10: Lift Coefficient increment associated to distributed electric propulsion ($T_0 = 60000 \text{ N}$, $\phi = 1$ and 62% of the wing covered by DEP).

actuated propellers on the wing are enabled at take-off and landing and are folded in all the other phases. The application of the previous equations drives the definition of the sizing plot (in Fig. 3.17). This results in a lower wing area at equal or similar maximum take-off weight, as shown in Fig.3.18.

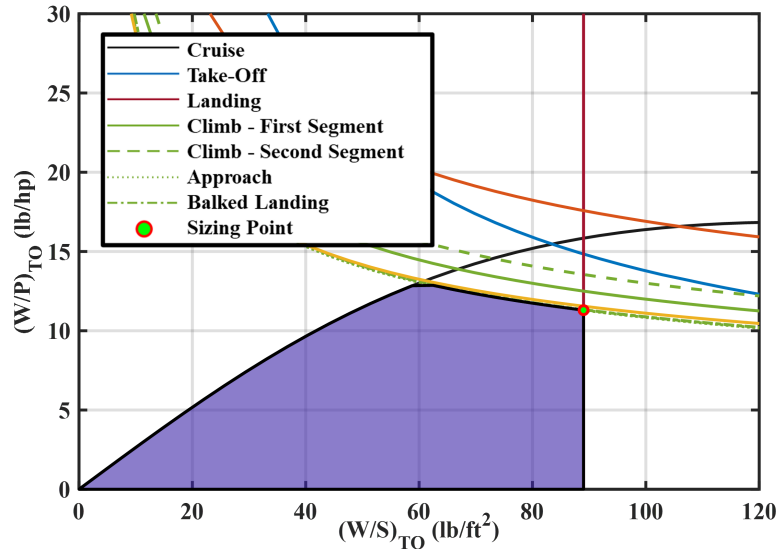


Figure 3.17: Sizing plot.

The influence of the aero-propulsive interaction between the wing and the distributed propellers is clarified in Fig. 3.19 and Fig. 3.20, where take-off and landing curves are compared for two different configurations, a conventional one and a hybrid-electric platform with 16 distributed propellers.

In both this section and the previous one, the choice of the sizing point plays a major role. In particular, the sizing point has been chosen targeting the maximum wing loading in order to maximize the effect of DEP on the wing surface reduction. In Fig. 3.21, the same sizing activity is performed when the sizing point chosen maximizes the power loading or the wing loading. Using the fuel saving percentage as the parameter of judgement, the most promising results have been obtained when maximizing the wing loading.

From the results obtained from the design space exploration, the sizing point should be chosen in order to maximize the wing loading and the number of distributed propellers should be as high as possible. Moreover, the distributed propulsion should

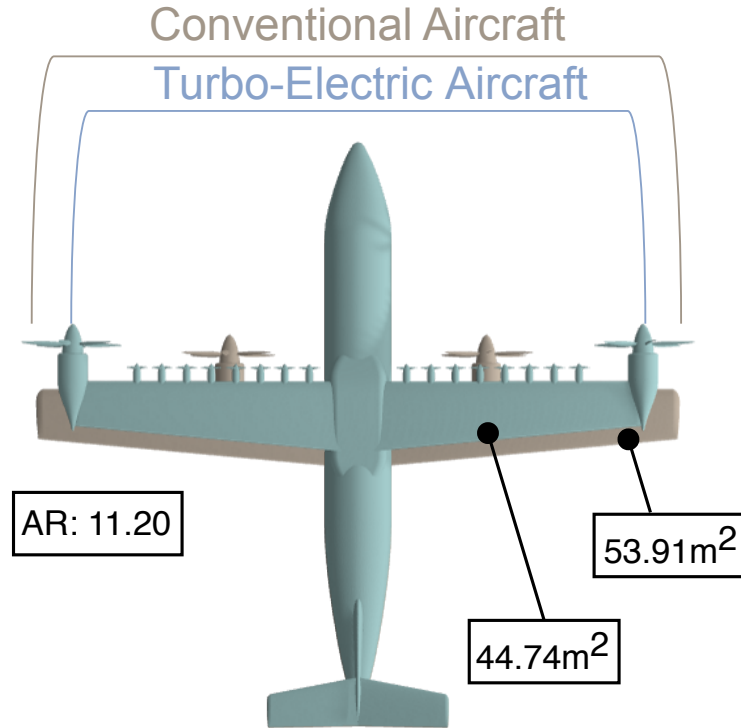


Figure 3.18: Comparison of two different regional-turboprop aircraft designed on a range of 600 *nmi* ($\phi = 0.90$ and 16 distributed propellers).

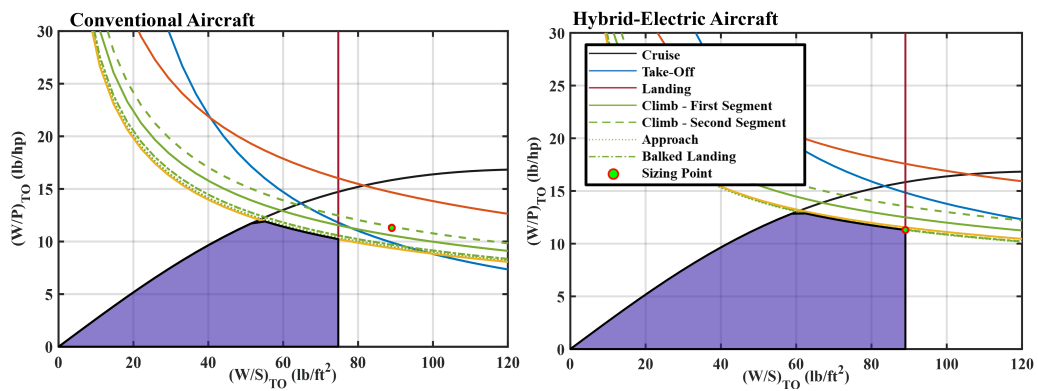


Figure 3.19: Sizing plots of turbo-electric and conventional concepts. The sizing points are both referred to the same turbo-electric aircraft.

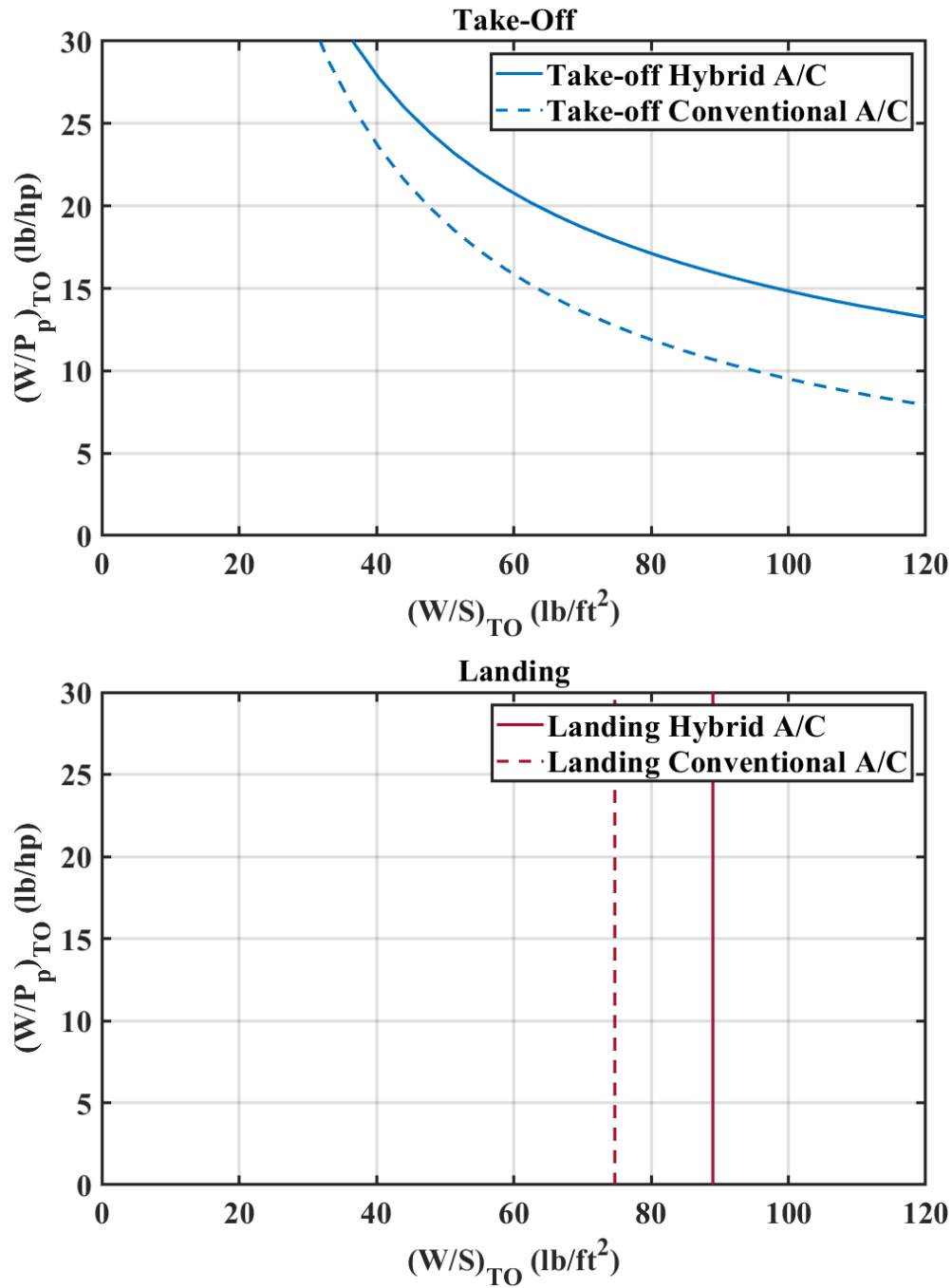


Figure 3.20: Sizing plot curves related to take-off and landing constraints.

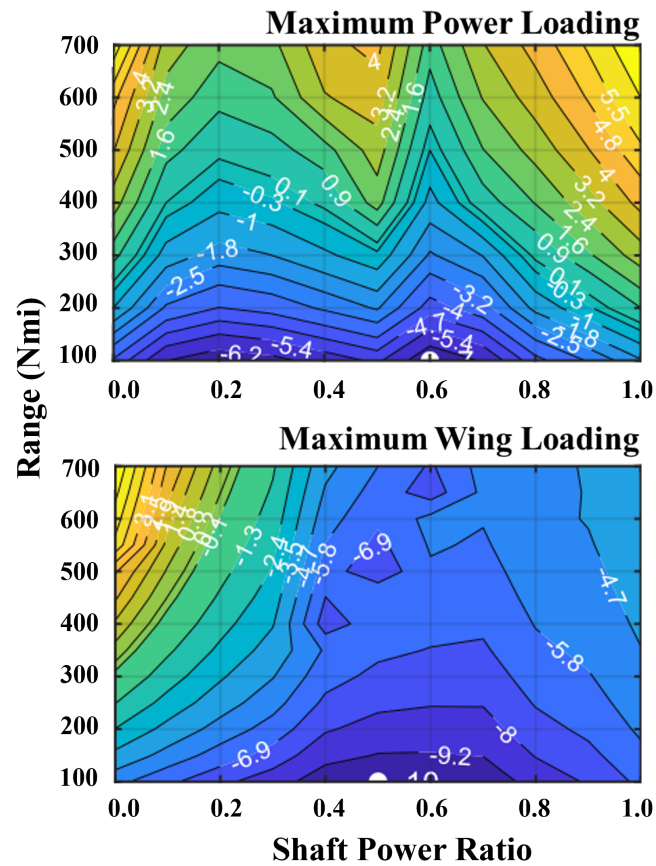


Figure 3.21: Fuel saving percentage against range and shaft power ratio for two different sizing points.

be employed during short phases where a wing area increment has a positive impact on performance, or, in other words, at take-off and landing.

It is here remarked that the increasing number of distributed propellers from 12 to 20 in the charts from Fig. 3.15 to 3.21) is related to the intent of balancing the penalty on the maximum take-off weight when changing the configuration from partial turbo-electric to hybrid-electric. In fact, by increasing the number of propellers and their disk loading, the increment in lift coefficient related to the aero-propulsive interaction is stronger. Results reported in Tab. 3.10 deals with a number of distributed propellers that goes from 8 to 20 and clarify this aspect. However, the experience maturated on regional turboprop during the Italian research project named PROSIB, side by side with industrial partners, imposes additional considerations. In fact, even if the promising results of 20 distributed

propellers would motivate that number, maintenance costs, noise and drag drive the choice on this category more than the aerodynamics benefits. In the end, 8 distributed propellers would be a better choice.

Hell, there are no rules here. We're trying to accomplish something.

— Thomas A. Edison

4

Flight Performance Analysis

Contents

4.1	Dynamic Model of the Propulsive System	204
4.1.1	Engine Deck Querying	205
4.1.2	Battery Discharging Cycle	210
4.2	The Flight Mission	211
4.2.1	Take-Off and Balanced Field Length	212
4.2.2	Climb and Ceiling	217
4.2.3	Cruise	222
4.2.4	Descent	224
4.2.5	Alternative Cruise	225
4.2.6	Loiter	226
4.2.7	Approach	227
4.2.8	Landing	227
4.3	Validation of the Algorithm	232

The conceptual design of hybrid-electric aircraft has been discussed in literature considering both point performance and mission analysis. Approaching the design of hybrid-electric aircraft, two main issues should be faced. The first issue deals with the complexity of the propulsive system, the second one is the correct estimation of aero-propulsive effects based on the actual thrust.

Considering the variety of operating modes associated with electric propulsive systems, approaching higher technological readiness levels, an accurate simulation of the powerplant is necessary. In literature, studies of the mission profiles measuring

the sensitivity of the flight performance at component level have been proposed [166]. However, in most cases, the two power sources are considered as additive regardless to the flight phase [166,167]. This can be true in case of serial/parallel hybrid concepts. However, in case of system architectures with a hybrid propulsive line coupled to a full-electric one (Fig. 2.3), the two power sources can interact in different and complex ways (Table 2.1). Powerplants have been described to approach the mission analysis of innovative concepts like NASA X-57 [168], coupling high-lift and primary propulsive systems of this full-electric aircraft. In some cases, models proposed in virtual environment have been validated with low scale prototypes [169]. However, even when the model is accurate, it cannot be assumed as general. Moreover, even when the propulsive system is perfectly modelled, aero-propulsive interactions are not directly coupled to thrust delivered at each step of the mission profile, discouraging simulation-based approaches in favour of less accurate but more rapid simulations. Aero-propulsive interactions have been largely investigated, but the mathematical form proposed in literature has been limited at the early stages of the design process [41]. The gap between flight simulation and the early stages of the design process appears still large.

On the one hand, the mission analyses proposed in literature for electrically powered aircraft are often not simulated. In other words, the analyses are performed without considering the variation of aerodynamics, speed, and thrust during each flight phase [25,71,170–172], or without estimating aero-propulsive effects at each time step [171,173,174]. On the other hand, the structural weight is often kept constant during the electrification of the platform even when the mass of the propulsive system increases [173,175,176].

The aerodynamic benefits of DEP and tip-mounted propellers have been deeply investigated by NASA, yielding to an amplification of lift coefficient [141,177], whereas wing-tip mounted propellers may decrease the induced drag, depending on the wing platforms, propeller characteristics, thrust and lift coefficient [31,178]. In literature, the integration of aero-propulsive effects at early stages of the conceptual design process has been largely discussed in Ref. [41,42,164]. However, in these

works, the aerodynamic interaction between the propeller slipstream and the lifting surfaces is the context of point performance estimation through semi-empirical approaches. The scientific community is progressively moving towards higher TRLs (Technology Readiness Levels) and this process is raising the need to perform high-fidelity mission analysis. A reliable fidelity level can be achieved by estimating, step by step, the energetic consumption, in terms of fuel and electric energy, and the aero-propulsive effects [70, 179].

The analysis activity is an iterative process that aims to estimate aircraft performance after geometric and aerodynamic characteristics are determined during a previous step of the design loop. The procedure starts with the estimation of the specification points, which are the most critical points of the mission profile in terms of power demand. From this estimation, the designer can make a first refinement of the masses. The procedure continues with the estimation of the energetic requirements necessary to complete the mission profile in terms of electric energy, fuel, and hydrogen. In case of a design mission, the designer can choose to optimize the use of the energy boarded to accomplish the mission or increase the energy stored while keeping constant the supplied power ratios of each flight segment. In this second case, an update of the weights is necessary and the mission is analysed iteratively until its accomplishment. Then, the flight performance is calculated to assess the compliance with the target performance. In case of misalignment, the supplied power is increased, as well as the associated rated powers of each element of the propulsive system. Based on these new rated powers, the weights are updated and a new mission analysis must be performed going back to the evaluation of the specification points. Even if it has been stated that the aerodynamics of the airframe and the geometry are frozen at this stage, it is advisable to analyse in parallel more than one concept to avoid neglecting the effects that some design variables have on the flight performance that are excluded from the sizing activity (e.g.: ceiling altitude and time to climb). Once the design mission has been analysed and the flight performance is met, for each concept considered, a set of typical missions should be analysed in order to minimize the energy used to complete them.

This optimization can be performed working on the choice of the right supplied power ratios.

In this section, a synthetic workflow of the analysis activity and the logic used to calculate aircraft performance are presented. This work proposes enhanced methodologies achieving two main objectives. The first one is to provide a coupling between aerodynamics and the aircraft engine deck. The second one is to perform a medium-fidelity analysis of the mission profile, measuring aircraft performance and energetic requirements. As shown in Fig. 4.1, the analysis process can be used for investigating flight performance or designing the platform which would better fulfil mission and performance requirements.

To enhance the estimation of hybrid-electric propulsion on aircraft performance, it is fundamental to perform detailed simulation-based mission analyses. A simulation-based analysis can be realized characterizing each single step of the whole flight mission of an aircraft by its aerodynamics and propulsive characteristics. Therefore, all the parameters defining the aircraft state at each step, such as Mach number, altitude, throttle setting, acceleration, rate of climb, and many others must be determined. In literature, similar algorithms have been described [180] and applications identified the trade-off between mass increment and hybridization ratio as a key parameter for optimizing hybrid-electric concepts. This is a valid consideration regardless of the accuracy level, but the impact of the hybridization on the mass increment varies when the powerplant is modelled at component level. Moreover, the evaluation of the aero-propulsive interactions is part of the simulation proposed in this work.

Approaching the mission analysis of hybrid-electric aircraft, there are many different methods from literature among which the designer can choose the most suited. However, in most cases, two issues remain unsolved. The first one deals with the complexity of propulsive architectures. In fact, the two power sources can be connected to more than one propulsive line and it can be characterized by multiple operating modes, unlike a conventional thermal engine. For example, an electric power source can be recharged using the exceeding power from another power

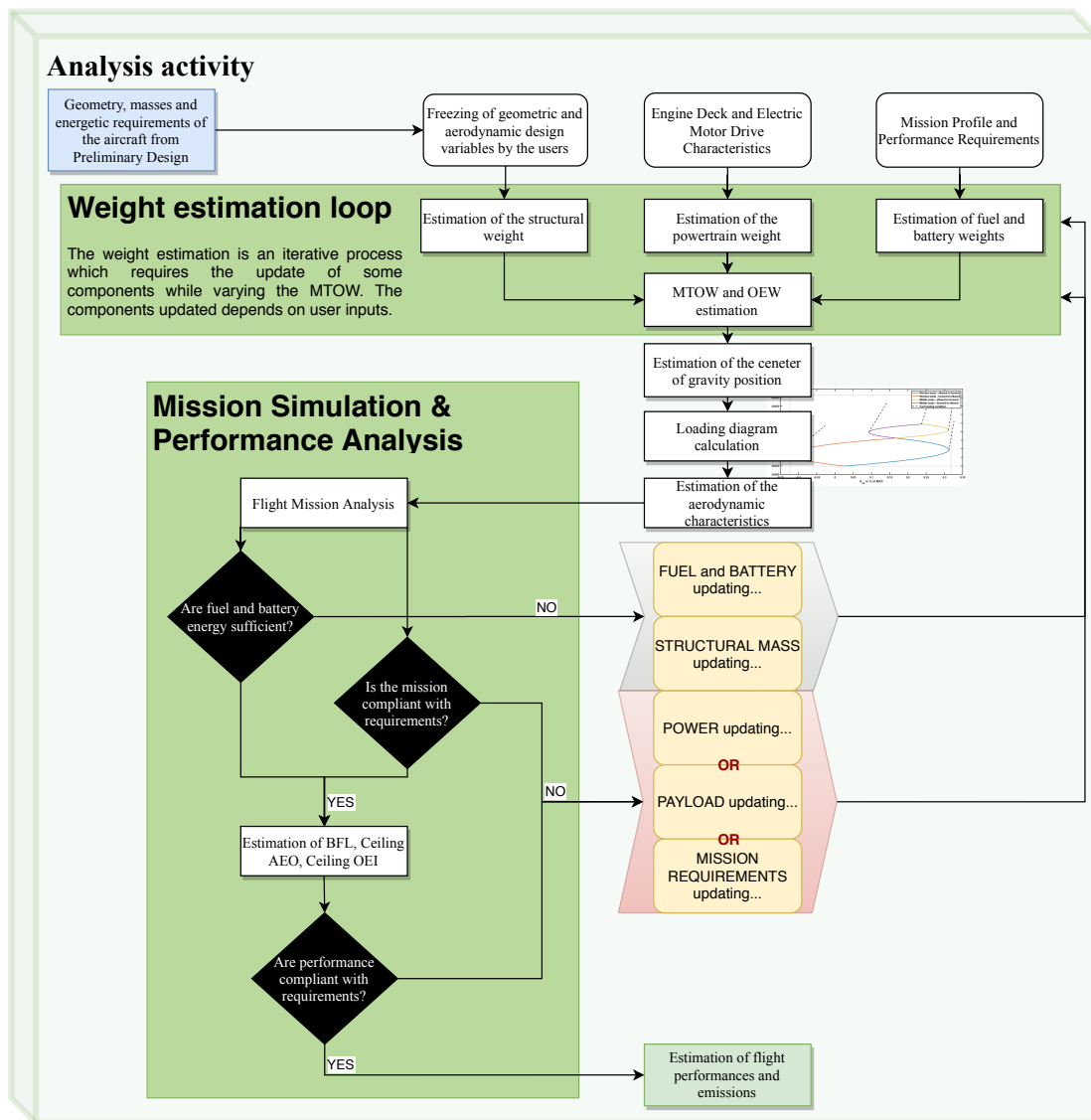


Figure 4.1: Analysis workflow.

source. These aspects cannot be neglected when the powertrain model aims to be as general as possible to describe any hybrid concept and operating condition. In the present section, the second issue dealt with is associated to those concepts where the aero-propulsive interactions are the main innovative feature. This is the case, for example, of distributed electric propulsion, boundary layer ingestion, and tip-mounted propellers. The problem of the simulation of aero-propulsive interactions is that step by step the aerodynamics characteristics must be measured on the basis of the actual thrust delivered by the propulsive system. Thus, both issues

discussed can be solved by an accurate description of the propulsive characteristics of the aircraft at each time step of the mission profile.

Before focusing the attention on the propulsive architecture and its modelling, it is here remarked that at each time step of the mission profile, the algorithm performs three different calculations defining aerodynamics, propulsive characteristics, and flight conditions. Depending on the flight segment, the three phases of the algorithm are performed in a different order. To summarize, at each time step the following activities are performed:

- starting from flight conditions at the beginning of the flight segment, the aerodynamic characteristics are computed;
- at the prescribed airspeed and altitude, the power distribution along the propulsive system is determined;
- having calculated aerodynamic and propulsive forces, the new flight conditions can be determined.

It is here explicitly remarked that in case of aero-propulsive interactions, the first and the second step are chained in an iterative process.

4.1 Dynamic Model of the Propulsive System

The objective of the present paragraph is to provide general guidelines for the estimation of the energy consumed and the power supplied by the power sources. However, before focusing the attention on the procedure, some remarks are necessary. Firstly, the propulsive system is assumed to instantly adapt to the flight conditions without accounting for any transient phase. In other words, assumed that the transient period is very small compared to the time step, it can be neglected. The second remark is related to the title of this paragraph. Since the mathematical model assumes that at each step the components are in equilibrium condition, it should be more appropriately defined quasi-static model. However, if the time step chosen is small enough, results from the procedure discussed in this paragraph are in line with more complex dynamic models.

4.1.1 Engine Deck Querying

As previously discussed, at each step, the description of power distribution along the powerplant starts from querying an engine deck similar to that described in 2.1, which can include or not the efficiencies of each element of the system. Based on the management of system efficiency data, the interpolation of the engine deck can be divided into two accuracy levels:

- I The first accuracy level for mission analysis requires fewer iterative loops since the efficiencies of each element of the powertrain system are fixed phase by phase.
- II The second level requires calculating the efficiencies of the power units at each time step.

The interpolation of the engine deck is divided into two steps. The first one is common to both accuracy levels, the second one is aimed to derive the efficiencies from data stored in the efficiency deck coming from appropriate look-up tables and, thus, it is applied to the second level.

The objective of the first step is to obtain power and/or fuel flow by querying the engine deck on the basis of Mach number, altitude, throttle, and temperature. The power can be referred to the thermal engines, the fuel cells, or the e-motor drives, depending on the propulsive architecture considered, as discussed in 2.1. Three different procedures can be considered depending on the information of interest and the information available at the beginning of the time step. In fact, different mission segments are differently constrained. Sometimes the airspeed is fixed, some others thrust. The three algorithms identified are presented associated, in example, to different flight conditions.

- 1 The first algorithm proposed is typically associated with a climb condition at constant calibrated airspeed. When the airspeed is fixed, but the altitude is not constrained to the current one, the exceeding propulsive power can be used to climb. The throttle is fixed as the maximum possible. Altitude, airspeed, and temperature are fixed by flight conditions. The engine deck is interrogated to fix the power based on the four input parameters.

- 2 The second algorithm proposed is typically associated to a flat cruise at constant Mach number and altitude. In the present case, an additional step is necessary. At first, the throttle is set as the maximum possible and the maximum available power is calculated as in the previous algorithm. However, this flight condition requires the equilibrium along the x-axis of the wind reference frame. Assuming low or null incidence of the propulsive system, the equilibrium can be assumed to be a simple equation: thrust is equal to drag. From the maximum available power, the propulsive power and its associated thrust are calculated. The drag value is calculated accounting for the aero-propulsive interactions. In case of constant efficiencies of the powertrain elements, a new throttle is set considering the ratio between drag and maximum available thrust. On the contrary, the throttle value is calculated through an iterative process to account for the different efficiencies related to a different power distributed along the powertrain elements.
- 3 The last algorithm considered when querying the engine deck deals with a condition that is related to a sustained descent phase. Conventionally, the descent phase procedures are distinguished in sustained and unsustained. The unsustained descent phase is generally flown at constant calibrated airspeed, considering the minimum throttle setting from cruise or flight idle power ratings. Thus, fixing step by step altitude, throttle, Mach number, and temperature, the associated power delivered is obtained from the engine deck. When the flight segment simulated is an **unsustained descent**, from the minimum power obtained from the engine deck and the calculated drag, the rate of descent is estimated as the difference between propulsive power and necessary power at level wing divided by the weight. Differently from the unsustained descent, **sustained descent** requires to calculate the necessary propulsive power for a fixed couple of rate of descent and constant airspeed. At fixed rate of descent and speed, the propulsive power is calculated. The power managed by each element is calculated from Eq. (2.3). The engine deck is then interpolated between the power associated at the minimum throttle

value of the cruise power rating and the one associated with flight idle setting. The outputs of this interpolation are the power supplied by the gasturbine, the fuel cells, or the e-motor drives, depending on the hybridization ratios, and the fuel flow associated.

Regardless of the hybridization ratios, the throttle is defined as the ratio between the power exiting from the gasturbine, the fuel cell, or the e-motor drives, with respect to the nominal power of the element.

However, some considerations are necessary about the relationship between supplied power ratio and throttle. When the objective of the mission analysis is fixing power requirements, the throttle setting is fixed according to the previous algorithms, and the dimensioning power of each component is derived by the coupling between the power supplied by the thermal power unit (or the fuel cell) and the power supplied by the e-storage. When approaching a less power demanding or shorter mission, that is, for example, the typical mission, the supplied power ratio can be increased in order to consume the same amount of electric energy stored to fly the design mission. In other words, to make the most of the e-storage sized for the design mission, the supplied power ratio must change. However, the sizing power of each component is limited to power requirements from the design mission and the increment of supplied power ratio at constant thermal power could result in an excessive power flow. This requires to evaluate a relationship between the engine deck throttle and the supplied power ratio in case of hybrid-electric architectures. Eq. 4.1 proposes a relationship to calculate the new throttle value when the supplied power ratio increases with respect to the one assumed for the design mission (Φ_1).

$$Throttle = \frac{1 + \frac{\Phi_1}{1-\Phi_1} \frac{1}{\eta_{ta_{GT}}}}{1 + \frac{\Phi}{1-\Phi} \frac{1}{\eta_{ta_{GT}}}} \quad (4.1)$$

The application of this equation along the flight simulation requires information about the engine deck power hooks.

The estimation of efficiencies is the objective of the second step of the engine deck interpolation. The estimation of power unit efficiencies is necessary when determining the power distribution along the powerplant. However, depending

on the level of accuracy, it may be performed or not. When a low accuracy is required, the mathematical model is based on phase by phase efficiencies chosen by the designer's experience. These well educated guesses can be sufficient to derive with good accuracy the aero-propulsive interactions and the fuel consumption. The limit of low accuracy is the evaluation of electric energy consumption. In fact, powertrain equations from which the battery power is estimated at each time step are a direct function of efficiencies. The reliability of results about mission energy consumption depends on the reliability of powertrain efficiencies, differently from the fuel consumption which depends on fuel flow data stored in the engine deck. The high-fidelity simulation is based on the engine deck, described in 2.1.2, storing the necessary information about powertrain efficiencies. The interpolation of this dataset is based on an iterative process whose application requires the preliminary knowledge of the nominal power or the rated power of each element of the powertrain.

- 1 From the gasturbine power or fuel cell power and the associated fuel flow, fixing the fuel energy density, the resulting thermal efficiency can be calculated by Eq. (2.11). In case of unitary supplied power ratio, the efficiency is equal to one.
- 2 First guess efficiencies are estimated with the only exception of η_{GT} , calculated previously.
- 3 The entering and exiting powers of each component are calculated through the appropriate set of powertrain equations.
- 4 At the power rating considered, associated with altitude, Mach number, temperature, and unitary throttle, the engine deck contains the design shaft power for which the propellers have been designed.
- 5 The dimensioning or nominal power of each component is fixed.
- 6 The entering power of each power unit of the powertrain system is compared to the dimensioning or nominal power to calculate the throttles. Each power unit is associated with a different throttle definition.
- 7 With the new throttles calculated, for the flight condition considered, the new efficiencies are estimated, as shown in Fig. 4.2.

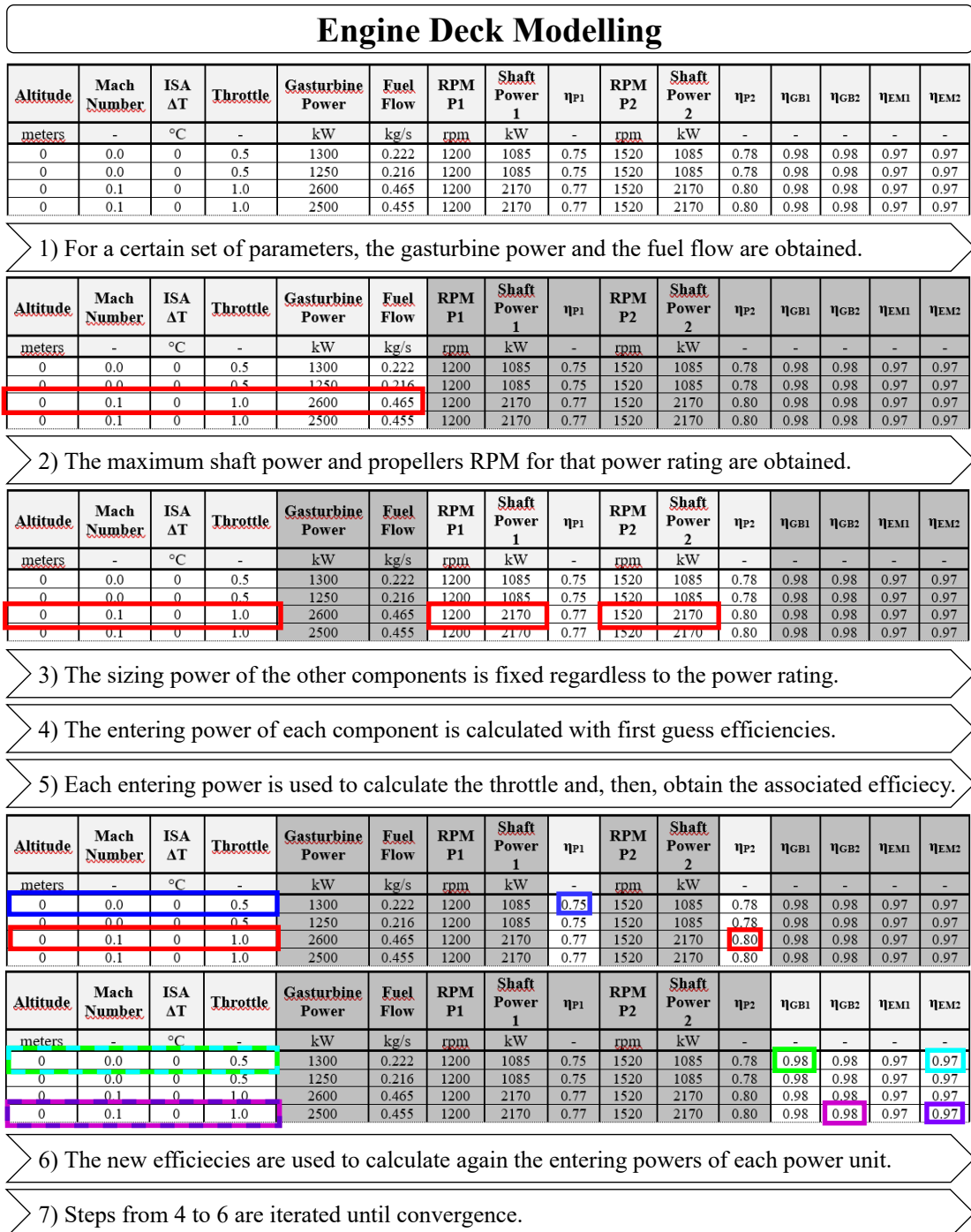


Figure 4.2: Procedure for the interpolation of an engine deck including efficiency data.

The process here proposed is iterative since at each loop the efficiencies change and the same goes for the power obtained from powertrain equations. The convergence criterion is the maximum variation among the entering power of each power unit from one loop to another since the same efficiency can be associated with more power values. Thus, when the efficiency is determined, the power distribution is calculated as well. Finally, when propulsive power and airspeed are known, thrust can be calculated.

4.1.2 Battery Discharging Cycle

The dynamic modelling of the battery has been discussed in 2.1.4 assuming a certain discharging cycle for a cell and, then, building up the characteristic curves of the battery at different discharging currents. Starting from the single cell curve, point by point the voltage is multiplied by the number of cells packed in series, and the capacity is multiplied by the number of cells in parallel. The curves obtained are generally reported in terms of voltage as a function of the state of charge or discharge capacity. The maximum **C-rate** of the battery is calculated considering the maximum output current supplied to the propulsive system, divided by the current necessary to deliver the total capacity in one hour. Nowadays, a suitable limit for the maximum C-rate is 2.5.

From this point, all the information required to define the discharging cycle is available. The maximum C-rate and, thus, the maximum discharging current available is fixed. On the other hand, the definition of the required current is calculated starting from two different parameters: the state of charge and the required power. At each step of the mission profile, the state of charge of the battery is known from the previous step. At constant state of charge, for each discharging current, the associated battery voltage can be obtained interpolating the characteristic curves. The power that can be supplied at that state of charge is obtained by multiplying the couple composed by each discharging current and the associated battery voltage, as shown in Fig. 4.3.

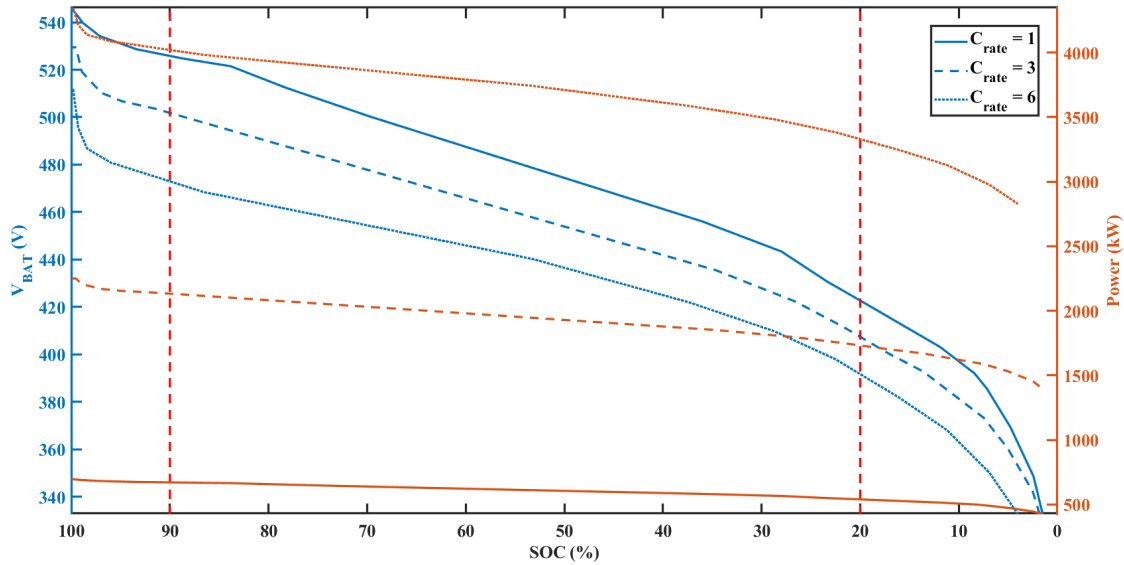


Figure 4.3: Battery characteristic curves and associated power supplied.

On the other hand, the required battery power is calculated from the procedure defined in 4.1.1 applying the powertrain equations from 2.1.1. At each time step, the necessary power is compared with the power supplied at the current state of charge to identify the necessary discharging current. If the required current exceeds the discharging current associated to with maximum C-rate, the number of cells in parallel had to be increased. The required power is multiplied by the time step to calculate the energy supplied and the new state of charge is estimated by subtracting this quantity to the remaining energy.

4.2 The Flight Mission

When the designer approaches the analysis of the mission profile, willing, contextually, to determine the effect of innovative propulsive architectures on flight performance, the algorithms proposed in literature [138, 143, 181] should be modified to integrate the new powertrain model and the aero-propulsive interactions. The analytical methods discussed in 2.1, 2.2, and 4.1 can be easily integrated into any simulation based algorithm as part of its modules dedicated to aerodynamics or propulsion. In the present section, preserving the generality of the work, the flight mission is discussed highlighting the main effects that distributed electric

propulsion, tip-mounted propellers, and unconventional power sources have on performance, fuel consumption, and sizing power, without detailing the equations modelling each phase.

4.2.1 Take-Off and Balanced Field Length

The *taxi-out* phase is here neglected since the energy consumption, whose evaluation is the primary objective of this chapter, is usually very low if related to the rest of the flight mission. The first flight phase discussed is the **take-off** phase. A detailed simulation of this phase can be fundamental to evaluate some aircraft performance, such as **balanced field length (BFL)** and decision speed (V_1 , Table 4.1 and Fig. 4.4), or the necessary sizing power of some components of the propulsive system. Take-off phase can be divided in two portions (Fig. 4.5),

Name	Airspeeds	FAR-25	FAR-23
Take-off stall speed	V_{STO}	-	-
Minimum control speed	V_{MC}	$\leq 1.13 V_{STO}$	$\leq 1.20 V_{STO}$
Minimum control speed on ground	V_{MCg}		$< V_{LO}$
Minimum control speed while airborne	V_{MCa}		-
Decision speed	V_1	$\geq 1.10 V_{STO}$	
Rotation speed	V_R		$\geq V_1$
Minimum unstick speed	V_{mu}		$> V_{STO}$
Lift-off speed	V_{LO}		$> 1.10 V_{mu}$
Take-off safety speed	V_2		$\geq 1.20 V_{STO}$

Table 4.1: Definition of characteristics airspeeds for take-off phase.

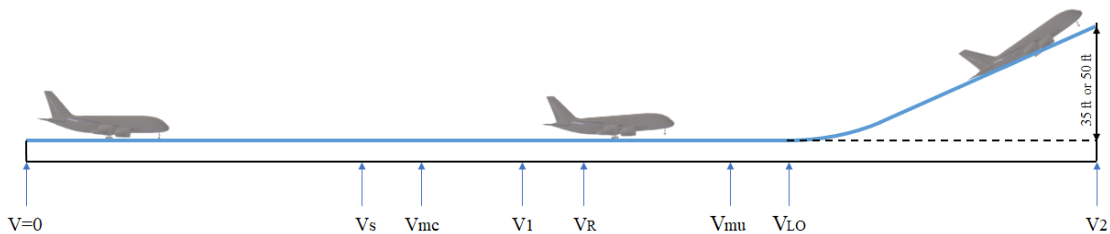


Figure 4.4: Take-Off phase characteristics speeds.

the ground roll phase (S_g) and the airborne phase (S_a). Take-off can be analysed considering any formulation from literature, but the presence of hybrid-electric architectures introduces three main differences. The first one has been discussed

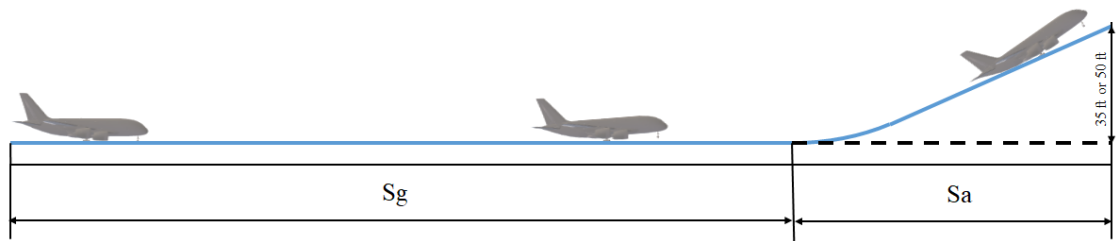


Figure 4.5: Take-Off phase main segments.

previously and deals with the engine deck and the algorithm to calculate the total thrust, summarized below.

- The take-off phase is divided into time steps. At the beginning of each time step, speed, altitude, and throttle are defined.
- Based on speed, altitude, and throttle, the engine deck is queried to determine power and fuel flow.
- This value of power is multiplied by the number of gasturbines, fuel cells or e-motor drives in the propulsive system, depending on which is the reference power of the engine deck.
- The powertrain equations provide the total propulsive power based on the efficiency of each element at the time step considered.

From propulsive power and airspeed, the total thrust can be determined.

The second difference is related to the *Balanced Field Length* (BFL) and its associated decision speed. The regulation requires a rotation speed greater than the decision speed. When considering these constraints at the early stages of the design process, a common approach is accounting for a rotation speed that is at least 10% higher than the stall speed. However, when the stall speed is lowered by the beneficial effect of high-lift propellers, this value of the rotation speed can be critical if compared to the decision speed. Thus, the simulation of the take-off phase is performed in two separate conditions: the all-engine operative condition and the one-engine inoperative condition associated with the most severe thrust loss, as discussed in 2.3.1. This second simulation is aimed to identify the balanced field length and

the decision speed in order to verify the compliance with regulation constraints and performance requirements, often provided in terms of maximum take-off run.

The last main difference with conventional take-off deals with the aero-propulsive interactions, whose details have been discussed in 2.2. In particular, aero-propulsive interactions associated with distributed electric propulsion cause an increment of the maximum lift coefficient. Consequently, stall speed is lowered, causing a significant change of the minimum allowed values of lift-off, rotation, and decision speeds.

In the present context, a simple formulation of the take-off phase would be sufficient to highlight the effect that these differences have on the total take-off distance. The first simplifying hypothesis consists in modelling the aircraft as a point-mass. In other words, the angular acceleration is constantly equal to zero. Thus, in the present context, the rotation speed will not be calculated but assumed to be equal to the limit value, which is 5% higher than the stall speed. As previously stated, the take-off phase can be divided in two flight segments. The first one, the ground phase, is ruled by dynamic equations derived from the free-body diagram in Fig. 4.6. In case of a perfectly horizontal and flat runway, considering a point-mass

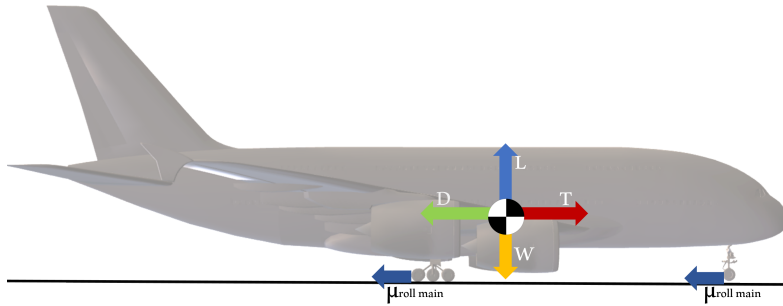


Figure 4.6: Take-off ground run equilibrium of forces.

model, Eq. (4.2) is sufficient to describe the acceleration phase.

$$\sum F_x = ma_x = \frac{W}{g} \frac{dV}{dt} \Rightarrow T - D - \mu_{roll}(W - L) = \frac{W}{g} \frac{dV}{dt} \quad (4.2)$$

In Eq. (4.2), the x-axis is the horizontal axis positively oriented according to speed direction. Reordering the equation, Eq. (4.3) is obtained.

$$\frac{dV}{dt} = \frac{g}{W} [T - D - \mu_{roll}(W - L)] \quad (4.3)$$

Opportunely integrated, Eq. (4.3) can be used to calculate ground roll distance and time, energy and fuel consumptions. Aero-propulsive interactions affect in opposite manners the acceleration and, thus, the time by which the lift-off speed is reached. Moreover, the effect of the aerodynamic forces on the acceleration time reflects on fuel and energy consumptions. Step by step, thrust is calculated considering the speed at the beginning of each time step; then, the interactions between the propulsive slipstream and the lifting surfaces are considered to calculate the aerodynamic forces. After substituting the obtained values in Eq. (4.3), the equation is integrated to calculate speed and distance covered at each time step. The value of S_g is given by the sum of these contributions.

Continuing with a simplified approach, the second part of the take-off phase, the airborne phase, can be dealt with as the portion of a pull-up manoeuvre performed at constant speed, whose value is equal to the arithmetic mean between V_{LO} and V_2 . The two airspeeds are constrained in connection to the take-off stall speed, directly affected by aero-propulsive interactions between distributed electric propellers and the main lifting surface. In the end, the minimum airspeed of the airborne phase is lowered and the same goes for the distance necessary to clear the screen required by regulation.

In order to highlight the effect of distributed electric propulsion on ground performance, considering a wide range of shaft power ratios, the different take-off runs will be measured for the same regional turboprop (Fig. 4.15). The aircraft

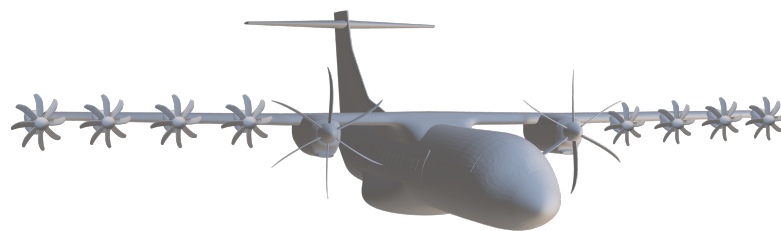


Figure 4.7: Regional turboprop considered.

chosen weights 24000 kg , with a thermal installed power of about 1880 kW per engine. At take-off, the maximum power provided by the battery has been fixed to 750 kW . The wing area is 43.60 m^2 . Associated to different shaft power ratios,

the thrust provided by the eight distributed propellers affects differently the lifting capability of the wing. The main effect of this interaction is the lower take-off stall speed, as reported in Table 4.2. In the end, keeping constant mass and installed

Shaft power ratio	Stall speed (m/s)	Maximum lift coefficient
0.0	64.79	2.1
0.5	59.40	2.5
0.8	56.87	2.7
1.0	55.46	2.9

Table 4.2: Take-off stall speed and lift coefficient associated to different shaft power ratios.

power, these differences result in as many take-off runs, as shown in Table 4.3.

Shaft power ratio	Stall speed (m/s)	Take-off run (m)
0.0	64.79	1291
0.5	59.40	1091
0.8	56.87	1020
1.0	55.46	983

Table 4.3: Take-off stall speed and run associated to different shaft power ratios.

When simulating a failure during the take-off run, a standard procedure for measuring the balanced field length is assuming that at each time step, the most critical failure for the propulsive system occurs. After the occurrence of the failure, the power management system performs the re-distribution of the remaining power proposed in 2.3.1. Starting from that moment, two different procedures can be adopted. On the one hand, the aircraft can perform its take-off phase with the resulting propulsive power, requiring a longer take-off run to reach the lift-off speed. On the other hand, the pilot can brake the aircraft within a certain distance. Both procedures are simulated to measure the balanced field length, that is the value where, at the occurrence of the failure, the distance to accelerate and stop is equal to the take-off distance. The speed associated with the occurrence of the failure is the decision speed, as shown in Fig. 4.8.

Associated with the same shaft power ratios of Table 4.3, the balanced field lengths obtained are presented in the Table 4.4.

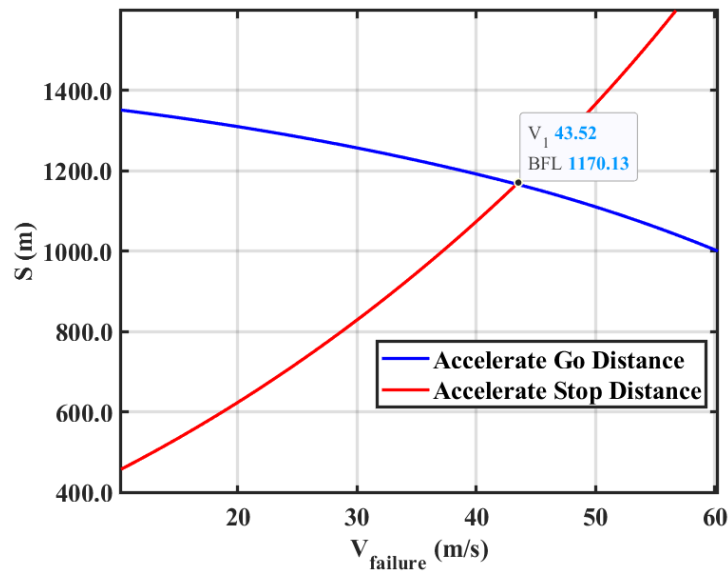


Figure 4.8: Balanced field length.

Shaft power ratio	Balanced field length (m)	Decision speed (m/s)
0.0	1594	50.69
0.5	1312	46.02
0.8	1216	44.33
1.0	1166	43.48

Table 4.4: Balanced field length and decision speed associated to different shaft power ratios.

4.2.2 Climb and Ceiling

In this work, the **climb** phase is divided into two different segments: the first part, up to 10000 ft, is governed by air traffic procedures, the second one ranges from 10000 ft to the cruise altitude. The importance of this split is related to the different power requirements and constant airspeed considered along with the two segments. The first part of the climb phase is strictly regulated by ICAO procedures [138] (Fig. 4.9).

Three different procedures are considered, as shown in Fig. 4.10 [138]. The *Standard* procedure prescribes the following sequence of steps: a first segment of climb, which goes up to 1000 ft, performed at constant CAS (V_2), an acceleration phase up to $CAS1 = V_2 + 20$ kts, a second segment of climb up to 3000 ft at constant CAS, a second acceleration phase up to 250kts and a last segment of climb performed at constant CAS. *ICAO A* is the second procedure presented. In this

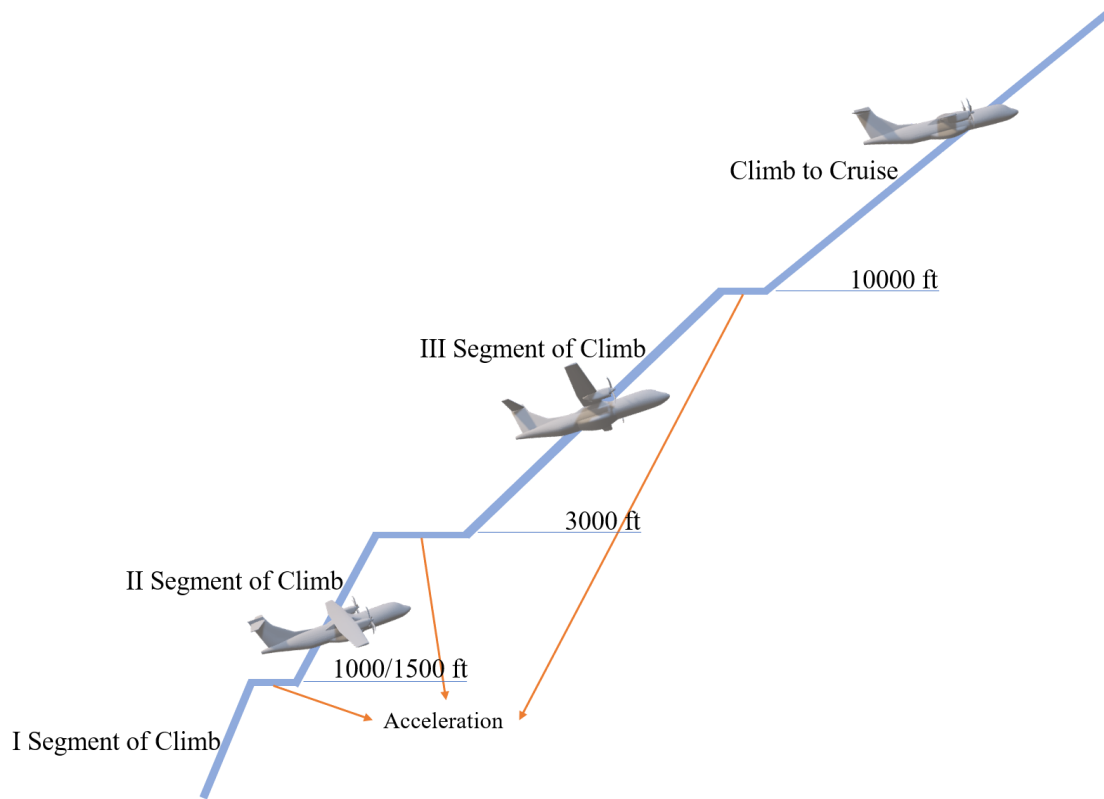


Figure 4.9: Illustration of a general ICAO procedure to climb up to 10000 ft.

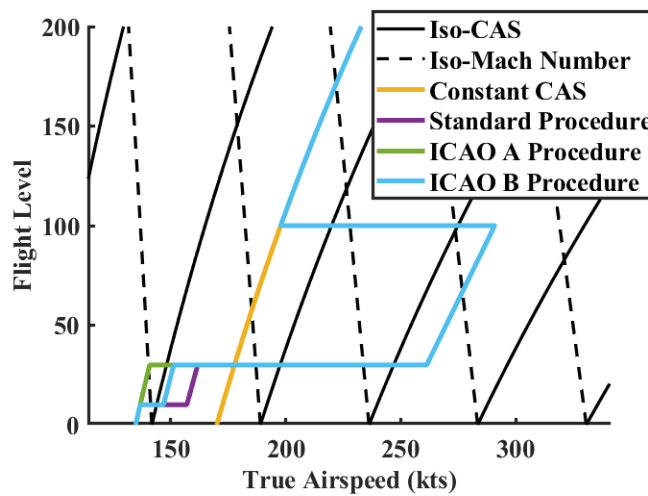


Figure 4.10: Different climb strategies adopted.

case, the climb segment up to 10000 ft is divided into the following parts: a first climb part up to 1500 ft, performed at constant CAS (V_2) and at take-off engine setting, a second part up to 3000 ft at the same CAS of the previous segment, but at climb engine setting, an acceleration phase to reach the optimal climb CAS of the aircraft and, finally, a third segment of climb performed at constant CAS. The last procedure, *ICAO B*, prescribes a first segment of climb up to 1000 ft, performed at constant CAS, an acceleration phase in which the aircraft passes from V_2 to $CAS1 = V_2 + 10\text{kts}$, a second segment of climb at constant CAS, which extends from 1000 ft to 3000 ft, a second acceleration phase up to the optimal climb airspeed and a last segment of climb performed at constant CAS. The presence of acceleration phases and the use of take-off settings during the early steps of these procedures require a different approach in terms of supplied and shaft power ratios with respect to the following segment of climb from 10000 ft up to the cruise altitude. In fact, on the one hand, considering the high attitude and low speed of the early stages, the use of distributed electric propellers could be beneficial during this phase; on the other hand, the power demand can be fulfilled by two power sources in order to reduce the required thermal power. These aspects related to the mission profile are often ignored in literature, preferring a unique segment at constant rate of climb or calibrated airspeed.

The considerations dealing with high attitude and power demand made for the previous climb step may not apply to the following segment. In other words, depending on the constant calibrated airspeed or the constant rate of climb at which the climb to cruise is performed, the use of distributed electric propulsion and supplied power ratio other than zero may have negligible or null benefits. The aero-propulsive interactions and the hybrid-electric power system affect the way the climb phase thrust, fuel consumption, lift and drag are estimated in a similar way as the one discussed for the take-off phase. Step by step, the thrust related to a certain value of the rate of climb or calibrated airspeed is calculated, then, from Eq. (2.3), the value of power required to the gasturbine is calculated and,

from the corresponding throttle setting, the corresponding fuel flow. A simple algorithm to climb at constant CAS is the following.

- At each time step, for the associated altitude, the climb setting of the engine deck is interrogated for the prescribed airspeed.
- Using Eq. (2.5), the propulsive power is calculated from the value obtained at the previous step.
- Drag and lift are calculated considering the aero-propulsive interactions.
- From the previous steps, the rate of climb associated with these aerodynamic and propulsive characteristics is calculated.

A more complex algorithm is required in case of climb at constant rate of climb. In fact, it is necessary to calculate the combination of speed and propulsive power required to obtain that value of rate of climb. The following algorithm can be used in case of constant rate of climb.

- At each time step, the query of the engine deck covers a wide range of plausible airspeed values.
- The propulsive power is calculated for each value obtained at the previous step.
- Drag and lift are calculated considering the aero-propulsive interactions.
- From the previous steps, the rate of climb associated with each power can be calculated.
- Interpolating the various rate of climb, the climb speed associated with the rate of climb prescribed is obtained and, therefore, the resulting propulsive and aerodynamic characteristics.

Independently from the chosen climb procedure, if the calculated power is higher than the one affordable by the thermal engine, the speed must be lowered. At the same time, considering the thrust delivered by each engine setting, the aero-propulsive effects are estimated in terms of variation of the aerodynamic coefficients.

One last consideration is here highlighted in connection to the propulsive power distribution. A neglected benefit associated with powertrain with multiple propulsive

lines is the opportunity to distribute the propulsive power during climb and take-off in order to reduce the sizing power of the single components. Thus, high-lift propellers can lower the mass of the main propulsive line, directly proportional to the sizing power, when used during both take-off and climb. From this point, further considerations related to the management of the power in case of failure should be made case by case.

The simulation of the climb phase is associated with the evaluation of another flight performance: the ceiling altitude. The minimum ceiling altitude in all-engine operative and one-engine inoperative conditions is often a requirement reflecting on the installed power. When coming to electric concepts, the effect of altitude on propulsive performance is lowered due to the insensitivity of the electric components to flight conditions. This is the second benefit of the electric propulsive systems, in addition to the power management in case of failure. This is especially true in case of batteries, but cannot be generally said for the case of breathing fuel cells since it depends on the power provided by an inlet and a compressor. Assuming the compressor map proposed in Fig. 2.8, the sensitivity of the fuel cell is not relevant at flying altitudes of interest, but it could be a limiting factor for the one-engine ceiling altitude, as shown in Fig. 4.11. Assuming the same installed power, the

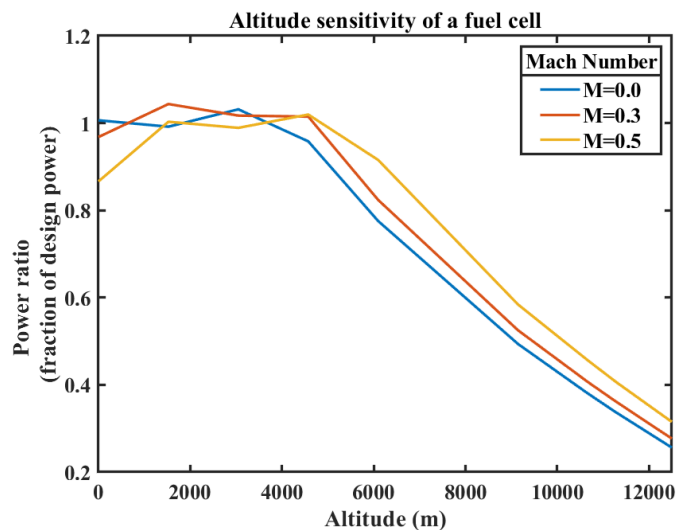


Figure 4.11: Altitude sensitivity of a fuel cell composed by 6 parallel stacks, with a resulting total design power of about 1167 kW.

comparison of Fig. 4.11 and Fig. 4.12 highlights the different sensitivities of the two propulsive technologies. In the end, the choice of power sources with negligible sensitivity to flight altitude can be beneficial for ceiling performance.

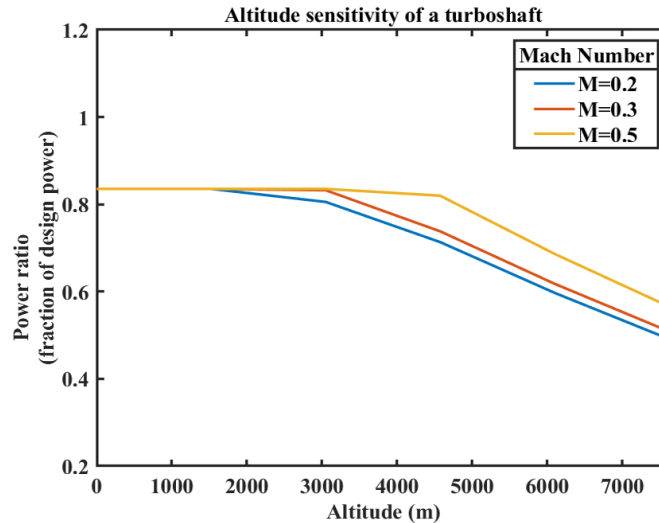


Figure 4.12: Altitude sensitivity of a turboshaft climb power rating with a rated power of about 1167 kW.

4.2.3 Cruise

The **cruise** phase can be flown considering different strategies: constant altitude and Mach number, constant Mach number and attitude, constant altitude and lift coefficient, and stepped. In particular, this last flight strategy is composed of steps at constant Mach number and altitude alternated to climb steps at constant calibrated airspeed.

Among the different strategies, the objective of maintaining *constant altitude and lift coefficient* requires adapting the airspeed to the variation of weight while burning fuel. Thus, the flight speed is calculated step by step. Aside from that, the following steps can be applied to all flight strategies.

- At each time step, flight Mach number and altitude are used to calculate the power delivered to the propulsive system at maximum throttle setting.
- Moving from the associated value of thrust, calculated as discussed in 4.1, the aero-propulsive effects on lift and drag are calculated.

- Drag and Thrust are compared to calculate the throttle setting required and the associated fuel consumption.
- The process is iterated considering the variation of the aerodynamic coefficient due to the aero-propulsive interactions as convergence criterion.

In case of stepped cruise strategy, the flight segment of climb at constant airspeed is managed as proposed for the climb phase.

Three main considerations related to this flight phase must be accounted when designing an electric vehicle. The first point deals with the mission strategies where attitude and/or Mach number vary while burning fuel. Differently from conventional concepts, the variation of weight during the phase is a small percentage of the total aircraft weight, leading to an approximatively constant set of flight parameters. At the extreme point of a full-electric concept, it is possible to maintain contemporaneously constant altitude, attitude, and Mach number. The following aspect discussed deals with the impact of this long time phase on global energy consumption. Even if take-off and climb could be critical aspects for power requirements, the effect of cruise range can be a killing requirement in terms of electric energy required. In fact, due to the low specific energy of batteries with respect to other power sources (e.g.: fuel or hydrogen), the design range could cause an abrupt increment of the maximum take-off weight and this, in turn, would affect aircraft performance. Thus, when estimating power and energy requirements, the designer should account for three different mission profiles with three different ranges: design mission, typical mission, and maximum range mission. In fact, when more than one power source is considered, the sizing powers cannot be preliminary referred to the design mission and the energy required to each source cannot be fixed based on the maximum range required. A common procedure would require of investigating the three mission profiles with levels of hybridization among the different power sources, then, choosing the most convenient alternative in terms of mass. However, some guidelines can be preliminary considered:

- the energy required to the battery should be aimed to minimize the fuel consumption during the typical mission;

- the power required to the battery is generally associated to the typical mission, where the shorter range allows higher supplied power ratios in all phases;
- fuel or hydrogen tanks should be dimensioned to carry the necessary mass to accomplish the mission with the highest range.

The last consideration deals with the reference altitude of this flight phase. As already discussed in the case of the climb phase, altitude is not a major issue when coming to electric components. However, since the reference altitude could be challenging for the thermal engine when the aircraft accelerates up to cruise speed, the following condition should be verified: assuming the minimum power supplied by the battery among the different mission profiles considered, the other power sources experimenting a certain sensitivity to flight conditions shall demonstrate their capability to withstand the power required by the acceleration phase up to maximum cruise flight speed. On the contrary, cruise airspeed or altitude shall be lowered.

4.2.4 Descent

The **descent** properly said is a phase ranging from cruise altitude up to 1500 ft above airport altitude. Differently from the previous flight phases, where the engine deck settings are clearly defined, the descent phase sometimes requires interpolating two different engine deck ratings: flight idle and cruise at minimum throttle setting. Since flight idle is the condition of minimum power supplied by the engine deck, throttle is always equals to 1 for this power rating. An intermediate power level between the two ratings can be necessary, for example, to maintain the constraints on the flight path angle when the flight idle power rating is not sufficient.

Three different approaches are possible for the present flight phase: a multi-stage descent, an unsustained descent at constant calibrated airspeed (CAS) or a sustained descent at constant calibrated airspeed and rate of descent (RD). The multi-stage descent procedure is illustrated in Fig. 4.13 [138]. In this case, the descent is divided into four flight segments. At the end of the cruise phase, airspeed could be higher or lower than the desired CAS. In the first case, the descent phase is preceded by a deceleration phase at cruise altitude. Otherwise, the first descent segment is

performed at constant Mach number up to the altitude where it reaches the desired calibrated airspeed for the descent phase. When the right CAS is reached, the aircraft descends to 10000 ft with a flight path constrained to an angle of -3 deg . At 10000 ft, a deceleration phase is performed up to the speed of maximum efficiency (called $V_{green \ dot}$) at 1500 ft plus 5 knots. At this newly calibrated airspeed, the last segment takes the vehicle at the approach altitude of 1500 ft.

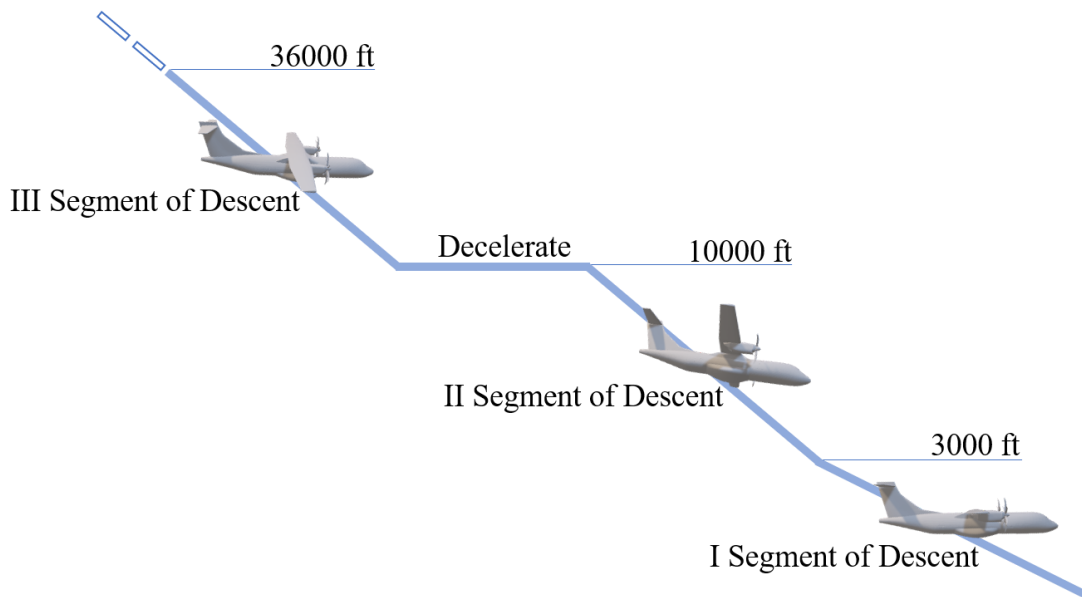


Figure 4.13: Illustration of the standard procedure for descent up to 1500 ft.

Independently from the strategy chosen for the descending phase, the use of distributed propulsion, tip-mounted propellers or boundary layer ingestion have a minor or negligible impact on the fuel consumption. However, if it is the case, the aero-propulsive interactions can be estimated after calculating the propulsive power. Similarly to the climb phase, two different algorithms are applied when simulating a descent segment at constant rate of descent or at constant calibrated airspeed.

4.2.5 Alternative Cruise

The **alternate** (or **divergence**) phase can be managed as a cruise phase at constant altitude and Mach number. When evaluating alternate and loiter requirements, it should be considered that these optional phases cannot be preliminary

included in the flight schedule, since they are imposed by air traffic control to face the occurrence of critical and unexpected conditions. Thus, the energy required to fly an alternative cruise cannot be consumed during the previous flight phases, even if it is not planned to be flown. In conclusion, the use of power sources with low values of specific energy (e.g.: batteries) is discouraged during these phases.

4.2.6 Loiter

In case of air traffic congestion at the landing airport, the aircraft could be required to hold the flight path. This is the **loiter** (or **holding**) phase. Differently from the cruise phase, loiter is flown at maximum efficiency or minimum necessary power. More specifically, the choice between the two airspeeds is made considering the minimum fuel flow required. In case of jet aircraft, the minimum fuel flow corresponds to the minimum drag, which, in turn, corresponds to the maximum efficiency. Conversely, in case of propeller aircraft, the minimum necessary power corresponds to the minimum fuel flow. However, the choice of one speed with respect to the other can be related to other variables, such as the proximity to the landing regulation screen. In fact, the holding altitude could be insufficient to descent and decelerate to the flight speed required over the obstacle. This phase has been widely discussed in literature [138,143] for conventional aircraft. However, some additional considerations should be made to highlight the difference with respect to electric aircraft. The first consideration deals with the flight speed associated with the minimum power required or the maximum efficiency [182]. Burning fuel, the aircraft weight changes and the same goes for the attitude and the airspeed associated with those flight conditions. This is true in case of aircraft consuming hydrogen or fuel, including hybrid-electric concepts. Furthermore, as previously stated discussing the alternate phase, in case of hybrid-electric concepts, the use of electric energy from sources with low values of specific energy is discouraged for reserves. On the other hand, full-electric aircraft are not affected by this variation.

Once the chosen airspeed or attitude has been fixed, loiter can be treated as a cruise phase at constant attitude and altitude.

4.2.7 Approach

The **approach** phase ranges from 1500 ft above the ground to the landing screen (50 ft above the airfield). It is a complex phase managed by landing instruments that couples descent and deceleration while changing high-lift devices settings [138]. In this context, the rectilinear flight path is constrained by a descent slope of -3 deg . Assuming equally spaced time steps and constant deceleration rate, the airspeed at each point of the flight segment is determined and the resulting rate of descent can be calculated. From this, the required propulsive power is determined.

The effect of high-lift propellers on this phase is related to the target value of the approach speed. In fact, approach speed is given as a fraction of the stall speed, which, in turn, is lowered by stall speed [22]. As a result, the deceleration phase depends on this.

4.2.8 Landing

The **landing** phase is the last step of the flight mission, excluding **taxi-out** that will not be discussed in this context. Generally, landing can be divided into an airborne phase and a ground phase, as shown in Fig. 4.14.

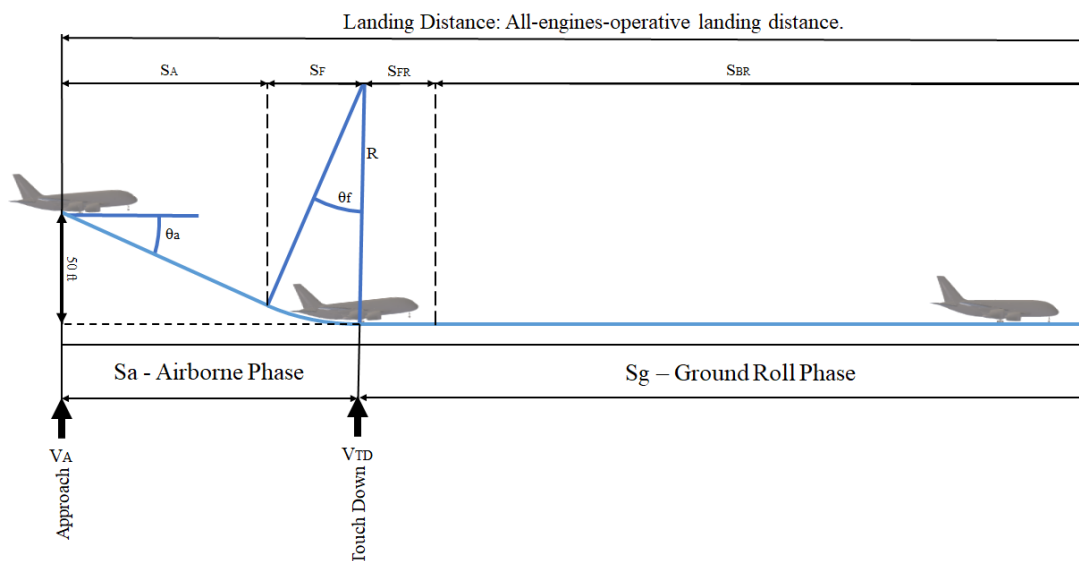


Figure 4.14: Landing phase.

Differently from take-off phase, the airborne phase and the ground phase are flown considering two different engine settings: flight idle and ground idle, respectively. However, the considerations dealing with the propulsive system and the aeropropulsive interactions made in case of take-off can be similarly applied to landing. The airborne phase is further divided into two segments. The first one is a descent at constant flight angle and speed. This segment starts upon reaching the landing obstacle, at 50 ft above the airfield, as prescribed by regulation. The second one, referred to as flare segment, joints the first one and the ground roll. The characteristic speeds delimiting each flight segment have been reported in Table 4.5.

Name	Airspeeds
Landing stall speed	V_{SL}
Approach speed	V_A
Flare speed	V_{FL}
Touchdown speed	V_{TD}

Table 4.5: Definition of characteristic velocities of the landing phase.

The dependence of the landing distance from the characteristic speeds indirectly connects this ground performance to the stall speed. Since approach speed cannot be lower than the stall speed at landing, one way of reducing the landing distance is by introducing high-lift propulsion to increase the maximum lift coefficient. Generally, approach speed is 30% higher than stall speed at landing.

In the present section, three simple mathematical models are considered to describe the flight segments composing the landing phase. The objective is to highlight the dependence of the main parameters governing the landing phase from lift, drag, and thrust. The effect of the unconventional propulsive systems on these forces determines the impact on landing performance.

The first airborne segment is flown at constant approach angle θ_a and airspeed. The approach angle can be calculated as reported in Eq. (4.4) and it should be maintained approximatively equal to -3 deg.

$$\theta_a = \frac{D - T}{W} \quad (4.4)$$

It is here highlighted that the effect of distributed propulsion on the approach angle is twofold: on the one hand, the drag increment caused by aero-propulsive interactions; on the other hand, the thrust provided by the propulsive system.

The last airborne part of the landing phase, the flare segment, is governed by the characteristic speeds ranging between approach speed and touch-down speed, which are defined as a function of the stall speed. Thus, the effect of aero-propulsive interactions on the stall speed affects this phase as well. This phase is characterized by a pitch-up manoeuvre while decelerating.

After touchdown, the last segment is the ground run, which is governed by the same forces reported in Eq. (4.2) with the only additional contribution to μ_{roll} provided by brakes. In this case, the thrust is null or negative (reverse thrust), where the propulsive system allows it.

As previously stated, regarding the engine power rating, the engine idling is applied during the approach. However, when considering concepts with distributed electric propellers, this procedure limits the competitiveness of the propulsive system whose benefits are strongly related to thrust. In this respect, the Federal Aviation Administration (FAA) adopted a different constraint for the propulsive units designed to provide advantages in aerodynamics [22]. In this case, the nominal thrust condition applies to the measure of stall speed. Even then, the approach angle must be kept approximatively equal to -3 deg , which requires equilibrating the thrust provided by high-lift propulsion with the drag increment or the reverse thrust of the primary propulsive system.

Regarding this second alternative, certification procedures require validating the landing distance without using reverse thrust, which results in a limiting factor when measuring the actual maximum lift coefficient allowed by high-lift propellers. In fact, without reverse thrust to equilibrate the forward thrust provided by high-lift propulsion, the angle of attack could exceed -3 deg because the drag increment is lower than the increment of thrust.

One last consideration is related to the flight idle power rating considered during the airborne phase. Differently from point performance discussed in the

Shaft power ratio	Flight idle rating (Total shaft power: 60 kW)		Take-off rating (Total shaft power: 2150 kW)	
	Maximum lift coefficient	Stall Speed (m/s)	Maximum lift coefficient	Stall Speed (m/s)
0.0	2.70	56.53	2.70	56.53
0.5	2.70	56.46	2.92	54.38
0.8	2.70	56.42	3.06	53.18
1.0	2.71	55.40	3.19	52.32

Table 4.6: Stall speed and maximum lift coefficient at landing for two different power ratings of a turboshaft powering eight distributed electric propellers.

previous chapter, landing simulation highlights a poor increment of the maximum lift coefficient when considering the flight idle setting, as shown in Table 4.6 for the case of a regional turboprop (Fig. 4.15). On the contrary, a different power rating requires using reverse thrust or air-brakes in the case of large aircraft landing with the support of high-lift propulsion.

The following part of this section regards some landing procedures to deal with this issue. The hybrid-electric regional turboprop shown in Fig. 4.15 is considered. The electrification of the platform requires an increment of the overall weight. The maximum landing weight considered is 22644 *kg*, which is 92% of the maximum take-off mass.

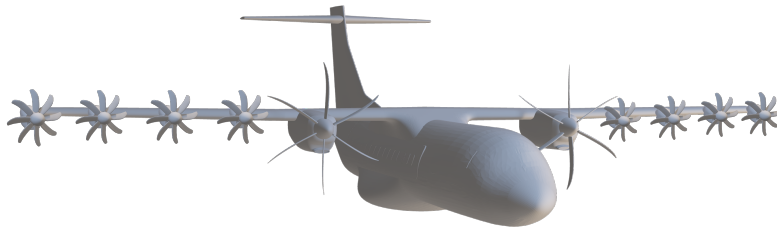


Figure 4.15: Hybrid-electric regional turboprop.

The hybrid-electric aircraft presented is similar to the ATR-42, but its wing area is reduced by about 20%. This value is in line with the point performance measured at landing when the distributed propulsion is enabled ($\phi = 0.8$). However, during the simulation of the landing phase, high values of thrust or aerodynamic efficiency can determine a longer run. Three different approaches are compared:

- 1 the certification procedure at flight-idle power rating;
- 2 the landing at take-off power rating;

3 the use of air-brakes to lower the landing distance while using distributed propulsion at nominal thrust.

The first procedure is studied by including the reverse thrust after the touchdown. This case is the benchmark for the comparison (Table 4.7). The second procedure

Landing		
Parameter	Value	Unit
Power rating	Flight Idle	-
Stall speed	55.65	m/s
Landing run	1164	m
Thrust at approach	11196	N
Thrust at touch down	-14417	N

Table 4.7: Results of the landing simulation performed considering the first procedure described.

described requires the mitigation of the thrust provided by the distributed propellers with the windmilling power of the main propellers. The reverse thrust generated after the touchdown is the 10% of the nominal thrust. Regarding the third landing protocol, the air-brakes are considered to have a drag coefficient of about 0.7. The three procedures can be optimized by studying different combinations of shaft power ratio, throttle, and air-brakes area. In this contest, the air-brakes area has been fixed at $3 m^2$ (Fig. 4.16). The stall speed at landing, without including the effects associated to high-lift propulsion, is $56.53 m/s$. The comparison of the two

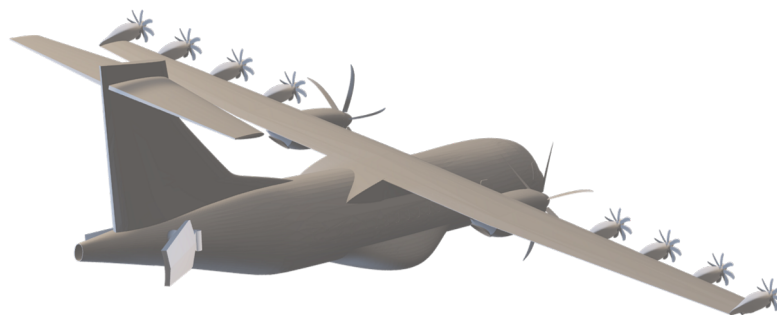


Figure 4.16: Particular of air brakes mounted on the tail cone the regional turboprop.

procedures is proposed in Fig. 4.17. The landing run is a critical performance for electric aircraft of this category. The inclusion of distributed propulsion may be insufficient to reduce the wing area due to the resulting approach angle. In the

end, a viable solution is found in the application of air-brakes and reverse thrust at landing, if the values of the reverse thrust are demonstrated to be feasible.

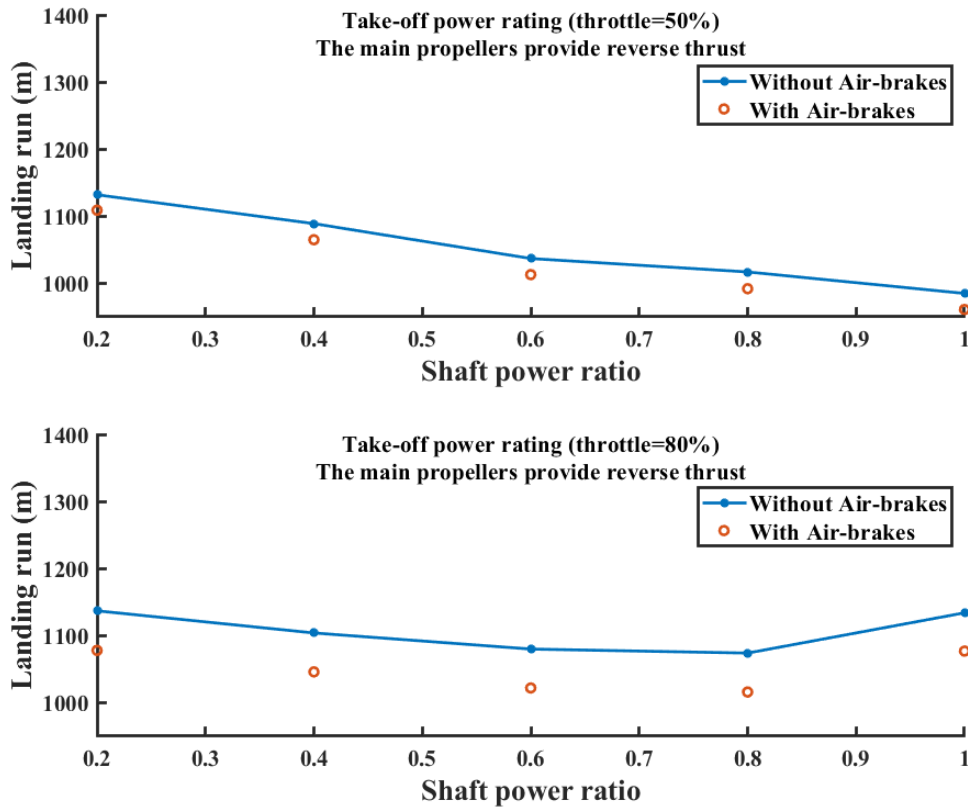


Figure 4.17: Comparison of different landing procedures for different values of the shaft power ratio and the throttle. The nominal thrust of the thermal engine at take-off is 1888 kW (the supplied power ratio is equal to zero).

4.3 Validation of the Algorithm

Concerning the validation of simulation algorithms, the procedure involves the comparison of flight performance estimated with those measured during the flight tests. On the other hand, since the main element of novelty is the integration of the electric propulsion, whose flight tests are difficult to find, the procedure has been adapted considering two main steps. The first one is the validation of the powertrain model by comparing the results with the simulation performed with high fidelity tools. The second step is the validation of the whole flight simulation by

comparing the results obtained with those concerning flying platforms or that have been shared by industrial partners. The separate validations at mission level and at system level are necessary for two reasons. Firstly, the comparison of the flight simulations performed with different tools is not a valid benchmark since similar errors can lead to similar results. This makes necessary the use of flight data or data that have been validated by industrial partners. Secondly, the simulation of a conventional aircraft or a hybrid-electric platform is here performed considering the same mathematical model constituted by the powertrain equations. However, the simulation at system level with high-fidelity tools can determine the reliability of the rated powers calculated through this algorithm.

The validation of the propulsive system model requires a large number of input elements describing the propulsive architecture and the characteristics of each component. The industrial background necessary to provide all the information to calculate high-fidelity results is one of the main disadvantages of this propulsive system model. The validity of the assumptions has been tested thanks to the support of Rolls-Royce and GE AVIO in the frameworks of two European research projects. Thanks to the involvement of these partners and high-fidelity simulations, as the one shown in Fig. 4.18, the mathematical powertrain model for hybrid-electric and full-electric aircraft has been validated with a good confidence level (98%).

The first step to validate the system is the collection of the data required by the powertrain model described in 2.1. In this perspective, the engine deck, the characteristics of the battery cells, and the efficiency maps of the e-motor drives are collected to describe the dynamics of the propulsive system through the procedure described in 4.1. Generally, this information is provided by the manufacturers or the industrial partners involved at the beginning of the design process. Alternatively, appropriate high-fidelity tools for the design of single components can be used. After this preliminary set-up, the following step is the simulation of each flight segment. The same simulation is performed using both the algorithm proposed in this chapter and the high-fidelity tools available for software architecting (e.g.: Simcenter or Simulink). The last step is the comparison of the data collected from

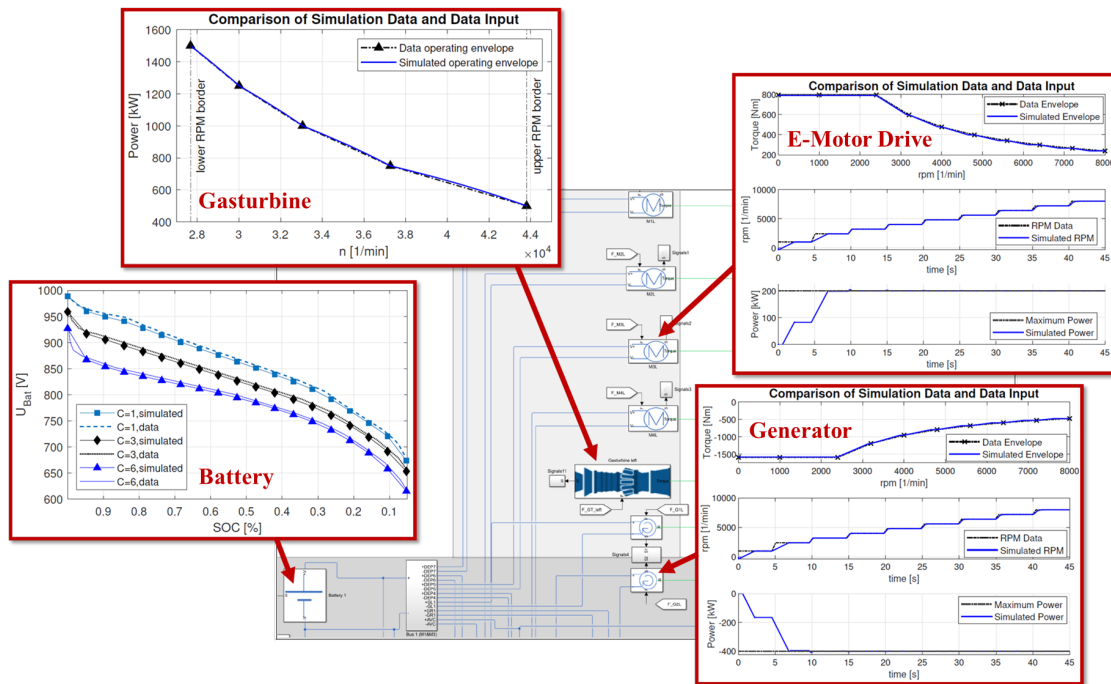


Figure 4.18: Simulation for the validation of the powertrain model used in the framework of the European project ELICA (ELeCtric Innovative Commuter Aircraft) [183].

the simulations.

By way of example, the hybrid-electric architecture in Fig. 4.19 is studied to validate the system model. The propulsive system powers the commuter aircraft studied in the European project ELICA (ELeCtric Innovative Commuter Aircraft). The comparison starts by verifying the compliance of the input data considered. In other words, the efficiency maps and the characteristics of the power sources are verified. For the present case, Fig. 4.20 and Fig. 4.21 show the comparison of the input data describing the thermal power source. In the same way, Fig. 4.22 shows the comparison of the inputs concerning electric power source. Finally, the input efficiencies are validated measuring the power losses measured by the high-fidelity tools (Fig. 4.23).

Once the inputs have been verified, the following step is the comparison of the dynamic behaviours simulated by the low and high fidelity methods. To sum up, the power managed by each element is calculated through the powertrain equations and, then, compared to the value at the same time-step calculated by the high-fidelity tool. For instance, considering the take-off phase, the power of each element is

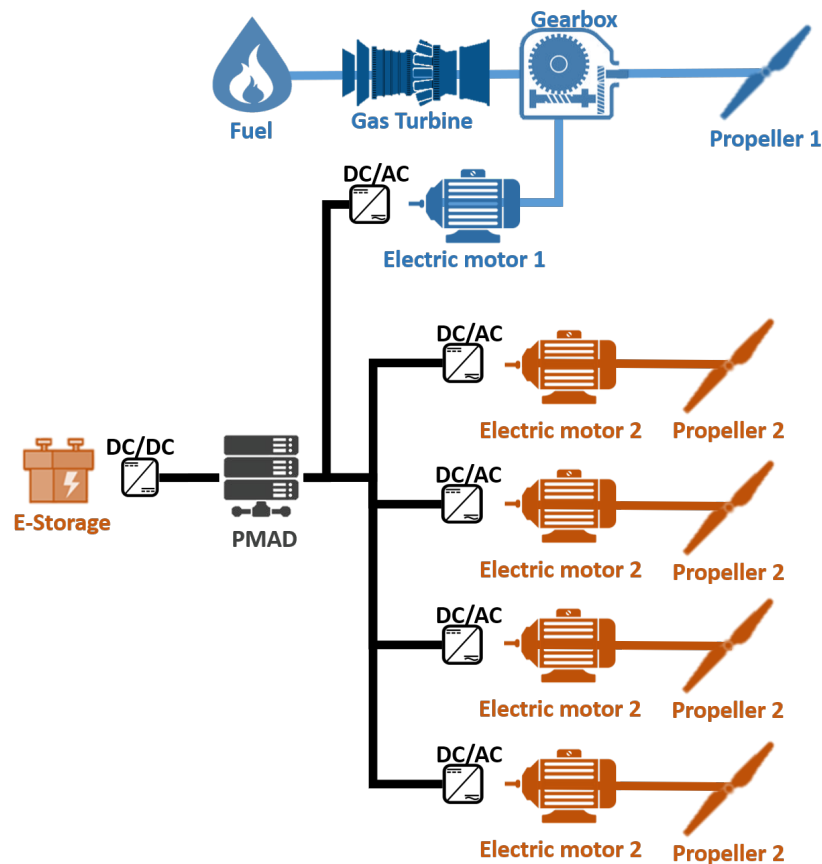


Figure 4.19: Serial/parallel partial hybrid-electric powertrain.

reported in Fig. 4.24 for the validation carried out in collaboration with Rolls-Royce.

In this section, the validation of the flight simulation is assessed by comparing the results concerning two different platforms: a regional turboprop similar to ATR-42 and a commuter aircraft similar to the one proposed in Ref. [184]. The two platforms have been modified with respect to the original aircraft to preserve the intellectual property of the owners. However, the consistency of the results has been assured by the supervision of Leonardo S.p.A. and Piaggio S.p.A. in the framework of different European projects.

Considering the regional turboprop shown in Fig. 4.25, the same data of the reference aircraft in terms of geometry, weight, and aerodynamics have been considered. An extract of these geometric data is provided in Table 4.8 and Table 4.9.

From the geometry of the three lifting surfaces described in Table 4.8, knowing

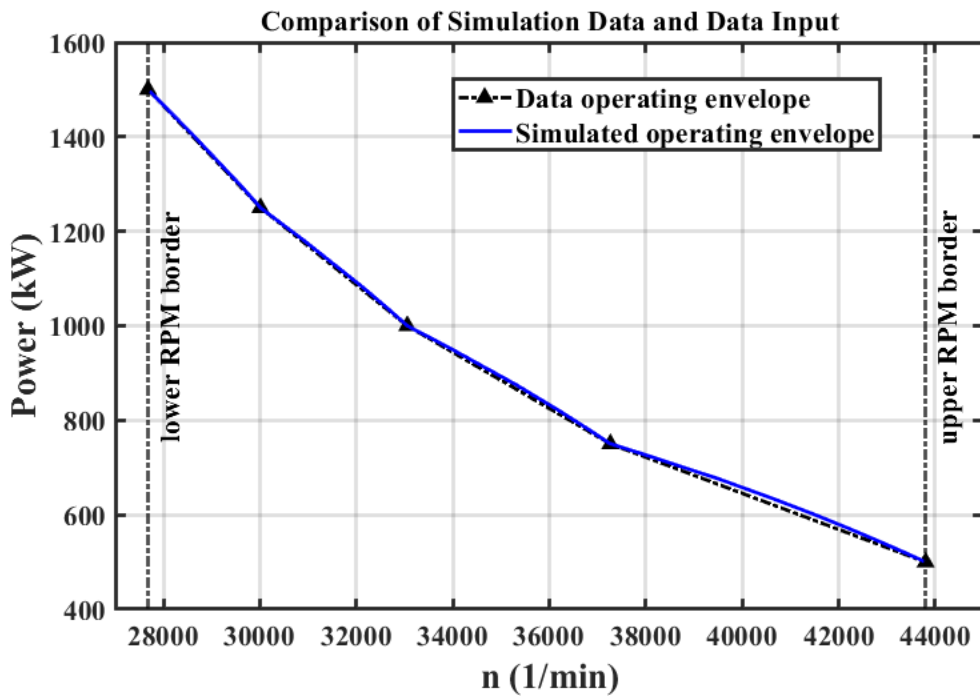


Figure 4.20: Comparison of the inputs used to describe the power supplied by the turboshaft to the propulsive system.

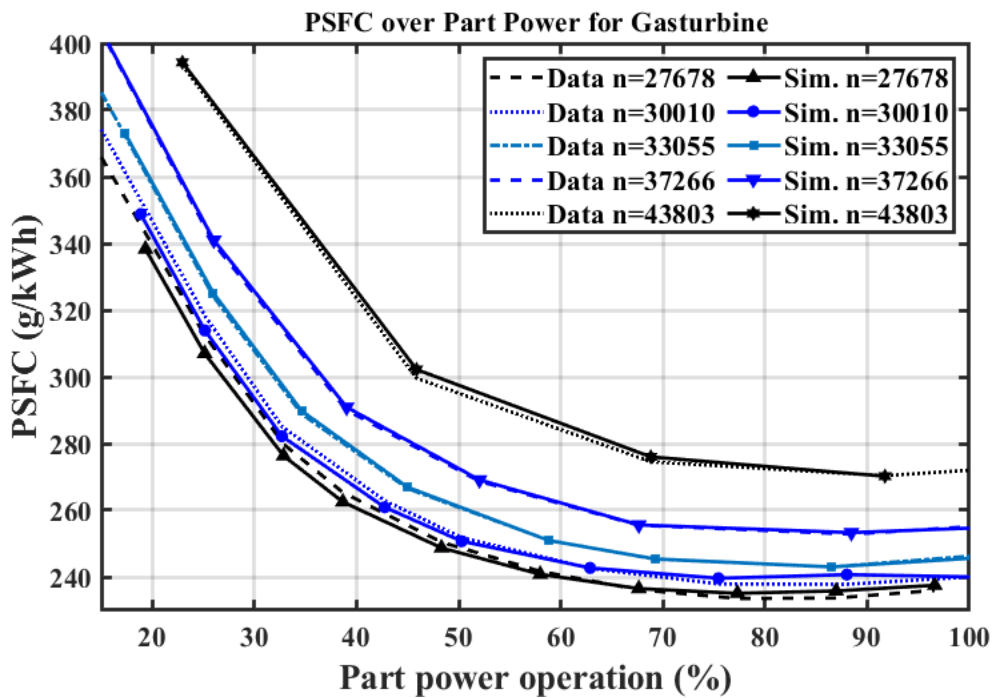


Figure 4.21: Comparison of the inputs used to describe the fuel flow associated with the thermal power supplied.

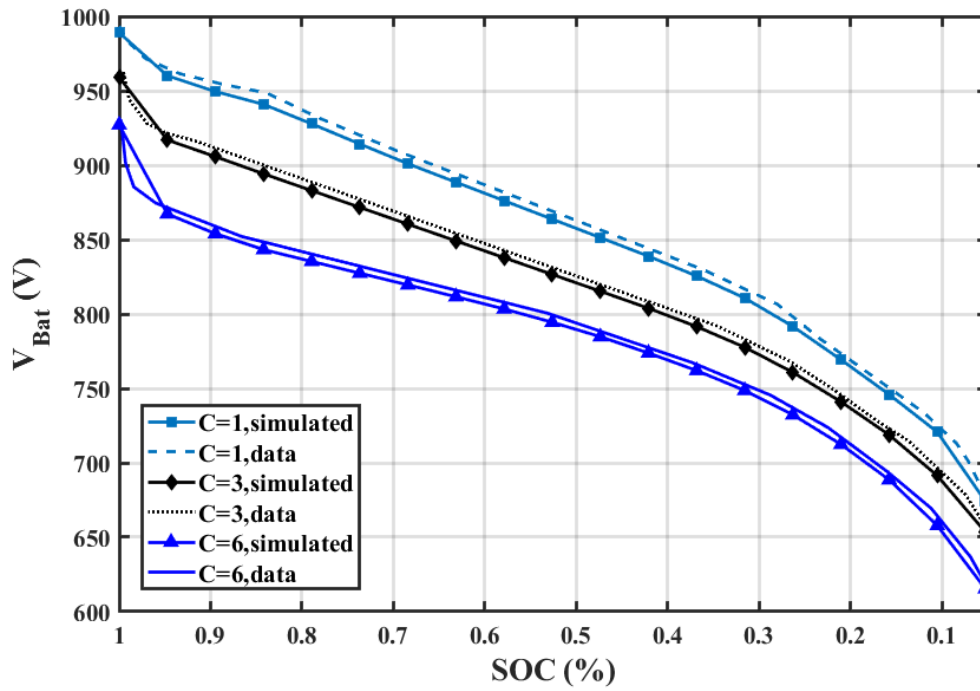


Figure 4.22: Comparison of the inputs used to describe the dynamics of the battery discharge cycle.

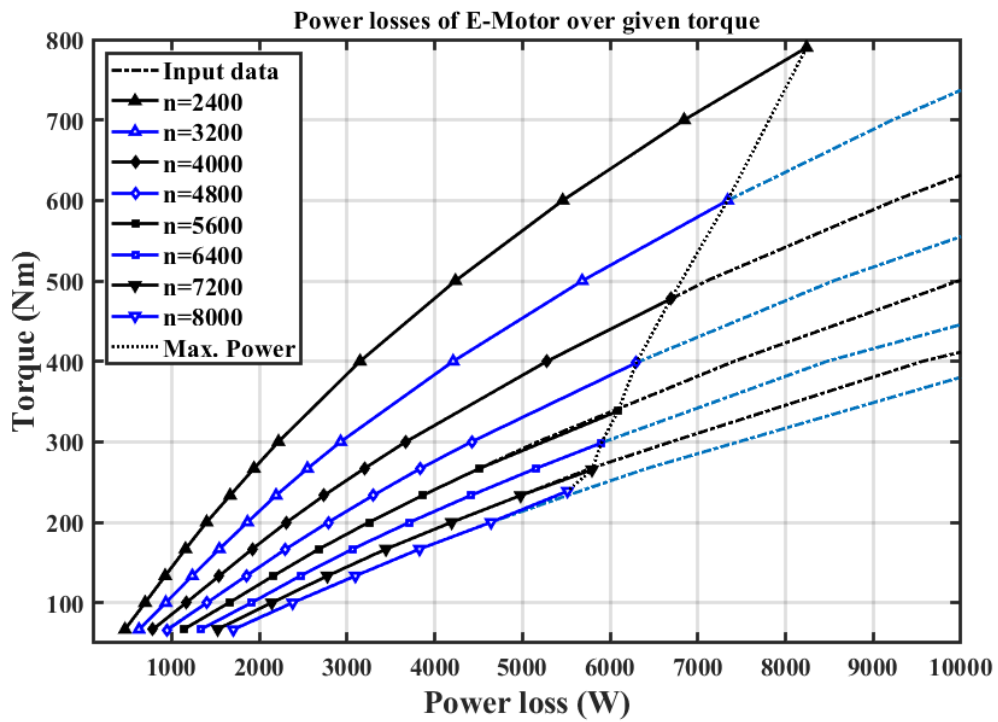


Figure 4.23: Comparison of the efficiency maps provided as input for the simulation of the e-motor drives.

	Wing	H-tailplane	V-tailplane	Unit
Area	54.48	11.70	12.61	m^2
Ref. area	54.48	–	–	m^2
Exposed area	50.48	11.00	12.19	m^2
Wetted area	105.22	22.94	25.21	m^2
Aspect ratio	11.08	4.12	1.53	–
Taper ratio	0.54	0.62	0.64	–
Span	24.57	6.94	4.39	m
Sweepback at leading edge	3.34	9.54	31.59	deg
Sweepback at quarter chord	1.22	6.32	28.50	deg
Sweepback at half chord	-0.89	3.05	25.22	deg
Sweepback at trailing edge	3.34	-3.51	18.10	deg
Mean aerodynamic chord	2.29	1.72	2.92	m
Geometric mean chord	2.22	1.69	2.87	m
Chord at centerline	2.62	2.08	3.51	m
Chord at root	2.62	2.05	3.47	m
Chord at kink	2.62	–	–	%
Chord at tip	1.41	1.29	2.24	m
Rel. thickness at centerline	18.00	17.00	13.70	%
Rel. thickness at root	18.00	17.00	13.70	%
Rel. thickness at kink	18.00	–	–	%
Rel. thickness at tip	13.00	17.00	13.70	%
Rel. root position	6.20	0.05	2.78	%
Rel. kink position	33.29	–	–	%
Tank group volume	8521	0	0	l
Position	8.9	20.5	18.2	m

Table 4.8: Geometric characteristics of the lifting surfaces.

Fuselage	Value	Unit
Width	2.87	m
Height	2.60	m
Total length	22.67	m
Length front-section	3.40	m
Length mid-section	10.20	m
Length rear-section	9.07	m
Wetted area	164.12	m^2
Volume	100.36	m^3
Tank group volume	0	l

Table 4.9: Geometric characteristics of the fuselage.

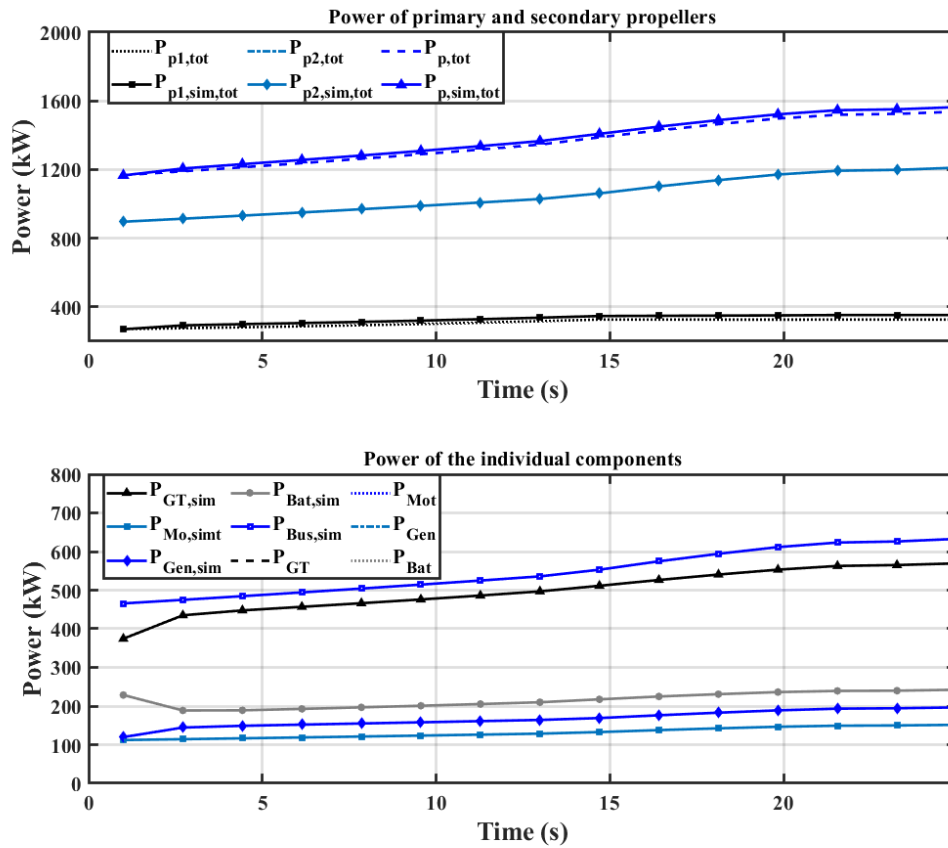


Figure 4.24: Comparison of the power distribution calculated through low and high fidelity methods during the take-off phase. The take-off run covers a distance of about 730 m in about 25 seconds.

the design parameters of each airfoil, the aerodynamic characteristics have been determined. Then, some corrections have been adopted to account for the additional drag contributions. The propulsion group is as similar as possible to the engine deck of a PW127. In other words, starting from the values of thrust and fuel consumption provided for each power rating, as shown in Fig. 4.26 and Fig. 4.27 for the cruise power rating, the engine deck has been built in terms of thermal power and fuel flow assuming certain efficiencies for the gearbox and the propellers.

The mission profile studied ranges 200 *Nmi*. Two different simulations are considered reliable concerning this conventional aircraft, based on the results obtained within the framework of the European project *Innovative turbopROp configuration* (*IRON*) and the Italian project *PROpulsione e Sistemi IBridi per velivoli ad ala*

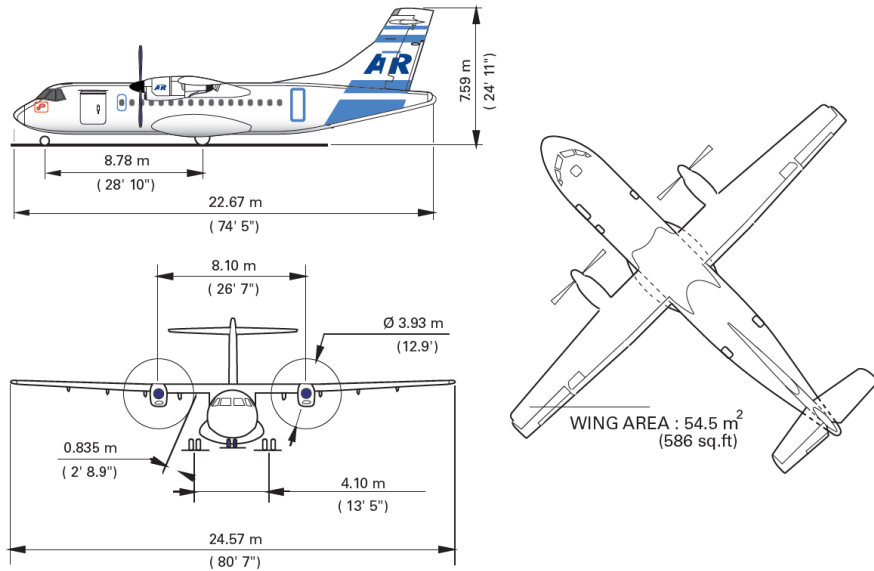


Figure 4.25: Geometry of ATR-42 (Source: cabin crew operating manual).

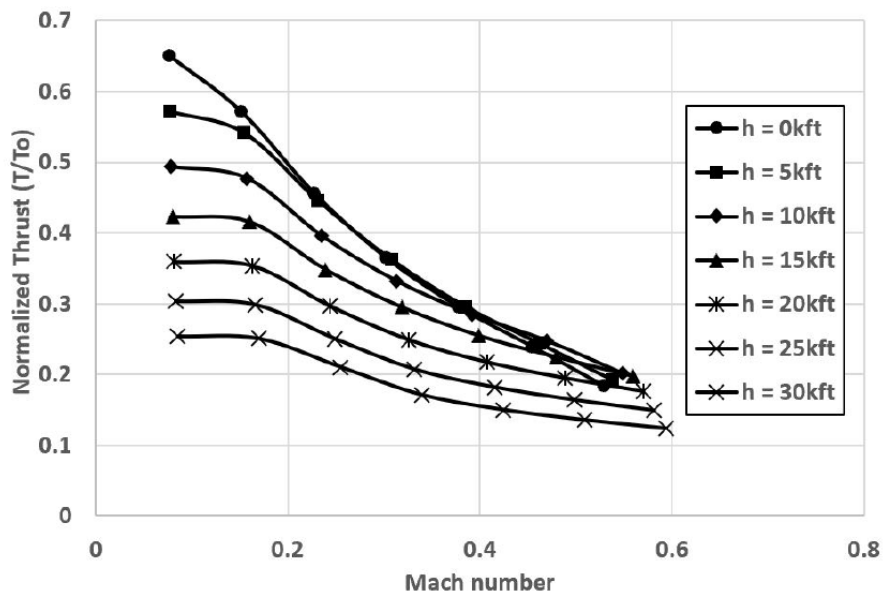


Figure 4.26: Cruise normalized thrust.

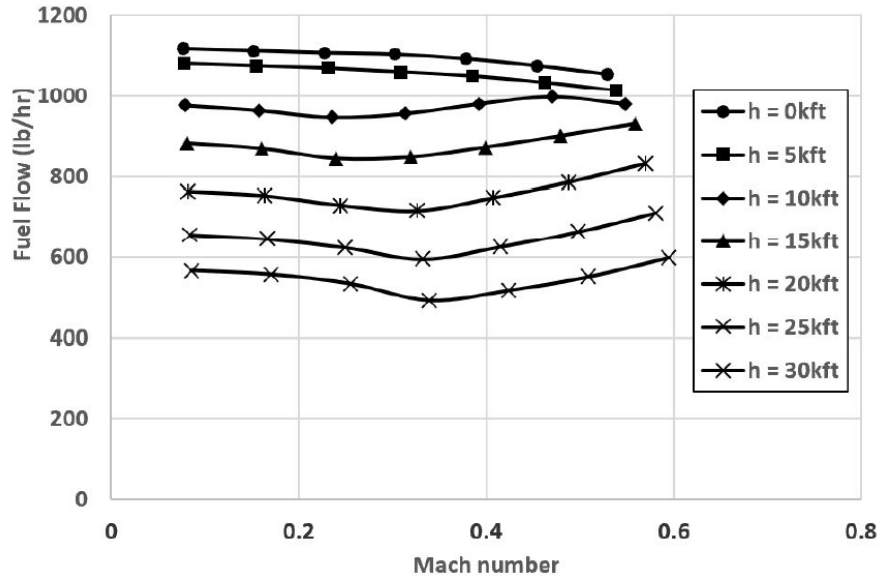


Figure 4.27: Cruise fuel flow.

fissa e rotante (PROSIB). The main flight parameters are reported in Table 4.10.

	Value	Unit
Take-Off		
Take-off mass	17618	kg
Stall speed	51.09	m/s
Lift-off speed	59.61	m/s
Climb		
Calibrated airspeed	82.30	m/s
Rate of climb	1500	ft/min
Cruise		
Mach number	0.46	–
Altitude	25000	ft
Descent		
Calibrated airspeed	102.87	m/s
Rate of descent	-1100	ft/min
Landing		
Stall speed	44.06	m/s
Approach speed	54.14	m/s

Table 4.10: Flight mission (200 Nmi).

The results validated in the framework of the two projects mentioned are compared with the mission analysis obtained by applying the algorithms discussed. The comparison is reported in Table 4.11.

	Calculated	IRON	PROSIB
Fuel consumption (kg)			
Block	473.1	513.0	494.4
Take-off	6.4	6.5	4.9
Climb	248.6	274.8	242.6
Cruise	129.2	116.2	141.3
Descent and landing	86.6	115.2	94.1
Time (min)			
Block	57.8	51.3	60.7
Take-off	0.3	0.3	0.3
Climb	18.8	21.1	16.6
Cruise	13.3	12.1	15.1
Descent and landing	25.3	17.8	28.2
Range (Nmi)			
Mission	204.7	200.0	205.3
Take-off	0.4	0.4	0.4
Climb	62.4	71.7	61.1
Cruise	60.8	55.7	61.4
Descent and landing	81.1	72.2	82.4

Table 4.11: Comparison of the results (200 Nmi).

The validation also highlighted the deviation in terms of results that a different approach to climb or descent can cause. For example, the flight simulation performed in case of the PROSIB project is at constant speed and rate of climb, requiring a lower time to climb with respect to the other two alternatives. In the same way, the sustained descent procedure considered in case of the IRON project reduces the time required to complete this phase. In these two cases, the thrust assessment can be related to flight performance by the excessive power models. Which is the second algorithm described in 4.1. However, alternative flight procedures require different and more complex approaches.

The second benchmark is the commuter aircraft designed by Piaggio S.p.A. as reference for the small air transport category and described in Ref. [184] (Fig. 4.28).

Geometry, aerodynamics, masses, and propulsive characteristics are designed to be as close as possible to the target values of the reference aircraft. Moreover, differently from the case of the regional turboprop, in this case, the data provided

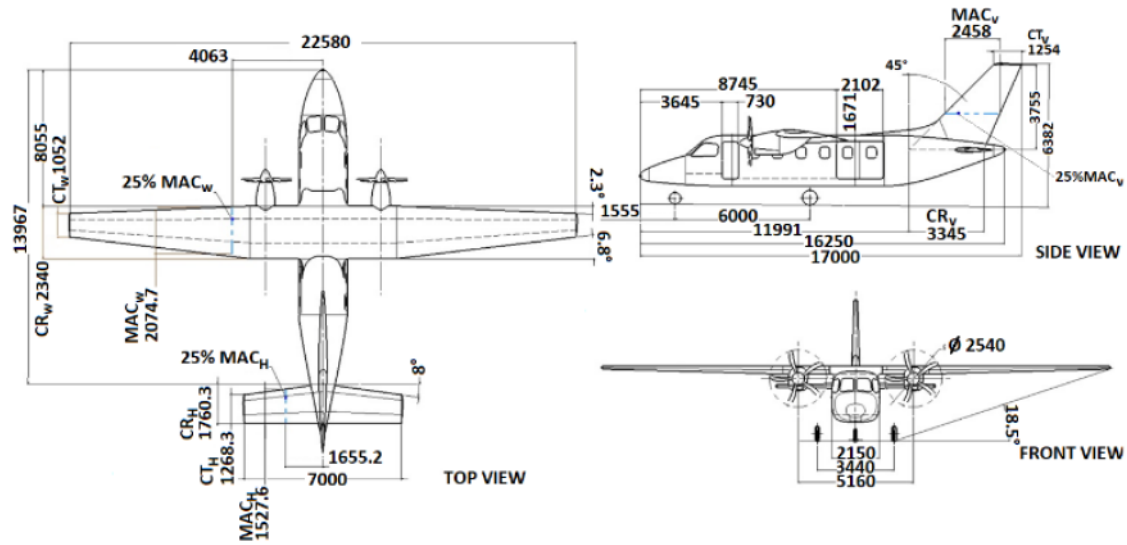


Figure 4.28: Geometry of the Piaggio reference aircraft [184].

allowed to simulate both the design and typical missions considering the same flight procedures. The assumptions made are summarized in Table 4.12.

	Design Mission	Typical Mission
Range (<i>Nmi</i>)	800	300
Take-Off		
Take-off mass (<i>kg</i>)	7810	7017
Maximum lift coefficient	1.90	
Climb		
Calibrated airspeed (<i>m/s</i>)	77.16	
Cruise		
Mach number	0.30	
Altitude (<i>ft</i>)	10000	
Descent		
Calibrated airspeed (<i>m/s</i>)	61.73	
Landing		
Maximum lift coefficient	2.1	

Table 4.12: Flight missions for the commuter reference aircraft.

It is here explicitly highlighted that both climb and descent phases are simulated at constant calibrated airspeed. Since take-off and landing also include assumptions related to the taxi-in and taxi-out operations, these are excluded from the comparison. The results concerning the simulation of the flight missions are reported in the following table. Table 4.13 shows that the results obtained through the algorithms

proposed are highly reliable when the aircraft model is accurate.

Calculated				Reference		
Design mission						
Phase	Time (min)	Range (km)	Fuel (kg)	Time (min)	Range (km)	Fuel Burned (kg)
Climb	3.93	19.28	42.63	3.90	19.37	41.70
Cruise	236.11	1418.80	1146.07	234.92	1415.21	1140.90
Descent	10.58	42.00	26.96	12.39	47.08	27.90
Total	250.62	1480.08	1215.66	251.21	1481.65	1210.50
Typical mission						
Phase	Time (min)	Range (km)	Fuel (kg)	Time (min)	Range (km)	Fuel Burned (kg)
Climb	4.55	22.20	37.30	3.43	19.37	41.70
Cruise	82.62	496.43	395.41	81.91	491.60	1140.90
Descent	10.81	42.46	27.93	11.66	47.00	27.90
Total	97.98	561.09	460.64	97.00	557.97	1210.50

Table 4.13: Comparison of the results concerning the two flight simulations for the commuter reference aircraft. For the two mission profiles, the time required to complete each flight segment, the fuel consumed, and the range flown are reported.

Never do things others can do and will do, if there are things others cannot do or will not do.

— Amelia Earhart

5

Application of the design process

Contents

5.1	PROSIB	246
5.1.1	Regional Turboprop Aircraft	247
5.1.2	Commuter Aircraft	260
5.2	ELICA	269
5.2.1	Hybrid-Electric Commuter Aircraft	273
5.2.2	Hydrogen Commuter Aircraft	281

The present work is concluded by the application of the conceptual design chain presented in the previous chapters. The flexibility of the design process is demonstrated through a wide range of concepts powered by different propulsive systems, referring to different technological levels. Supported by the industrial partners of two different research projects, the hybrid-electric aircraft designed are in line with the ambitious goals reported by the European Commission in the *Flightpath 2050 - Europe's Vision for Aviation* [185]. Formulated in the year 2011, the roadmap to the future of European aviation is based on two main objectives:

- 1 90% of travellers within Europe are able to complete their journey, door-to-door within 4 hours.
- 2 Technologies and procedures available allow a 75% reduction in CO_2 emissions per passenger kilometre and a 90% reduction in NO_x emissions. Moreover,

the perceived noise emission of flying aircraft is reduced by 65%¹.

However, since the future aviation moves its steps in the new concepts that will be available in the near future, long before the year 2050, the new concepts cover different years of entrance in service: 2025 and 2035.

With the purpose of protecting the intellectual property of partners involved in the projects, the data assumed for the following studies have been collected from literature, leaving intact only the contribution to the project provided by the author of this work.

5.1 PROSIB

The Italian project named *PROpulsione e Sistemi IBridi per velivoli ad ala fissa e rotante (PROSIB)*, namely Hybrid Propulsion and Systems for fixed and rotary wing aircraft, is funded by the Italian Ministry of research and university. Differently from other projects, often referring to *Flight Path 2050*, the objective proposed by this project is referred to the year 2035, chosen for the entrance in service of the new hybrid-electric regional turboprop. The market analysis carried out by the project leader, *Leonardo S.p.a.*, identified for that year the following strategic objective: the reduction of the energy required for air transport of about 20% compared to not-electric propulsion solutions available at that time. The development of hybrid-electric aircraft is progressing in parallel with the evolution of the thermal engines, thereby, the competitiveness of innovative propulsive systems is assessed with respect to the conventional concepts referred to the same year of entrance in service.

The project investigates multiple configurations, but the focus of the present section will be on two of them: the regional turboprop aircraft and the commuter aircraft. The identification of the most promising concepts is supported by trend analysis of the main enabling technologies. Then, the multidisciplinary analysis of the vehicles provides an adequate knowledge of potential benefits and main issues associated with the new technologies introduced in the aviation field.

¹These percentages are relative to the capabilities of typical new aircraft in the year 2000

In conclusion, PROSIB promotes the development of a national ecosystem ready to contribute to the technological challenges envisaged by the European Commission in Flight Path 2050. In this perspective, in the near future, the project prepares technicians for the further technical and industrial developments necessary for future aviation. In the medium to long term, it is the first step for the maturation of innovative short-range air transport solutions.

Differently from the other projects discussed in this section, the conceptual design chain of this project has been implemented considering the classical approach of a sizing activity performed with the objective of reducing the design space up to one single promising concept. Results discussed in the previous chapter (3.4.1 and 3.4.2) have supported the choices leading to the concepts presented in the present paragraph.

5.1.1 Regional Turboprop Aircraft

The design of the hybrid solution introduced in this paragraph is driven by a set of top-level aircraft requirements reported in Table 5.1 [42]. These requirements have been fixed according to literature studies on this aircraft category [186] and market analysis within the framework of the PROSIB project. The optimised set of

Requirements	Value	Unit
Design payload	4240	<i>kg</i>
Maximum payload	4560	<i>kg</i>
Cruise Mach number (at 6096 m)	0.42	—
Design range	600	<i>nmi</i>
Typical mission range	200	<i>nmi</i>
Take-off field length (at Sea Level and MTOW)	≤900	<i>m</i>
Landing field length (at Sea Level and MTOW)	≤900	<i>m</i>
Balanced field length	≤1100	<i>m</i>
Max ceiling altitude	7620	<i>m</i>

Table 5.1: Top-Level Aircraft Requirements (TLAR) for the regional turboprop configuration of the PROSIB project.

requirements aims at minimizing the hub-to-hub time within the European scenario,

accounting for the possible development of new routes to connect also remoter regions and small airports. With the objective of demonstrating the competitiveness of the electric concepts on the future market segment, a baseline similar to the regional turboprop ATR-42 has been designed according to the same top-level requirement considered for the hybrid-electric concept.

From literature studies based on the same enabling technologies considered in this project [43, 165, 187], the development expected for the year 2035 is reported in Table 5.2.

Technological level		
	Value	Unit
E-storage		
Specific energy	500	<i>Wh/kg</i>
Specific power	1	<i>kW/kg</i>
Energy density	800	<i>Wh/l</i>
Minimum S.O.C.	20	%
E-motor drive		
Specific power	7.7	<i>kW/kg</i>

Table 5.2: Main characteristics of the enabling technologies.

The first step of the design process, the sizing activity, has been carried out based on the requirements and the technological level introduced in the previous tables. At this stage, several concepts are explored choosing the values of the design parameters in a wide range, considering both turbo-electric and hybrid-electric aircraft concepts, always starting from a conventional configuration used as a baseline for the comparison. The importance of this step has been already highlighted in 3, thus, in the present section, the objective is showing the trends of the objective function, that is minimizing the fuel consumption, with respect to the variables of interest. Point performance is evaluated considering different enabling strategies and values of the two hybridization factors. The maximum take-off weight and the operative empty weight of concepts powered by hybrid powerplant are greater than in case of conventional concepts, due to the higher number of powertrain components. Thus, the chosen figure of merit for a sound comparison of the different aircraft configurations is the fuel weight. The exploration of the possible concepts

aims to identify the set of design variables guaranteeing a lower fuel consumption for a given mission, yielding to a cleaner aircraft. It is here remarked that the choice of the sizing point plays a major role in minimizing the energy required, as discussed in 3.4.2. The most promising results in terms of fuel saving percentage have been obtained when maximizing the wing loading. In fact, the higher structural weight associated with the choice of maximizing the power loading is a critical drawback when coming to the estimation of the energy required to accomplish the mission profile. Thus, in the present context, the objective will be minimizing the maximum wing loading by taking advantage of distributed electric propulsion. Regarding the different mission strategies dealing with the use of distributed electric propulsion, some considerations should be done referring to Fig. 3.15. The figure represents only two enabling strategies: the use of DEP at take-off and landing, or its use also during climb. In fact, the use of distributed propulsion in all phases has been excluded, due to the additional mechanical losses extended over time and undesired increment of drag. Since distributed propulsion is intended to increase lift, its benefits in cruise are lost when the increment of efficiency is compared to the lower global efficiency of the propulsive system. On the other hand, at low values of the shaft power ratio, ϕ , the effect can be mitigated with a low percentage of power supplied by the battery. In Fig. 3.15, it is also shown that the use of DEP during the climb phase should be discouraged. This is not generally true during a flight mission, whose climb phase should be compliant with both regulation constraints, air traffic procedures, and performance requirements. In fact, under certain required performance in terms of rate of climb or calibrated airspeed, the required propulsive power can be more demanding than what is imposed by the sizing curves. In other words, when climb performance requires an excessive disk load or an increment of the generator rated power and mass, an appropriate use of distributed electric propellers during climb could be beneficial. Further considerations have already been discussed in the previous parts of this work (3.4.2).

The first vehicle introduced is the conventional baseline of the project, whose geometric characteristics are reported in Table 5.3 (Fig. 5.1).



Figure 5.1: Conventional regional turboprop designed for the PROSIB project.

Geometry of the baseline		
	Value	Unit
Wing		
Area	54.48	m^2
Span	24.57	m
AR	11.07	—
Horizontal tail		
Area	10.58	m^2
Span	7.10	m
AR	4.76	—
Vertical tail		
Surface	12.53	m^2
Span	4.55	m
AR	1.65	—
Fuselage		
Length	22.67	m
Height	2.65	m
Width	2.86	m

Table 5.3: Main geometric characteristics of the conventional baseline.

Two flight missions have been considered for the analysis and the comparison of performance. On the one hand, the design mission of about 600 nautical miles is the sizing mission for the platform, assuring a certain flexibility. On the other hand, the typical mission flown by ATR-42 of about 200 nautical miles is the reference for the comparison of the fuel emissions. In Table 5.4, the fuel consumed for the design and the typical mission by the conventional platform is reported, including reserves for the operational flexibility up to 200 nmi of cruise divergence and 30 minutes of loiter.

The hybrid-electric aircraft introduces a second power source: the battery. Thus, the thermal engine of the conventional aircraft is opportunely scaled to be included in the hybrid-electric powertrain according to the new power requirements, mitigated

Weight breakdown of the baseline		
	Value	Unit
MTOW	17615	<i>kg</i>
OEW	11339	<i>kg</i>
MZFW	15899	<i>kg</i>
Design mission		
Take-off weight	17521	<i>kg</i>
Fuel	1850	<i>kg</i>
Block fuel	1336	<i>kg</i>
Typical mission		
Take-off weight	16696	<i>kg</i>
Fuel	1025	<i>kg</i>
Block fuel	512	<i>kg</i>

Table 5.4: Weight breakdown of the conventional baseline.

by the presence of the new electric power source with higher efficiency. Additionally, distributed electric propulsion has been included as the secondary propulsive line of the present concept. When approaching these enabling technologies, the right choice of geometric characteristics and hybridization factors can be challenging. The most convenient propulsive architecture cannot be based on choices exclusively related to the fuel saving percentage. For example, in the present context, the increment in lift coefficient has been partially sacrificed in favour of lower maintenance costs. In other words, the number of distributed propellers has been limited to eight to limit the maintenance cost. As a further example, the choice of the battery size is often linked to the available space and the cooling capability, in addition to the power required. The space potentially suited for battery storage on-board is constrained to 3 m^3 , divided into two different volumes of about 1 m^3 and 2 m^3 . Considering the energy density assumed, the resulting maximum storable energy is 2400 kWh . Accounting for the necessary cooling systems, the maximum battery weight is about 4300 kg (2150 kWh), resulting in a volume of about 2.68 m^3 . For this project, the weight of the battery has been distributed in two battery packs to stabilize the center of gravity in the same position as the conventional aircraft. In terms of geometry, the hybrid-electric configuration is similar to the conventional concept, with the only exception of the wing area. According to results from the

sizing activity, the wing area can be reduced thanks to the increment of the lift coefficient allowed by high-lift propellers, as shown in Table 5.5 and Fig. 5.2. By reducing the wing area to the 83% (44.71 m^2) of the conventional configuration while keeping constant the wingspan, the resulting aspect ratio is 13.50.

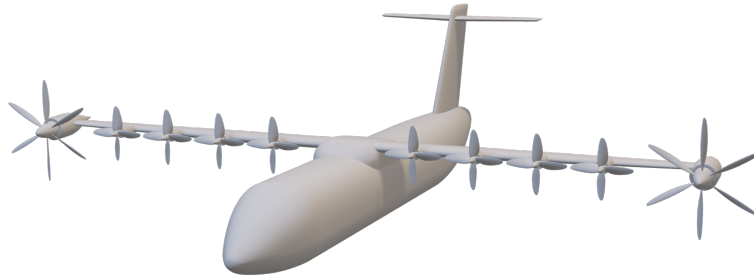


Figure 5.2: Hybrid-electric regional turboprop designed for the PROSIB project.

Geometry of the electric concept		
	Value	Unit
Wing		
Area	44.71	m^2
Span	24.57	m
AR	13.50	—
Horizontal tail		
Area	10.58	m^2
Span	7.10	m
AR	4.76	—
Vertical tail		
Surface	12.53	m^2
Span	4.55	m
AR	1.65	—
Fuselage		
Length	22.67	m
Height	2.65	m
Width	2.86	m
Propellers		
Number of main propellers	2	—
Main propeller diameter	3.93	m
Number of DEP propellers	8	—
DEP propeller diameter	2.20	m

Table 5.5: Main geometric characteristics of the hybrid-electric concept.

Even from a first glance at Fig. 5.2, an increase of the maximum take-off weight

can be expected due to the higher number of propulsive elements. The mass increment with respect to conventional vehicles requires a parallel increase of power. The rated powers of each element composing the powertrain is reported in Table 5.6.

Rated powers (kW)		
Element	Hybrid-electric concept	Conventional concept
Gasturbine	1414	2189
Generator	1525	0
E-Motor	770	0
Battery	4000	0

Table 5.6: Comparison of installed power for the two regional turboprop of interest.

Energy and power requirements have been fixed iterating mission and performance analysis until their compliance with power requirements. Assuming the battery power reported in Table 5.6 and the energy necessary to accomplish the mission profile, two battery packs have been designed according to characteristics in Table 5.7.

Battery packs		
	Value	Unit
Cells in parallel	425	—
Cells in series	308	—
Maximum cell voltage	4.2	<i>V</i>
Nominal cell voltage	3.6	<i>V</i>
Max pack voltage	1800	<i>V</i>
Number of packs	2	—
Nominal pack voltage	1170	<i>V</i>
Maximum C-rate	2.5	<i>1/hr</i>
Maximum S.O.C.	100	%
Minimum S.O.C.	20	%
Energy stored	2150	<i>kWh</i>

Table 5.7: Battery model considered for the regional turboprop of the PROSIB project.

Besides the effect on the induced drag of the higher aspect ratio, accounting for the new wetted area, the parasite drag coefficient is modified considering both the reduction due to the lower wing area and the increment related to the 8 additional nacelles. Another effect of the lower chord length is the reduction of the airfoil's

Reynolds number and, thus, of the maximum lift coefficient. Table 5.15 describes the main aerodynamics parameters.

Coefficient	Value
Max lift – clean	1.54
Max lift – take-off	2.05
Max lift – landing	2.58
DEP Max lift – take-off	3.13
DEP Max lift – landing	2.72
Minimum drag	0.0338
Drag increment – landing gear	0.0127
Drag increment – take-off flap	0.0167
Drag increment – landing flap	0.0672

Table 5.8: Aerodynamics coefficients of the hybrid-electric concept.

Finally, the mass breakdown is reported in Table 5.9 comparing the two platforms designed. In the same table, a preliminary indication of the fuel necessary to accomplish the mission profiles is reported.

In the context of the PROSIB project, the mass of lifting surfaces is evaluated considering the III-level methods discussed previously in this work. The most critical load condition is evaluated from the flight envelope of the aircraft depicted according to CS-25 guidelines. In particular, stall, cruise, and dive conditions are considered to have a clear picture of the loads encountered during a flight mission. For the concept discussed in this section, the dive condition with no fuel in the tank and maximum load factor is the most critical design condition, providing very high flexural and torsional loads due to the combination of maximum velocity and maximum load factor. The strength requirements are specified in terms of limit loads (the maximum loads to be expected in service) and ultimate loads (limit loads multiplied by prescribed safety factors). A safety factor of 1.5 is applied to the prescribed limit load to calculate the ultimate load. Applying a beam-like theory, internal forces are derived in terms of shear, bending moment, and twist. Wing mass, aerodynamic load, and engine mass cause shear stresses (Fig. 5.3) with different amplitude and directions whose sum and integration along the wingspan

Weight (kg)	Hybrid-Electric concept	Conventional concept
MTOW	23021	17521
OEW	17200	11339
Structural mass	6102	5659
Wing mass	1519	1392
H-tail mass	170	170
V-tail mass	220	220
Fuselage mass	2376	2376
Max zero fuel mass	21760	15899
Maximum payload	4560	4560
Design payload	4240	4240
Powertrain mass	6875	2059
Thermal engine mass	307 x2	449
E-Motor drive mass	100 x8	0
Generator mass	198 x2	0
Battery	4300	0
Design mission		
Fuel consumed	1506 (-19%)	1850
Block fuel	1506 (-23%)	1336
Typical mission		
Fuel consumed	707 (-31%)	1025
Block fuel	249 (-51%)	512

Table 5.9: Comparison of the weight estimated for the two 40-pax concepts of the PROSIB project.

returns the resulting spanwise distribution, as shown in Fig. 5.4 for the unitary load factor at dive speed. The shear stress is the dimensioning load of the spar web.

In addition to the shear force distribution, twist and bending moments are considered to size the structural layout. The former moment is mostly due to the airfoil aerodynamic moment. The latter is due to the shear force acting on each wing section inducing a bending effect according to the distance from the fuselage. Integrating all the contributions, the spanwise distribution is calculated allowing the sizing of the remaining bearing components. The effect of the powertrain masses on the wing torsion is negligible with respect to the aerodynamic twist. On the other hand, the bending moment induced by the powertrain elements is more relevant.

Once the wing primary and secondary structures have been weighted according to methods from literature Ref. [61], the effect related to the powertrain system on the aeroelastic characteristics of the aircraft is evaluated. The resulting increment

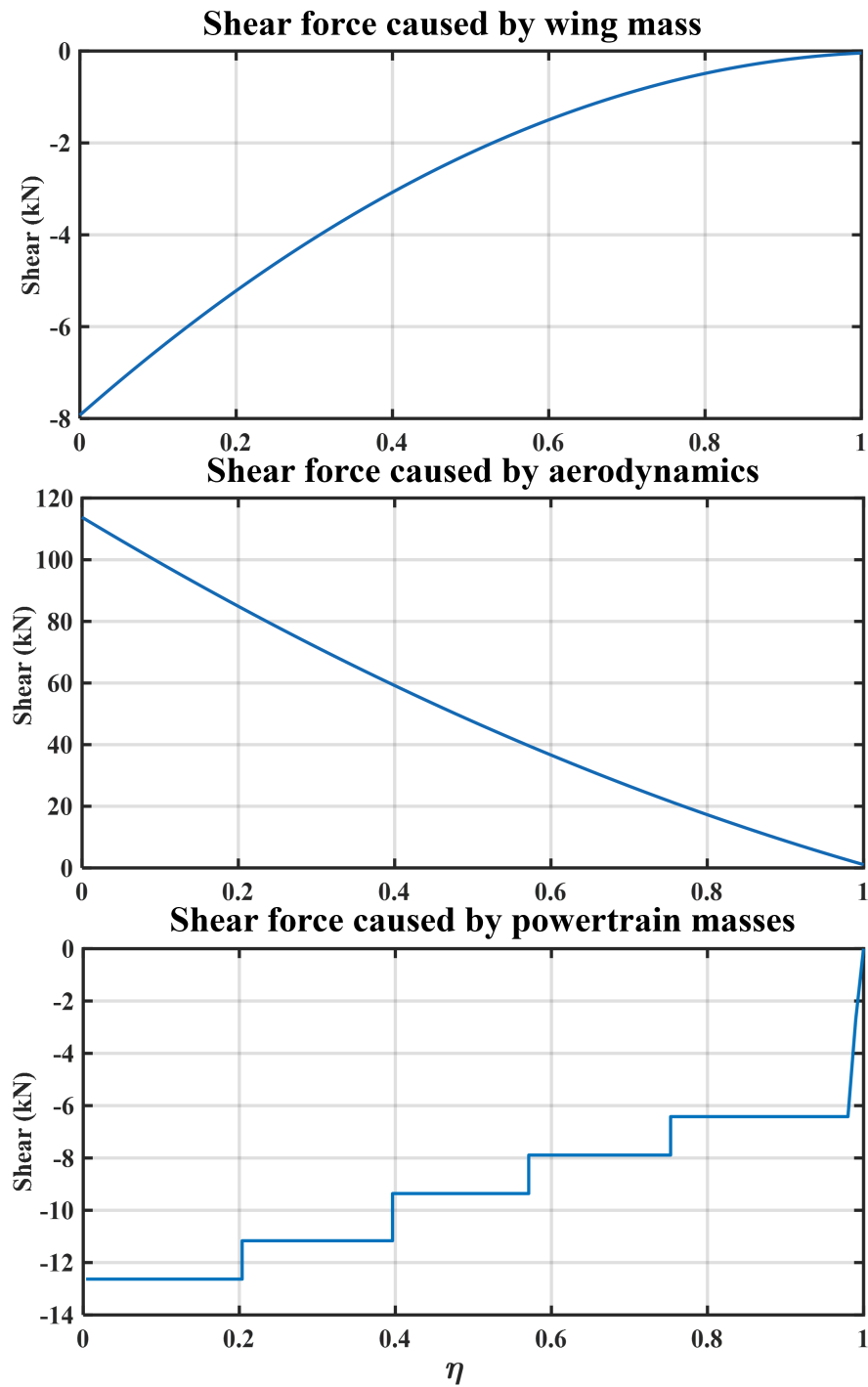


Figure 5.3: Shear forces acting on the wing at dive speed and unitary load factor.

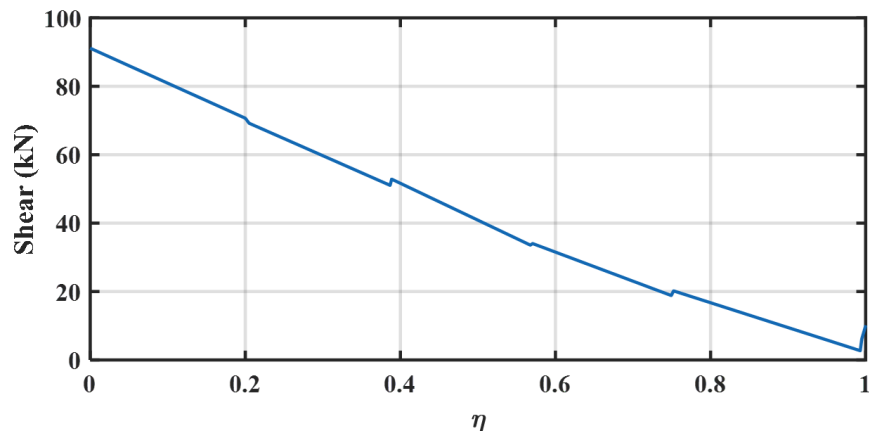


Figure 5.4: Total shear force on the wing at dive speed and unitary load factor.

of mass required to keep the flutter speed constant is 70.87 kg , which is included in the wing structural mass shown in Table 5.9.

Concerning flight performance and safety, the OEI condition considered in case of ceiling and balanced field length is a major issue when coming to configurations with distributed propellers. However, regarding this concept, the OEI condition has been identified with the failure of a thermal engine and generator (e-motor 1 in Fig. 5.6) associated with it. The other engine provides additional energy in APR or Max Continuous power ratings to the electric motor drives on the other semi-span where the failure occurred. The comparison between the two semi-spans presented in Fig. 5.5 and Fig. 5.6 highlights the power distribution at take-off for the two propulsive systems considered. The failure of a thermal engine is less critical for the hybrid-electric concept that would lose 20% of the total power supplied, with respect to the 50% lost by the conventional vehicle.

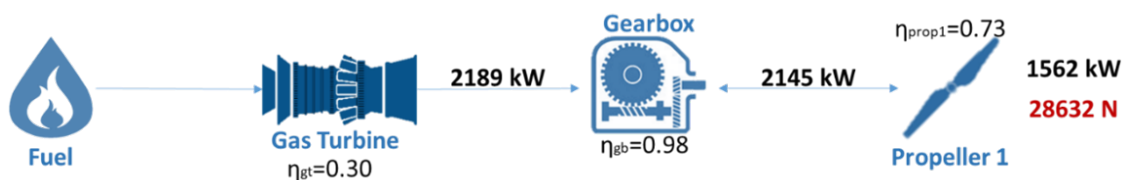


Figure 5.5: Turboprop engine at take-off.

As a result, performances are less affected by OEI condition, as shown in Table 5.10.

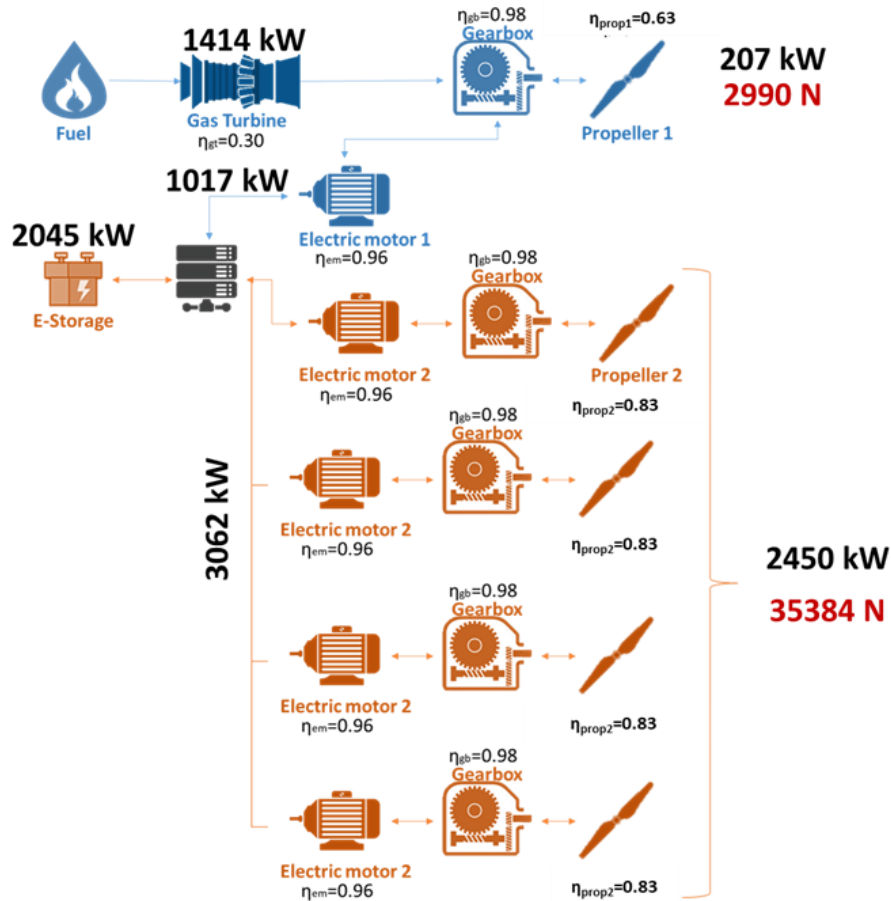


Figure 5.6: Hybrid-electric powertrain at take-off.

Performance	Hybrid-Electric concept	Conventional concept
Balanced field length (m)	721	910
Ceiling OEI (ft)	34414	21313
Ceiling AEO (ft)	36630	36448
Take-Off run (m)	673	681
Landing run (m)	798	730

Table 5.10: Comparison of performance estimated for the two 40-pax concepts of the PROSIB project.

In the context of the mission analysis, a wise use of the hybridization factors is the main issue, since it can minimize fuel consumption. As introduced in 4.2, the climb phase is composed of two different segments: the first one from take-off to 10000 ft, the second one from 10000 ft to cruise altitude, which is 20000 ft. This split allows a more efficient control of the hybridization factors along the flight path. For example, the use of distributed electric propellers to distribute the power supplied by the battery during climb and take-off phases can drastically reduce the rated power of the generator. Furthermore, with the objective of limiting the rated power, the battery is used during phases demanding high values of power supplied. In conclusion, the hybridization factors proposed in Table 5.11 are considered for the two mission profiles. Results associated to the two flight

Flight Phases	Supplied power ratio		Shaft power ratio	
	Typical Mission	Design Mission	Typical Mission	Design Mission
Take-Off	0.28	0.30	0.90	0.90
First climb segment	0.38	0.30	0.50	0.50
Second climb segment	0.28	0.30	0.50	0.50
Cruise	0.57	0.05	0.00	0.00
Descent	0.00	0.00	0.00	0.00
Climb to alternate	0.00	0.00	0.00	0.00
Divergence cruise	0.00	0.00	0.00	0.00
Descent from alternate	0.00	0.00	0.00	0.00
Loiter	0.00	0.00	0.00	0.00
Approach	0.00	0.00	0.50	0.50
Landing	0.00	0.00	0.50	0.50

Table 5.11: Hybridization factors considered for the two mission profiles.

missions are reported in Table 5.12 highlighting the energy consumption in terms of both fuel burned and electric energy consumed.

Flight Phases	Design mission		Typical mission	
	Fuel Burned (kg)	E-Energy (kWh)	Fuel Burned (kg)	E-Energy (kWh)
Take-Off	4.04	20.79	4.08	19.45
First climb segment	39.55	130.41	31.78	142.31
Second climb segment	41.95	215.74	42.68	203.44
Cruise	883.03	535.97	92.06	1423.40
Descent	73.5	0.00	73.54	0.00
Climb to divergence	103.35	0.00	102.94	0.00
Divergence cruise	108.06	0.00	108.11	0.00
Descent from divergence	46.63	0.00	46.65	0.00
Loiter	201.26	0.00	200.96	0.00
Approach	4.07	0.00	4.07	0.00
Landing	0.42	0.00	0.42	0.00

Table 5.12: Energy consumption provided by fuel and battery for the two mission profiles.

Results reported highlight that fuel saving percentages on regional turboprops are possible thanks to the use of e-storage units as the secondary power source. Considering the typical mission, the fuel saving percentage is about 51%, but this value cannot be directly related to the reduction of emissions. From Ref. [188], the emission indexes in Table 5.13 are considered for the thermal engine. Converting

E.I. (g/kg)	NO _x	CO	HC
Take-off	16.089	0.588	0.093
Climb-out	12.636	0.669	0.109
Approach	7.003	6.001	0.328
Idle	3.305	32.703	4.162

Table 5.13: Emission indexes of the turboprop engine PW150A [188].

the indexes in equivalent carbon dioxide ($CO_{2_{eq}}$) index, a mean emission index of about 3162 g/kg is calculated. As a result, 787 kg of $CO_{2_{eq}}$ are emitted per typical mission flight, against the 1618 kg produced by the conventional aircraft. However, this conclusion omits the contribution to emissions due to electric energy production. Assuming a mean value equal to 86 g/kWh², the resulting contribution in terms of $CO_{2_{eq}}$ is 185 kg. In conclusion, the total $CO_{2_{eq}}$ mass emitted by the hybrid-electric aircraft is 972 kg, which is 40 % lower than the quantity emitted by the conventional baseline.

The sizing activity demonstrated that the benefits of aero-propulsive effects on the fuel saving percentage are limited by the negative impact of the increase of powerplant's weight. A relieving effect to this increment has been obtained on the structural weight of the wing. In fact, it has been highlighted that the net effect of the new mass distribution along the wingspan (even considering the aeroelastic penalty associated) is beneficial in terms of structural weight.

5.1.2 Commuter Aircraft

Differently from the regional aircraft introduced in the previous section, the commuter aircraft has been intended to be a white sheet project integrating the enabling technologies studied in PROSIB. In other words, without a baseline

²https://www.eea.europa.eu/ds_resolveuid/DAT-13-en

for comparison, the main objective was applying the project know-how on a configuration freely designed with only one objective: minimizing the emissions.

However, together with the commuter category, new challenges are introduced. The first challenge introduced by regulation is related to the maximum take-off weight, which cannot exceed 19000 lb. Moreover, the limited space on board could result in a limit for the battery volume allowed. Actually, a convenient technological level can easily solve these issues, but in the context of the PROSIB project, the entrance in service has been fixed to the year 2035 and the same goes for the technological level, reported in Table 5.2.

The top-level aircraft requirements have been identified from the market analysis towards the year 2035. Table 5.14 reports the resulting requirements. Comparing

Requirements	Value	Unit
Design payload	1767	<i>kg</i>
Maximum payload	2000	<i>kg</i>
Cruise Mach number (at 3048 <i>m</i>)	0.31	–
Design range	500	<i>nmi</i>
Typical mission range	200	<i>nmi</i>
Take-off field length (at Sea Level and MTOW)	≤900	<i>m</i>
Landing field length (at Sea Level and MTOW)	≤900	<i>m</i>
Balanced field length	≤1000	<i>m</i>
Max ceiling altitude	7620	<i>m</i>

Table 5.14: Top-Level Aircraft Requirements (TLAR) for the commuter configuration of the PROSIB project.

these requirements with those reported in Table 5.1, performance requirements related to the commuter concept are more in line with those reported in literature for door-to-door aircraft [186]. This is due to the divergent objectives of the two platforms. On one hand, the regional turboprop aims to highlight issues and benefits of an electrification process. On the other hand, the completely new aircraft is only intended to be competitive on the market segment of small air transports.

A high-wing configuration was preferred in order to meet regulatory requirements for clearance with the ground. Part 23 (§23.925) requires that *there must be a*

clearance of at least seven inches (for each airplane with nose wheel landing gear) or nine inches (for each airplane with tail wheel landing gear) between each propeller and the ground with the landing gear statically deflected and in the level, normal takeoff, or taxiing attitude, whichever is most critical [189]. A conventional vertical tailplane has been selected, dismissing the hypothesis of the T-tail, by virtue of the greater simplicity of construction and the saving in structural weight. Although a T-tail plane would provide more control power and stability, this was deemed unnecessary given the sufficient tolerance to failure conditions, guaranteed by a proper system reconfiguration of the hybrid-electric powerplant. CFD analysis on this configuration, performed by other partners of the consortium involved in the PROSIB project, also excluded the necessity of a T-tail to avoid the interaction between the wing wake and the lifting surfaces. The two nacelles containing the thermal engines and the primary electric machines have been allocated at 33% of the wingspan, in correspondence with the kink. The 8 secondary propellers have been distributed on the outermost wing panel to improve low-speed aerodynamics. The wing area is designed with the objective of high aspect ratio. Airfoil and twist angle of each section are chosen to minimize the drag coefficient associated to cruise attitude. Two plain flaps per semi-span have been considered to increase the lifting capability of the wing. The geometry of the fuselage has been designed to assure

Coefficient	Value
Max lift – clean	1.30
Max lift – take-off	1.79
Max lift – landing	2.07
DEP Max lift – take-off	2.67
DEP Max lift – landing	2.09
Minimum drag	0.0268
Drag increment – landing gear	0.0179
Drag increment – take-off flap	0.0518
Drag increment – landing flap	0.0743

Table 5.15: Aerodynamics coefficients of the hybrid-electric commuter aircraft.

high standards of comfort and enough space for boarding the e-storage. Seats are distributed in 3-abreast separated by a single aisle. The cabin is non-pressurized

and this is the main limit to the operative ceiling altitude. Table 5.16 reports the geometric characteristics of this concept, shown in Fig. 5.7.

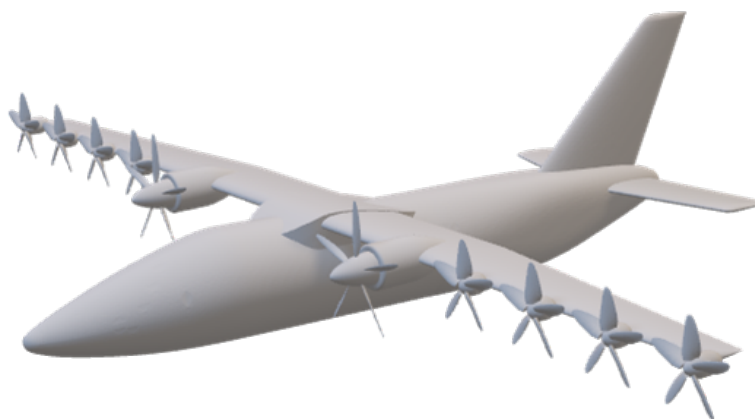


Figure 5.7: Hybrid-electric commuter aircraft designed for the PROSIB project.

Geometric characteristics		
	Value	Unit
Wing		
Area	33.95	m^2
Span	20.20	m
AR	12.00	—
Horizontal tail		
Area	10.60	m^2
Span	7.00	m
AR	4.62	—
Vertical tail		
Surface	8.63	m^2
Span	3.76	m
AR	1.63	—
Fuselage		
Length	16.25	m
Height	2.26	m
Width	2.15	m
Propellers		
Number of main propellers	2	—
Main propeller diameter	2.54	m
Number of DEP propellers	8	—
DEP propeller diameter	1.61	m

Table 5.16: Main geometric characteristics of the hybrid-electric commuter aircraft.

The rated power of each element of the propulsive system has been measured

simulating two mission profiles and checking the compliance with flight performance. The resulting powers are reported in Table 5.17. The nomenclature of the elements is clarified by Fig. 5.8.

Rated powers (kW)	
Turboshaft	600
E-motor 1	400
E-motor 2	200
Battery	900

Table 5.17: Sizing power of each element of the propulsive system.

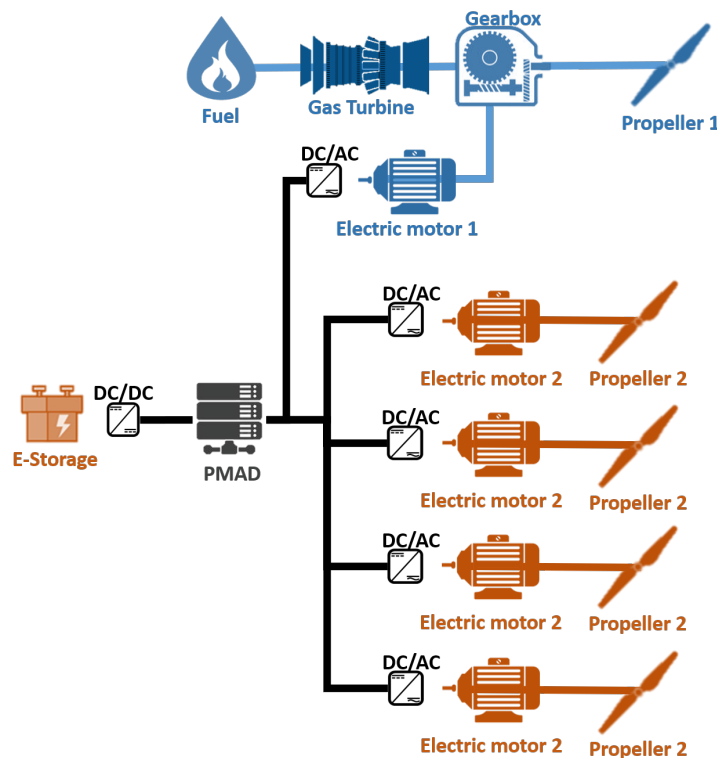


Figure 5.8: The hybrid-electric powertrain considered for the commuter aircraft of the PROSIB project.

In the same way, fuel and electric energy necessary to accomplish the mission profile have been measured. Assuming the battery power reported in Table 5.6 and the energy necessary to accomplish the mission profile, two battery packs have been designed according to characteristics in Table 5.7.

The two battery packs are boarded in an appropriate hold section at the bottom of the fuselage. The main objective when positioning the battery packs is related

Battery packs		
	Value	Unit
Cells in parallel	35	–
Cells in series	415	–
Maximum cell voltage	4.2	<i>V</i>
Nominal cell voltage	3.6	<i>V</i>
Number of packs	2	–
Max pack voltage	1800	<i>V</i>
Nominal pack voltage	1170	<i>V</i>
Maximum C-rate	2.7	<i>1/hr</i>
Maximum S.O.C.	100	%
Minimum S.O.C.	20	%
Energy stored	475	<i>kWh</i>

Table 5.18: Battery model considered for the commuter aircraft of the PROSIB project.

to the balance of the aircraft. For this reason, the battery packs are positioned at 35% and 45% of the fuselage length. Once the position of the electric components has been frozen, the cabling is designed according to the available space and the necessary current, as shown in Fig. 5.9. The distribution system is composed of a total of 18 cabling segments for a total mass of about 419 kg. The conductor material is copper, and each cable is composed of 30 wires sizing 0/1 *AWG* with a rated temperature of about 90°C. All cables are designed to work at a continuous voltage of 270 *VDC*, with the only exception of the main power line going from the PMAD to the distributed electric propellers, requiring 540 *VDC* to work efficiently.

Differently from the case of the regional turboprop, it cannot be excluded that the worst-case scenario may correspond to the failure of one of the secondary electric motors, due to their large distance from the center of gravity. Once geometry, aerodynamics, and propulsive system have been defined, the fault tolerance analysis is the following step of the design process. The failure analysis is aimed to prove the latero-directional controllability of the aircraft. The propulsive architecture is characterized by 4 electrically-driven distributed propellers per semispan and one main propeller powered by the thermal engine. The failure of each element is simulated obtaining the results shown in Table 5.19. It is here explicitly noted that the simulation scenario referring to the failure of a gasturbine is related to the

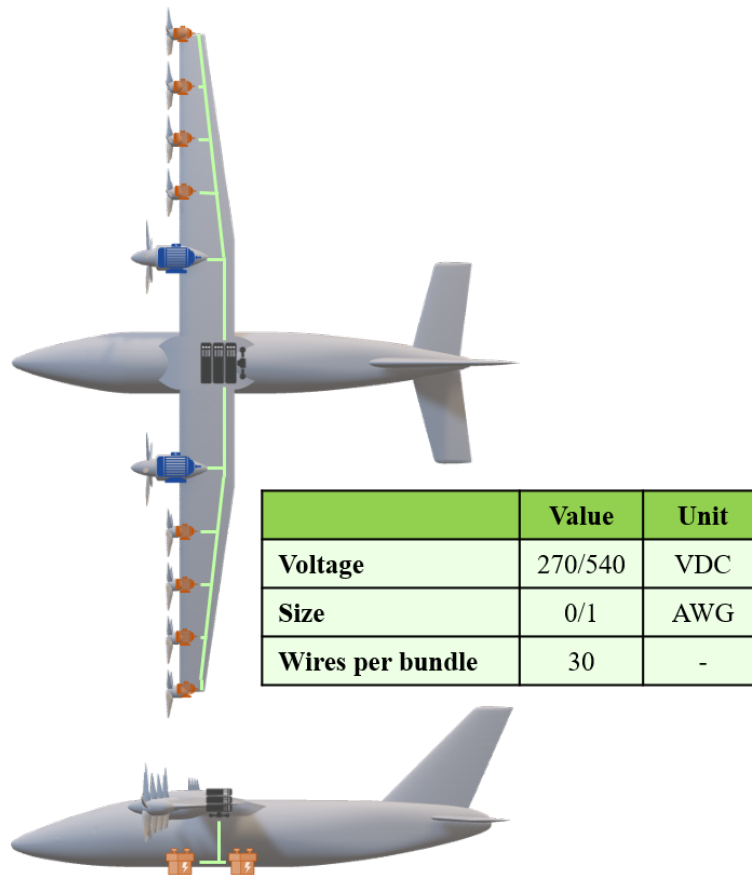


Figure 5.9: Hybrid-electric commuter aircraft with a scheme of the cabling required to power the propulsive system.

Failing element	Residual moment (N m)	Thrust loss (%)
Gasturbine no. 1	44238.8	- 31.80
Gasturbine no. 2	- 44238.8	- 31.80
Primary electric motor no. 1	19009.6	+ 1.25
Primary electric motor no. 2	- 19009.6	+ 1.25
Secondary electric motor no. 1	- 21850.0	+ 1.25
Secondary electric motor no. 2	- 19966.6	+ 1.25
Secondary electric motor no. 3	- 18062.4	+ 1.25
Secondary electric motor no. 4	- 16159.6	+ 1.25
Secondary electric motor no. 5	16159.6	+ 1.25
Secondary electric motor no. 6	18062.4	+ 1.25
Secondary electric motor no. 7	19966.6	+ 1.25
Secondary electric motor no. 8	21850.0	+ 1.25
Battery pack n. 1	0.0	- 18.20
Battery pack n. 2	0.0	- 18.20

Table 5.19: Thrust loss and yaw moment associated with the failure of each element of the propulsive system.

disablement of the propeller mounted on its shaft. In other words, the failure of a gasturbine makes also the associated primary electric motor inoperative. As a result, the element causing with its failure the greatest yawing moment and most critical thrust loss is the gasturbine. The battery does not result to be a critical element thanks to the division in independent battery packs. Furthermore, the failure of the electric motors could result in an increase in propulsive power. In fact, by redirecting the power towards primary propellers in case of emergency, the overall efficiency increases as well. The resulting minimum control speed is 39.5 m/s , which is compliant with the limit imposed by regulation (20% above stall speed).

With respect to the 48-seat configurations presented in the previous section, the battery usage has been limited by the certification limit on the maximum take-off weight. The 950.0 kg battery on board is optimally used to provide a moderate contribution to take-off and climb, while the rest of the energy is spent during the cruise to get as much as possible fuel saving. From this perspective, an overview of the mass breakdown is necessary (Table 5.20).

The use of the hybridization factors in modelling the use of the two power sources and propulsive lines facilitates the optimization of the energy consumption during the flight mission. The particular focus on the typical mission to assess the competitiveness of the configuration is due to the fact that this type of mission covers up to 80% of the total operative life of the vehicle. Since weight and volume of the battery are limited on commuter aircraft, the maximum sizing power for the battery is determined by comparing the specific power and the maximum allowed weight. As a result, the battery provides a moderate contribution during take-off and climb in terms of energy (around 20% of the total energy), even if the power provided is close to the sizing value, while the remaining part of the electric energy stored is spent during cruise. Table 5.21 shows the energy consumption phase by phase.

Differently from Table 5.12, in Table 5.21 there is only one climb segment since the cruise altitude for this aircraft is equal to 10000 ft. From the perspective of market demand, the aircraft is designed with the specific aim of covering the small air transport segment, deputed to compete with railways and highways for the

Weight breakdown (kg)	
	Value
Structure	
Wing	677.55
Fuselage	928.93
Nose undercarriage	87.37
Main undercarriage	322.19
Horizontal tailplane	16.64
Vertical tailplane	33.27
Control surface	70.92
Nacelle	94.12
Total	2231.00
Powertrain	
Engine group	629.43
Generator	103.90
E-motor drives	207.79
Battery	950.00
Cabling	419.35
T.M.S.	89.99
Total	2400.46
Systems	
Air conditioning	175.25
Electrical	210.26
Pneumatic/Hydraulic	123.31
Instruments	120.87
Total	629.69
Operating equipment	
Operating items	175.25
Crew	210.26
Total	629.69
Furnishing	
Furnishing	550.65
Operative empty	
Operative empty	6161.52
Payload	
Payload	1766.74
Maximum zero fuel	
Maximum zero fuel	7298.24
Fuel	
Fuel	686.22
Maximum take-off	
Maximum take-off	8614.45

Table 5.20: Mass breakdown of the hybrid-electric commuter aircraft.

Flight Phases	Design mission		Typical mission	
	Fuel Burned (kg)	E-Energy (kWh)	Fuel Burned (kg)	E-Energy (kWh)
Take-Off	1.88	3.99	1.56	4.68
Climb	26.54	72.90	25.08	68.92
Cruise	440.08	162.03	80.86	306.60
Descent	10.94	0.00	10.93	0.00
Climb to divergence	18.92	0.00	18.86	0.00
Divergence cruise	76.16	0.00	76.16	0.00
Descent from divergence	5.68	0.00	5.67	0.00
Loiter	71.22	0.00	71.15	0.00
Approach	1.94	0.00	1.94	0.00
Landing	0.47	0.00	0.47	0.00

Table 5.21: Energy consumption provided by fuel and battery for the two mission profiles flown by the commuter aircraft of the PROSIB project.

transport of passengers and goods. The competitiveness of this market segment is driven by short landing and take-off distances, as well as the reduced passenger mile per gallon of fuel. Considering the typical mission of 200 nmi, which covers up to 80% of the total operative life of the aircraft, the passenger mile per gallon is about 119 *nmi/gallon*, which is a remarkable result.

5.2 ELICA

The project named *ELectric Innovative Commuter Aircraft (ELICA)* is funded in the framework of Clean Sky 2, under the thematic topic titled *Conceptual Design of a 19-passenger Commuter Aircraft with near-zero emissions*. The ambition of this project is to design Small Air Transports with near-zero emissions. As stated in 1, 90% of aviation emissions are due to commercial aircraft carrying more than 100 passengers. However, reduction of carbon and noise emissions from general aviation and commuter airline can potentially impact global emissions generated by other means of transport with the same operative range. From this perspective, green door-to-door flights are a strategic objective for the market segment covered by Small Air Transports. With the objective of near-zero emissions, two different years of entrance in service (2025 and 2035), with the respective technological levels, have been chosen to explore the effective feasibility of the concepts associated with the development of the enabling technologies.

The market analysis carried out by Air s.Pace has identified some top-level aircraft requirements to drive the design toward a competitive aircraft. The most

important link between market and design is the definition of the reference mission. This mission is generally addressed as design mission and it can be used to calculate aircraft performance, as well as to update the business plan of the project. However, even if the design mission is defined to calculate the required aircraft performance, in case of electric aircraft, the typical mission is of primary importance for the assessment of energy consumption and the life cycle analysis. For this reason, both missions are introduced as requirements in Table 5.22. The main limit on this concept

	Value	Unit
Max take-off weight	<8618	<i>kg</i>
Maximum payload	2000	<i>kg</i>
Design payload	1767	<i>kg</i>
Design Mission		
Cruise range	500	<i>nmi</i>
Cruise Mach number	0.32	–
Cruise altitude	10000	<i>ft</i>
Diversion range	100	<i>nmi</i>
Diversion Mach number	0.22	–
Diversion altitude	5000	<i>ft</i>
Loiter time	30	<i>min</i>
Loiter altitude	1500	<i>ft</i>
Calibrated climb speed	170	<i>kts</i>
Calibrated descent speed	120	<i>kts</i>
Typical mission		
Cruise range	200	<i>nmi</i>
Cruise Mach number	0.32	–
Cruise altitude	10000	<i>ft</i>
Diversion range	100	<i>nmi</i>
Diversion Mach number	0.22	–
Diversion altitude	5000	<i>ft</i>
Loiter time	30	<i>min</i>
Loiter altitude	1500	<i>ft</i>
Calibrated climb speed	170	<i>kts</i>
Calibrated descent speed	120	<i>kts</i>
Performance		
Balanced field length	<1000	<i>m</i>
Ceiling altitude (AEO)	>25000	<i>ft</i>
Ceiling altitude (OEI)	>10000	<i>ft</i>

Table 5.22: Top-level aircraft requirements of the ELICA project.

is provided by the regulation constraint on maximum take-off weight of commuter

aircraft, which must be at most 8618 *kg*. The maximum payload has been fixed through statistics at 2000 *kg* and a design payload of 1767 *kg* has been considered.

The design activity proposed in the context of the ELICA project starts from the exploration of the design space through the evaluation of point performance presented in 3.4.1. The sizing activity has been carried out considering three design variables: number of distributed propellers, shaft power ratio, and supplied power ratio. Considering the results exposed in Fig. 3.14, the effect on the fuel saving percentage discouraged numbers of distributed propellers higher than eight and shaft power ratio higher than 0.8. For this set of variables and a design mission of about 500 *nmi*, the maximum battery mass, before exceeding the MTOW limit, is around 1000 *kg*.

Regarding the two target years of entrance in service, different technological levels have been considered for e-storage, e-motor drives, thermal engines, and fuel cells. The data provided by industrial partners are not discussed in the present section, but some considerations can be preliminary made. The first consideration deals with the choice of the battery, whose specific energy is inversely proportional to the specific power. In principle, it cannot be preliminary stated which one between energy and power is the sizing requirement for the battery of commuter aircraft. In fact, due to the lower energy requirements with respect to the regional turboprop category, the necessary masses derived by energy and power requirements are generally comparable. From this perspective, Eq. (2.146) adds a degree of freedom to the optimization process. In Fig. 5.10, three batteries capable of accomplishing the same mission profile are compared to highlight the different required mass when the sizing is based on energy and power, respectively.

Another consideration deals with the design of electric motors, which should be aimed to minimize the element mass, more than maximizing efficiency. In fact, the effect of the weight increment on required power is higher than that of the most optimistic increment of efficiency. However, it should be remarked that another way of optimizing the weight is by increasing the angular speed of both propellers and e-motor drives, interposing a convenient gearbox among them. In other words,

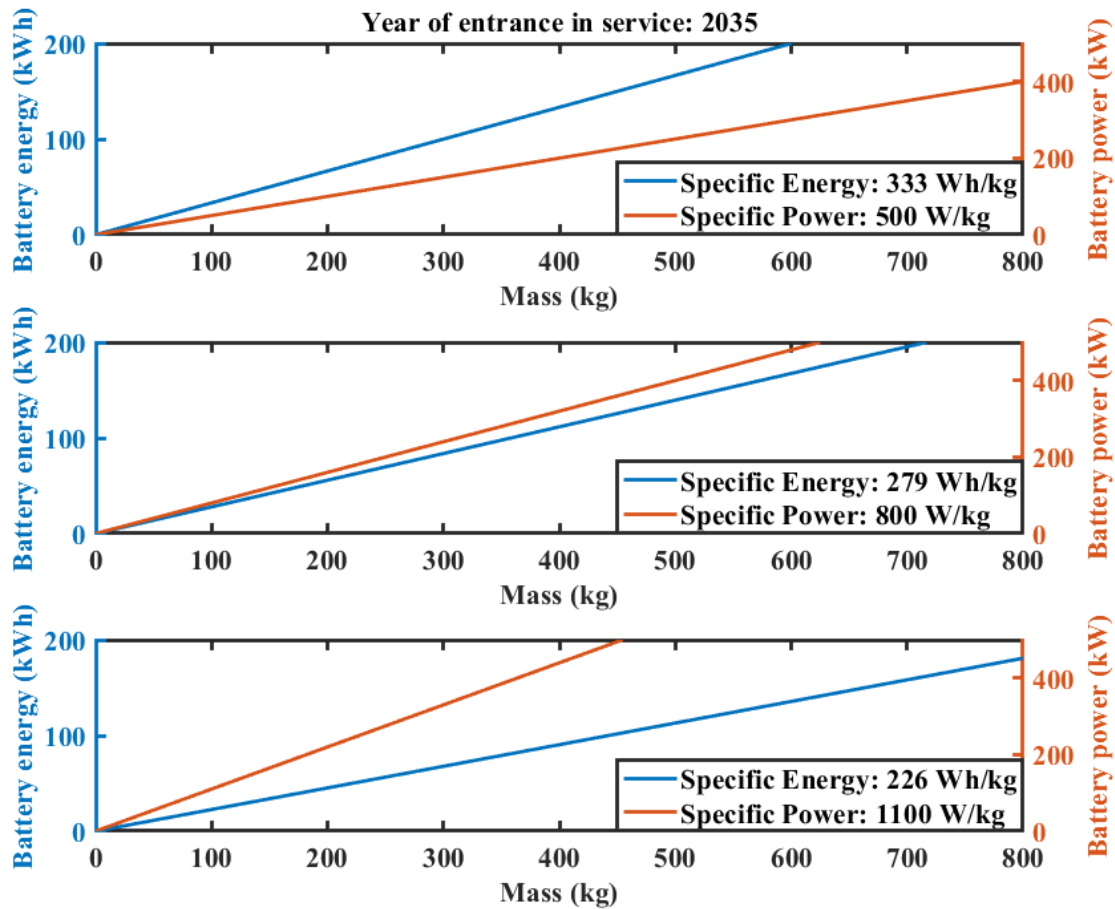


Figure 5.10: Available power and energy with respect to the battery mass for three e-storage units with different values of specific power and specific energy.

the constraints dealing with the optimization of the e-motor drive mass must relate to the e-motor drive mass and angular speed, the gearbox mass and ratio, and the propeller angular speed and efficiency.

The baseline indicated by the local board of the ELICA project as a reference to assess the competitiveness of the future concepts is the *Green A/C* described in Ref. [184]. However, the aircraft has been studied according to the same top-level requirements proposed in the ELICA project to make a sound comparison between homogeneous design and typical missions. The reference weights are described in Table 5.23.

As already discussed for the other projects, the severity of one-engine inoperative

Weight breakdown (kg)	
Max take-off weight	7989
Max zero fuel weight	7750
Operative empty weight	4750
Max Fuel weight	2000
Design payload	1767
Design mission	
Fuel consumed	1111
Block fuel	803
Typical mission	
Fuel consumed	642
Block fuel	334

Table 5.23: Weight breakdown of the reference aircraft.

conditions is greatly mitigated by electric power sources. Thus, the main interest of this project is the design of an aircraft with near-zero emissions.

5.2.1 Hybrid-Electric Commuter Aircraft

Two hybrid-electric concepts are discussed in the present section, diversified by the propulsive architectures. Both concepts are powered by a serial/parallel hybrid-electric powertrain, but two different driving factors have been considered for the design of the secondary propulsive line. The first concept introduced in the present section, privileging performance and fuel saving, is powered by distributed electric propulsion and two main propellers. The second concept, favouring maintainability and low production cost, is powered by only four propellers, two of which are electrically driven and mounted at the wing-tip. In order to facilitate the comprehension of this section where multiple vehicles are discussed, the former concept is addressed as DEP, the latter as TIP. Each concept is here analysed considering the two years of entrance in service (2025 and 2035).

Concerning the commuter aircraft including distributed electric propulsion, namely DEP, the geometry shown in Fig. 5.11 has been considered for both target years, even if the structural layout and the propulsive architecture have been designed according to the different technological levels.

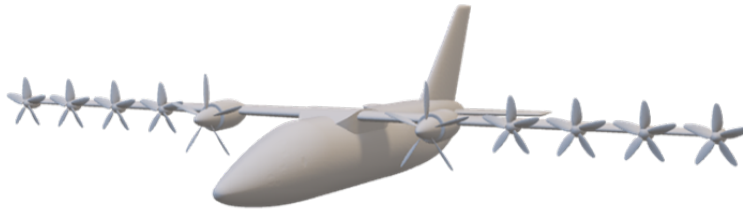


Figure 5.11: DEP concept of the ELICA project.

The non-pressurized cabin has been drawn according to high comfort standards, assuming the same geometry considered for the baseline (Ref. [184]) and reported in Fig. 5.12. The same fuselage has been adopted for four hybrid-electric commuter aircraft of the ELICA project.

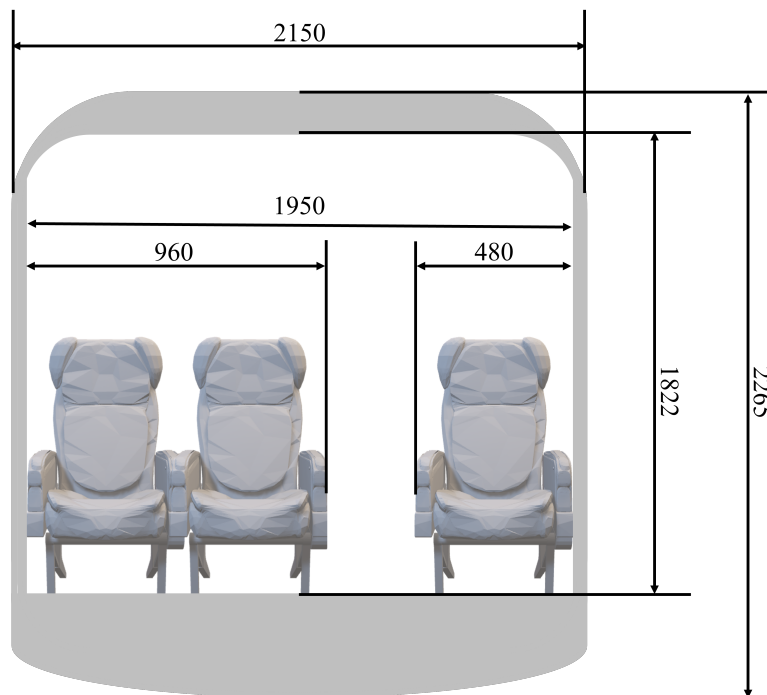


Figure 5.12: Cabin section.

Concerning the wing, the design has been carried out according to the minimum required wing loading and the maximum lift coefficient allowed by distributed electric propellers.

On the other hand, the design of the horizontal tailplane is based on stability requirements measured considering the most unfavourable position of the center of gravity, and the controllability requirement at landing, as shown in Fig. 5.13.

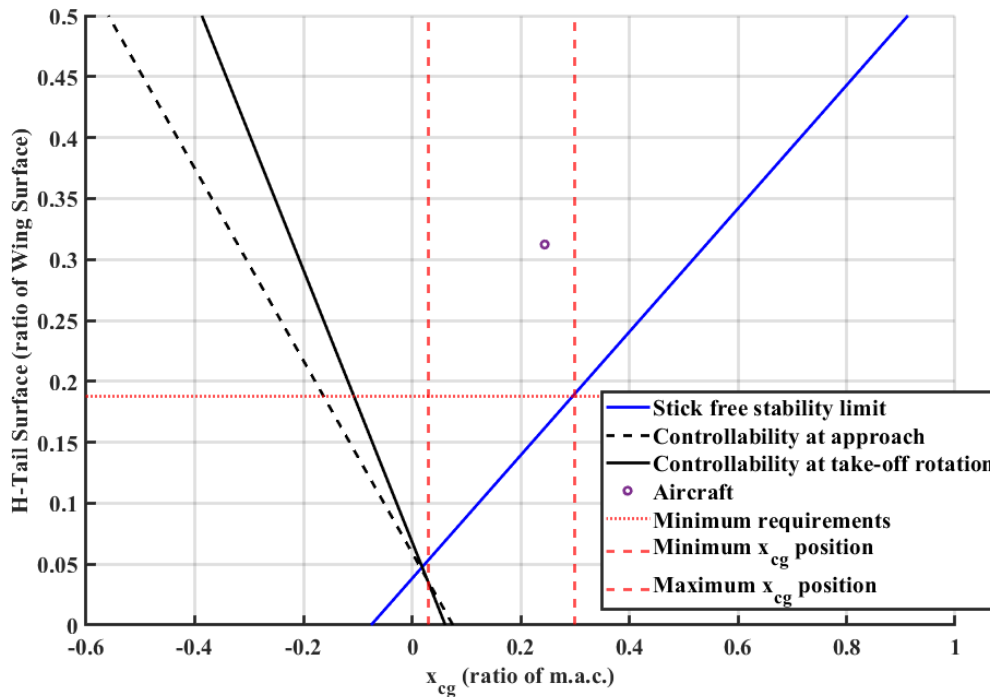


Figure 5.13: Sizing of the horizontal tailplane.

The vertical tailplane is designed to assure the necessary directional stability and controllability even in the most critical failure scenario. The fault tolerance analysis highlighted that the failure of the gasturbine is the most critical condition, causing a thrust loss of about -31% and a residual moment of about 54371 Nm . The resulting minimum control speed is 47.20 m/s .

In the end, the geometry of the aircraft is summarised in Table 5.24. Fig. 5.13 shows that the minimum necessary horizontal tailplane area is about 6.36 m^2 , but Table 5.24 indicates an area of about 10.60 m^2 , as for the reference aircraft. This has been done considering that in case of distributed propulsion, only high-fidelity analysis could accurately predict the effect of the propellers slipstream on the tailplane, thus, it is always advisable to avoid an excessive reduction before performing CFD analysis or wind tunnel tests.

The aerodynamics of the concept is reported in Table 5.25, where the effect of high-lift propulsion on lift coefficient and stall speed is highlighted.

Geometry of DEP configuration		
	Value	Unit
Wing		
Area	33.94	m^2
Span	22.58	m
AR	15.02	—
Horizontal tail		
Area	10.60	m^2
Span	7.00	m
AR	4.62	—
Vertical tail		
Surface	8.63	m^2
Span	3.75	m
AR	1.63	—
Fuselage		
Length	16.25	m
Height	2.26	m
Width	2.15	m

Table 5.24: Main geometric characteristics of DEP configuration.

In Table 5.26, the hybrid-electric concepts mounting distributed electric propulsion are compared to the reference aircraft.

The installed power is increased due to the higher weight, but the total energy necessary to accomplish the mission is reduced due to the higher efficiency of the propulsive system. The serial/parallel hybrid-electric architecture has the advantage of a secondary power source whose efficiency is about 90%. Considering that the efficiency of a thermal engine is around 30%, the advantage of batteries is indisputable. Details regarding the mission analysis of DEP configuration are reported in Table 5.27 and Table 5.28 for the design and typical missions, respectively. Flight performance is compliant with requirements.

The promising results in terms of fuel saving are summarized in Table 5.29, where it is reported a maximum fuel saving percentage of about -52% on the block fuel of the typical mission.

It is here remarked that the promising results in terms of fuel saving percentage cannot be directly reported to the reduction of CO_2 , NO_x , CO , and SO_x . In fact, three factors should be accounted when considering the impact that a new

Aerodynamic data		
Lift coefficient	Value	Unit
$C_{L\alpha}$	0.1049	1/deg
$C_{L_{\max}}$	1.46	-
$C_{L_{\max,reverse}}$	-1.16	-
$C_{L_{\max_L}}$	2.29	-
$C_{L_{\max_L}}(\text{DEP})$	2.60	-
$C_{L_{\max_{TO}}}$	2.03	-
$C_{L_{\max_{TO}}}(\text{DEP})$	2.59	-
Characteristic speeds	Value	Unit
Stall speed	56	m/s
Stall speed (take-off)	48	m/s
Stall speed (take-off + DEP)	42	m/s
Stall speed (landing)	45	m/s
Stall speed (landing + DEP)	42	m/s
Cruise speed	104	m/s
Climb speed	87	m/s
Drag coefficient	Value	Unit
C_{D_0}	0.0247	-
Pitching moment coefficient	Value	Unit
$CM_{ac_{wing}}$	-0.0069	-
$CM_{0_{fus}}$	-0.0490	-
$CM_{\alpha_{fus}}$	0.0252	1/deg

Table 5.25: Aerodynamics coefficients of the DEP concept.

technology has on the environment: production, transport, storage, and usage. Even if electric energy does not produce pollutants during its use, the same cannot be said for its production. For this reason, before assessing the competitiveness of an aircraft, a **life cycle assessment** is necessary to evaluate its environmental impact [190]. From this perspective, considering some simplifying hypotheses, the emissions related to these concepts can be measured. Firstly, the greenhouse gases emitted are measured in terms of $CO_{2_{eq}}$, whose reduction is the main objective of the hybridization. Secondly, neither the emissions related to the production of airframe and systems nor those derived from the disposal are valued. In fact, without the necessary information on the **life cycle inventory**, these emissions cannot be accurately measured. In conclusion, only the emissions related to the power sources are considered and, in particular, to their production and usage.

Year	Reference	DEP	
	2020	2025	2035
Mass (kg)			
Maximum take-off weight	7989	8612	8486
Operative empty weight	5055	6225	6105
Payload	1767	1767	1767
Thermal engines	507	458	458
Generators	0	107	91
E-motor drives	0	268	198
Battery packs	0	500	500
Cabling	0	177	177
Power units	0	91	64
Powertrain	1118	2586	2461
Structure	2412	2607	2607
Fuel	1167	620	614
Rated powers (kW)			
Turboshaft	1119	1180	1180
Generator	0	785	785
E-Motor drive	0	195	195
Battery	0	250	250
Energy (kWh)			
Electric	0	135	167
Fuel	14000	7440	7369

Table 5.26: Comparison of DEP concepts with respect to the reference aircraft.

Year	Reference		DEP			
	2020		2025		2035	
Mission phases	Fuel (kg)	E-energy (kWh)	Fuel (kg)	E-energy (kWh)	Fuel (kg)	E-energy (kWh)
Take-off	3.28	0	2.94	0.35	2.93	0.35
First climb	47.83	0	37.73	4.21	37.56	4.19
Cruise	705.32	0	365.14	44.21	361.63	43.79
First descent	36.69	0.00	18.03	4.21	17.82	4.16
Second climb	15.92	0.00	10.22	0.00	10.18	0.00
Alternative cruise	140.40	0.00	71.13	0.00	70.37	0.00
Second descent	17.38	0.00	8.56	0.00	8.46	0.00
Loiter	134.29	0.00	73.39	0.00	72.63	0.00
Approach	9.21	0.00	2.57	0.00	2.54	0.00
Landing	1.01	0.00	0.76	0.00	0.75	0.00

Table 5.27: Results of the design mission analysis of the DEP concepts compared the reference aircraft.

Year	Conventional		DEP			
	2020		2025		2035	
Mission Phases	Fuel (kg)	E-Energy (kWh)	Fuel (kg)	E-Energy (kWh)	Fuel (kg)	E-Energy (kWh)
Take-off	3.11	0.00	2.80	0.50	2.75	0.63
First climb	44.51	0.00	35.55	5.89	34.96	7.42
Cruise	239.29	0.00	100.91	96.27	95.46	118.85
First descent	36.66	0.00	16.24	5.94	14.73	7.28
Second climb	15.85	0.00	10.20	0.00	10.17	0.00
Alternative cruise	140.44	0.00	71.10	0.00	70.15	0.00
Second descent	17.36	0.00	8.57	0.00	8.46	0.00
Loiter	134.22	0.00	73.32	0.00	72.58	0.00
Approach	9.21	0.00	2.57	0.00	2.54	0.00
Landing	1.01	0.00	0.76	0.00	0.75	.00

Table 5.28: Results of the typical mission analysis of the DEP concepts compared the reference aircraft.

Year	Reference	DEP	
	2020	2025	2035
Design mission			
Fuel consumed (kg)	1111	590 (-47%)	585 (-47%)
Block fuel (kg)	803	427 (-47%)	423 (-47%)
Typical mission			
Fuel consumed (kg)	642	322 (-50%)	312 (-51%)
Block fuel (kg)	334	159 (-52%)	151 (-52%)

Table 5.29: Comparison of DEP concepts with respect to the reference aircraft in terms of fuel consumed to accomplish design and typical missions.

Concerning production, the $CO_{2_{eq}}$ emitted per electric kWh produced in Europe is 150 g/kWh for year 2025 and 86 g/kWh for year 2035³. On the other hand, fuel emissions should account for both production and transport to the refuelling pipeline. From Ref. [191], a mean value of $CO_{2_{eq}}$ emission related to jet-fuel production is assumed: 43 g/kWh .

Regarding the flight mission, the battery does not emit pollutants during its operative life. On the contrary, the emissions produced by the thermal engine are measured according to a specific set of emission indexes. Considering the indexes reported in Table 5.13 [188], a mean emission index of about 3162 g/kg is calculated.

The emissions related to the operative life of the aircraft are reported in Table 5.30.

Differently from the previous concept, whose lifting capability is increased thanks to the use of distributed electric propellers, this concept has the same

³https://www.eea.europa.eu/ds_resolveuid/DAT-13-en

		Reference	DEP	
Year		2020	2025	2035
Design mission: kg of equivalent carbon dioxide				
Production	Fuel	573	305	302
	Electric energy	0	1053	54
Operation	Fuel	3519	1867	1849
	Electric energy	0	0	0
Total	Fuel	4087	2172	2151
	Electric energy	0	1053	54
% from block mission		28%	9%	1%
Typical mission: kg of equivalent carbon dioxide				
Production	Fuel	331	166	161
	Electric energy	0	195	138
Operation	Fuel	2029	1018	988
	Electric energy	0	0	0
Total	Fuel	2360	1184	1150
	Electric energy	0	195	138
% from block mission		48%	7%	6%

Table 5.30: Emissions of DEP concepts in kg of equivalent carbon dioxide for the two mission profiles considered.

geometric characteristics as the reference aircraft, including the wing area (42.43 m^2). Moreover, in this second case, the ratio between the area of the horizontal tailplane and the wing area is about 0.25, which is still compliant with the minimum requirements. In Fig. 5.14, the TIP configuration is presented.



Figure 5.14: TIP concept of the ELICA project.

Without the contribution of high-lift propulsion, the aerodynamics is characterized by the coefficients reported in Table 5.31, where the lower parasite drag coefficient is due to the lower number of nacelles that gives an even higher contribution with respect to the different wing area.

Both TIP concepts, regardless of the year of entrance in service, are characterized by lower fuel saving percentages with respect to the promising results of DEP

Aerodynamic data		
Lift coefficient	Value	Unit
$C_{L\alpha}$	0.1049	1/deg
$C_{L_{\max}}$	1.46	-
$C_{L_{\max\text{reverse}}}$	-1.16	-
$C_{L_{\max L}}$	2.29	-
$C_{L_{\max TO}}$	2.02	-
Characteristic speeds	Value	Unit
Stall speed	49	m/s
Stall speed (take-off)	41	m/s
Stall speed (landing)	39	m/s
Cruise speed	104	m/s
Climb speed	87	m/s
Drag coefficient	Value	Unit
C_{D_0}	0.0247	-
Pitching moment coefficient	Value	Unit
$CM_{ac\text{wing}}$	-0.0069	-
$CM_{0\text{fus}}$	-0.0314	-
$CM_{\alpha\text{fus}}$	0.0161	1/deg

Table 5.31: Aerodynamics coefficients of the TIP concept.

configurations. Since the two platforms have access to the same electric energy, the main difference causing this gap is the induced drag. The reduction of induced drag during the cruise phase is particularly important to reduce the required power, but DEP and TIP configurations approach this issue in two different ways. The former is characterized by a high aspect ratio that permits a considerable increment of efficiency. The latter reduces its induced drag thanks to the slipstream of the tip-mounted propeller.

The results regarding the TIP configurations are reported in Table 5.32 compared to the reference aircraft.

For sake of completeness, ground performances of the four concepts proposed in this section are reported in Table 5.33.

5.2.2 Hydrogen Commuter Aircraft

With the objective of near-zero emissions, the hybrid-electric concepts result to be unsatisfactory, even when the equivalent carbon dioxide emissions are reduced

	Reference	TIP	
Year	2020	2025	2035
Design mission			
Take-off weight (kg)	1111	8438	8415
Fuel consumed (kg)	1111	647 (-42%)	641 (-42%)
Block fuel (kg)	803	470 (-42%)	466 (-42%)
Typical mission			
Take-off weight (kg)	1111	8129	8108
Fuel consumed (kg)	642	352 (-45%)	348 (-46%)
Block fuel (kg)	334	175 (-47%)	173 (-48%)

Table 5.32: Comparison of TIP concepts with respect to the reference aircraft in terms of fuel consumed to accomplish design and typical missions.

	Reference	DEP		TIP	
Year	2020	2025	2035	2025	2035
Balanced field length (m)	995	993	992	995	999
Take off run (m)	570	732	731	730	728
Landing run (m)	710	871	871	736	735

Table 5.33: Ground performance of the hybrid-electric concepts designed for the ELICA project.

by about 50%. For this reason, a new technology has been introduced to power the aircraft: hydrogen fuel cells.

However, powering the aircraft with such an innovative technology, some issues must be faced. Firstly, considering liquid hydrogen, the storage system requires a huge volume. Moreover, the geometry of the tank shall be such as to reduce the tensile stress caused. For this reason, the tank is designed as a cylinder closed by two spherical caps. Secondly, the low specific power of fuel cells causes a huge increment of the maximum take-off weight that could exceed the limits imposed by regulation for commuter category. Finally, a compressor should be designed to keep constant the air pressure entering the fuel cells, as discussed in 2.1.3.

Four powertrain architectures have been investigated, as shown in Fig. 5.15 where the acronym chosen are reported.

The challenging design of the fuel system is divided into two different steps focused on the aluminium tank and the insulation, respectively. The results are reported in Table 5.34 and Fig. 5.16 shows the geometry of the storage system.

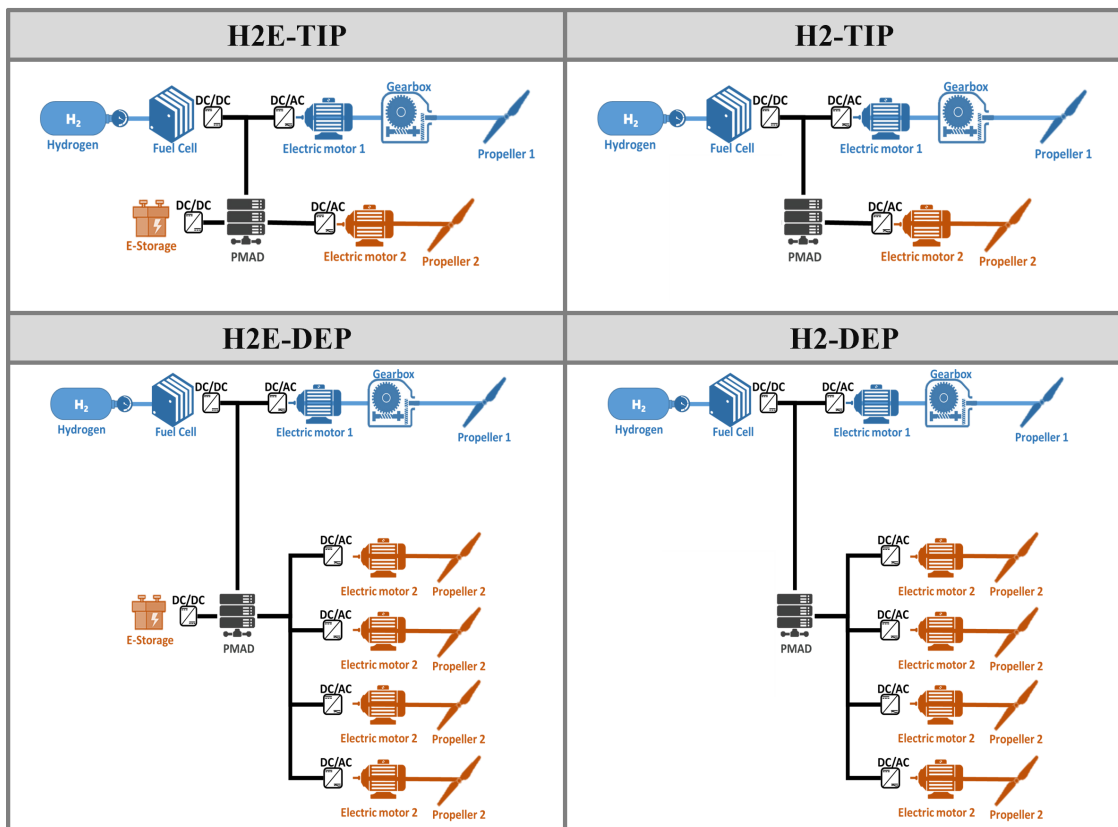


Figure 5.15: Propulsive architectures considered in this section.

The same tank has been considered for both concepts, assuming a maximum hydrogen mass of about 250 kg.

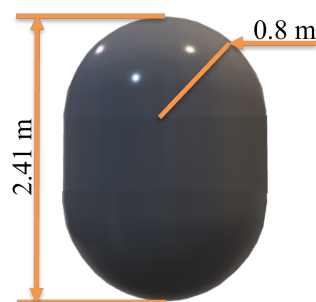


Figure 5.16: Hydrogen tank.

The geometry shown in Fig. 5.16 is not suited to be boarded between the two spars of the main lifting surface. Thus, the fuselage has been stretched to store the hydrogen tank in the fuselage. This has shifted the loading diagram towards the tail and complicated the distribution system with longer pipelines.

Hydrogen tank		
Hydrogen volume	3.53	m^3
Required tank volume	3.78	m^3
Volumetric density H_2	71.00	kg/m^3
Temperature H_2	13.15	K
Pressure H_2	0.15	MPa
Safety margin	7.20	%
Tank wall		
Thickness	0.0010	m
Required thickness	0.0002	m
Aluminium alloy	2014 - T6	
Aluminium density	2800	kg/m^3
Stress safety margin	50	%
Sigma aluminium	410	MPa
Volume of the layer	0.01	m^3
Weight of the layer	34.02	kg
Insulation		
Insulation thickness	0.024	m
Insulation type	Rigid closed cell polyvinylchloride	
Insulation density	49.8	kg/m^3
latent heat of vaporization	446592	J/kg
Thermal conductivity	0.0046	$W/(mK)$
Desired boil-off rate	0.5	kg/h
Outer temperature	333.15	K
Volume of the layer	0.30	m^3
Weight of the layer	14.70	kg

Table 5.34: Characteristics of the hydrogen tank.

A more critical effect on the center of gravity position is related to the weight of the fuel cells. The specific power considered for the year 2025 is 1.6 kW/kg , while a value of about 2.5 kW/kg is expected for the year 2035. From these values and the required installed power, the fuel cells mass is calculated. The fuel cells are stored in the wing to reduce the bending load, but, in this way, an accurate positioning of the lifting surface is of primary importance for balance.

Even if the fuel cells are characterized by a lower specific power with respect to thermal engines, the value is still higher than the one characterizing e-storage units. For this reason, the use of the battery cannot mitigate the installed power, but only slightly reduce the hydrogen mass. Moreover, the introduction of the

battery packs does not increase significantly the safety of the system. In fact, each stack operates independently and it can be separated from the system when one of its elements is experiencing a failure, without critically affect the total power supplied. Such considerations make architectures powered by both battery and hydrogen inefficient in terms of power loading. Thus, since not all the architectures designed are then considered promising, after a comparison based on the data presented in Table 5.35 and the graphs shown in Fig. 5.17 and Fig. 5.18, only one configuration will be detailed.

Concept	H2E-DEP			
Year	2025		2035	
Maximum take-off mass (kg)	11016		10331	
Battery mass (kg)	800		800	
Mission	Design Mission	Typical Mission	Design Mission	Typical Mission
Block H2 (kWh)	3797	1503	3751	1491
Total H2 (kWh)	5170	2870	5099	2834
Block E-energy (kWh)	25	104	23	102
Total E-energy (kWh)	25	104	23	102
Concept	H2E-TIP			
Year	2025		2035	
Maximum take-off mass (kg)	10438		9815	
Battery mass (kg)	1000		1000	
Mission	Design Mission	Typical Mission	Design Mission	Typical Mission
Block H2 (kWh)	3798	1475	3772	1472
Total H2 (kWh)	5159	2833	5116	2813
Block E-energy (kWh)	18	176	17	174
Total E-energy (kWh)	18	176	17	174
Concept	H2-DEP			
Year	2025		2035	
Maximum take-off mass (kg)	9871		9199	
Battery mass (kg)	0		0	
Mission	Design Mission	Typical Mission	Design Mission	Typical Mission
Block H2 (kWh)	3718	1565	3689	1559
Total H2 (kWh)	5040	2885	4993	2861
Block E-energy (kWh)	0	0	0	0
Total E-energy (kWh)	0	0	0	0
Concept	H2-TIP			
Year	2025		2035	
Maximum take-off mass (kg)	9229		8618	
Battery mass (kg)	0		0	
Mission	Design Mission	Typical Mission	Design Mission	Typical Mission
Block H2 (kWh)	3742	1590	3737	1517
Total H2 (kWh)	5050	2896	5034	2807
Block E-energy (kWh)	0	0	0	0
Total E-energy (kWh)	0	0	0	0

Table 5.35: Comparison of the four commuter aircraft concepts powered by fuel cells considering two different years of entrance in service (2025 and 2035).

In the end, considering the most promising alternatives among hybrid-electric and full-electric aircraft presented in the ELICA project, a roadmap can be defined.

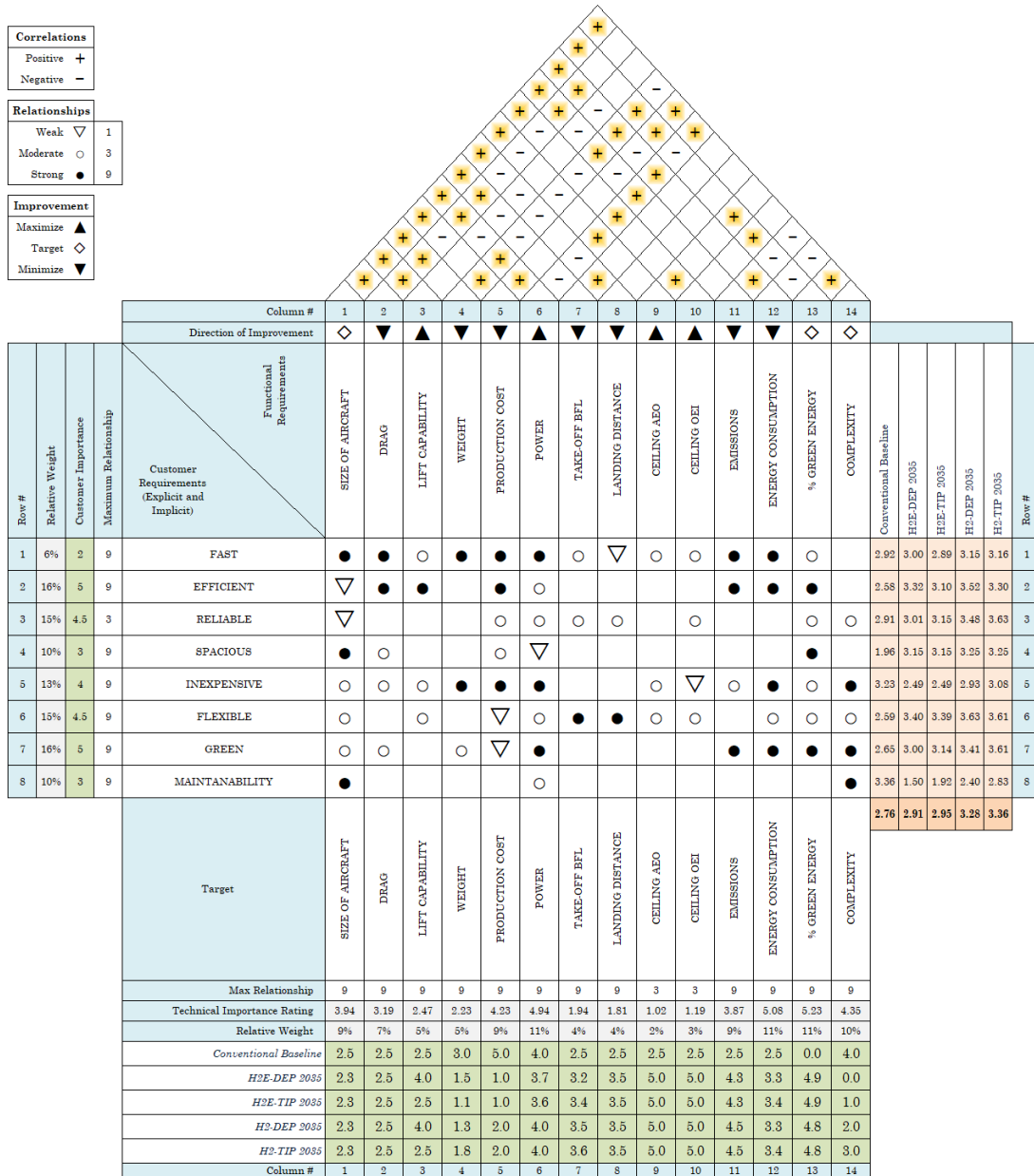


Figure 5.18: House of quality comparing the four concepts designed to enter in service in 2035.

The transition to clean aviation by 2035 should pass through hybrid-electric concepts powered by both jet-fuel and batteries in 2025 to land on a concept fully powered with hydrogen (Fig. 5.19).

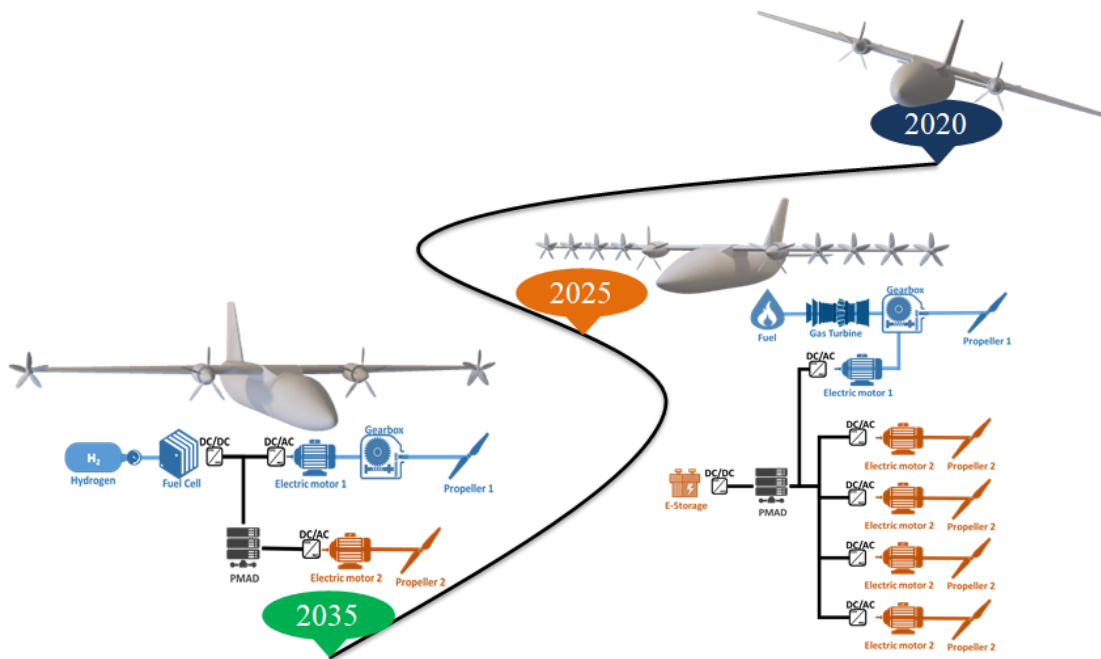


Figure 5.19: Roadmap toward a green aviation by 2035.

The geometry of the aircraft chosen for the final assessment, namely H2-TIP, is summarized in Table 5.36. Moreover, the position of the wing has been shifted 0.15 m towards the tail to limit the center of gravity variation with respect to the hybrid concepts.

The rated powers of each element of the propulsive system, shown in Fig.5.20 have been measured by iterating the mission analysis.

At each step of the iterative loop of the mission analysis, updating power and energy requirements, the operative center of gravity is measured considering the new masses associated with each element of the propulsive system, as shown in Fig. 5.21. Moreover, associated with the new weights, both the required wing load and tailplanes areas are verified.

In the end, concerning results presented in Table 5.35, Table 5.37 reports the mass breakdown of the configuration.

Geometry of DEP configuration		
	Value	Unit
Wing		
Area	42.43	m^2
Span	22.56	m
AR	12.00	—
Horizontal tail		
Area	10.60	m^2
Span	7.00	m
AR	4.62	—
Vertical tail		
Surface	8.63	m^2
Span	3.75	m
AR	1.63	—
Fuselage		
Length	18.00	m
Height	2.26	m
Width	2.15	m

Table 5.36: Main geometric characteristics of H2-TIP configuration.

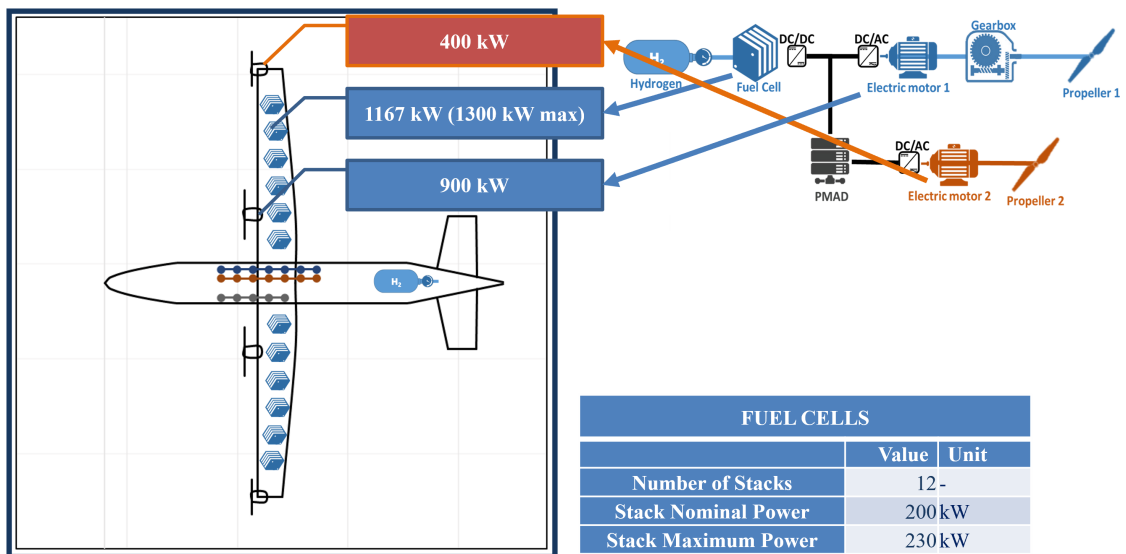


Figure 5.20: Propulsive system of the H2-TIP concept.

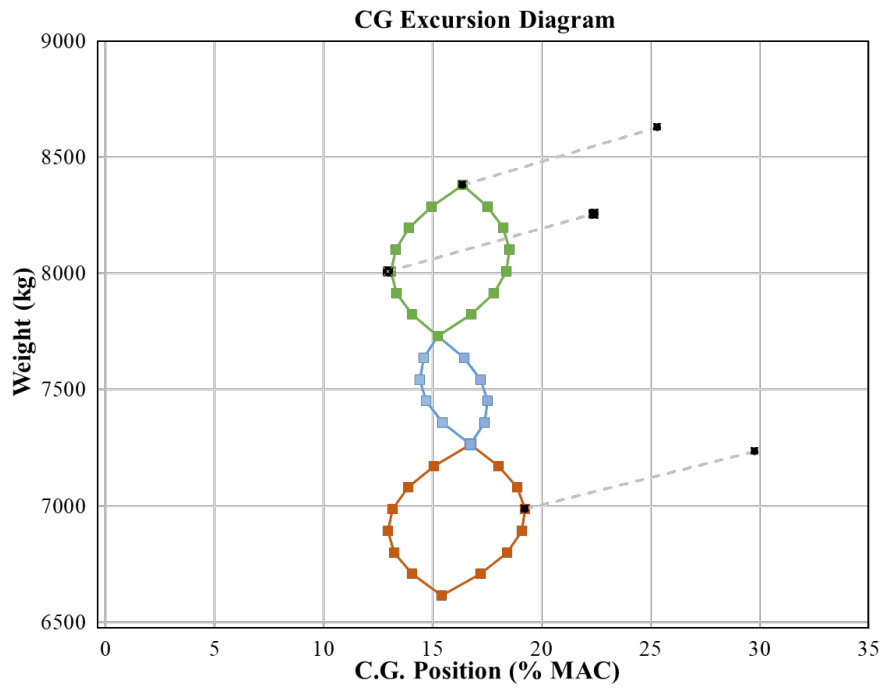


Figure 5.21: Loading diagram of the H2-TIP concept.

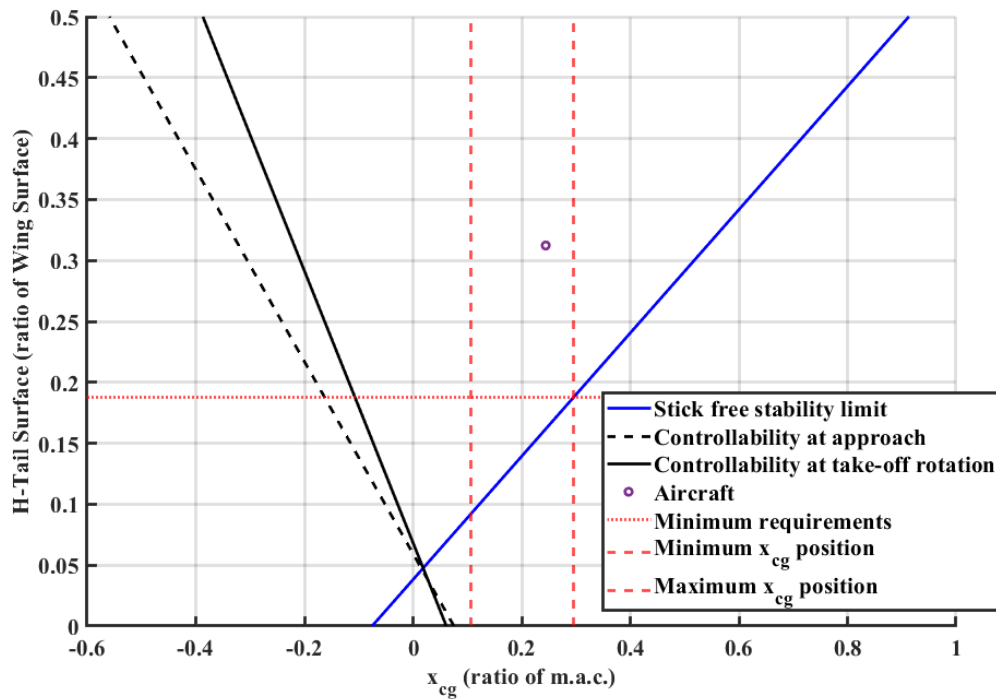


Figure 5.22: Sizing of the horizontal tailplane for the H2-TIP concept.

Weight breakdown (kg)	Value	N° units
Hydrogen	150	
Powertrain		
Tank	48	1
Generator/Motor	50	2
E-Motor drive	49	2
DC/DC fuel cell	17	2
DC/AC e-motor drive	7	2
DC/AC generator	13	2
Cabling	66	1
Gearboxes	126	1
PMAD	2	2
Propeller DEP	160	2
Propeller main	158	2
Fuel cell	467	2
Total	2090	
Structure		
Wing	905	1
Fuselage	1068	1
Undercarriage main	428	1
Undercarriage nose	109	1
Horizontal tail	16	1
Vertical tail	32	1
Control surface	88	1
Nacelles	200	1
Total	2846	
Systems		
Air conditioning	207	1
Electrical	237	1
Pneumatic/Hydraulic	137	1
Instruments	139	1
Total	720	
Operating equipment		
Operational items	164	1
Crew	186	1
Total	350	
Furnishing	598	
Operative empty	6614	
Payload	1767	
Maximum zero fuel	8381	
Maximum take-off weight	8618	

Table 5.37: Weight breakdown of the H2-TIP concept.

It is explicitly remarked that this concept has the potential to be a zero-emission concept, at least for what concerns its operative life. In fact, the only fuel cell emission is water vapour and hydrogen production can potentially be at *negative environmental impact*. In other words, instead of emitting greenhouse gases, hydrogen can be produced by consuming CO_2 from atmosphere. This is the case of the serpentinization of olivine [192], for example. Moreover, good results have been obtained by bio-production in microbial cells containing electrolytic bacteria [193].

Airplanes are beautiful dreams. Engineers turn dreams into reality.

— Hayao Miyazaki, *The Wind Rises*

6

Conclusions and perspectives

Contents

6.1	Added value and State of the Art	293
6.2	Achievements and Considerations	306
6.3	Roadmap to Clean Aviation	308

6.1 Added value and State of the Art

The reduction of global emissions is absolutely the hardest challenge that aviation has ever faced. Differently from other studies, the research published in this work firmly states that more than unconventional concepts, the future of aviation lies in unconventional propulsive systems. Rather than reorganizing the manufacturing chain to pursue disruptive solutions, result of the creativity and geniality of small groups of designers, the conventional tube-and-wing configuration, developed for the past 60 years, can offer an immediate answer to the challenge posed by global warming. Among the available technologies, an answer to this challenge has been found considering innovative and electric propulsive systems. However, the lack of methods suited to approach the conceptual design of hybrid-electric aircraft with a certain flexibility, as it is convenient at the early stages of the design process,

has laid the foundations of the research proposal: *how can the conceptual design process be revised to design electric aircraft?*

The answer has been found merging the know-how coming from different research fields in a unique workflow. In this way, even when the new aircraft has its starting point in a blank sheet project, the designer has the mean of easily explore the design space investigating the effect of multiple propulsive architectures and enabling technologies. To accomplish this result, this work presented mathematical models capable of describing with a good level of fidelity the effects of the different propulsive systems on different characteristics of the aircraft. The characteristics are updated at each step of the design process according to a simplified and recursive scheme:

- 1 aerodynamics modelling;
- 2 performance evaluation;
- 3 powertrain sizing;
- 4 mass estimation.

As previously stated, the mathematical models are the result expertises coming from different engineering fields, simplified, where possible, to be adapted to the early stages of the design process.

However, incremental innovation and integration are rarely recognized and rewarded by the market. Thus, this paragraph is aimed to highlight the added value compared to the state of the art. Addressing the future designers, the structure of the work makes accessible the methods to the reader in 2 and describes the single procedures concerning the workflow in 3 and 4, without emphasizing the state of the art, its limits, and the innovation achieved. In this respect, the following paragraphs summarize the outcomes of this research, giving importance to each aspect, even when the complexity can appear unnecessary.

To support this research activity and comparing different methods, the author of this work created HEAD (Hybrid-Electric Aircraft Designer), a MATLAB[®] based tool. The methods and the satisfactory results obtained have been validated thanks to continuous interaction with industrial partners providing feedback within different research frameworks.

Analytic model of the propulsive system

The modelling of the propulsive architecture is based on the energy balance, as suggested in literature [41]. The set of equations can be freely chosen by the designer depending on the propulsive architecture of interest. Two alternatives, with the associated set of operating modes, are presented to highlight the flexibility of this type of model based approach (2.1.1 and 2.1.3).

State of the art

Analytic model of the propulsive system through powertrain equations.

However, the mathematical model is not as general as stated in literature. Some values of the supplied power ratio, coupled to specific values of the efficiencies, can make the matrices shown in 2.1.1 singular. Moreover, even when the analytic solution is obtained, its physical sense is not assured. The last issue deals with the management of the power sources. In fact, the introduction of the supplied power ratio automatically limits the number of power sources to two. Actually, in the same way, the introduction of the shaft power ratio limits the number of propulsive lines to two. In other words, the simplicity of powertrain equations is also a limiting factor.

Issues

- 1 - The singularity of the solution in specific operating conditions is not discussed.
- 2 - Not all the operating conditions make physical sense.
- 3 - The powertrain equations cannot include more than two power sources.

The direct consequence of the first and second issues can be clearly stated: the reliability of the results is compromised. At each step, the designer must verify the solution. However, this control can be automatized thanks to the algorithm proposed in this work. The algorithm has been designed to be deployed on a power management unit to handle both non-physical and singular solutions.

More complex is the solution to the last issue. As a consequence, the limit to two propulsive lines and two power sources results in the difficult management of multiple subsystems composing the same powertrain. This critical point has been solved

through the algorithm proposed in 2.3.1. The added value of this solution is keeping the simplicity of powertrain equations while considering multiple subsystems. On the other hand, the method has been enlarged considering additional technologies and different propulsive architectures, as discussed in 2.1.3 for the case of fuel cells.

Added value

- 1 - Identification of the operating conditions that do not make physical sense.
- 2 - Identification of the operating conditions that cause analytical singularity.
- 3 - Definition of a procedure to handle these conditions.
- 4 - Identification of an alternative set of powertrain equations suited for fuel cells.

Modelling and sizing of the powertrain elements

Before underlining the innovative aspects related to the modelling of the single elements, some critical aspects should be highlighted. The present work deals with the design of hybrid-electric aircraft assuming that the state of the art concerning the modelling of thermal engines and batteries is at the peak of technological innovation. In other words, the research activity is focused on the issues related to the integration of the single technologies, rated than on innovating mathematical models concerning the design of the specific components. In fact, except for disruptive technologies that are still not available, all the batteries, from the classical packs to the structural batteries, can be modelled considering the same mathematical dynamics model. The same goes for the fuel cells and the engine deck. In the present work, the engine decks are not reported since the data have been provided by industrial partners.

The solutions proposed in literature to face the challenges associated with the integration of batteries and electric motors have been validated with flying prototypes. In this context, the elements of novelty are limited to the modelling of fuel cells and the sizing procedure of cabling. In literature, there are many mathematical models capable of simulating the dynamics of fuel cells. Moreover, the dependency of the output power from the entering oxygen pressure is known.

State of the art

- 1 - Many mathematical models can be applied to simulate the dynamics of fuel cells.
- 2 - The dependency of the power supplied on the input oxygen pressure is known.

However, the integration at aircraft level cannot neglect an important aspect: the pressure of the oxygen is related to the flight conditions. In fact, even when inlet and compressor are coupled to the fuel cell, Mach number and altitude variations affect the oxygen pressure. Consequently, the variation of the power supplied by the redox reaction can be directly related to these two flight conditions, as already done for the engine decks.

Issues

The integration of fuel cells in a flight simulation has never been related to the flight conditions.

In the end, the use of an engine deck to model the dynamic behaviour of the fuel cell is the most suited method to link the flight conditions to the supplied power. Since this approach has never been proposed before in literature, its novelty required the description of each step in 2.1.3.

Added value

Starting from the dynamics of fuel cells and its dependency on the input oxygen pressure, an engine deck is designed to relate the Mach number and the altitude to the power delivered. The contribution of inlet and compressor is included.

Differently from conventional aircraft, in case of electric propulsion, the cabling system must be capable of distributing high values of power. This requires larger diameters and weights of the bundles, as discussed in 2.1.5. All the constraints related to the sizing procedure of these elements are regulation matters. However, in general, the procedure to minimize the weight of the bundles is not a major task and this element is seldom considered at conceptual design level.

State of the art

Regulation provides the necessary constraints for the sizing of cabling.

The large number of information required to design the cabling system discourages its sizing at this stage of the design chain. In general, information concerning voltage and current requirements are considered at the preliminary stage of the design procedure, where a certain maturity level is reached. As already stated, except for the fuel cells, the models for the individual components of the electric systems are state of the art. However, the simplified approach by which these models are included in the design procedure is necessary to design the cabling system. Similarly to what has been done in literature and in this work for the aero-propulsive interactions, the novelty is not related to the knowledge of the physical phenomenon or the introduction of new technologies, but to the simplified approach that makes available at this level all the information necessary to minimize the weight of the cabling system. In conclusion, the added value is the conceptual design procedure of the cabling system.

Issues

At conceptual design level, the cabling systems is seldom considered in case of conventional aircraft.

Added value

An iterative procedure to size the cabling system is proposed based on the information available at this stage of the design process.

Aero-propulsive interactions

The estimation of the effects on aerodynamics coefficients when the propellers' slipstreams interact with the lifting surfaces has been widely discussed and verified in literature. Starting from the computational fluid dynamics and ending to the wind tunnel tests, many methods are available to quantify these effects. However, at conceptual design level, these methods are time-consuming and inefficient. This reason is behind the success of the simplified approach proposed in literature

[41] for the estimation of the aero-propulsive interactions between distributed propellers and lifting surfaces (2.2.1).

State of the art

Analytic method to estimate aero-propulsive effects related to distributed electric propulsion.

Issues

Lack of a similar method for the estimation of aero-propulsive effects in case of tip-mounted propellers.

Added value

Design of an analytic method to estimate aero-propulsive effects in case of tip-mounted propellers.

In this work, a simplified approach for the estimation of the induced drag reduction achieved by installing tip-mounted propellers is proposed. Even if the effect may appear limited with respect to distributed propulsion, the magnitude is the same of the winglets, as shown by the results reported in 2.2.3.

Airworthiness

The airworthiness of hybrid-electric architectures has been largely discussed from the perspective of the risk assessment [23–25] or the fault tolerance [135]. The second procedure considering the fault tree analysis is the most suited when no information is available about the failure rate of each component, as at this stage of the design process. On the other hand, the estimation of the minimum control speed in case of one engine inoperative is a well-known procedure for conventional aircraft.

State of the art

- 1 - The fault tolerance analysis has been performed on hybrid-electric propulsive systems.
- 2 - The evaluation of the minimum control speed for concepts powered by distributed propellers has already been discussed.
- 3 - The importance of the failure rate on the assessment of fault tolerance has been highlighted in literature.

However, at conceptual design level, the designer lacks the necessary information to perform a risk assessment (e.g.: the failure rate of each component). A fault tolerance analysis assures the safety of the propulsive system regardless of the reliability of each element. On the other hand, the fault tolerance analysis does not account for the varying aero-propulsive effects when the thrust distribution changes. Moreover, the possible failure of the power sources is often neglected. These aspects are more critical than they could appear at first, particularly in case of high-lift propulsion. Firstly, the critical failure of a power source could drastically affect stall speed, yaw, and roll. Secondly, the asymmetric thrust can cause an increment of the minimum control speed beyond the stall speed.

It cannot be preventively stated which is the element whose failure is critical. Thus, a fault-tolerance analysis is necessary to identify the most critical one and the necessary oversizing of the elements to mitigate the severity of this condition thanks to the redistribution of the power. Moreover, the algorithm must be sensitive to the number of subsystems and connections, the storage of the electric energy in multiple battery packs, and the redundancies.

Issues

- 1 - The failure conditions considered in literature do not include the failure of the battery packs.
- 2 - The maximum thrust loss and the maximum residual yaw moment are often identified in the same failure condition.
- 3 - The importance of the power redistribution, the element oversizing, and the connections among the subsystems is not sufficiently stressed, nor subject to any optimization process.

The workflow proposed in this work to perform the fault tolerance analysis of hybrid-electric systems starts from the powertrain equations previously discussed. Without lacking of generality and simplicity, the method is adapted to propulsive systems composed of multiple parallel subsystems, connected or not.

The critical conditions are studied considering both the maximum thrust loss and the residual yaw, which can be caused by different failures. The inclusion of the aero-propulsive effects to assess controllability and stability of the aircraft is an

element of novelty appreciated by the industrial partners.

Finally, the mathematical model obtained allows mitigating the severity of the risk conditions through the introduction of additional elements and the over-sizing of others.

Added value

- 1 - The mathematical model based on the powertrain equations is adapted to each subsystem composing the propulsive system.
- 2 - A general procedure to verify the most critical condition in terms of power loss and residual yaw moment is provided.
- 3 - The same procedure evaluates the effect of this condition on longitudinal and latero-directional trim and stability.
- 4 - This algorithm has been shared with Siemens that based on it a generative engineering tool for powertrain architecting.

The minimum control speed and the stall speed are related by regulation constraints. In this work, the certification aspects are not neglected when considering the capability of reducing the stall speed at take-off and landing. The fault tolerance analysis for take-off, landing, and climb conditions is a crucial aspect stressed in 2.3.

Weight estimation

The weight estimation is a mandatory step concluding each phase of the design process. Different levels of fidelity are necessary depending on the design stage and the maturity of the concept. Generally, at conceptual design level, the weight estimation of conventional aircraft is based on the statistic correlation between each system mass and some geometric parameters. In literature [165], the integration of these methods in the innovative conceptual design chain leads to results that are strongly dependent on the well-educated guesses of the designer concerning the electric components.

State of the art

II-class methods for weight estimation are widely discussed in literature, as well as the revisions necessary to allow their application to electric concepts.

Two issues have been identified by aviation industry during the evaluation of the innovative electric concepts that are spreading. Firstly, the results are often related to the optimistic assumption of the designers about the technological level reached by the electric components by the entrance in service. Secondly, the electrification of existing platforms is often performed keeping the structural layout unchanged. In this case, the increment of static and aeroelastic loads is not considered.

Issues

- 1 - At conceptual design level, the estimation of electric components of the propulsive system lies in the well-educated guess of the designer regarding specific energy and power.
- 2 - The change of wing's aero-elastic characteristics due to the presence of new elements along the wingspan is not considered.

The added value in terms of weight estimation methodology is the statistic correlation between data provided by industrial partners and the mass of each electric component. The equations proposed in 2.4.3 guide the estimation of the weight without requiring well-educated guesses about the specific power or the specific energy. Additionally, the variation of the structural weight of the lifting surfaces mounting multiple propellers is discussed proposing a method that can scale the necessary mass to keep the flutter speed constant during the hybridization of existing platforms.

Added value

- 1 - A new method for the estimation of the electric components is provided according to data collected from literature and industrial partners.
- 2 - The variation of the wing's structural mass has been calculated considering the correlation between the flutter speed and the position of the masses along the wingspan.

Estimation of Point Performance

The estimation of point performance for electric aircraft has been discussed by the authors of Ref. [41, 165]. Starting from the procedure proposed in Ref. [64],

the authors proposed some small changes to estimate the sensitivity of the design space to aero-propulsive interactions and hybridization ratios.

State of the art

- 1 - Methods for the estimation of point performance of electric vehicles have been largely discussed.
- 2 - The new methods proposed in literature include the aero-propulsive effects associated to distributed electric propulsion.

Most of the sizing procedures proposed in literature are suited for the electrification of existing aircraft. Nevertheless, the integration of the aero-propulsive interactions between distributed propulsion and lifting surface can open the path to innovative configurations. On the other hand, the I-class method for weight estimation can be considered a weak point.

Issues

- 1 - Most of the methods proposed in literature deal with the electrification of already existing platforms.
- 2 - The aero-propulsive effects related to tip-mounted propellers are not included.
- 3 - The weight estimation is often related to I-class methods, which do not accurately take into account the additional increment of structural mass.

The estimation of point performance has been enhanced with the introduction of the aero-propulsive effects caused by tip-mounted propellers. The design process is based on a statistical approach to the market segment identified by the top-level requirements, which makes the sizing activity independent from a specific baseline. In other words, the geometry used to compare a conventional aircraft and its hybrid version is fictitious, but effective in terms of sensitivity analysis. Finally, the weight assessment is based on the II-class methods, modified as proposed in 2.4.

Added value

- 1 - The sizing activity discussed in this work can start from a blank sheet project.
- 2 - The aero-propulsive effects related to the tip-mounter propellers are included.
- 3 - The weight assessment is based on II-class methods.

Estimation of Flight Performance

The assessment of flight performance is not of secondary importance when coming to hybrid-electric or full-electric aircraft. Their competitiveness on the market can only be assessed if they have similar performance with respect to conventional concepts. In literature, many different simulation based approach are reported [138, 143] and software integrating those approaches populates the market (e.g.: FLOPS¹, JPAD², and Pacelab APD³). In general, the state of the art regarding flight simulation is valid, as long as the system design can be detailed through the introduction of engine decks and response surfaces.

Nevertheless, some issues are reported concerning the integration of hybrid-electric systems. Supported by TxT⁴ and Leonardo S.p.A.⁵, the comparison of the methods adopted to perform the flight simulation highlighted the lack of results including the aero-propulsive effects at the state of the art. This has been the starting point of the research activity performed in the Italian research project named PROSIB, whose results produced by the author are discussed in 5.1. Moreover, the sizing of the electric energy storage is often performed considering the typical mission, which results in lower operative flexibility of the platform. Finally, the calculation of fuel consumption from engine decks is often related in literature to the specific fuel consumption or the thrust specific fuel consumption. This can be a

¹NASA FLOPS webpage: <https://software.nasa.gov/software/LAR-18934-1>

²SmartUp software webpage: <https://www.smartup-engineering.com/engineering/software/32-jpad>

³TxT software webpage: <https://pace.txtgroup.com/products/preliminary-design/pacelab-apd/>

⁴TxT webpage: <https://pace.txtgroup.com/>

⁵Leonardo S.p.A. webpage: <https://www.leonardocompany.com/>

limiting factor when the thermal source is not directly connected to the propulsive shaft or when the propulsive unit is alimented by more than one power source.

State of the art

- 1 - Simulation based approaches integrating complex propulsive systems are already applied to flight simulation.
- 2 - The query of thermal engine decks built through appropriate software, such as GasTurb, has already been discussed.
- 3 - The dynamics of batteries and fuel cells is part of the state of the art.
- 4 - The integration of look-up tables for the efficiencies is already part of Simulink Aerospace Blockset or Pacelab SysArc.

Issues

- 1 - Flight simulation do not include aero-propulsive effects.
- 2 - Most of the simulation algorithms do not include acceleration phases and flight control procedures.
- 3 - Flight performance associated to the dependence of fuel cells from Mach number and altitude has never been discussed.
- 4 - The minimization of the thermal energy used along the typical mission, optimizing the use of the battery sized to accomplish the design mission, is often considered a secondary task.
- 5 - The fuel consumption cannot be related to the thrust specific fuel consumption or the power specific fuel consumption

The main added value of this work concerning the assessment of flight performance is the inclusion of the aero-propulsive effects in the simulation loop. However, in the difference with respect to other simulation algorithms, some other elements of novelty can be identified. The first aspect deals with the thrust assessment. Typically the necessary thrust is calculated through the excessive power models straight forward. This is the case of the second algorithm proposed in 4.1. However, the complexity added by the introduction of the other two algorithms play a role in calculating the rated power. When approaching a stepped climb, the procedures presented in 4.2.2 allows the use of the maximum throttle, which is a flight condition described by the first algorithm in 4.1. An inappropriate value of the supplied power ratio could result in an uncomfortable acceleration that is symptomatic of an oversizing of the thermal engine. More specifically, since most of the algorithms simulate a unique segment of climb at constant rate-of climb and

calibrated airspeed, they neglect the stepped climb and the associated procedures that have been included in this work. On the other hand, neglecting these procedures, the time necessary to climb is fixed neglecting one of the variables necessary to optimize the energy use. The same considerations apply to the unsustained descent. The three algorithms presented in this work propose the necessary variations to the procedures discussed in Ref. [138] to be applied at hybrid-electric aircraft and full-electric aircraft. On the other hand, the fuel cell models proposed in literature [23] are pushed forward to integrate the dependency from both Mach number and altitude.

Added value

- 1 - The flight simulation includes the evaluation at each step of the aeropropulsive effects.
- 2 - The rated power of each element of the powertrain is based on the maximum value required during the whole design mission.
- 3 - The evaluation of flight performance takes into account the effect that Mach number and altitude have on the maximum power supplied by the fuel cells.
- 4 - An equation to scale the thermal power when the electric power supplied changes is provided (Eq. 4.1). This is an additional constraint to the powertrain equations assumed when minimizing the energy consumption of the typical mission.
- 5 - Definition of an algorithm relating the thermal power to the fuel flow through the thermal efficiency.

6.2 Achievements and Considerations

The conclusive part of this work aims to identify the main achievements and critically discuss the limits. Three years and many concepts after the beginning of this research activity, there is still much more to do. Nevertheless, some challenges have been successfully faced. Firstly, the mathematical model to describe the powertrain at the early stages of the design process has been studied to exclude all those solutions that are not operatively feasible. Moreover, the model has been enlarged to include additional power sources and components. The fidelity level is varied by including additional information at each step of the design process. For instance, by assuming constant values of the efficiencies or introducing the

appropriate look-up tables. The tests, carried out with the support of different industrial partners on different categories, confirmed the reliability of the results (4.3). The major drawback of this approach is related to the large number of details required as inputs. Moreover, since the efficiency maps and the engine decks are often not provided to the designer from the early stages of the design process, the reliability of the model depends on the assumptions made. In principle, the model should be capable of simulating any powertrain architecture, but the lack of tests associated with the case of jet aircraft makes this a personal assumption of the author. Moreover, the validation of the fuel cell model is still ongoing. The inclusion of flight altitude and the Mach number in the high-fidelity tools employed to simulate the dynamics of the system architecture required a dedicated effort by the manufacturers involved. However, the preliminary results at altitudes lower than 10000 *ft* and Mach numbers lower than 0.30 are promising.

Concerning the design procedures, the validation of point performance is done by comparing the results obtained by different methods. Even when the disagreement of the results is higher than 5%, the method proposed in this work seems conservative with respect to the others (3.4). On the other hand, the algorithm for estimation of flight performance can be considered particularly reliable, even when compared to the software available on the market (4.3). Even after these reliable results, the design procedure requires additional tests to verify its applicability to aircraft categories other than commuter category and regional category.

The applications concerning the regional turboprop category highlighted the necessity of a precise optimization of the typical mission. The long-range design mission required by the market for this aircraft category is particularly demanding but necessary to preserve the operative flexibility. On the other hand, since 80% of the operative life of a regional aircraft is composed of typical missions, the design of the electric energy storage should aim to maximize the fuel-saving percentage during this flight profile with a shorter range. Moreover, the turbo-electric propulsive architecture demonstrated a negligible effect on fuel consumption; thus, the battery packs are the key to reducing emissions. Unfortunately, the results highlighted

that all the expected benefits lie in the optimistic technological advancement of these components. In other words, everything depends on the future values of specific energy and power. Applications discussed in 5.1.1 demonstrated that the hybridization of regional aircraft allows a CO_{2eq} reduction of about -50% in the most optimistic scenario.

Regarding general aviation, results presented in 5.2 demonstrate the feasibility of near-zero-emissions concepts by 2035. The values refer to the emitted quantity of greenhouse gases per flight. However, before assessing the feasibility of these concepts, the designers must deal with some additional challenges. The first challenge deals with the safety issues associated with the integration in the fuselage of the hydrogen tank. This aspect is of primary importance, and the present work tries to account for as many elements as possible to approach this problem, but it neglects some higher-order details associated with the venting system and the pipelines. The second challenge identified concerns the thermal management system. The low operative temperature of the cryogenic hydrogen and the power dissipated as heat by the fuel cells can create a critical operative condition for the thermal management system. For example, the hydrogen temperature changes between the $-260^{\circ}C$ in the tank and the $20^{\circ}C$ of the fuel cell. This variation can cause a disruptive phase change. When designing this system, the phase changes must be considered accurately (both for the coolant and the hydrogen).

One last consideration regards the hybrid commuter aircraft proposed in the same section. It can be considered a feasible concept for a closer entrance into service. However, in this case, the spread of new diesel engines on the market can easily make these concepts less competitive.

6.3 Roadmap to Clean Aviation

The conclusions of this work cannot neglect the negative aspects that emerged from this research so that the context of the prosecution can be established. At odds with many literature studies dealing with technical aspects, one of the conclusions of the present work is that the use of batteries as power sources must be limited

to the short period. A more sustainable alternative should be found to face the future market demand. This consideration is not related to the emissions caused by production and disposal of batteries, which must be in any case reduced by applying an appropriate recycling chain, but it is motivated by the actual capability of producing the number of batteries necessary to sustain aviation at today's level (pre Covid-19).

Considering the battery breakdown proposed in Ref. [194], the battery mass is composed of multiple metals, like cobalt and nickel, whose prices are strictly related to three factors: availability on Earth, market demand, and production rate (in *kg/year*). On the other hand, magnesium can be derived from seawater and other minerals, making this resource potentially unlimited, so that in this case the market is ruled by demand and production rate. Considering a specific type of battery, namely NCA batteries, described in Ref. [194], the following percentages of the aforementioned materials will be considered:

- Cobalt: 2.3%;
- Nickel: 12.1%;
- Magnesium: 0.0%;

Considering the promising results presented in this work about the hybridization of regional aircraft, a mean battery mass is considered of about 3000 *kg*. From Table 1.3, the number of cycles has been fixed to 1500, which is barely sufficient to fly 4 flights per day each year. In other words, to sustain the current level of air traffic, which implies that a regional aircraft should fly between 4 and 20 typical missions per day [195], the battery should be substituted each year, at least.

Considering the major fleets flying among mainlines aircraft and regional aircraft, the impact of the hybridization of these categories on natural resources is measured considering the data presented in Table 6.1⁶.

Assuming that each battery has a mean operative life of about one year, the impact of the material production is measured on a yearly basis. Information provided by the *United States Geological Survey* about mineral production has been used

⁶Flight Global webpage: <https://www.flightglobal.com/>

Aircraft fleets			
Mainline aircraft: top 10 fleets	Number of Aircraft	Regional aircraft: top 10 fleets	Number of Aircraft
Airbus A320ceo family	7198	Embraer 170/175/190/195	1491
Boeing 737-600/700/800/900	6492	ATR 42/72	1209
Boeing 777	1515	Bombardier CRJ700/900/1000	843
Airbus A330ceo/A340 family	1478	Embraer ERJ-135/140/145	686
Airbus A320neo family	1377	Bombardier CRJ100/200	677
Boeing 737-200/300/400/500/	976	De Havilland Canada Dash 8-400	553
Boeing 787	965	Bombardier Dash 8 Q100/200/300	435
Boeing 767	800	Beechcraft 1900	384
Boeing 757	715	De Havilland Canada Twin Otter	368
Boeing 747	497	Fairchild Swearingen Metroliner	262
Total	22013		6908
Batteries			
Number of batteries	22013		6908
Mean battery weight (kg)	3000		3000
Weight of batteries (kg)	66039000	100%	20724000
Necessary materials			
Cobalt (kg)	1518897	2.30%	476652
Nickel (kg)	7990719	12.10%	2507604
Magnesium (kg)	0	0%	0
Total			
Weight of batteries (kg)		86763000	
Cobalt (kg)		1995549	
Nickel (kg)		10498323	
Magnesium (kg)		0	

Table 6.1: Aircraft fleets and the associated battery mass required to hybridize each aircraft.

to measure the effect that aviation will have at the beginning of the hybridization process. The results are reported in Table 6.2 as percentage of absorbed annual production of the major cobalt⁷ and nickel⁸ producers.

Table 6.2 shows that the hybridization process that is about to begin in aviation has the potential of changing the mineral market equilibrium, reducing the reserves of many countries and drastically increasing the prices of any electronic product. The comparison between the two resources highlights that the effect of cobalt demand can be particularly critical for the future of aviation. The supply risk can be divided in three main groups [196, 197] depending on the reason that make its supplies inadequate for the demand. The first group deals with the physical unavailability of cobalt. However, comparing the future demand to reserves (Table 6.2, resources, and recycling, it can be assessed to be a modest risk [198]. The second type of risk is connected to cobalt market, due to its by-product dependence and

⁷U.S. Geological Survey webpage: <https://www.usgs.gov/centers/nmic/cobalt-statistics-and-information>

⁸U.S. Geological Survey webpage: <https://www.usgs.gov/centers/nmic/nickel-statistics-and-information>

	Aviation absorption of cobalt produced (%)		
	Production in 2019	Production in 2020	Reserves
United States	399.1%	332.6%	3.8%
Australia	34.8%	35.0%	0.0%
Canada	59.7%	62.4%	0.9%
China	79.8%	86.8%	2.5%
Congo	2.0%	2.1%	0.1%
Cuba	52.5%	55.4%	0.4%
Madagascar	58.7%	285.1%	2.0%
Morocco	86.8%	105.0%	14.3%
New Guinea	68.6%	71.3%	3.9%
Philippines	39.1%	42.5%	0.8%
Russia	31.7%	31.7%	0.8%
South Africa	95.0%	110.9%	5.0%
Other countries	31.6%	31.2%	0.4%
World total	1.4%	1.4%	0.0%
	Aviation absorption of nickel produced (%)		
	Production in 2019	Production in 2020	Reserves
United	77.8%	65.6%	10.5%
Australia	6.6%	6.2%	0.0%
Brazil	17.3%	14.4%	0.1%
Canada	5.8%	7.0%	0.4%
China	8.7%	8.7%	0.4%
Cuba	21.3%	21.4%	0.2%
Dominican Republic	18.5%	22.3%	0.0%
Indonesia	1.2%	1.4%	0.0%
New Caledonia	5.0%	5.2%	0.0%
Philippines	3.3%	3.3%	0.2%
Russia	3.8%	3.7%	0.2%
Other countries	3.4%	3.6%	0.1%
World total	0.4%	0.4%	0.0%

Table 6.2: Production absorbed by aviation each year for battery substitution on the 10 major mainline fleets and the 10 major regional fleets.

the future demand trends. In other words, the demand for cobalt in batteries will grow with a trend that cobalt production will not be able to meet, due to the limits imposed by its by-product nature. The mitigation strategy proposed in literature to mitigate this risk is the introduction of fuel cells as alternative power sources [196]. On the other hand, a balance between the mined supply and the refined demand can be reached paying attention to investments in refined supply of cobalt as well as in secondary recovery [199]. This could allow a stable price of cobalt. The last and more concrete risk is related to economic situation, institutions, firm behaviour, and

government involvement. This is a high supply risk due to two main reasons: firstly, among the major producers there are also the main polluting countries that would be interested in slowing down the policies aimed to penalize emitters; secondly, the main reserves of cobalt are in geographic area subject to political instability [198].

Thus, drawing a cleaner future in aviation is a complex task since drawbacks on the long period and the large scale must be taken into account. Moreover, the evaluation of the designer choices cannot be confined to the single industrial cluster, project, or region, evaluating the competitiveness of an aircraft according to limited economic interests.

From this perspective, transnational organizations should coordinate the efforts proposing a new roadmap that, passing through the temporary solution of hybrid-electric aircraft, will go to greener and economically feasible alternatives, like fuel cells. It could be argued that fuel cells are composed of anodes and cathodes made by the same materials as the batteries. However, the longer life cycle and the possibility of regenerating the filters makes fuel cell a more promising alternative to e-storage units. From this perspective, the ELICA project is an example of the roadmap to follow.

Bibliography

- [1] Bethan Owen, David S. Lee, and Ling Lim. Flying into the future: Aviation emissions scenarios to 2050, 2010.
- [2] L J Archer. Aircraft emissions and the environment: Cox, sox, hox and nox, Jan 1993.
- [3] M. Gauss, I. S.A. Isaksen, D. S. Lee, and O. A. Søvde. Impact of aircraft NOx emissions on the atmosphere - Tradeoffs to reduce the impact. *Atmospheric Chemistry and Physics*, 2006.
- [4] Youdi Schipper. Environmental costs in European aviation. *Transport Policy*, 2004.
- [5] Lee Chapman. Transport and climate change: a review. *Journal of Transport Geography*, 2007.
- [6] Annela Anger. Including aviation in the European emissions trading scheme: Impacts on the industry, CO2 emissions and macroeconomic activity in the EU. *Journal of Air Transport Management*, 2010.
- [7] Janina Scheelhaase, Wolfgang Grimme, and Martin Schaefer. The inclusion of aviation into the EU emission trading scheme - Impacts on competition between European and non-European network airlines. *Transportation Research Part D: Transport and Environment*, 2010.
- [8] Kelsey Perlman. Addressing aviation emissions under the EU Emissions Trading System. *Carbon Market Watch*, 2017.

- [9] Kaitano Dube, Godwell Nhamo, and David Chikodzi. Covid-19 pandemic and prospects for recovery of the global aviation industry. *Journal of Air Transport Management*, 92:102022, 2021.
- [10] Doaa Salman, Dina Seiam, and Eman Fayaz. How can the aviation sector survive after covid-19? *Virtual Economics*, 3(4):91–105, 2020.
- [11] International Civil Aviation Organization – ICAO. The World of Air Transport in 2017. Technical report, 2017.
- [12] Brandon Graver, Kevin Zhang, and Dan Rutherford. CO2 emissions from commercial aviation, 2018. *Working Paper 2019-16*, (September):13, 2019.
- [13] Moshe Givoni and Piet Rietveld. The environmental implications of airlines' choice of aircraft size. *Journal of Air Transport Management*, 2010.
- [14] Rene Nardi Rezende and Jose Eduardo Mautone Barros. General aviation 2025 – a study in electric propulsion. In *2018 Joint Propulsion Conference*, 2018.
- [15] Krzysztof Piwek and Witold Wisniowski. Small air transport aircraft entry requirements evoked by FlightPath 2050. *Aircraft Engineering and Aerospace Technology*, 2016.
- [16] Engineering National Academies of Sciences and Medicine. *Commercial Aircraft Propulsion and Energy Systems Research: Reducing Global Carbon Emissions*. The National Academies Press, Washington, DC, 2016.
- [17] EASA. European Aviation Safety Agency 'Prototype' Commission Regulation on Unmanned Aircraft Operations. pages 1–72, 2016.
- [18] EASA. Notice of Proposed Amendment 2015-22 (Open rotor engine and installation). Technical report, 2015.
- [19] EASA. Certification Specifications for Normal, Utility, Aerobatic and Commuter Category Aeroplanes CS-23. (July):482, 2012.

- [20] EASA. Certification Specifications for Large Aeroplanes CS-25 Amendment 20. *Easa*, (September), 2017.
- [21] Federal Aviation Regulations. Title 14 — Aeronautics and Space. *US government Printing Office, Washington*, 2015.
- [22] Michael D. Patterson and Nicholas K. Borer. Approach considerations in aircraft with high-lift propeller systems. In *17th AIAA Aviation Technology, Integration, and Operations Conference, 2017*, 2017.
- [23] Saeed Farokhi. *Future Propulsion Systems and Energy Sources in Sustainable Aviation*. 2019.
- [24] Hans Jörg Steiner, Patrick C. Vratny, Corin Gologan, Kerstin Wieczorek, Askin T. Isikveren, and Mirko Hornung. Optimum number of engines for transport aircraft employing electrically powered distributed propulsion. *CEAS Aeronautical Journal*, 2014.
- [25] H.-J. Steiner, P. C. Vratny, C. Gologan, K. Wieczorek, A. T. Isikveren, and M. Hornung. Performance and Sizing of Transport Aircraft Employing Electrically-Powered Distributed Propulsion. In *Deutscher Luft- und Raumfahrtkongress 2012*, 2012.
- [26] Eric Nguyen Van, Pierre Troillard, Joël Jézégou, Daniel Alazard, Philippe Pastor, and Carsten Döll. Reduction of Vertical Tail Using Differential Thrust: Influence on Flight Control and Certification. In *Advanced Aircraft Efficiency in a Global Air Transport System (AEGATS'18)*, pages 1–8, Toulouse, France, November 2018.
- [27] Eric Nguyen Van, Daniel Alazard, Philippe Pastor, and Carsten Döll. Towards an aircraft with reduced lateral static stability using electric differential thrust. In *2018 Aviation Technology, Integration, and Operations Conference*, 2018.

- [28] Gerald V. Brown. Weights and efficiencies of electric components of a turboelectric aircraft propulsion system. In *49th AIAA Aerospace Sciences Meeting Including the New Horizons Forum and Aerospace Exposition*, 2011.
- [29] Engineering National Academies of Sciences and Medicine. *Commercial Aircraft Propulsion and Energy Systems Research: Reducing Global Carbon Emissions*. The National Academies Press, Washington, DC, 2016.
- [30] Michael D. Patterson. Conceptual Design of High-Lift Propeller Systems for Small Electric Aircraft Coceptual Design of High-Lift Propeller. *Dissertation at Georgia Institute of Technology*, 2016.
- [31] Pierluigi Della Vecchia, Daniele Malgieri, Fabrizio Nicolosi, and Agostino De Marco. Numerical analysis of propeller effects on wing aerodynamic: Tip mounted and distributed propulsion. *Transportation Research Procedia*, 29:106–115, 2018.
- [32] Pictographic Representations and Combined Properties. Commercial aircraft propulsion and energy systems research: Reducing global carbon emissions. *Commercial Aircraft Propulsion and Energy Systems Research: Reducing Global Carbon Emissions*, pages 1–122, 2016.
- [33] Bernard L. Koff. Gas turbine technology evolution - a designer's perspective. 2003.
- [34] Kavindu Ranasinghe, Kai Guan, Alessandro Gardi, and Roberto Sabatini. Review of advanced low-emission technologies for sustainable aviation. *Energy*, 188:115945, 2019.
- [35] Gerrit J. J.J.) Ruijgrok and D. M. van Paassen. *Elements of aircraft pollution*. Delft University Press, 2005.
- [36] U.S. Department of Defense. MIL-STD-704F Notice 2 Aircraft Electric Power Characteristics, 2013.

- [37] A. Cavallini, L. Versari, and L. Fornasari. Feasibility of partial discharge detection in inverter-fed actuators used in aircrafts. 2013.
- [38] Efstathios E.(Stathis) Michaelides. Alternative energy sources. *Green Energy and Technology*, 20, 2012.
- [39] Holger Kuhn, C. Falter, and A. Sizmann. Renewable energy perspectives for aviation. *3rd CEAS Air & Space Conference*, 2011.
- [40] L. Q. Maurice, H. Lander, T. Edwards, and W. E. Harrison. Advanced aviation fuels: A look ahead via a historical perspective. *Fuel*, 80, 2001.
- [41] Reynard de Vries, Malcom T Brown, and Roelof Vos. A preliminary sizing method for hybrid-electric aircraft including aero-propulsive interaction effects. *2018 Aviation Technology, Integration, and Operations Conference*, pages 1–29, 2018.
- [42] F Orefice, P Della Vecchia, D Ciliberti, and F Nicolosi. Aircraft Conceptual Design Including Powertrain System Architecture and Distributed Propulsion. In *AIAA Propulsion and Energy Forum - IEEE Symposium*, pages 1–20, 2019.
- [43] Jacopo Zamboni, Roelof Vos, Mathias Emeneth, and Alexander Schneegans. A method for the conceptual design of hybrid electric aircraft. In *AIAA Scitech 2019 Forum*, 2019.
- [44] Sarah J. Gerssen-Gondelach and André P.C. Faaij. Performance of batteries for electric vehicles on short and longer term. *Journal of Power Sources*, 212:111–129, 8 2012.
- [45] Bruno Scrosati and Jürgen Garche. Lithium batteries: Status, prospects and future. *Journal of Power Sources*, 195:2419–2430, 5 2010.
- [46] Keith F. Blurton and Anthony F. Sammells. Metal/air batteries: Their status and potential - a review. *Journal of Power Sources*, 4:263–279, 1 1979.

- [47] Kevin G. Gallagher, Steven Goebel, Thomas Greszler, Mark Mathias, Wolfgang Oelerich, Damla Eroglu, and Venkat Srinivasan. Quantifying the promise of lithium-air batteries for electric vehicles. *Energy and Environmental Science*, 7:1555–1563, 4 2014.
- [48] Anna Elena Scholz, Andreas Hermanutz, and Mirko Hornung. Feasibility analysis and comparative assessment of structural power technology in all-electric composite aircraft. In Deutsche Gesellschaft für Luft- und Raumfahrt (DGLR), editor, *67. Deutscher Luft- und Raumfahrtkongress*, Friedrichshafen, Deutschland, 2018. Deutsche Gesellschaft für Luft- und Raumfahrt (DGLR).
- [49] Kaushik Rajashekara, James Grieve, and David Daggett. Hybrid fuel cell power in aircraft. *IEEE Industry Applications Magazine*, 14:54–60, 2008.
- [50] Thomas Kadyk, Christopher Winnefeld, Richard Hanke-Rauschenbach, and Ulrike Krewer. Analysis and design of fuel cell systems for aviation. *Energies*, 11, 2018.
- [51] Sebastian Nicolay, Yaolong Liu, and Ali Elham. Conceptual design and optimization of a general aviation aircraft with fuel cells and hydrogen. *Aerospace Europe Conference 2020*, 2020.
- [52] M. Santin, A. Traverso, and A. Massardo. Technological aspects of gas turbine and fuel cell hybrid systems for aircraft: A review. *Aeronautical Journal*, 112:459–467, 2008.
- [53] Thomas H. Bradley, Blake A. Moffitt, Dimitri N. Mavris, and David E. Parekh. Development and experimental characterization of a fuel cell powered aircraft. *Journal of Power Sources*, 171:793–801, 2007.
- [54] D Verstraete, K Lehmkuehler, A Gong, J R Harvey, G Brian, and J L Palmer. Characterisation of a hybrid , fuel-cell-based propulsion system for small unmanned aircraft. *Journal of Power Sources*, 250:204–211, 2014.

- [55] Thomas H. Bradley, Blake A. Moffitt, Dimitri N. Mavris, Thomas F. Fuller, and David E. Parekh. Hardware-in-the-loop testing of a fuel cell aircraft powerplant. *Journal of Propulsion and Power*, 25:1336–1344, 2009.
- [56] Grant D. Rhoads, Nick A. Wagner, Brian J. Taylor, Derek B. Keen, and Thomas H. Bradley. Design and flight test results for a 24 hour fuel cell unmanned aerial vehicle. 2010.
- [57] Thomas H. Bradley, Blake A. Moffitt, Thomas F. Fuller, Dimitri N. Mavris, and David E. Parekh. Comparison of design methods for fuel-cell-powered unmanned aerial vehicles. *Journal of Aircraft*, 46:1945–1956, 2009.
- [58] Kolja Seeckt and Dieter Scholz. Jet versus prop, hydrogen versus kerosene for a regional freighter aircraft. In *Deutscher Luft-und Raumfahrtkongress*, volume 121195. Citeseer, 2009.
- [59] Florian M Troeltsch, Marc Engelmann, Anna E Scholz, Fabian Peter, Jochen Kaiser, and Mirko Hornung. Hydrogen powered long haul aircraft with minimized climate impact. In *AIAA AVIATION 2020 FORUM*, page 2660, 2020.
- [60] Snorri Gudmundsson. *General Aviation Aircraft Design : Applied Methods*. 2013.
- [61] Egbert Torenbeek. *Advanced Aircraft Design*. 2013.
- [62] California) Raymer, Daniel (President, Conceptual Research Corporation, Sylmar. *Aircraft Design: A Conceptual Approach*. 2013.
- [63] Egbert Torenbeek. *Synthesis of Subsonic Airplane Design*. 1982.
- [64] J Roskam. Part V: Component weight estimation, 1985.
- [65] D. Felix Finger, Cees Bil, and Carsten Braun. Initial Sizing Methodology for Hybrid-Electric General Aviation Aircraft. *Journal of Aircraft*, 2019.

- [66] C. Pernet and A. T. Isikveren. Conceptual design of hybrid-electric transport aircraft, 2015.
- [67] Carsten Braun Felix Finger, Cees Bil. Initial Sizing Methodology for Hybrid-Electric General Aviation Aircraft e. *AIAA Journal of Aircraft*, pages 1–11, 2019.
- [68] Mark Voskuijl, Joris van Bogaert, and Arvind G. Rao. Analysis and design of hybrid electric regional turboprop aircraft. *CEAS Aeronautical Journal*, 2018.
- [69] Maicon Secchi, Pedro Teixeira Lacava, Luis Gustavo Trapp, and Raphael Felipe Gama Ribeiro. Evaluation of a regional aircraft with fuselage boundary layer ingestion. In *AIAA Propulsion and Energy Forum and Exposition, 2019*, 2019.
- [70] F. Orefice, S. Corcione, F. Nicolosi, D. Ciliberti, and G. De Rosa. Performance calculation for hybrid-electric aircraft integrating aero-propulsive interactions. In *AIAA Scitech 2021 Forum*, 2021.
- [71] Benjamin J Brelje and Joaquim R R A Martins. Electric, hybrid, and turboelectric fixed-wing aircraft: A review of concepts, models, and design approaches. *Progress in Aerospace Sciences*, 104(August 2018):1–19, 2019.
- [72] Francesco Orefice, Pierluigi Della Vecchia, Danilo Ciliberti, and Fabrizio Nicolosi. Correction: Aircraft Conceptual Design Including Powertrain System Architecture and Distributed Propulsion. (August):1–20, 2019.
- [73] Ahmed F. El-Sayed. *Aircraft Propulsion and Gas Turbine Engines*. 2008.
- [74] Trevor M. Young. International Standard Atmosphere (ISA) Table. In *Performance of the Jet Transport Airplane: Analysis Methods, Flight Operations and Regulations*. 2017.
- [75] Njoya M. Souleman, Olivier Tremblay, and Louis A. Dessaint. A generic fuel cell model for the simulation of fuel cell vehicles. 2009.

- [76] Marie-Cécile Péra, Daniel Hissel, Hamid Gualous, and Christophe Turpin. *Electrochemical Components*. 2013.
- [77] Frano Barbir. *PEM fuel cells: theory and practice*. 2013.
- [78] L. Carrette, K. A. Friedrich, and U. Stimming. Fuel cells - fundamentals and applications. *Fuel Cells*, 1, 2001.
- [79] P.T. Moseley. Fuel cell systems explained. *Journal of Power Sources*, 93, 2001.
- [80] J. C. Amphlett, R. M. Baumert, R. F. Mann, B. A. Peppley, P. R. Roberge, and T. J. Harris. Performance modeling of the ballard mark iv solid polymer electrolyte fuel cell: Ii. empirical model development. *Journal of The Electrochemical Society*, 142, 1995.
- [81] D. Guida and M. Minutillo. Design methodology for a pem fuel cell power system in a more electrical aircraft. *Applied Energy*, 192, 2017.
- [82] Johannes Hoefflinger and Peter Hofmann. Air mass flow and pressure optimisation of a pem fuel cell range extender system. *International Journal of Hydrogen Energy*, 45, 2020.
- [83] Seung Won Ji, No Sung Myung, and Tong Seop Kim. Analysis of operating characteristics of a polymer electrolyte membrane fuel cell coupled with an air supply system. *Journal of Mechanical Science and Technology*, 25, 2011.
- [84] A. A. Kulikovskiy. The effect of stoichiometric ratio λ on the performance of a polymer electrolyte fuel cell. *Electrochimica Acta*, 49, 2004.
- [85] Tatyana V. Reshetenko, Guido Bender, Keith Bethune, and Richard Rocheleau. Systematic study of back pressure and anode stoichiometry effects on spatial pemfc performance distribution. *Electrochimica Acta*, 56, 2011.

- [86] Bhaskar Balasubramanian, Frano Barbir, and Jay Neutzler. Optimal operating temperature and pressure of pem fuel cell systems in automotive applications. *ACS Division of Fuel Chemistry, Preprints*, 44, 1999.
- [87] Joseph W. Pratt, Jacob Brouwer, and G. Scott Samuelsen. Performance of proton exchange membrane fuel cell at high-altitude conditions. *Journal of Propulsion and Power*, 23, 2007.
- [88] J. Seddon. Air intakes for aircraft gas turbines. *The Journal of the Royal Aeronautical Society*, 56(502):747–781, 1952.
- [89] Xu Li, Chuanlei Yang, Yinyan Wang, Hechun Wang, Xianghuan Zu, Yongrui Sun, and Song Hu. Compressor map regression modelling based on partial least squares. *Royal Society Open Science*, 5, 2018.
- [90] Xu Li, Yulong Ying, Yinyan Wang, and Jingchao Li. A component map adaptation method for compressor modeling and diagnosis. *Advances in Mechanical Engineering*, 10, 2018.
- [91] Gianluigi Alberto Misté and Ernesto Benini. Improvements in off design aero-engine performance prediction using analytic compressor map interpolation. *International Journal of Turbo and Jet Engines*, 29, 2012.
- [92] Robert McMullen and Yiroto Pino. Conditioning turbocharger compressor map data for use in engine performance simulation. *SAE International Journal of Engines*, 11, 2018.
- [93] Lars Eriksson and Lars Nielsen. *Modeling and Control of Engines and Drivelines*, volume 9781118479995. 2014.
- [94] Patrick Christoph Vratny, Corin Gologan, Clément Pernet, Askin T Isikveren, and Mirko Hornung. Battery Pack Modeling Methods for Universally-Electric Aircraft. *Ceas 2013*, (May 2016):525–535, 2013.

- [95] Félix A. LeBel, Louis Pelletier, Pascal Messier, and João Pedro Trovão. Battery pack sizing method - Case study of an electric motorcycle. In *2018 IEEE Vehicle Power and Propulsion Conference, VPPC 2018 - Proceedings*, 2019.
- [96] Jingsi Lilly. *Aviation Propulsive Lithium-Ion Battery Packs State-of-Charge and State-of-Health Estimations and Propulsive Battery System Weight Analysis*. PhD thesis, 2017.
- [97] Giulio Avanzini, Emanuele L de Angelis, and Fabrizio Giulietti. Optimal performance and sizing of a battery-powered aircraft. *Aerospace Science and Technology*, 59:132–144, 2016.
- [98] C Pernet, S Kaiser, A T Isikveren, and M Hornung. Integrated fuel-battery hybrid for a narrow-body sized transport aircraft. *Aircraft Engineering and Aerospace Technology*, 86(6):568–574, 2014.
- [99] Patrick Christoph Vratny, Corin Gologan, Clément Pernet, Askin T Isikveren, and Mirko Hornung. Battery Pack Modeling Methods for Universally-Electric Aircraft. In *CEAS 2013*, 2013.
- [100] Min Chen and Gabriel A. Rincón-Mora. Accurate electrical battery model capable of predicting runtime and I-V performance. *IEEE Transactions on Energy Conversion*, 2006.
- [101] Olivier Tremblay and Louis A. Dessaint. Experimental validation of a battery dynamic model for EV applications. *World Electric Vehicle Journal*, 2009.
- [102] Ian Cotton, Richard Gardner, Daniel Schweickart, Dennis Grosean, and Christopher Severns. Design considerations for higher electrical power system voltages in aerospace vehicles. In *2016 IEEE International Power Modulator and High Voltage Conference, IPMHVC 2016*, 2017.

- [103] Sebastian Oberschwendtner and Mirko Hornung. The influence of the wiring harness on the system performance of eVTOL aircraft on the example of common reference models. In *76th Annual Forum of the Vertical Flight Society*. The Vertical Flight Society, Oct 2020.
- [104] Wiring aerospace vehicle. Aerospace standard, SAE International, August 2019.
- [105] Adolfo Dannier, Andrea Del Pizzo, Luigi Pio Di Noia, and Santolo Meo. Weight Estimation of the Wiring in a Distributed Propulsion System for Aircraft. In *2019 AEIT International Annual Conference, AEIT 2019*, 2019.
- [106] Mike Holt. Conductors for general wiring : Do you know the rules for selecting and sizing the right conductor for the application? *EC and M: Electrical Construction and Maintenance*, 2017.
- [107] Geoffrey Stokes. *A Practical Guide to the Wiring Regulations*. 2008.
- [108] D. W. Pryer and P. F. Gale. Cables. In *Electrical Engineer's Reference Book: Sixteenth Edition*. 2003.
- [109] Roy Langton, Chuck Clark, Martin Hewitt, and Lonnie Richards. *Aircraft Fuel Systems*. 2009.
- [110] D. Verstraete, P. Hendrick, P. Pilidis, and K. Ramsden. Hydrogen fuel tanks for subsonic transport aircraft. *International Journal of Hydrogen Energy*, 35, 2010.
- [111] G. L. Mills, B. W. Buchholtz, and A. Olsen. Design, fabrication and testing of a liquid hydrogen fuel tank for a long duration aircraft. volume 1434, 2012.
- [112] Davide Comincini and Lorenzo Trainelli. A powertrain sizing method for hydrogen-driven aircraft. *15th Pegasus-AIAA Student Conference*, 2019.
- [113] Anthony J Colozza. Hydrogen storage for aircraft applications overview, 2002.

- [114] Raghu Chaitanya Munjulury, Ingo Staack, Adrián Sabaté López, and Petter Krus. Knowledge-based aircraft fuel system integration. *Aircraft Engineering and Aerospace Technology*, 90, 2018.
- [115] Christopher Winnefeld, Thomas Kadyk, Boris Bensmann, Ulrike Krewer, and Richard Hanke-Rauschenbach. Modelling and designing cryogenic hydrogen tanks for future aircraft applications. *Energies*, 11, 2018.
- [116] Ernest B. Keen and William H. Mason. A conceptual design methodology for predicting the aerodynamics of upper surface blowing on airfoils and wings. volume 2, 2005.
- [117] Pasquale M Sforza. Chapter 10 - Propellers. In Pasquale M B T Theory of Aerospace Propulsion (Second Edition) Sforza, editor, *Aerospace Engineering*, pages 487–524. Butterworth-Heinemann, 2017.
- [118] Joseba Murua, Rafael Palacios, and J. Michael R. Graham. Applications of the unsteady vortex-lattice method in aircraft aeroelasticity and flight dynamics, 2012.
- [119] Robert J.S. Simpson, Rafael Palacios, and Joseba Murua. Induced-drag calculations in the unsteady vortex lattice method. *AIAA Journal*, 2013.
- [120] Michael D. Patterson and Brian J. German. Simplified aerodynamics models to predict the effects of upstream propellers on wing lift. *53rd AIAA Aerospace Sciences Meeting*, (January):1–15, 2015.
- [121] Karen A Deere, Jeffrey K Viken, Sally A Viken, Melissa B Carter, Michael R Wiese, and Norma Farr. Computational analysis of a wing designed for the X-57 distributed electric propulsion aircraft. *35th AIAA Applied Aerodynamics Conference, 2017*, (June), 2017.
- [122] J E Lamar; W J Alford. Aerodynamic-center considerations of wings and wing-body combinations. *NASA Technical Note*, NASA SP-12, 1966.

- [123] Oliviu Şugar Gabor, Andreea Koreanschi, and Ruxandra Mihaela Botez. A new non-linear vortex lattice method: Applications to wing aerodynamic optimizations. *Chinese Journal of Aeronautics*, 2016.
- [124] H Multhopp. Methods for Calculating the Lift Distribution of Wings (Subsonic Lifting-Surface Theory). *Aeronautical Research Council*, 1950.
- [125] Christian Agostinelli, Chenhui Liu, Christian B. Allen, Abdul Rampurawala, and Giovanna Ferraro. Propeller-flexible wing interaction using rapid computational methods. In *31st AIAA Applied Aerodynamics Conference*, 2013.
- [126] Giovanna Ferraro, Timoleon Kipouros, A. Mark Savill, Abdul Rampurawala, and Christian Agostinelli. Propeller-Wing Interaction Prediction for Early Design. In *52nd AIAA Aerospace Sciences Meeting - AIAA Science and Technology Forum and Exposition, SciTech 2014*, 2014.
- [127] Christian Agostinelli, Simone Simeoney, Christian B. Allen, Feng Zhu, and Abdul Rampurawala. A fast approach to model the effects of propeller slipstream on wing load distribution. In *53rd AIAA Aerospace Sciences Meeting*, 2015.
- [128] K. Jacob. Computation of the flow around wings with rear separation. *Journal of Aircraft*, 1984.
- [129] J. D. Anderson. Fundamentals of aerodynamics. 1984.
- [130] M. K. Rwigema. Propeller blade element momentum theory with vortex wake deflection. In *27th Congress of the International Council of the Aeronautical Sciences 2010, ICAS 2010*, 2010.
- [131] A B Haines Young A.D. AGARD. *Scale effects on aircraft and weapon aerodynamics*. AGARD, 1994.

- [132] Mehmet Burak Şenol. Evaluation and prioritization of technical and operational airworthiness factors for flight safety. *Aircraft Engineering and Aerospace Technology*, 92, 2020.
- [133] James Fraser. De florio f. airworthiness, an introduction to aircraft certification,. *Aviation, Space*, 2007.
- [134] EASA. Certification Specifications for Large Aeroplanes. *Cs-25*, 2008.
- [135] Jonathan Menu, Mike Nicolai, and Marc Zeller. Designing fail-safe architectures for aircraft electrical power systems. 2018.
- [136] Lizhi Wang, Yusheng Sun, Xiaohong Wang, Zhuo Wang, and Xuejiao Zhao. Reliability Modeling Method for Lithium-ion Battery Packs Considering the Dependency of Cell Degradations Based on a Regression Model and Copulas. *Materials (Basel, Switzerland)*, 12(7):1054, mar 2019.
- [137] Pasquale M. Sforza. *Commercial Airplane Design Principles*. 2014.
- [138] Antonio Filippone. *Advanced aircraft flight performance*. 2010.
- [139] Dieter Scholz. *Aircraft Systems*. McGraw-Hill Education, 2018.
- [140] Fabrizio Nicolosi, Pierluigi Della Vecchia, Danilo Ciliberti, and Vincenzo Cusati. Fuselage aerodynamic prediction methods. *Aerospace Science and Technology*, 55, 2016.
- [141] Karen A. Deere, Sally A. Viken, Melissa B. Carter, Jeffrey K. Viken, Michael R. Wiese, and Norma Farr. Computational analysis of powered lift augmentation for the LEAPTech distributed electric propulsion wing. In *35th AIAA Applied Aerodynamics Conference, 2017*, 2017.
- [142] John R. Wilson and Timothy T. Takahashi. The doghouse plot: History, construction techniques, and application. 2017.
- [143] Trevor M. Young. *Performance of the Jet Transport Airplane: Analysis Methods, Flight Operations and Regulations*. 2017.

- [144] Douglas P. Wells, Bryce L. Horvath, and Linwood A. McCullers. The Flight Optimization System Weight Estimation Method. *Nasa/Tm-2017-219627*, 2017.
- [145] Charlie Svoboda. Turbofan engine database as a preliminary design tool. *Aircraft Design*, 2000.
- [146] Michel Armand, Peter Axmann, Dominic Bresser, Mark Copley, Kristina Edström, Christian Ekberg, Dominique Guyomard, Bernard Lestriez, Petr Novák, Martina Petranikova, Willy Porcher, Sigita Trabesinger, Margret Wohlfahrt-Mehrens, and Heng Zhang. Lithium-ion batteries – Current state of the art and anticipated developments. *Journal of Power Sources*, 2020.
- [147] C. M. Costa, E. Lizundia, and S. Lanceros-Méndez. Polymers for advanced lithium-ion batteries: State of the art and future needs on polymers for the different battery components, 2020.
- [148] Jinqing Sun, Zhuzhu Du, Yuhang Liu, Wei Ai, Ke Wang, Tian Wang, Hongfang Du, Lei Liu, and Wei Huang. Li-Se Batteries: State-Of-The-Art and Future Challenges in High Energy Lithium–Selenium Batteries (Adv. Mater. 10/2021). *Advanced Materials*, 2021.
- [149] Seongyun Park, Jeongho Ahn, Taewoo Kang, Sungbeak Park, Youngmi Kim, Inho Cho, and Jonghoon Kim. Review of state-of-the-art battery state estimation technologies for battery management systems of stationary energy storage systems, 2020.
- [150] Ghassan Zubi, Rodolfo Dufo-López, Monica Carvalho, and Guzay Pasaoglu. The lithium-ion battery: State of the art and future perspectives, 2018.
- [151] T. H.G. Megson. *Aircraft Structures for Engineering Students*. 2013.
- [152] Jorge Luis González-Velázquez. *Stress*, pages 1–42. Springer International Publishing, Cham, 2020.

- [153] Egbert Torenbeek. *Synthesis of subsonic airplane design: an introduction to the preliminary design, of subsonic general aviation and transport aircraft, with emphasis on layout, aerodynamic design, propulsion, and performance*. Delft University Press, Delft, 1982.
- [154] Christian B. Hoover, Jinwei Shen, Andrew R. Kreshock, Bret K. Stanford, David J. Piatak, and Jennifer Heeg. Whirl flutter stability and its influence on the design of the distributed electric propeller aircraft x-57. 2017.
- [155] Pezhman Mardanpour, Dewey H. Hodges, and Reza Rezvani. Nonlinear aeroelasticity of high-aspect-ratio wings excited by time-dependent thrust. *Nonlinear Dynamics*, 75, 2014.
- [156] W. G. Molyneux. Approximate formulae for flutter prediction: With particular reference to main surface flexure-torsion flutter in the transonic region. volume 32, 1960.
- [157] Pezhman Mardanpour and Dewey H. Hodges. On the importance of nonlinear aeroelasticity and energy efficiency in design of flying wing aircraft. *Advances in Aerospace Engineering*, 2015, 2015.
- [158] Pezhman Mardanpour, Dewey H. Hodges, Ryan Neuhart, and Nathan Graybeal. Engine placement effect on nonlinear trim and stability of flying wing aircraft. volume 50, 2013.
- [159] V Memmolo, A D Marano, L Maio, F Nicolosi, and F Marulo. Aeroelastic assessment of distributed electric propulsion wings. 2021.
- [160] Vittorio Memmolo, Francesco Orefice, Fabrizio Nicolosi, and Fabrizio Ricci. Design of near-zero emission aircraft based on refined aerodynamic model and structural analysis. 2021.
- [161] Dominik Felix Finger, Carsten Braun, and Cees Bil. A Review of Configuration Design for Distributed Propulsion Transitioning VTOL Aircraft. *Asia-Pacific International Symposium on Aerospace Technology, Seoul, Korea*, 2017.

- [162] Carlo E.D. Riboldi, Federico Gualdoni, and Lorenzo Trainelli. Preliminary weight sizing of light pure-electric and hybrid-electric aircraft. In *Transportation Research Procedia*, 2018.
- [163] Maicon Secchi, Pedro Teixeira Lacava, Gustavo Luis Trapp, and Raphael Felipe Gama Ribeiro. Evaluation of a Regional Aircraft with Fuselage Boundary Layer Ingestion. (August):1–17, 2019.
- [164] F Orefice, F Nicolosi, P Della Vecchia, and D Ciliberti. Conceptual Design of Commuter Aircraft including Distributed Electric Propulsion. pages 1–18, 2020.
- [165] D. Felix Finger, Reynard de Vries, Roelof Vos, Carsten Braun, and Cees Bil. A Comparison of Hybrid-Electric Aircraft Sizing Methods. 2020.
- [166] Tyler S. Dean, Gabrielle E. Wroblewski, and Phillip J. Ansell. Mission analysis and component-level sensitivity study of hybrid-electric general-aviation propulsion systems. *Journal of Aircraft*, 2018.
- [167] Gabrielle E. Wroblewski and Phillip J. Ansell. Mission analysis and emissions for conventional and hybrid-electric commercial transport aircraft. *Journal of Aircraft*, 2019.
- [168] Sydney L. Schnulo, Dustin L. Hall, Jeffrey C. Chin, and Andrew D. Smith. Further development of the nasa x-57 maxwell mission planning tool for mods ii, iii, and iv. In *AIAA Propulsion and Energy Forum and Exposition, 2019*, 2019.
- [169] C. Friedrich and P. A. Robertson. Hybrid-electric propulsion for aircraft. In *Journal of Aircraft*, 2015.
- [170] Matthias Strack, Gabriel Pinho Chiozzotto, Michael Iwanizki, Martin Plohr, and Martin Kuhn. Conceptual Design Assessment of Advanced Hybrid Electric Turboprop Aircraft Configurations. In *17th AIAA Aviation Technology*,

- Integration, and Operations Conference*, Reston, jun 2017. American Institute of Aeronautics and Astronautics.
- [171] A T Isikveren, S Kaiser, Clément Pernet, and P C Vratny. Pre-design strategies and sizing techniques for dual-energy aircraft. *Aircraft Engineering and Aerospace Technology*, 86(6):525–542, 2014.
- [172] C E D Riboldi and F Gualdoni. An integrated approach to the preliminary weight sizing of small electric aircraft. *Aerospace Science and Technology*, 58:134–149, 2016.
- [173] Gokcin Cinar, Dimitri N Mavris, Mathias Emeneth, Alexander Schneegans, Carsten Riediger, Yann Fefermann, and Askin Isikveren. Sizing, integration and performance evaluation of hybrid electric propulsion subsystem architectures. *AIAA SciTech Forum - 55th AIAA Aerospace Sciences Meeting*, (January 2017):1–18, 2017.
- [174] Taewoo Nam, Danielle S Soban, and Dimitri N Mavris. Power based sizing method for aircraft consuming unconventional energy. In *43rd AIAA Aerospace Sciences Meeting and Exhibit - Meeting Papers*, 2005.
- [175] Gabrielle E Wroblewski and Phillip J Ansell. Mission analysis and emissions for conventional and hybrid-electric commercial transport aircraft. *AIAA Aerospace Sciences Meeting, 2018*, (210059):1–22, 2018.
- [176] Tyler S Dean, Gabrielle E Wroblewski, and Phillip J Ansell. Mission analysis and component-level sensitivity study of hybrid-electric general aviation propulsion systems. *AIAA Aerospace Sciences Meeting, 2018*, (210059):1–18, 2018.
- [177] Karen A. Deere, Sally A. Viken, Melissa B. Carter, Jeffrey K. Viken, Joseph M. Derlaga, and Alex M. Stoll. Comparison of high-fidelity computational tools for wing design of a distributed electric propulsion aircraft. In *35th AIAA Applied Aerodynamics Conference, 2017*, 2017.

- [178] Tomas Sinnige, Nando Van Arnhem, Tom C.A. Stokkermans, Georg Eitelberg, and Leo L.M. Veldhuis. Wingtip-mounted propellers: Aerodynamic analysis of interaction effects and comparison with conventional layout. *Journal of Aircraft*, 56(1):295–312, nov 2019.
- [179] Francesco Orefice, Fabrizio Nicolosi, Salvatore Corcione, and Pierluigi Della Vecchia. Hybridization and mission analysis of a regional turboprop. 2021.
- [180] Gilbert Tay, Paul Keller, and Mirko Hornung. Development of a software tool for comprehensive flight performance and mission analysis of hybrid-electric aircraft. In *Transportation Research Procedia*, 2018.
- [181] Vittorio Cipolla and Fabrizio Oliviero. Hysim: A simulation tool for hybrid aircraft performance analysis. In *Variational Analysis and Aerospace Engineering*, pages 95–116. Springer, 2016.
- [182] Giulio Avanzini and Fabrizio Giulietti. Maximum range for battery-powered aircraft. *Journal of Aircraft*, 50(1):304–307, 2013.
- [183] Jeremias Fleger. Modeling of propulsion architectures for hybrid-electric commuter aircraft with fault tolerance analysis. Master’s thesis, Technical University of Munich, 12 2021.
- [184] Diego Giuseppe Romano, Gianvito Apuleo, and Jiri Duda. Affordable and environmental friendly small commuter aircraft improving european mobility. *International Journal of Aerospace and Mechanical Engineering*, 14(9):341 – 349, 2020.
- [185] M Dareck, C Edelstenn, and T Ender. Flightpath 2050 europe’s vision for aviation, 2011.
- [186] Dominik Eisenhut, Nicolas Moebs, Evert Windels, Dominique Bergmann, Ingmar Geiß, Ricardo Reis, and Andreas Strohmayer. Aircraft requirements for sustainable regional aviation. *Aerospace*, 8, 2021.

- [187] Askin T Isikveren, Clément Pernet, Patrick Christoph Vratny, and Michael Schmidt. Conceptual Studies of Future Hybrid Electric Regional Aircraft. *Isabe 2015*, (November):1–20, 2015.
- [188] Antonio Filippone and Nicholas Bojdo. Statistical model for gas turbine engines exhaust emissions. *Transportation Research Part D: Transport and Environment*, 59:451–463, 2018.
- [189] European Aviation Safety Agency. Certification Specifications for Normal, Utility, Aerobatic and Commuter Category Aeroplanes (CS-23). *Director*, 2003.
- [190] International Standards Organization. En iso 14040:2006. *Environmental Management*, 14040, 2006.
- [191] Russell W Stratton, Hsin Min Wong, James I Hileman, et al. Life cycle greenhouse gas emissions from alternative jet fuels. *PARTNER project*, 28:133, 2010.
- [192] Thomas M. McCollom, Frieder Klein, Mark Robbins, Bruce Moskowitz, Thelma S. Berquó, Niels Jöns, Wolfgang Bach, and Alexis Templeton. Temperature trends for reaction rates, hydrogen generation, and partitioning of iron during experimental serpentization of olivine. *Geochimica et Cosmochimica Acta*, 181:175–200, 2016.
- [193] Bruce E Logan, Douglas Call, Shaoan Cheng, Hubertus VM Hamelers, Tom HJA Sleutels, Adriaan W Jeremiasse, and René A Rozendal. Microbial electrolysis cells for high yield hydrogen gas production from organic matter. *Environmental science & technology*, 42(23):8630–8640, 2008.
- [194] Linda Gaines, John Sullivan, Andrew Burnham, and Ilias Belharouak. Life-cycle analysis for lithium-ion battery production and recycling. In *Transportation Research Board 90th Annual Meeting, Washington, DC*, pages 23–27, 2011.

- [195] Fauzia Dianawati and Liananda Deliputri. Destination and number of flight determination using multi objective goal programming and integer linear programming. In *Proceedings of the 4th International Conference on Industrial and Business Engineering, ICIBE' 18*, page 60–64, New York, NY, USA, 2018. Association for Computing Machinery.
- [196] Gary A Campbell. The cobalt market revisited. *Mineral Economics*, 33(1):21–28, 2020.
- [197] Gary Campbell. The marketing of cobalt. In *Natural resources forum Dordrecht*, volume 7, pages 81–82, 1983.
- [198] Christoph Helbig, Alex M Bradshaw, Lars Wietschel, Andrea Thorenz, and Axel Tuma. Supply risks associated with lithium-ion battery materials. *Journal of Cleaner Production*, 172:274–286, 2018.
- [199] Xinkai Fu, Danielle N Beatty, Gabrielle G Gaustad, Gerbrand Ceder, Richard Roth, Randolph E Kirchain, Michele Bustamante, Callie Babbitt, and Elsa A Olivetti. Perspectives on cobalt supply through 2030 in the face of changing demand. *Environmental science & technology*, 54(5):2985–2993, 2020.